A buffer-gas cooled Bose-Einstein condensate

A thesis presented
by

Stephen Charles Doret

to
The Department of Physics
in partial fulfillment of the requirements
for the degree of
Doctor of Philosophy
in the subject of

Physics

Harvard University
Cambridge, Massachusetts
October 2009

©2009 - Stephen Charles Doret

All rights reserved.

Thesis advisor | Author

John Morrissey Doyle | **Stephen Charles Doret**

A buffer-gas cooled Bose-Einstein condensate

Abstract

We report the creation of a Bose-Einstein condensate using buffer-gas cooling, the first realization of BEC using a method which relies neither on laser cooling nor unique atom-surface properties. Metastable helium (^{4}He*) is buffer-gas cooled and magnetically trapped using an optimized buffer-gas trapping apparatus, followed by evaporative cooling to quantum degeneracy. Evaporative cooling proceeds in two stages, each traversing approximately five orders of magnitude in phase space density. An initial stage of evaporation uses a surface to adsorb atoms, while a later stage uses radio-frequency induced spin-flips to evaporate atoms. Trapped atoms are detected using absorption and phase-contrast imaging both *in-situ* and in time-of-flight expansion. 10^{11} atoms are initially trapped, leading to Bose-Einstein condensation at a critical temperature of 5 μK and threshold atom number of 1.1×10^6. The method developed here is applicable to a wide array of paramagnetic atoms as well as molecules, many of which are impractical to laser cool and all of which are impossible to surface cool.

Contents

List of Figures

List of Tables

Citations to Previously Published Work

Portions of this thesis have appeared previously in the following papers:

> "Buffer-gas cooled Bose-Einstein condensate," S. Charles Doret, Colin B. Connolly, Wolfgang Ketterle, and John M. Doyle, *(Phys. Rev. Lett.* **103**, 103005 (2009). [1]

> "Evaporative cooling of metastable helium in the multi-partial-wave regime," Scott V. Nguyen, S. Charles Doret, Colin B. Connolly, Robert A. Michniak, Wolfgang Ketterle, and John M. Doyle, *Phys. Rev. A* **72**, 060703(R) (2005). [2]

Acknowledgements

Getting a PhD has been a long and sometimes arduous process. Thanks to:

Professor John Doyle, my PhD advisor, for knowing when to push and when to hang in the background. I imagine that one of the few tasks that can be more frustrating than doing physics experiments is advising a frustrated experimenter — particularly in cryogenics — and John does so with understanding and grace. Also not to be overlooked is his essential role in providing a well funded laboratory; sometimes problems can be best solved with subtle application of money, and it has been a blessing to have an advisor who was occasionally more inclined to spend than I was.

Professor Wolfgang Ketterle (M.I.T.), the project co-PI, for knowing the answers to so many questions, and for anticipating the questions I should have asked. It is impossible to overstate the advantages of working with someone who has spent his career developing and perfecting so many of the techniques used to accomplish the work described in this thesis. Wolfgang also generously loaned us the camera used for the imaging discussed in this thesis.

Colin Connolly, my fellow basement-dweller, with whom I spent so many hours over the past five years. His contributions have been innumerable, but thanks especially for dealing with literally all of the LabView headaches. Also, thanks to Nathalie Roy (Colin's wonderful wife) and to the Harvard Cycling Association morning rides, both of which contributed to keeping Colin's schedule sensible, and thus mine by association.

Nathaniel Brahms, who wrote the *MATLAB* code used for spectrum simulations, and who held my hand every time I did something foolish that made it not work as expected.

Dave Patterson, who had the idea of making peel-off Teflon magnet coil forms and who showed me how to operate the (hated) coil winding machine.

Jack Harris and Bob Michniak, who built the original iteration of the experimental apparatus, and Scott Nguyen, who was the lead student on the early metastable helium work.

The Doyle group as a whole, for making the time spent at the lab pleasant and often fun even at those moments when the experiment itself was not. Even after two thousand lunchtime conversations I continue to be entertained; thank you for discussing movies, politics, and the Red Sox instead of physics.

Jim MacArthur, Harvard's truly brilliant electronics wizard. He put up with my foolish questions while also solving the hard problems we threw his way, particularly with respect to stabilizing and shutting off the QUIC trap. Ask for his rag-doll impression if you need a pick-me-up in the middle of a long afternoon of soldering.

Stan Cotreau, the machinist in the physics shop, whose expertise and wry sense of humor could at times make time in the shop feel a lot more rewarding than time in the lab.

Professor Tiku Majumder (Williams College), who probably thought I would leave him alone when I finished my bachelor's degree seven years ago yet has graciously continued to provide advice whenever asked.

Finally, special thanks to my parents and sister, who have always provided endless encouragement for all of my endeavors, and to my wife Lida, who has always acted interested when I was enthusiastic about graduate school while never asking questions when I was not.

Chapter 1

Introduction

Were they alive today, surely Bose and Einstein would be proud. The quantum-statistical phenomenon they described in 1924-1925 (Bose-Einstein condensation, or BEC) [3–5] was initially dismissed as "having only a purely imaginary existence" before being linked to the λ-point in liquid helium [6], but we now recognize their early papers as the seminal works in a rapidly growing, rich, new field: research with ultracold atoms and molecules. Whereas physics waited 70 years for a clear experimental signature of a nearly-pure BEC to be achieved in a dilute system with well understood interactions in 1995 [7–9], in the 14 years since then the field spawned by this work has exploded with new research. Building on those first BECs we have now seen BEC in several novel species [10–16] as well as the production of quantum degenerate Fermi gases [17, 18]. Newer developments include work in coherent atom and molecular optics [19, 20] and nonlinear atom optics [21, 22], observation of superfluidity in atomic gases [23, 24], study of the BEC-BCS crossover [25–28], and research with new quantum systems [29, 30].

Despite the breadth of this new research, the fundamental technologies underlying cold atom research remain largely the same as those used in 1995: laser precooling [31–33] of a hot atomic sample to achieve low temperatures and high densities, followed by magnetic trapping [34, 35] and evaporative cooling [36, 37] to reach quantum degeneracy. The field thus relies critically on this initial laser cooling step, limiting both the number/density [38–40] of atoms that may be trapped and the classes of species which may be cooled [33]. Efforts to develop new cooling strategies that relax or remove these limitations are ongoing in many groups worldwide, including mechanical techniques [41, 42], electric and magnetic decelerators [43, 44], and buffer-gas cooling [45]. Buffer-gas cooling has been quite successful in this regard, having demonstrated cooling and trapping of more than 20 species (including alkalis, transition metals, rare-earths, metastable helium, and several molecules), and has also trapped samples with atom or molecule number several orders of magnitude larger than those cooled using lasers (see [46] and references therein). However, buffer-gas cooling has generally been limited to working with cold (rather than ultracold) atoms and molecules. The work described in this thesis extends buffer-gas methods to the quantum degenerate regime, demonstrating the first creation of a quantum degenerate gas using techniques that rely neither on laser cooling nor singularly unique atom-surface interactions (as with ^{1}H [10]).

1.1 Research with cold atoms and molecules

Research with cold, ultracold, and quantum degenerate gases is a diverse and changing field. Motivated initially by the fundamental physics and precision measurement community, the field has expanded into new areas of quantum computation and quantum simulation, blurring the boundaries between “traditional” atomic physics, information theory, and condensed matter. Here we briefly introduce some of the sub-fields utilizing cold gases.

Precision measurement

Use of cold atoms and molecules benefits precision measurements in three key ways. First, cold particles travel slowly, giving rise to reduced Doppler shifts and correspondingly narrowed resonance lines for cooled samples. Though first-order shifts may be removed using Doppler-free spectroscopic techniques, experiments with sufficient precision to note contributions from second-order Doppler effects require cooling [47–49]. Second, slow moving atoms allow for lengthened measurement time, permitting improved sensitivity, especially for Ramsey-type measurements. Both of these benefits are particularly important for metrology and atomic clocks. Finally, cold samples often offer improved state selection/purity, particularly with molecular samples that are often distributed among many rovibrational states. Increasing numbers of experiments propose to take advantage of these benefits, including searches for time variation of fundamental constants [50] and the permanent electric dipole moment (EDM) of the electron [51, 52] using cold molecules.

Cold collisions

Cold or quantum degenerate gases provide a superb laboratory for studying fundamental questions in quantum mechanics. Whereas at higher energies particles behave classically, interactions at low temperature can be dominated by quantum mechanical effects. For example, collisions between low temperature atoms or molecules are quite sensitive to details of the inter-atomic potentials [53, 54], and shape resonances that may be quite pronounced for mono-energetic collisions are averaged over by broader thermal distributions [55]. Low temperature samples also offer the opportunity to study cold chemistry, and even to control chemical reactions through the use of laboratory fields [56] in ways not possible at room temperature.

Atom optics

The production of ultracold atoms and molecules makes possible the study of atom optics, in which the deBroglie waves of the particles interfere, as with light in conventional optics experiments. Use of atoms rather than light, however, has opened a door to both improved measurement techniques and new experiments probing quantum mechanical behavior. BECs have been used to generate atom number-squeezed states that may lead to improved atom-interferometry based detectors [57], and current atom-interferometry based gyroscopes rival conventional rotation sensors [58]. Experiments have also shown atom-atom correlation effects resulting from quantum statistics, demonstrating bunching [59] and anti-bunching [60] between ultracold atoms.

Many-body physics

A particular advantage of ultracold atom experiments is that they provide clean, simple systems for the study of many existing models from many-body physics and condensed matter [61]. Use of different atomic or molecular species (such as polar molecules or strongly magnetic atoms like Cr or Dy) makes it possible to change the nature or range of interactions between particles. Furthermore, when combined with a Feshbach resonance [62, 63] ultracold atom systems afford the ability to tune the strength and the sign of inter-particle interactions, providing an additional knob to turn while exploring disparate limits of a theory. For example, Feshbach resonances in Fermi gases have been used to investigate the BEC-BCS crossover, reversibly tuning the interaction from the BEC side of the resonance (where pairs of atoms are tightly bound into molecules) to the BCS side (weakly attracting pairs, as in metallic superconductors or superfluid ^{3}He).

Ultracold gases may also be combined with optical potentials to realize more complicated strongly-correlated configurations. Optical lattices can be used to create 1D or 2D gases, or to model solids, with the optical lattice replacing the regular array of ion cores in a crystal. Such systems permit simulation of Hamiltonians, such as extensions to the Bose-Hubbard model [30, 64]. Experiments with these systems can provide insight into unresolved questions in condensed matter physics, such as the origin of high-T_c superconductivity, and may allow investigation of regimes not accessible in conventional condensed-matter physics.

Quantum computation and quantum information

Quantum computation, in which superpositions of two-state quantum systems are used as quantum bits (qubits) to store and process information, has become one of the fastest growing areas of research. Proposals for building such a computer in many different media exist; those of interest to atomic physics utilize cold, trapped ions [65], polar molecules [66, 67], and atoms [68, 69]. Compared to solid state alternatives, atomic systems generally have significantly better coherence properties. These systems have other advantages as well. Scaling to many qubits is quite natural, since trapping arrays of particles on a chip or in an optical lattice is already a solved problem. Individual addressing of qubits may be achieved with laser or microwave fields, discriminating between adjacent sites in real or frequency space, respectively. Coupling between atomic and photonic qubits has also been demonstrated (see [70] and references therein), providing an avenue for distributed computing and secure communication over long distances using optical fibers. Though many challenges remain, the fidelity of operations in these systems are steadily improving, and trapped ion, atom, or molecule systems are excellent candidates for future quantum computing applications.

1.2 Cooling and Trapping

The initial step in any research with cold atoms or molecules must necessarily be to face the challenge of getting the sample cold in the first place. While in some experiments there is no particular target temperature that must be achieved (for example, when using a beam in EDM experiments), in a freely moving gas the temperature of the particles sets a limit on the possible duration of the experiment. For a "typical" atom or molecule[1] the thermal velocity at 1 K is of order 25 m/s. In a standard 1 m scale vacuum chamber, then, experiments cannot last longer than about 40 msec without the gas colliding with the chamber walls. These collisions are problematic; with the exception of helium[2] any gas in equilibrium with a wall at this temperature will condense.

With this restriction in mind, nearly all research with cold atoms or molecules turns to some sort of trap to hold the gas in place and isolate it from its environment. Trapping, however, does set a stringent limit on the maximum temperature of any gas we wish to study. In order for our trap to be able to confine a significant fraction of a gas cooled to a temperature T we require that

$$T \lesssim \frac{U_{trap}}{k_B}, \tag{1.1}$$

where U_{trap} defines the depth of some local minimum of the potential energy of particles in our trap. The achievable trap depth U_{trap} is dependent both on the type

---

[1] arbitrarily defined to have a mass of roughly 40 amu

[2] and spin-polarized hydrogen; see section 1.2.2

and geometry of the trap used as well as the details of the species to be trapped, and varies from less than 100 μK to more than 10 K.

1.2.1 Traps for neutral atoms and molecules

Experiments with cold atoms and molecules rely principally on three different trap types: optical, electric (static and AC), and magnetic.

Optical traps

Optical traps take advantage of the AC Stark effect, in which the energy eigenvalues of an atom or molecule are shifted in the presence of a rapidly oscillating laser field. For a two level atom the calculation of these "light shifts" is straightforward [33, §1.2]. Assuming a laser with Rabi frequency Ω and detuning δ, in the limit that $\Omega \ll |\delta| \ll \omega_{res}$ the ground state is shifted by

$$\Delta E = \frac{\hbar\Omega^2}{4\delta}. \tag{1.2}$$

As such, for negative δ (red-detuning) atoms are attracted to the high-intensity center of a laser beam. Experiments have used optical traps in a number of different ways. The simplest is to focus a single beam, providing tight confinement in the transverse dimension and looser confinement along the axial dimension. Tight confinement in all directions may be achieved using crossed lasers; "boxes" have also been constructed using sheets of blue-detuned light, thereby repeling the trapped particles away from the box. These various configurations allow a wide range of options in terms of trap shapes and volume, and offer superb access for manipulating or probing the trapped particles.

Unfortunately, in practice optical traps have quite limited trap depths. For a two-level atom with transition strength Γ, photons are scattered at a rate

$$\gamma_s = \frac{\Omega^2\Gamma}{4\delta^2}. \tag{1.3}$$

Thus to avoid excessive scattering of photons (and corresponding heating) during an experiment one must work in the limit of large detuning, reducing the strength of the trapping potential. Typically powerful, focused IR lasers are used to generate the deepest traps possible while maintaining low scattering rates, but at the expense of small trap volumes. For example, a 10 W, 1064 nm YAG laser focused to a 25 μm waist yields a 1.5 mK trap depth for sodium. CO_2 lasers may also be used to further reduce photon scattering at the expense of making traps shallower still.

Electric traps

Like optical traps, electric traps are also based on Stark shifts. However, in this case atoms or molecules are trapped utilizing energy shifts due to the DC Stark effect. As such, achievable trap depths are strongly dependent on whether the species to be trapped may be fully polarized by an applied field. Using maximum realizable laboratory fields of order tens of kV/cm this is impossible for atoms, thus for an electric field $\mathcal{E}$ energies shift quadratically according to

$$\Delta E = -\alpha\,\mathcal{E}^2, \tag{1.4}$$

where α is the atomic polarizability. For molecules the situation is generally quite different. Due to the presence of rotational levels, Ω doublets, etcetera, molecules have low lying excited states of opposite parity which often may be completely mixed with laboratory fields, polarizing the molecule and giving rise to a dipole moment $\vec{d}$. This leads to a linear Stark shift of the form

$$\Delta E = \vec{d} \cdot \vec{\mathcal{E}}. \tag{1.5}$$

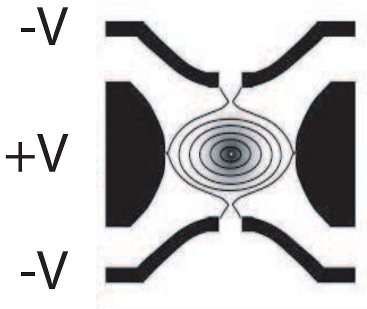

Figure 1.1: An electrostatic quadrupole trap (from [72]).

Ground state atomic polarizabilities vary over more than two orders of magnitude and are largest for the alkalis [71], but average perhaps a few tens of atomic units.[3] This gives maximum trap depths of only a few hundred microKelvin. In contrast, heteronuclear molecules often have dipole moments as large as a Debye[4] or more, yielding trap depths of 24 $\frac{|\vec{d}|}{\mathrm{D}}\frac{\mathrm{mK}}{\mathrm{kV/cm}}$.

Many different varieties of electric traps have been designed, including both electrostatic [72] and electrodynamic [73, 74] varieties of varying geometries, as well as chip traps [67]. For static traps the simplest geometry is a quadrupole trap, as in figure 1.1. Such a trap is quite useful for polar molecules, but less so for atoms due to limited trap depth and the requirement that the atom be trapped in a low-field seeking (and therefore electronically excited) state. Electrodynamic traps are noteworthy in that they permit the trapping of "high-field seeking" states which cannot be trapped in static fields.

Though deep microwave traps have not yet been realized, they in particular should offer a number of advantages for trapping polar molecules [74]. As microwave traps permit the trapping of high-field seeking states, molecules can be trapped in their

---

[3] the atomic unit for polarizability is $\frac{m_e e^2 a_o^4}{\hbar^2}$

[4] 1 D = .4 ea_o = 2.08×10^{-9} e-cm

absolute ground state. This eliminates the possibility of two-body inelastic collisions, which can be greatly enhanced in molecules as compared to atoms due to the additional rotational degrees of freedom. Suitably built traps should afford large trap depths (> 1 K) and substantial trapping volumes (> 1 cm^{-3}), making loading more straightforward than for some other traps. Use of open trapping geometries (such as a Fabry-Perot microwave cavity) permits excellent optical access, making possible the introduction of optical traps or the overlap of trapped molecules with a magneto-optical trap of atoms to be used for sympathetic cooling. Perhaps most importantly, the strong-field seeking states that may be trapped reside in the region of maximum field, so that the trapped molecules are electrically polarized. This gives rise to large dipole-dipole interactions and enormous elastic collision cross sections, opening the possibility of evaporative cooling even at low molecule densities [74].

Magnetic traps

Magnetic traps utilize the Zeeman shift of atomic or molecular states in the presence of a $\vec{B}$ field, according to

$$\Delta E = \vec{\mu} \cdot \vec{B}, \tag{1.6}$$

where $\vec{\mu}$ is the magnetic dipole moment of the state in question. $\vec{\mu}$ has contributions from the intrinsic magnetic moment of each of the constituent particles of the atom (protons, neutrons, and electrons), as well as a contribution from electronic orbital angular momentum. However, since nuclear magnetic moments are about three orders of magnitude smaller than electronic ones, for most practical purposes we may consider an atom or molecule to be magnetically “neutral” unless it contains unpaired electron spins. Even so, approximately two-thirds of the naturally occuring elements have at least one such unpaired electron. The intrinsic moment of the electron thus

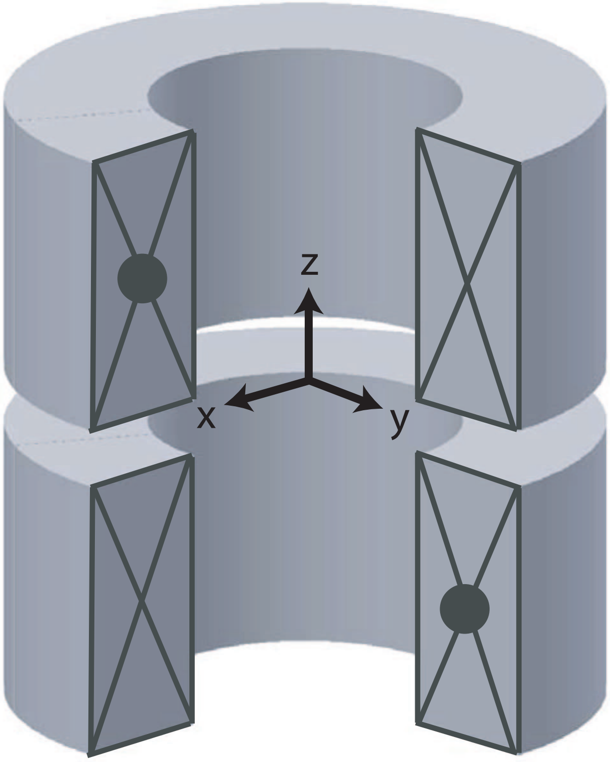

Figure 1.2: A magnetic quadrupole trap.

sets the natural energy scale for magnetic trapping: 1 $\mu_B = 0.67$ K/T.

As with electric traps, only low-field seeking states may be trapped using DC fields since magnetic field maxima cannot be formed in free space [34]. Thus the simplest geometry for creating a local magnetic field minimum is again a quadrupole field, here generated with an anti-Helmholtz magnet, as in figure 1.2. With superconducting coils useful trapping fields of approximately four Tesla are possible [75], yielding trap depths of 2.67 K/μ_B. Large trapping volumes may also be realized. Whereas optical trap volumes are of order 100 μm^3 and electric traps less than 1 cm^3, deep magnetic traps may be built with trap volumes of 100 cm^3, permitting trapping of large numbers of atoms or molecules.

1.2.2 Atom and molecule cooling methods

In light of equation 1.1 and the depths of the traps described above, it is clear that no atom or molecule may be trapped without cooling to temperatures significantly lower than those at which gaseous samples are produced in ovens, etcetera. There exist three general strategies for cooling, including using interactions with light, direct contact with a cold surface, and collisions with a cold gas. Here we describe the advantages and limitations of each strategy.

Laser cooling

Laser cooling, an implementation of cooling with light, is by far the most widely used method for cooling atoms so that they may be trapped. Most often when one refers to laser cooling s/he is thinking of Doppler cooling, in which the absorption and spontaneous emission of red-detuned photons are used to slow an atom's motion. The Doppler shift of a moving atom leads to it preferentially absorbing photons when it is counter-propagating with the laser, each of which gives momentum kicks of $\sim \hbar k$, slightly slowing its motion. This method permits slowing the atom to the point that its Doppler shift is comparable to half its natural linewidth, the so-called "Dopper limit," which is approximately 100 μK for strong transitions [33]. More involved cooling techniques approach the recoil temperature ($\sim$ 1 μK). The combination of these methods has made laser cooling a natural choice for loading traps for experiments with cold atoms, as even shallow optical traps may be loaded directly from laser-cooled samples [76].

Because they slow atoms one photon momentum kick at a time, a common feature of laser cooling techniques is that they require the scattering of many, many photons. Efficient cooling requires the use of a strong, technologically accessible transition, "closed" against decay to non-resonant states. While decay to intermediate states may be resolved through the use of additional "re-pump" lasers which return atoms to the cooling transition, the additional complexity associated with re-pumping has limited laser cooling to atoms with simple structure, such as the alkalis, alkaline earths, and a few others. Proposals exist for laser cooling limited classes of molecules [77, 78], but to date no molecules have been laser cooled due to the complications presented by their many intermediate states. Traps loaded using laser cooling are also limited to not more than $\sim 10^{10}$ atoms [40] due to re-absorption of scattered photons and collisional losses that become relevant at large atom densities [38, 39].

Cryogenic surface-contact cooling

In light of the host of refrigeration technologies developed by the condensed matter community, an obvious alternative to laser cooling is to let an atomic or molecular gas thermalize directly with a cryogenic surface. This is the idea upon which the hydrogen BEC work was based [10]; in that work samples of up to 10^{14} ^{1}H atoms were loaded into a magnetic trap at temperatures as low as 40 mK. Unfortunately, this method is limited by the constraint of vapor pressures that drop exponentially with temperature, thus gaseous samples cannot generally be cooled to temperatures much below their boiling point. Spin-polarized ^{1}H is a unique exception, benefiting from an unusually weak binding energy to superfluid helium coated walls; all other species condense out of the gas phase at temperatures low enough to permit trapping.

Buffer-gas cooling

Unlike laser cooling or surface-contact cooling, cooling via collisions with a gas is a general, chemically unselective cooling method. Experiments have used two different implementations to produce cold atoms and molecules, both of which rely on elastic collisions between a hot sample of interest and a cold auxiliary gas to cool the sample. In supersonic expansion the sample is introduced into a pressurized, room temperature auxiliary gas and forced through a nozzle, cooling as it expands into vaccuum. While supersonic expansion is an effective cooling technique, it is not directly useful for trapping experiments since additional beam slowing is required to make the beam trappable in the laboratory frame [41–44].

In contrast with supersonic expansion, buffer-gas cooling produces samples that may be readily trapped using magnetic fields. In buffer-gas cooling helium (usually) is used as the auxiliary gas and is pre-cooled inside a cell thermally anchored to a cryogenic refrigerator. The hot sample is then introduced[5] into the cell and cooled via elastic collisions with the auxiliary "buffer" gas. In this way the buffer gas serves as a thermal link between the refrigerator and the hot sample while simultaneously preventing the sample from contacting the cold walls onto which it would otherwise condense.

Buffer-gas cooling has shown considerable success in producing large trapped samples [46]. Upwards of $10^{12} - 10^{13}$ atoms or molecules have been trapped — more than two orders of magnitude larger than achieved with laser cooling techniques, and approximately six orders larger than produced from slowed molecular beams [79]. These large, dense samples are ideal starting points for evaporative cooling, offering excellent opportunities to produce degenerate Bosonic and Fermionic gases of unprecedented size for new hydrodynamic studies or sympathetic cooling. Buffer-gas methods also access a temperature range generally bypassed by laser cooling, providing a unique laboratory in which to study collisional physics in the multi-partial wave regime be-

---

[5] by ablation, RF- or DC-discharge, or other means

tween 1 mK and 1 K. For example, recent experiments have measured spin relaxation in atom-atom [80, 81] and atom-helium collisions [82–84]. Buffer-gas cooling also provides an environment for the creation and study of atom-helium van der Waals molecules [85]. These dimers can form when quasi-bound molecules produced in elastic collisions are de-excited via collisions with a second helium atom, or directly via three-body collisions. Since dimer formation tends towards a thermal equilibrium between atoms and atom-helium dimers, loss processes affecting the dimers (such as spin relaxation) can cause atom loss at a rate proportional to the equilibrium dimer fraction. Dimer formation pose a limitation for buffer-gas cooling of some atoms, particularly for certain heavy species with large atom-helium binding energies.

1.3 Bose-Einstein condensation via buffer-gas cooling

The chemical generality and ability to trap large samples makes buffer-gas cooling an appealing alternative to other cooling techniques for research with cold and ultracold gases. However, producing quantum degenerate gases from buffer-gas cooled samples provides several unique challenges. First, the initial temperature cannot be so cold that the buffer-gas is condensed, limiting to $T \geq 200$ mK or so. This leaves an extra three orders of magnitude in temperature to traverse when compared to laser cooled samples. Second, trapping requires buffer-gas densities of $\sim 10^{16}$ cm^{-3} [86, §3.2], whereas thermal isolation and efficient evaporative cooling requires densities below $\sim 10^{8}$ cm^{-3}. Reaching quantum degeneracy thus requires achieving ultra-high vacuum shortly after trap loading in a low-vacuum environment, all without losing atoms from the trap. Third, whereas the deep traps used initially are created by massive superconducting anti-Helmholtz coils, later stages of cooling and reaching degeneracy require a different trapping geometry (see section 2.2.3) and precise field control. Finally, the cryogenic apparatus limits the resolution and photon collection efficiency of any detection optics.

This thesis describes several years of work overcoming these challenges, culminating with the creation of a BEC of metastable helium using buffer-gas methods. Chapter 2 briefly discusses previous buffer-gas experiments aimed towards producing a BEC, explains their limitations, and motivates the modifications and additions necessary to extend those experiments to reach quantum degeneracy. Chapter 3 describes the implementation of these modifications, including the installation of a dilution refrigerator, construction of a new magnetic trap, and changes to the experimental cell and optical system. Chapter 4 describes the production of metastable helium in the new apparatus as well as the initial stages of evaporative cooling, including changes to the cooling trajectory used in the multi-partial wave regime. This chapter also describes detection of the atom cloud, including the optical system used for absorption imaging.

Chapter 5 describes the later stages of evaporative cooling, including transfering the atoms between anti-Helmholtz and Ioffe-Pritchard trapping geometries, characterizing the new Ioffe-Pritchard style trap, and implementing evaporative cooling using a RF knife. It also details steps taken to stabilize the magnetic trap to reduce heating of the cloud during evaporation, and discusses the implemention of phase-contrast imaging to prevent excessive heating and provide improved signal-to-noise while imaging clouds at temperatures below 50 μK. Chapter 6 discusses characterization of the BEC itself, including measuring the transition temperature and critical atom number. It also introduces the use of time-of-flight imaging to aid in detection of clouds too small to be well resolved in *in-situ* images, aiding in distinguishing between thermal and Bose-condensed clouds. Finally, chapter 7 describes potential improvements to the experiment as well as future directions, including extensions to BEC in atomic nitrogen and silver, and production of ultracold NH.

Chapter 2

Recap of buffer-gas BEC efforts

The work described in this thesis builds upon previous experiments described in detail in the theses of Jonathan Weinstein [87], Bob Michniak [88], and Scott Nguyen [89]. This chapter provides a brief overview of these past experiments to motivate the modifications and improvements to the experimental apparatus needed for the present experiment, which shall be described in chapter 3.

2.1 Previous experiments

2.1.1 Buffer-gas loading and evaporative cooling of chromium in a closed cell

The first buffer-gas loading experiments conducted in our group aimed towards BEC that are relevant to the current work concerned the magnetic trapping and evaporative cooling of atomic chromium. These experiments were conducted in an apparatus described in [87, §5.5]; see figure 2.1. A metallic chromium target was located inside a double-walled plastic (G-10 fiberglass-epoxy composite) cell, thermally anchored to

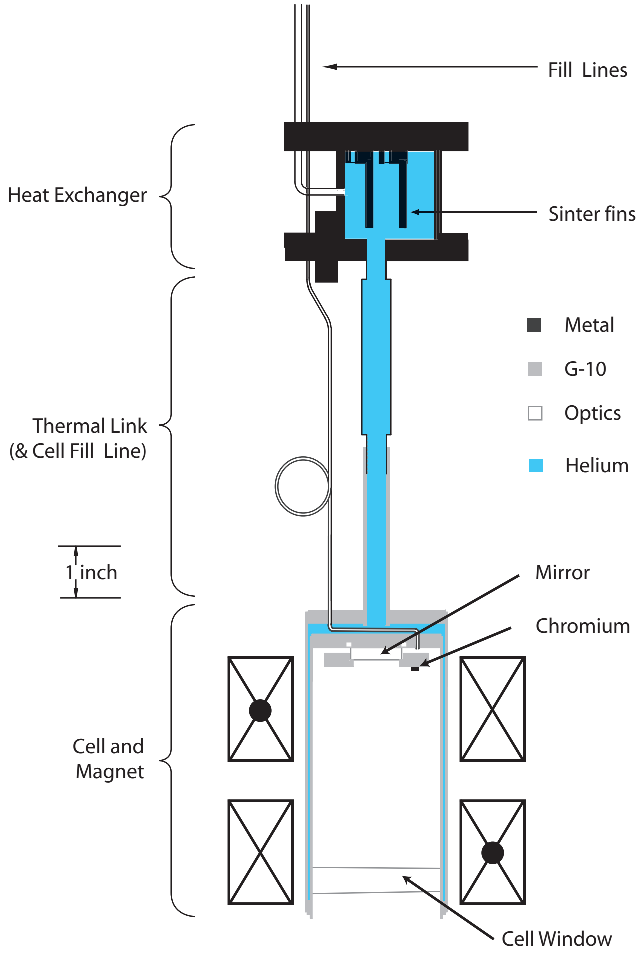

Figure 2.1: The chromium trapping cell, from [87, §5.5].

a dilution refrigerator via a superfluid helium thermal link and capable of attaining temperatures as low as 130 mK. The cell sat inside the bore of a large superconducting anti-Helmholtz magnet (the "Mark-III"), generating trap depths of up to 3.5 T at the inner cell wall.

To trap chromium, a brief pulse of current was sent to a resistive heater, temporarily heating the cell to $\sim$ 700 mK to vaporize ^{4}He from a "puddle" in the cell, producing a buffer gas. The metallic target was then ablated using a Nd:YAG laser, leading to cooling and trapping of 10^{12} chromium atoms. The cell was allowed to cool sufficiently to re-liquefy the buffer gas, and the trapped atoms were evaporatively cooled by reducing the currents in the trapping magnet, reducing the trap depth and causing forced evaporation over the trap edge.

This experiment suffered from two major limitations. First, the method used to produce and then remove the buffer gas — relying on the helium vapor pressure curve — was slow. To generate sufficient buffer-gas density to efficiently cool and trap the chromium atoms the entire cell was heated to 700 mK; removing the buffer gas required waiting for the cell to cool back down to temperatures below 300 mK. This meant that the pump-out time of the cell was identical to the thermal time constant for cell cooling (a few seconds). Unfortunately, this makes loading of less strongly magnetic species impossible, as they can be lost from the magnetic trap while the cell is cooling (see [90, §2.2,2.3] for details), and limited the use of the technique to atoms with magnetic moments of 3 μ_B or greater.

Second, the magnet used in this experiment had only two current leads, with the two anti-Helmholtz coils wired in series. As such, the trapping field could only be reduced uniformly. While reducing the current fed to the coils led to reduced trap depths and corresponding evaporation of atoms over the trap edge, it also reduced the gradient of the confining potential. This caused the density of the atom cloud to drop as the trap depth was reduced, slowing the atoms' collision rate and eventually causing evaporative cooling to stall. The stalling of evaporative cooling manifested itself in the atoms' temperature ceasing to drop as the trap depth was reduced, causing rapid atom loss and preventing the attainment of temperatures below a few mK.

2.1.2 Buffer-gas loading weakly magnetic atoms in a valved cell

A new buffer-gas loading experiment sought to resolve the first limitation faced by work with the closed cell. The major focus was on rapidly removing the buffer gas after initially loading the magnetic trap. Once removed the buffer gas can no longer thermally link the sample to the cell, thus avoiding background gas collisions that can drive continued evaporation of atoms out of the trap without a corresponding decrease in temperature. This was achieved by implementing a three chambered cell with a fast-acting, cryogenic valve that could expose the trapping chamber to a pumping chamber containing a charcoal sorption pump [88], as in figure 2.2. Buffer gas could be introduced one "puff" at a time by briefly heating a small sorb in a third ante-chamber, the "waiting room." The trap was loaded by first filling the cell with one of these puffs, follwed by production of a gaseous sample for study via ablation. Shortly thereafter the valve was opened to pump away the buffer gas, leaving the magnetic sample trapped in the anti-Helmholtz field. As this new design was specifically intended to permit the trapping of atoms with small magnetic moments (such as the alkalis), the cell was made single-walled with copper wire thermal links to reduce the total cell wall thickness and increase the useable trap depth. Since sorb pump-out of the buffer gas meant re-liquefying the helium was no longer neccessary, the temperature requirements on the cell were relaxed, and a pumped ^{3}He refrigerator was used instead of a dilution refrigerator.

Along with a new cell, this experiment also used a new magnet ("Mark-IV") in which the two coils could be independently controlled. While the leads could be connected for series operation from a single power supply, different connections permitted either coil to be operated with a current of any size or direction. This was

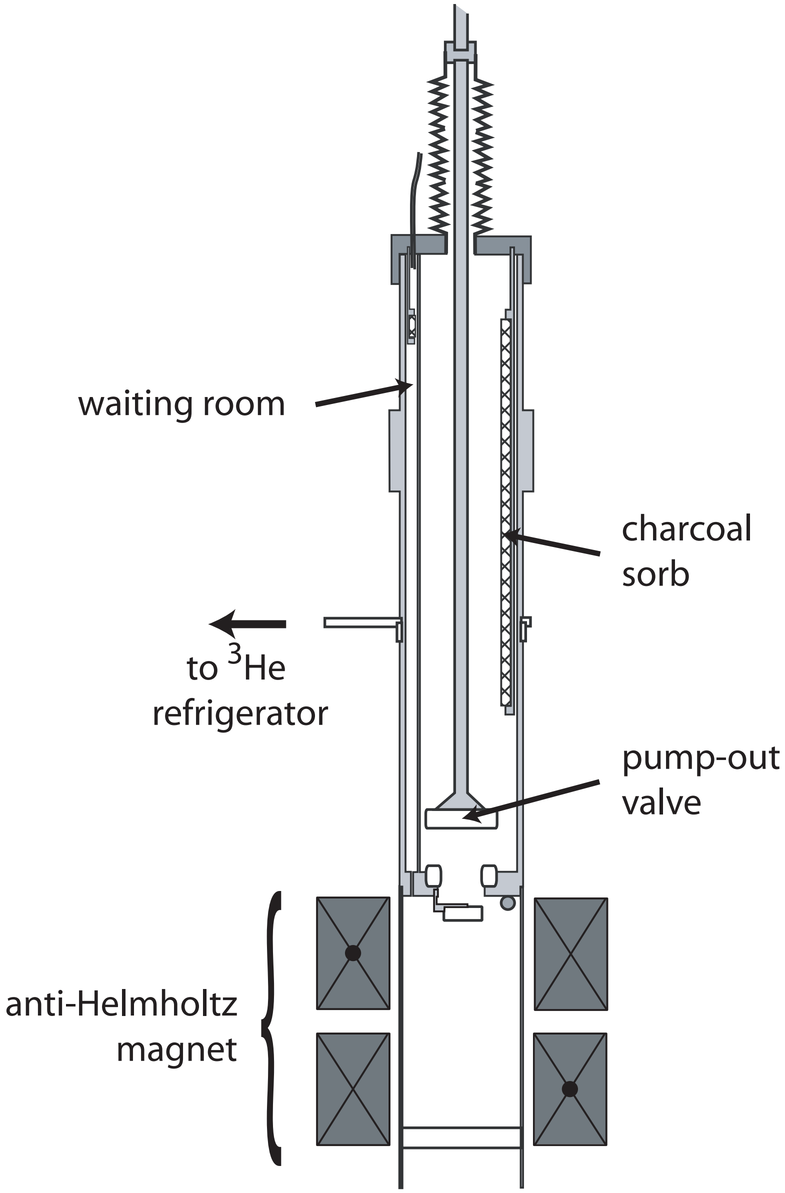

Figure 2.2: The valved cell with charcoal sorb for rapid buffer gas pumpout, from [89, §5.1].

principally intended to permit operating the magnet in Helmholtz configuration for doing experiments in a spatially uniform field. However, independent control can also be used to create trapping fields for which the potential minimum is displaced along the symmetry axis.

Unfortunately, work with this cell did not ultimately achieve the goal of trapping weakly magnetic atoms with long lifetimes. Loading the trap was straightforward, but while using a charcoal sorb rapidly pumps the vast majority of the helium buffer gas out of the trapping chamber, a thin film remains on the cell walls. This film can then slowly desorb over the ensuing seconds or minutes, poisoning the vacuum in the cell and causing loss of trapped atoms due to collisions with the desorbing helium [88, §5]. While the film desorption can be mitigated with "cryo-baking" the cell (a < 1 K analog to baking out room temperature UHV chambers - see section 4.1.2 and appendix D), such bakeouts were not possible for 1 μ_B atoms in this apparatus. Unfortunately, the poor performance of the copper heat links used with the single-walled cell combined with the limited cooling power of the ^{3}He refrigerator meant the cell could not reach temperatures below 480 mK, too warm to allow bakeouts without severe atom loss. As such, the experiment shifted away from 1 μ_B atoms and began work with metastable helium, a 2 μ_B atom.

2.2 Buffer gas loading and evaporative cooling of metastable helium

Metastable helium (He*) is an attractive species for for cold atom research for a variety of reasons. First and foremost, helium in the long-lived 2^3S_1 metastable state has 20 eV of internal energy (see figure 2.3). This energy provides for straightforward single-

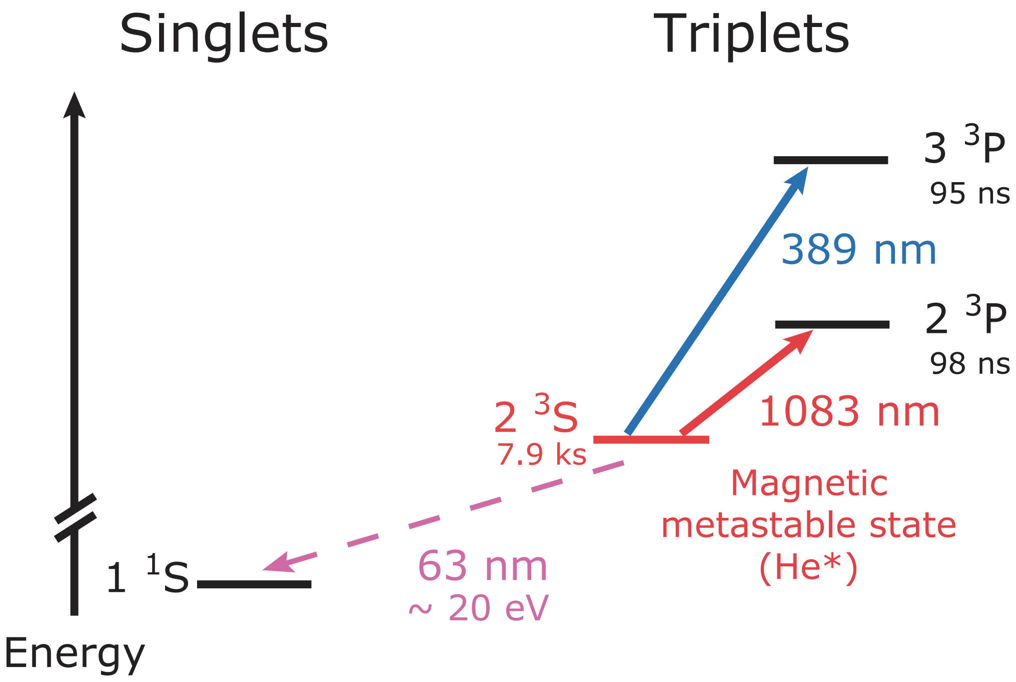

Figure 2.3: Some low lying levels of helium. The 2^3S_1 metastable state is magnetic ($2\ \mu_B$) and its radiative decay is strongly forbidden.

atom detection with micro-channel plates. Such detection gives excellent temporal and spatial resolution, and makes He* a superb choice for atom optics experiments such as measurements of quantum statistical effects [59, 60]. Second, He* has both Bosonic (^{4}He*) and Fermionic (^{3}He*) isotopes with isotopically enriched samples readily available, making it a suitable choice for studies with degenerate Fermi gases, such as the BEC-BCS crossover. Third, there are two readily accessible E1 transitions which may be used for spectroscopic detection (as well as for laser cooling) at 1083 and 389 nm.

He* is also particularly well suited to buffer-gas loading. The $2\ \mu_B$ magnetic moment makes it significantly easier to magnetically trap than $1\ \mu_B$ species, and He* may be easily produced by igniting a RF discharge in the buffer gas itself. Also, He* is somewhat challenging to laser cool in large numbers due to light-assisted Penning ionization collisions limiting peak densities to $\sim 10^9$ cm^{-3} [91, 92]; buffer-gas loaded samples can easily achieve significantly higher densities, providing a superior starting point for evaporative cooling. Finally, ^{4}He* collisional properties are known to be favorable for evaporative cooling all the way from the $\sim$ 500 mK loading temperature to quantum degeneracy, making it a good choice as a test species to explore extending buffer-gas techniques into the ultracold regime.

2.2.1 Original metastable helium trapping cell

The first He* trapping and evaporative cooling experiments (described in references [2, 89]) were carried out in a valved, double-walled cell with an amalgam of features from the double-walled chromium and single-walled small effective magnetic moment cells. Despite the advantage of thin walls and concomitantly increased useful trap depth in the single-walled cell, this cell could not be used for He*. Unfortunately, the copper wires providing thermal conductivity down the single-walled cell's length would not pass the RF fields needed to excite helium to the trappable 2^3S_1 metastable state, making He* production impossible. To reolve this a new cell was built, mirroring the upper waiting-room and pumping chambers of the single-walled cell but replacing the copper thermal links surrounding the trapping chamber with a jacket of superfluid helium, as in figure 2.4.

As with the single-walled cell, the new cell featured a pumping chamber with a charcoal sorb, a roughly 1 inch apperture pump-out valve, and a small, secondary "waiting room sorb" in a third chamber that could be loaded with buffer gas from room temperature. Cell walls were constructed from G-10 fiberglass/epoxy composite tube stock[1] and glued with Stycast 1266 epoxy [93]. The new trapping chamber

---

[1] Note that rod or plate stock is *not* interchangeable with tube stock. Tubes cut

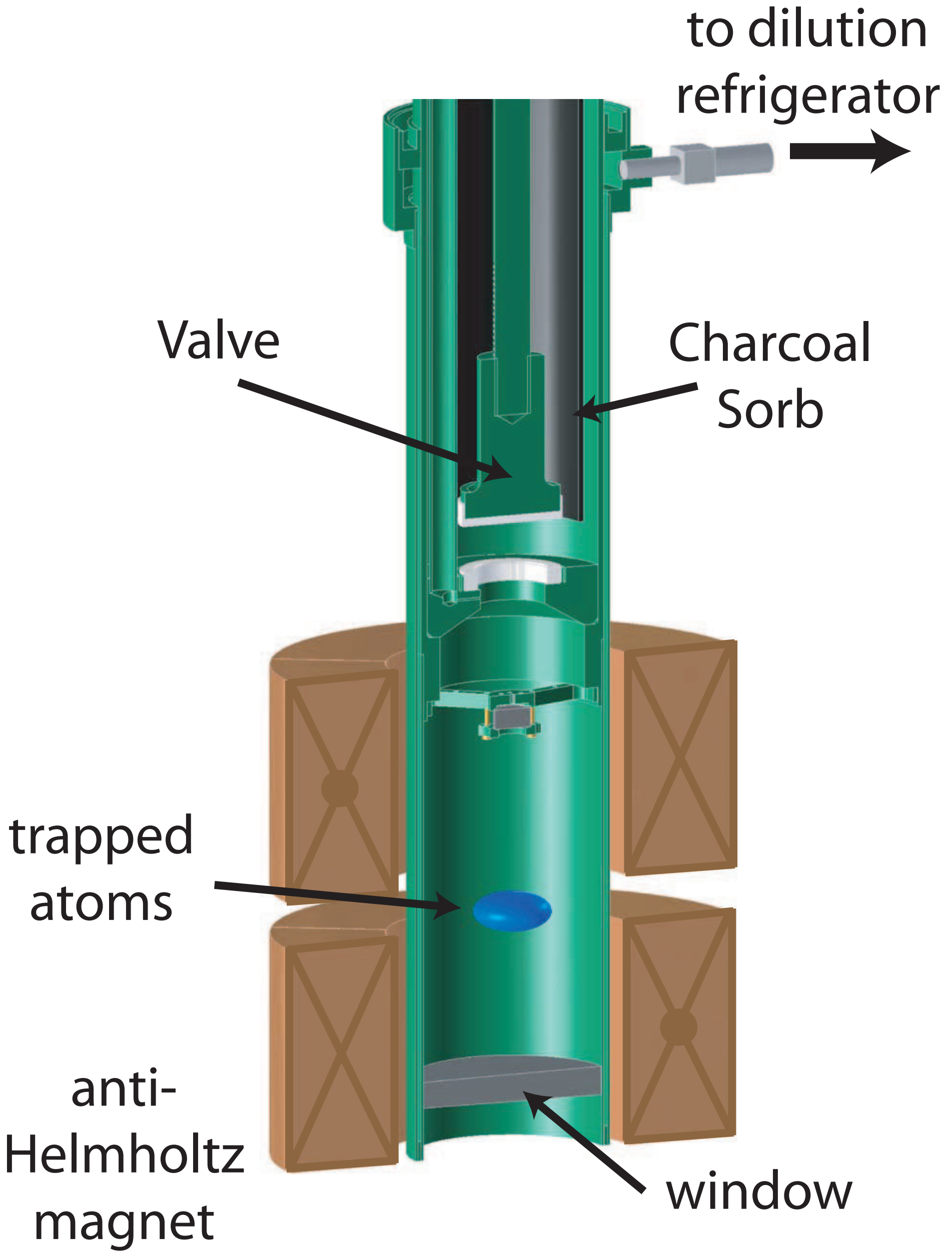

Figure 2.4: The cell used for the preliminary ^{4}He* evaporative cooling experiments.

was double-walled, with the space between the walls forming the superfluid thermal jacket. This jacket was in turn linked to a heat exchanger mounted on the ^{3}He refrigerator cold plate via a 3/8 inch stainless steel bellows. Silver sintered fins in the heat exchanger improved thermal contact between the refrigerator and the superfluid helium. Besides passing the RF fields needed for He* production, the superfluid thermal link significantly outperforms the previous copper link (presumably due to work hardening of the copper), resulting in a cell base temperature of 400 mK. Sitting coaxially in the bore of the Mark-IV trapping magnet, the 3.16 cm inner diameter of the cell limited the useful trap depth to 3.64 T with the magnet fully energized to 102 A.

2.2.2 Valve-open loading of He*

Using the new cell, up to $\sim 10^{12}$ He* atoms atoms could be produced and trapped [89, §6.4] by igniting a RF discharge in a buffer gas density in the $10^{15} - 10^{16}$ cm^{-3} range. Unfortunately, the helium film left on the cell walls after opening the valve to the charcoal sorb once again prevented the attainment of UHV conditions, making efficient evaporative cooling impossible. Fortunately, a new trap loading technique made it possible to improve the cell vacuum: valve-open loading.

As before, preparation for trap loading began by closing the valve and filling the cell with buffer gas. Instead of igniting the RF discharge at this point to produce He* and load the magnetic trap, however, an additional cell preparation step was added. The valve was opened, pumping most of the the gas onto the sorb, and the cell heated to approximately 700 mK to thin the helium film coating the walls.

---

from rod stock will crack under thermal cycling, whereas tube stock maintains its strength due to the circumferential wrapping of the fiberglass.

The cell was then allowed to cool back to the 400 mK base temperature, tightly binding any remaining helium film to the cell walls. Only then was the RF discharge ignited; we believe the discharge etches sufficient helium out of the film to create an instantaneous buffer gas density of $> 10^{14}$ cm^{-3}, leading to the production and trapping of $\sim 10^{11}$ He* atoms at a peak density of 10^{11} cm^{-3}. Remaining buffer gas is rapidly cryo-pumped back to the cell walls and is tightly bound, preventing contamination of the cell vacuum. Although this method leads to the production of an order of magnitude fewer He* atoms, the collision rate of the trapped atoms is quite adequate for evaporative cooling, and the improved cell vacuum significantly reduces atom loss due to background gas collisions. The quality of the vacuum tended to vary from day-to-day, often without apparent cause, but this cell preparation method generally worked well enough to continue with evaporative cooling.

2.2.3 Surface evaporation

As with chromium, forced evaporative cooling was achieved by reducing the currents in the anti-Helmholtz coils of the trapping magnet. However, the ability to displace the minimum of the trapping potential along the symmetry axis offered by the new magnet made for significantly improved evaporative cooling by using surface adsorption [94, 95]. Instead lowering the trap to allow atoms to “leak” over the edges of the confining potential at the expense of reduced trap gradients, the entire trap was displaced towards the window at the bottom of the cell. Because only those atoms with the most energy make orbits taking them far from the center of the trap, it is these warmest atoms that strike the window first as the atom cloud moves towards it. These atoms are adsorbed onto the window and lost from the distribution, leading to a lower average temperature. Since the trap depth is set by a combination of the trap gradient and the distance of the trap minimum from the surface, the atoms can be cooled while remaining tightly confined simply by pushing the cloud close to the window.

This new evaporative cooling technique leads to significantly improved evaporation efficiency. As described in reference [89, §6.6], using the window to define the trap depth permits evaporative cooling to milliKelvin temperatures with 60 times stronger trap gradients. Since the atom density scales as the cube of the gradients and evaporative cooling is driven by elastic collisions that occur at a rate proportional to atom density, surface evaporation performs much better than uniform lowering. Whereas the chromium evaporative cooling saw a negligible increase in phase-space density[2] [87, §6.5], using surface evaporation with He* we observed an increase in phase-space density from $\sim 10^{-11}$ to 3×10^{-5}, achieving temperatures of a few mK at densities of approximately 10^{12} cm^{-3}.

Unfortunately, continuing evaporative cooling to reach quantum degeneracy was impossible in this experiment due to the limitations of the anti-Helmholtz trap. The quadrupole field generated by this trap features a magnetic field zero at its center, allowing atoms traversing the low-field region around the minimum to make nonadiabatic transitions to untrapped states (Majorana flops — see [87, §a.D]). This leads to loss of cold atoms from the center of the cloud at a rate proportional to the flux of atoms into a "hole" around the trap center, giving rise to a lifetime scaling as the ratio of the surface area of the atom cloud to that of the hole [98, 99] — see figure 2.5. Whereas the comparatively hot (and correspondingly larger) atom cloud initially loaded into the trap has a Majorana limited lifetime of hundreds of seconds,

---

[2] Chromium also suffers from fairly poor collisional parameters, contributing to inefficient evaporation. However, the poor cooling performance described in reference [96] was dominated by slow re-thermalization due to low collision rates [97].

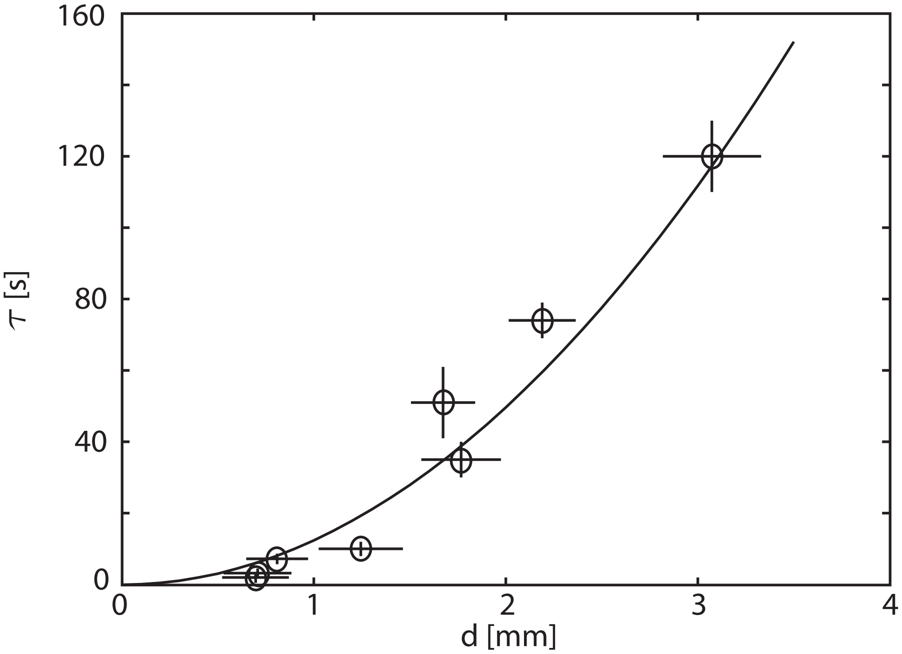

Figure 2.5: Trap loss due to Majorana flops. Open circles are exponential lifetimes of ^{4}He* trapped in a magnetic quadrupole field plotted as a function of cloud diameter $d \equiv \frac{k_B T}{\mu_B B'}$, where B' is the average gradient of the quadrupole trapping field. Solid line is an estimated lifetime of $\tau = 12.4 d^2$ sec/mm^2 based on measured trap parameters. From reference [2].

as the cloud shrinks during evaporative cooling the lifetime drops to only a few seconds. Further cooling requires "plugging" the hole optically [8], using a time-orbiting potential trap [98], or switching to a trapping geometry with a non-zero field minimum.

2.3 Improvements needed for achieving Bose-Einstein condensation

Having demonstrated efficient evaporative cooling of buffer-gas loaded ^{4}He* in the temperature range from 500 mK down to a few mK, extending this evaporation to lower temperatures to achieve BEC seemed a tantalizingly close goal. As described above, however, several challenges remained, including struggles with atom loss due to inconsistent quality of the cell vacuum and a need to resolve the Majorana flop issue for evaporative cooling below 10 mK. Also, two more additional problems were anticipated once lower temperatures were reached. First, because the trap minimum - cell window distance sets the trap depth for surface evaporation, this technique suffers from increased sensitivity to cell vibrations and magnetic field noise as the trap depth is decreased. Second, our typical method of probing the atom cloud — laser absorption spectroscopy — ceases to provide very much information for temperatures at which the Zeeman and Doppler broadenings become small compared to the natural linewidth of the transition used for detection. For ^{4}He* this occurs at temperatures on the order of 100 μK, so further evaporative cooling requires a different method for probing the atoms.

These challenges were addressed through four major technological improvements to the experimental apparatus. First, the pumped ^{3}He refrigerator was replaced with a dilution refrigerator to provide increased cooling power and lower base temperatures to assist in achieving good vacuum. Second, an Ioffe-Pritchard style trap was added inside the bore of the anti-Helmholtz trap, permitting the atoms to be transfered to a geometry free from Majorana loss before pursuing further evaporative cooling. Third, an additional RF coil was added to allow for a new evaporative cooling technique for use at temperatures below 1 mK. Finally, changes were made to the optical system used for detection to implement absorption and phase-contrast imaging. These modifications shall be described in chapter 3.

Chapter 3

The buffer-gas BEC apparatus

The experimental apparatus used to create a buffer-gas BEC is based on that used for earlier ^{4}He* evaporative cooling experiments, introduced in section 2.2 and also described in references [2, 89]. Major changes include the replacement of the pumped ^{3}He refrigerator with a dilution refrigerator, construction of a quadrupole-Ioffe configuration (QUIC) magnetic trap [100], modifying the cell to accomodate the new QUIC trap, and winding of new RF coils directly around the cell for production of ^{4}He* and RF evaporation. In addition to the changes to the cryostat, the optical system has also been updated to permit frequency stabilization of the detection laser.

3.1 The dilution refrigerator

By far the most involved change was the replacement of the pumped ^{3}He refrigerator with a dilution refrigerator. As introduced in section 2.3, we hoped to use the increased cooling power and lower base temperature offered by a dilution refrigerator to improve the quality of the vacuum in the experimental cell. Generally speaking, we intended to take advantage of the best features of both methods of buffer gas

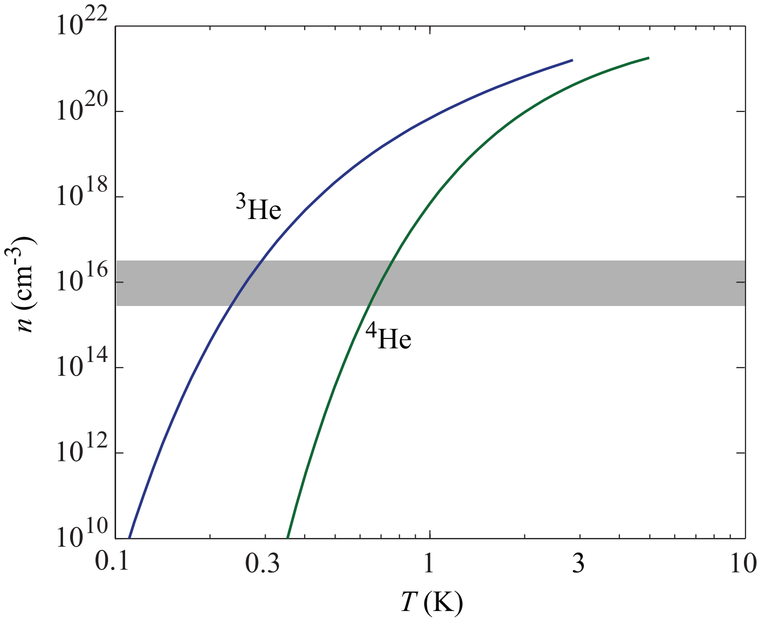

Figure 3.1: Vapor pressure curves of ^{3}He and ^{4}He [101, 102]. The grey band indicates helium densities most often used for buffer-gas loading of magnetic traps.

removal demonstrated in previous experiments: rapid pumpout of the majority of the buffer gas to a charcoal sorb to quickly thermally isolate the trapped ^{4}He*, followed by liquefying any remaining gas by appealing to the ^{4}He vapor pressure curve to ensure long one-body lifetimes for evaporative cooling (see figure 3.1). To achieve vapor pressure limited background helium gas densities below the 10^8 cm^{-3} required for good evaporative cooling, cell temperatures below 300 (100) mK for ^{4}He (^{3}He) are necessary — significantly lower than the 400 mK cell temperatures achieved with the ^{3}He refrigerator. In addition to improved vacuum, we hoped that the combination of a valved cell with a dilution refrigerator would permit "ordinary" loading of ^{4}He* (instead of loading with buffer gas produced from a thin helium film) since previous experiments indicated 10 times greater production when loading from an initial buffer gas density of 10^{16} cm^{-3}.

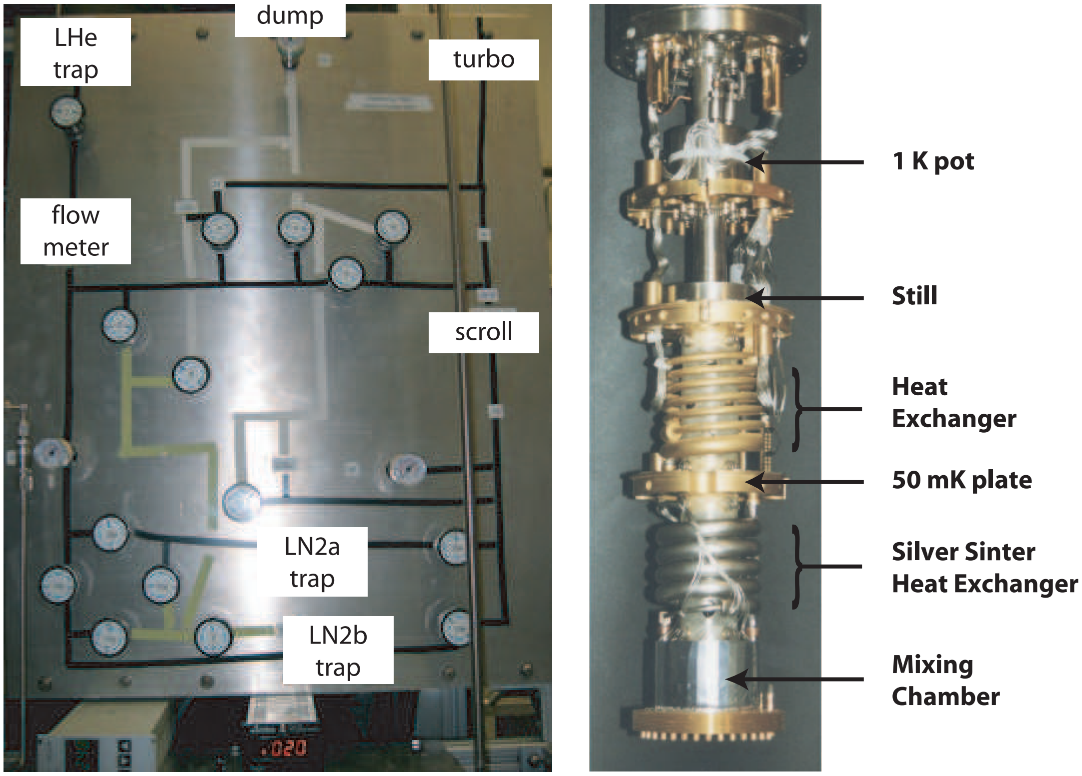

Figure 3.2: The dilution refrigerator. The left panel shows the valve assembly and relative locations of pumps and cold traps. The right panel shows the insert itself.

3.1.1 Refrigerator details

Our refrigerator insert is a MNK126-500, manufactured by Leiden Cryogenics [103], capable of 500 μW of cooling power at 120 mK (figure 3.2). It features a continuous silver heat exchanger, a stainless steel mixing chamber to reduce eddy current heating, gold plated cold plates, and numerous factory installed DC and RF electronic feedthroughs to the 1 Kelvin or mixing chamber levels. This insert utilizes two liquid helium sipper lines: one with fixed impedance adequate for ordinary circumstances, and a second equiped with a needle valve for greater 1 K pot heat loads, such as during initial cooldown. It also uses a unique pumping line, whereby the entire 5" diameter baffle stack extends as a sealed tube nearly to the 1 K pot level to provide a large pumping conductance for the ^{3}He circulation loop.

The room temperature ^{3}He circulation loop is home-built so as to take advantage of the reliability of VCR [104] fittings not ordinarily used in standard commercial gas handling systems. It is modeled on the valve layout of the Oxford Instruments Kelvinox-300 refrigerator, but includes some improvements. Most importantly, the ^{3}He is circulated by oil-free pumps rather than a traditional roots blower and rotary pump. A Varian V-551 turbo [105] pumps on the still, backed by a BOC Edwards XDS-10 scroll pump[1] [106]. Pressure interlocks have also been incorporated, turning off the pumps and stopping circulation of the mix in the event of an overpressure condition (set at 5 mbar) between the turbo and scroll pumps. The mix consists of 35 STP liters of ^{3}He and 113 STP liters of ^{4}He. This is actually about 20 STP liters more mix than specified, so not all of it need be condensed to operate the refrigerator. Cold traps at liquid nitrogen and liquid helium temperatures collect any impurities in the mix and prevent clogging. The helium cold trap is operated in an external storage dewar due to the lack of an extra port into the cryostat.

3.1.2 Refrigerator performance

For its first cooldown the refrigerator was operated with no additional components attached in a bucket dewar. In this situation it attained a minimum base temperature of 52 mK[2], measured by a calibrated resistor (stolen from the ^{3}He refrigerator). The

---

[1] While generally adequate, the pumping speed of the XDS-10 limits the overall pumping speed of the system at large circulations. BOC also sells the XDS-35 for a few thousand dollars more; while slightly overkill, its greater pumping speed would resolve this issue.

[2] None of the refrigerator heat shields were used for this cooldown, so there were heat loads of about 5 μW from 4.2 K blackbody radiation, and perhaps 10-20 μW from residual background gas.

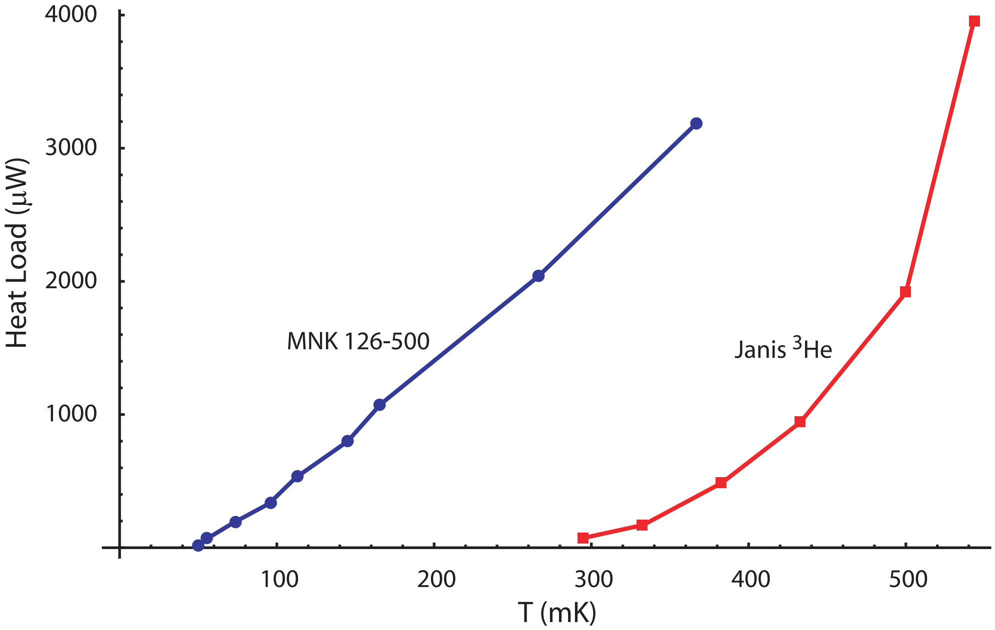

Figure 3.3: Cooling power curves. Data from the new MNK 126-500 dilution refrigerator is shown with circles. The old Janis pumped ^{3}He refrigerator is shown for comparison, plotted as squares.

refrigerator exceeded its cooling power specification, providing approximately 600 μW at 120 mK, as in figure 3.3. With the cell attached the refrigerator reaches a base temperature of approximately 75 mK, corresponding to a steady-state heat load of order 200 μW.

A major advantage of this refrigerator setup is the use of oil-free pumps. Whereas the traditional roots blower and rotary pump setup requires cleaning of the liquid nitrogen trap every other month or so, as well as occasional cleaning of the liquid helium trap, there has never been any evidence of impurities in the cold traps of the new refrigerator. Furthermore, there is never any need to change pump oil; the only maintenance necessary is changing of the tip seals on the scroll pump every 18 months or so. The pressure interlock on the circulation loop is also a significant improvement, preventing the refrigerator from semi-catastrophically “crashing” (i.e. sudden blowoff of the mix into the dump). For example, if an overpressure condition is triggered by the 1 K pot running dry, by stopping circulation of the mix and thus reducing the incoming heat load, the refrigerator takes approximately 12 hours to warm to 4 K. This gives ample time to notice problems and resolve them without having to re-condense the mix.

3.1.3 Additional dewar improvements

Installing the new refrigerator required fairly major rebuilding of many elements of the cryostat. The dewar top-plate, baffle stack, and IVC top-plates all needed to be re-made, as did the many elements linking these pieces. These changes required disassembling the dewar, permitting simultaneous improvements to a handful of other hard to access pieces, including the vapor-cooled leads and busbar assemblies for the anti-Helmholtz magnet, electronic feedthroughs, cell valve shaft, and the baffle stack itself.

Anti-Helmholtz magnet current feedthroughs

During the cooldown immediately preceeding the installation of the refrigerator the anti-Helmholtz magnet ceased functioning properly. Ordinarily the magnet may be smoothly ramped to any current between zero and its critical current of 102.5 A by driving it with a voltage $V = LdI/dt$ ($L \sim 5$ H) or maintained at a constant current using a voltage $V = IR$ ($R \sim .01\ \Omega$), with fluctuations of order 10 mA. On this cooldown we initially observed ordinary behavior, but at the end of this cooldown, we noted increasingly dramatic voltage and current oscillations as the current in the magnet was increased. These oscillations were negligible at currents below 40 A, but led to quenching of the magnet at currents of approximately 60 A. The cause of the oscillations was unclear, but we suspected a problem with the vapor-cooled current leads, perhaps caused by inadequate vapor flow at some point during the run of the experiment. To distinguish between a problem with the leads or the magnet coils the magnet was tested in a separate dewar using different leads, and the magnet was confirmed to operate normally.

Several aspects of the magnet lead assembly in the previous iteration of the experimental apparatus were not ideal. First, the vapor-cooled leads were rated to only 100 A. This was less than the maximum operating current of the magnet, and the leads were often operated at a few Amps above this rating. Second, for best performance it is important to have the bottom of the vapor-cooled leads (where the helium vapor enters for cooling) extend below the lowest baffle of the dewar neck so that the entering vapor is as cold as possible. However, the 100 A leads only projected about halfway down the baffle stack. Third, copper-clad Nb_3Sn busbars were used between the vapor-cooled leads and the Nb:Ti magnet leads. The copper cladding on these busbars is intended to keep their entire length cold so long as one end is immersed in liquid helium, allowing them to remain superconducting even as the level of helium in the 4 K bath space drops. In the old assembly these busbars were both too high and not long enough to remain in liquid unless the level was quite high. Furthermore, Nb_3Sn is quite brittle; bends that were added to the busbars to fit them into the experiment may have compromised the superconductor.

In reconstructing the dewar to accomodate the new refrigerator we addressed each of these issues. The short 100 A leads were replaced with beefier 150 A leads that were long enough to project just below the bottom of the baffle stack. New 150 A busbars were installed such that the lower end would remain immersed during ordinary operation. A new current path was selected so that these busbars would not be jostled and did not need to be bent. Finally, care was taken to ensure joints between components were accessible without disassembling the baffle stack, meaning the vapor-cooled leads can be easily pulled and replaced should any future problems arise.

Valve shaft alignment decoupler

A more minor improvement made possible as a result of disassembling the dewar to install the new refrigerator was adding an "alignment decoupler" (see reference [90, §B.2] to the cell valve shaft assembly. Because our valve is of the "flat on flat" design, it is imperative that the boot and seat be precisely aligned to ensure a good seal — challenging to achieve with a rigid, 2 meter long, multi-piece valve shaft and an over-constrained valve boot. The decoupler is made of a ~ 1 inch diameter teflon ball attached to the lower section of the valve shaft just above the cell and a flat brass plate attached to the upper valve shaft that enters the dewar at room temperature. When the valve is actuated the plate pushes against the ball, closing the valve; however, the ball is free to slide a small distance side to side against the plate, providing some angular freedom for the lower portion of the valve shaft and boot, thereby allowing the boot to seal flat against the (fixed) valve seat. The decoupler thus acts a bit like a hinge in the middle of the valve shaft, relaxing the alignment constraints between the shaft entering the dewar from room temperature and the valve seat located inside the cell.

With the addition of the alignment decoupler the sealing performance of the valve improves significantly. A valve closing force of 80 lbs. yields a leak rate of 5×10^{-3} mbar $\cdot$ L/sec with the one piece valve shaft, improving to a leak rate of 1.5×10^{-4} mbar $\cdot$ L/sec with only 30 lbs. of closing force after adding the alignment decoupler. However, this improvement has dissipated with time, presumably due to plastic deformation forming a flat spot on the teflon ball in the decoupler. This could hopefully be avoided through the use of smaller closing forces and/or putting a larger ball in the decoupler, ideally attaining performance equal to or exceeding that described in reference [90].

Electrical feedthroughs and baffle stack

Most of the electrical feedthroughs for the dewar previously consisted of manganin wire soldered to Microtech connectors [107]. While the connectors make good electrical contact and are themselves reliable at low temperature, soldering small manganin wires to them is somewhat challenging, and the solder connections are notoriously weak without stress relief. The wires to each connector were run parallel to one another without twisting, making them more susceptible to electrical pickup as well as to becoming tangled. We replaced the wiring with twisted-pair or quad-twist wire, and switched to 4-pin square connectors from International Circuit Sales [108] that would also mate with the wiring integrated into the dilution refrigerator insert. To make the connections more robust each connector was potted in molded Stycast 2850 epoxy [93] with nylon tubing around the exiting wires for strain relief, making the connections more robust and providing a larger surface to grip when making connections. The baffle stack and dewar neck assembly were also rebuilt. While this was necessary simply to fit the new dilution refrigerator, it also afforded an opportunity to add additional feedthroughs and to better close off holes that allowed passage of blackbody radiation. Stainless steel wire fish-tapes were also left penetrating unused feedthroughs in the baffle stack to simplify the addition of new components as needed.

3.2 Quadrupole-Ioffe configuration trap

As introduced in section 2.2.3, the earlier ^{4}He* evaporative cooling was limited by atom loss due to cold atoms undergoing Majorana transitions when traversing the central field minimum of the anti-Helmholtz trap. While the simplest solution to this problem is to "plug" the hole with a blue-detuned laser that repels the atoms from the trap minimum [8], use of an optical plug is not compatible with the cryogenic environment used for buffer-gas loading. Instead we are forced to resolve the problem by switching the atoms to a magnetic trap with a non-zero minimum.

3.2.1 Ioffe-Pritchard traps

The lowest-order, most tightly confining trap that can have a non-zero bias field at its minimum is a parabolic (harmonic) potential. Different options for such a trap exist (see [34, 98, 100, 109, 110]), but for atom trapping the variants most commonly used are implementations of the Ioffe-Pritchard (IP) trap [34]. The IP trap is cylindrically symmetric, with its bias field oriented along the symmetry axis: $B_z = B_o + \frac{1}{2}B''z^2$. However, to leading order the transverse field is linear, with $B_x = B'x$. More generally, the field can be written as [111]:

$$\vec{B}(x,y,z) = B_o \begin{pmatrix} 0 \\ 0 \\ 1 \end{pmatrix} + B' \begin{pmatrix} x \\ -y \\ 0 \end{pmatrix} + \frac{B''}{2} \begin{pmatrix} -xz \\ -yz \\ z^2 + \frac{1}{2}(x^2+y^2) \end{pmatrix} \tag{3.1}$$

This field configuration gives the IP trap two distinct regimes depending on the temperature (and size) of the trapped atom cloud. For temperatures $T < \mu B_o/k_B$ the confining potential is essentially harmonic in all three dimensions according to

$$U \simeq \frac{\mu}{2}\Big(B''_\rho \rho^2 + B''z^2\Big) \tag{3.2}$$

with

$$\rho = (x^2 + y^2) \tag{3.3}$$

$$B''_\rho = \frac{B'^2}{B_o} - \frac{B''}{2}. \tag{3.4}$$

For larger temperatures the potential is mostly linear in the radial dimensions while remaining harmonic in the axial dimension. This detail is important for evaporative cooling. By choosing a suitably small value for B_o, the linear nature of the trap in the radial dimensions gives tighter confinement, larger collision rates, and superior evaporation as compared to a 3D harmonic trap.

3.2.2 Design considerations

Besides preferring a tightly confining potential, in adding an IP trap to our existing ^{4}He* experiment there were several important considerations:

- The new trap had to fit inside the bore of the large anti-Helmholtz trapping magnet. We intended to replace the cell bottom with a narrower section into which the atoms could be transferred during surface evaporation. The new trap would thus fit outside of this extension but inside the anti-Helmholtz magnet.

- The new trap must be superconducting. Comparable traps in room-temperature setups generally dissipate $\sim$ 1 kW of power, which would definitely be problematic in a liquid helium cryostat.

- A trap depth of order 10 mK is necessary. Evaporatively cooling far enough to load a shallower trap would spend too much time in a regime with rapid Majorana losses in the anti-Helmholtz trapping potential.

- The trap should operate at fairly low amperage ($\sim$ 10 A or less) to preclude the need for special leads to introduce currents into the cryostat.

- It is desirable to have external "knobs" to control B_o, B', and B'' by adjusting appropriate trap currents, allowing maximal flexibility of the trapping potential without disassembling the cryostat.

In addition to these primary concerns, however, there was a more subtle point to consider, namely the actual process of transfering atoms from the anti-Helmholtz trap into the Ioffe-Pritchard trap. Most room temperature experiments accomplish this transfer suddenly. Lasers and magnetic field coils making up a magneto-optical trap are rapidly turned off, followed immediately by suddenly turning on coils to build an Ioffe-Pritchard trapping potential around the atoms. To preserve phase-space density and prevent heating and atom loss it is important that the new trap be energized before the atoms have had a chance to expand non-adiabatically[3]. This requires that the new trap be energized in a time

$$\begin{aligned} T_{on} &\lesssim r_o/v_{rms} \\ &\sim 1/\omega_{trap}. \end{aligned} \tag{3.5}$$

For a quadrupole trap,

$$\omega_{trap} \sim \frac{\mu B'}{2}\sqrt{\frac{1}{mk_BT}} \tag{3.6}$$

which means that trap turn-on must be accomplished in times of order 1 msec or less for atoms at 1 mK in typical traps.

For room temperature IP traps with inductances of order 100 μH and large, well insulated wires operating at approximately 100 A, a 1 msec turn-on is no problem. Low current superconducting coils with many turns of fine wire can be considerably more inductive, however. This makes it challenging to rapidly energize the trap, as

---

[3] It is similarly important to match the stiffness of the new confining potential to the original cloud size and temperature, known as "mode-matching" the trap to the cloud [112].

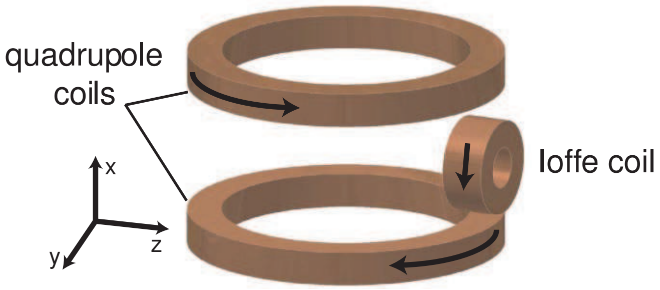

Figure 3.4: A quadrupole-Ioffe configuration trap. Current directions are as shown, producing a trapping potential as in equation 3.1.

the larger voltages necessary can potentially arc between the adjacent turns or to any nearby ground. Even more troubling is the problem of turning *off* the large anti-Helmholtz trap. The evaporative cooling described in references [2, 89] reached 1 mK with $\sim$ 10 A currents in the magnet; turning the 5 H trap off in 1 msec would require 50 kV! Fortunately, there is a variant of the Ioffe-Pritchard trap for which rapid turn-on is not required: the quadrupole-Ioffe configuration, or QUIC trap [100]. Also, besides permitting adiabatic transfer of atoms between trapping geometries, the QUIC trap is the simplest possible IP trap, consisting of only three coils, making it easy to construct. Two coils form a quadrupole field, while a third "Ioffe coil" is oriented off of the quadrupole axis to create a bias field in the horizontal direction, as in figure 3.4.

Transfer of atoms between the two traps is accomplished by increasing the current in the Ioffe coil. Due to the relative direction of the magnetic fields from the quadrupole coils and the Ioffe coil, the Ioffe field adds to the quadrupole field on the side of the quadrupole minimum far from the Ioffe coil while cancelling the field on the near side. As the current to the coil is increased, the magnetic field zero of the quadrupole trap is pulled towards the Ioffe coil, simultaneously creating a second minimum where the stronger fringing field near the coil overwhelms the quadrupole field. Further increasing the Ioffe coil current causes the two minima to merge, leaving a harmonic minimum with a bias field in their wake, as in figure 3.5.

Having settled on a QUIC trap, a few more design considerations presented themselves. For ease of detecting atoms held in either the large anti-Helmholtz trap or the QUIC trap, it is convenient to center the QUIC quadrupole coils off-axis relative to the anti-Helmholtz trap. In this way the QUIC quadrupole and Ioffe coils tend to pull the minimum in opposite directions relative to the initial anti-Helmholtz minimum such that the final QUIC minimum is nearly aligned with the anti-Helmholtz minimum. Also, putting current through the QUIC coils while the anti-Helmholtz trapping magnets are still energized can apply considerable forces ($\sim$ 10 lbs.) to the QUIC trap. This makes it desireable to anchor it to the robust inner vacuum can (IVC) rather than the cell. Unfortunately, field simulations indicate that successful transfer of atoms between the anti-Helmholtz and QUIC traps is critically reliant on the proximity of the Ioffe coil to the cell walls. Anchoring the QUIC trap to the 4 K IVC requires that vacuum space be left between the trap and the 200 mK cell to thermally isolate them from one another. This means we would have to toe a fine line between keeping the trap far from the cell to prevent a touch while keeping it close enough to allow for atom transfer.

3.2.3 Winding the QUIC trap

To build a QUIC trap that met the considerations described in section 3.2.2, we decided to wind three new small magnetic field coils: two to form a new quadrupole field centered off-axis from the anti-Helmholtz magnet, and a third Ioffe coil. These magnets were designed to operate at currents below 10 A, meaning a simple one-wire lead could be used to introduce currents into the cryostat. Achieving the desired

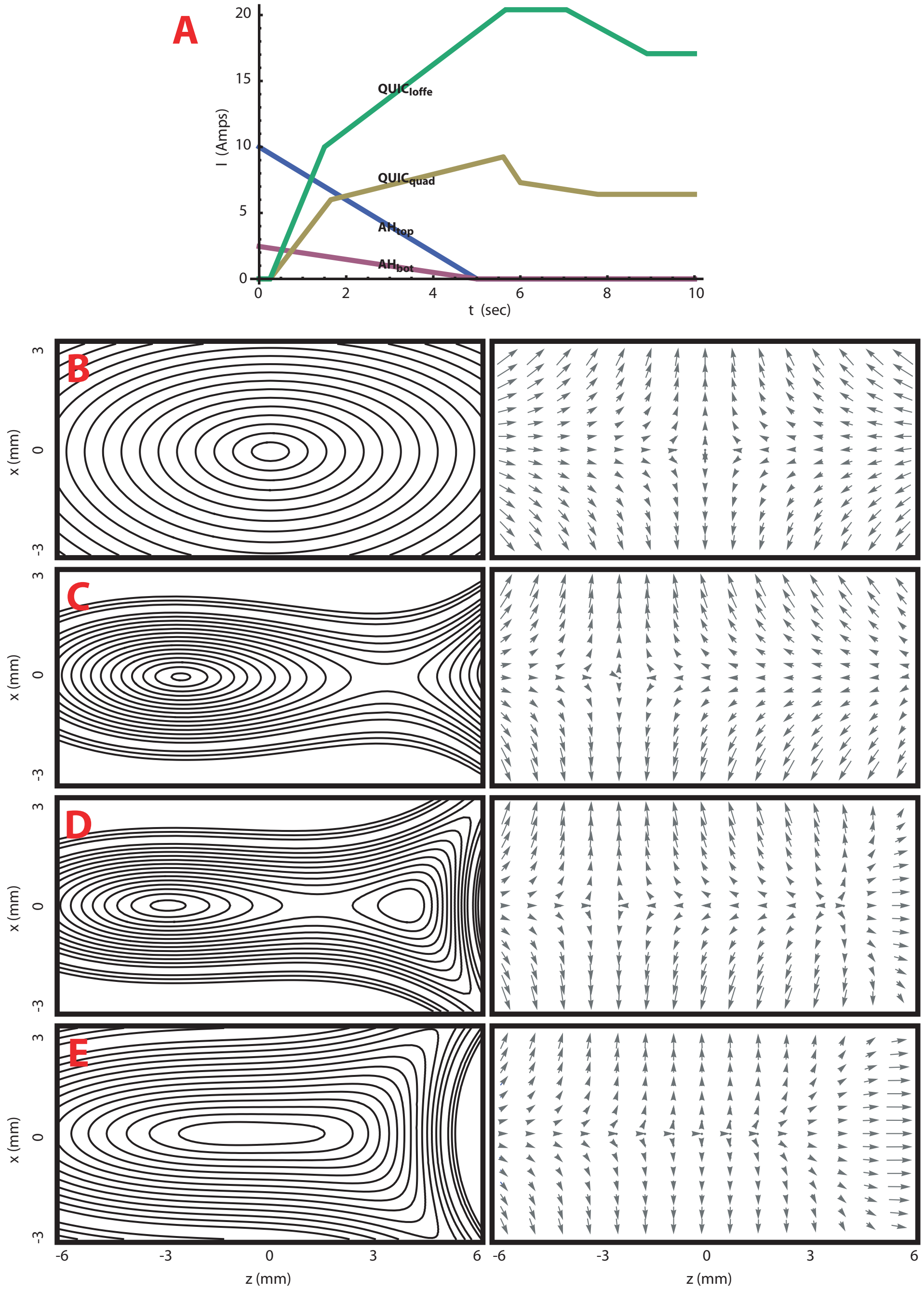

Figure 3.5: Transforming a quadrupole trapping field into an Ioffe-Pritchard trap by manipulating coil currents as in (a). The minimum formed by the large anti-Helmholtz trap (b). This minimum is initially pulled towards a smaller pair of quadrupole coils centered at -6.75 mm (c), and then is drawn toward a second minimum nearer the Ioffe coil (d), merging to form a harmonic potential with a bias field (e). Contours are every 10 Gauss.

$\sim$ 10 mK trap depth at this current requires approximately 400 turns in the Ioffe coil, meaning thin wires had to be used to keep the coils small enough to fit inside the bore of the anti-Helmholtz magnet.

Fortunately, suitably thin superconducting wire is easy to find. Nb:Ti superconducting wire is readily drawn to almost any size, with the only penalty of smaller wires being a lower critical current. Because our QUIC trap is not intended to operate in particularly large magnetic fields[4], large critical currents are not terribly important. Our QUIC trap is wound from 54S-43 54 filament Nb:Ti wire in a copper matrix with a Cu:SC ratio of 1.2 made by Supercon [113], drawn down to 0.007" diameter, with a critical current of 26 A at 3 Tesla. This sort of wire is typically insulated with Formvar enamel, but ours was special ordered with tougher polyimide enamel insulation (the same material as Kapton) to protect against shorts. The enamel coating increases the overall diameter to 0.008".

To help prevent quenching of the superconductor due to wire movement while energized we intended to pot the superconducting coils in our QUIC trap in epoxy, filling any voids between wires. While it is possible to vacuum impregnate a coil after winding, this is usually achieved by "wet-winding" the coil onto a permanent form, i.e. painting wet epoxy onto the turns as the coil is wound, both filling any voids and affixing the coil to the form. For our trap this presents a conundrum. Any form used must be robust enough to not deform under the tension applied to the wire during winding, but a thick form further complicates the challenge of positioning the Ioffe coil close to the cell while maintaining a thermal disconnect. Fortunately, this issue can be resolved by using "peel-off" Teflon forms. Teflon, the material used to make

---

[4] The largest field in the region of the QUIC trap at the starting point of figure 3.5 is less than 0.5 Tesla, and the QUIC trap itself creates fields on the order of .1 Tesla near the coils.

the non-stick coating on cookware, machines well and is not wet by epoxy. By cutting a channel in a sturdy Teflon cylinder with dimensions matching those planned for the coil to be wound one can thus make a non-stick form. After wet-winding the coil, the Teflon can be carefully machined away to within a millimeter or two of the windings, allowing the remainder of the form to be easily pulled away from the finished coil.

The finished quadrupole coils have an 18.4 mm inner radius, 23.4 mm outer radius, and 5 mm length, with 430 turns. The Ioffe coil measures 3 mm inner radius, 6.8 mm outer radius, and a 6.3 mm length, with 410 turns[5]. Each coil was wet-wound with Epon epoxy resin 815C and cured with Epicure 3140 curing agent [114], a clear epoxy with good thermal stability and suitable open time. The coil leads were enclosed in thin PVC tubing where they exit the coil for protection and strain relief, the tubing anchored to the coil with the same epoxy. After removing the coils from the Teflon forms, thin (0.01") G-10 plates were then epoxied onto the faces of each coil to protect the sides from scratches and damage and to better insulate them from their surroundings.

3.2.4 Coil assembler

To appropriately position the newly wound coils relative to the cell we also needed to build an insert to fit in the bottom of the IVC. This insert needed to be non-magnetic with adequate thermal conductivity to ensure the coils would remain superconducting. For ease in machining and to prevent excessive eddy currents while ramping the anti-

---

[5] Typically one can expect only about an 85-90% filling fraction even for a well wound coil. These coils are not perfectly wound, particularly in the outer layers, and hence have a filling fraction closer to 70%. However, since they were to be operated far from their critical currents the imperfect winding was not expected to pose a problem.

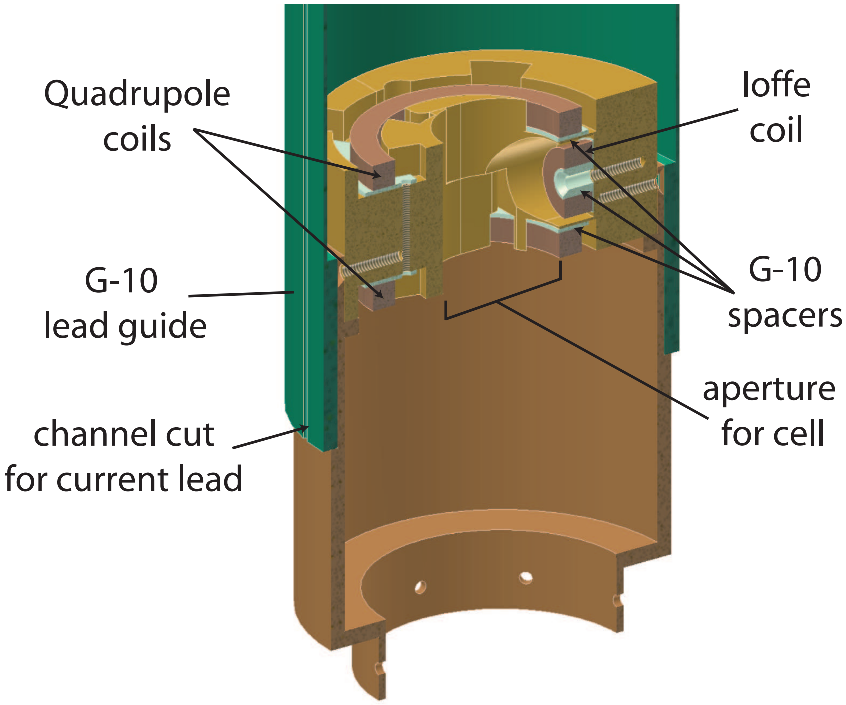

Figure 3.6: The QUIC trap coil assembler, also showing trap coils, G-10 spacer plates, and part of the G-10 sleeve that channels current leads up out of the IVC.

Helmholtz magnets we chose brass[6]. This “coil assembler” holds the quadrupole coils off-axis from the cell and positions the Ioffe coil between them. It also has a notch on which a G-10 cylinder sits - a sleeve fitting snuggly inside the IVC with channels cut in it to hold the current leads, keeping them away from the cell as they pass upwards to an electrical feedthrough and out of the IVC, as in figure 3.6. Non-magnetic titanium screws hold the QUIC coils in place, secured via holes in tabs on the G-10 spacer plates epoxied to the coil faces. The assembler is made of three pieces. The coils are affixed to two interlocking parts that separate to allow easy access (and machining simplicity) to a pocket holding the Ioffe coil, while a third part anchors the two piece assembly to the IVC and holds the G-10 sleeve.

---

[6] In retrospect, eddy currents from the QUIC trap itself are also an annoyance - see section 6.3.2.

3.3 Cell modifications

To accomodate the QUIC trap assembly it was necessary to modify the lower part of the cell from the initial design described in section 2.2.1. As introduced above, the bottom window region of the old cell was replaced with a narrow extension into which the atoms could be shifted during evaporative cooling. To allow an off-the-shelf window to be used the extension was designed to have a 0.5” inner diameter, giving it an outer diameter of about 0.8”. This creates an annulus of empty space around it inside the 3.1” diameter IVC, providing plenty of space for the QUIC trap.

3.3.1 Replacing the cell bottom

Rather than building an entirely new cell, we elected to modify the existing cell to save on time and construction costs while also minimizing the number of newly glued joints that had not yet been leak tested. This involved cutting off the lower region of the old cell, replacing the window with new G-10 components. The modified cell was designed to locate the constriction at a magnetic field which would match the limiting field at the trap wall. This would maintain the maximum trap depth possible for initial loading while minimizing the distance the anti-Helmholtz minimum would have to shift to permit transfer of atoms into the QUIC trap. Furthermore, it left as much room as possible in the bottom of the IVC to hold the trap assembly and current leads. This involved removing between 1 and 2 inches from the bottom of the old cell, as in figure 3.7.

The new extension to the cell had to be designed to continue the superfluid jacket all the way to the bottom, maintaining thermal conductivity and cooling the window. It was also imperative that any new construction remain within the outside diameter of the old cell. The cell was originally designed to maximize the useful trap depth

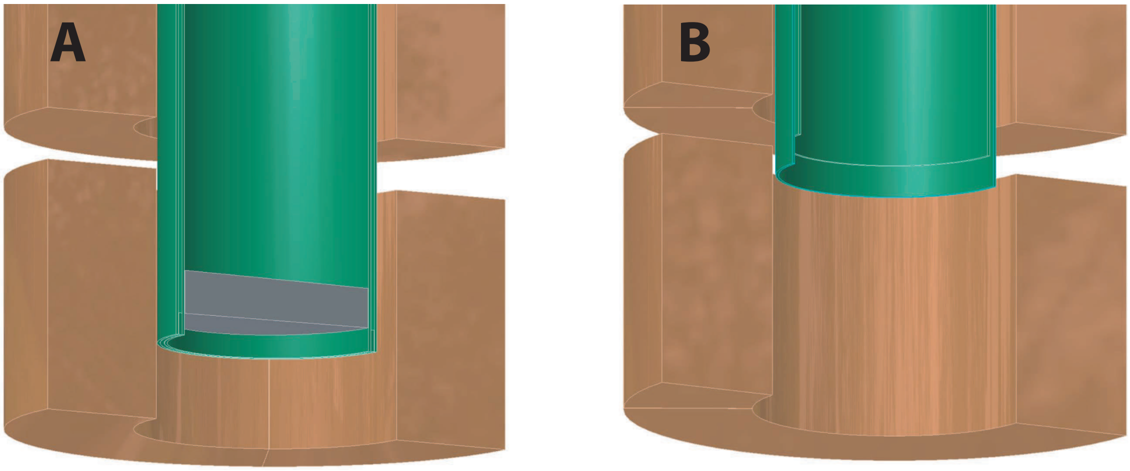

Figure 3.7: Cutting the old cell to incorporate the narrow extension. (a) shows the unmodified cell, while (b) shows the location of the cuts to the inner and outer cell walls. The anti-Helmholtz coil is included as a reference.

and had minimal vacuum space between the outer wall and the IVC; any components extending to larger diameter would increase the risk of a touch thermally linking the cell to the IVC. To achieve this while also maintaining sufficient (0.2" or greater) overlap in all of the glue joints required offset cuts in the inner and outer cell walls with glue joints located on the inner faces.

To actually cut the bottom off the old cell we first removed the cell from the cryostat and disassembled it as much as possible, removing the valve and charcoal sorb. After measuring and marking the appropriate cut location using calipers, the cell bottom was removed by cutting through both walls using a Dremel tool with an abrasive cutting wheel. Finally, the cut location for the inner wall was marked and cut from the inside, taking care not to cut or score the outer wall. After cleaning, the new G-10 pieces were epoxied to the old using Stycast 1266 epoxy [93]. Glue joints were made one or two at a time, orienting the cell such that gravity would help wick the epoxy into the joint whenever possible. The modified cell is pictured in figure 3.8.

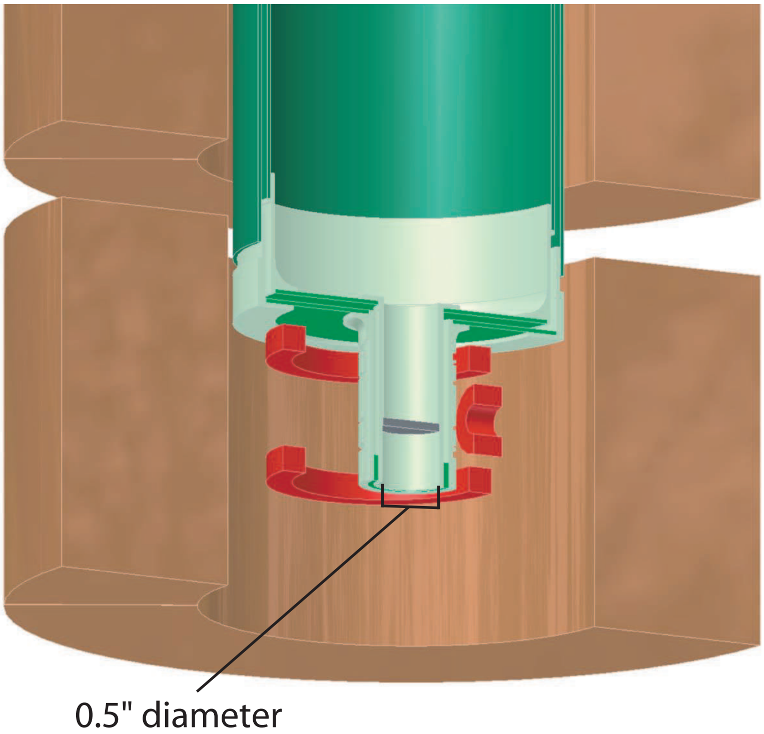

Figure 3.8: The modified cell bottom. New G-10 components are shown in alternating colors to highlight joint locations. The QUIC trap coils are shown in red.

3.3.2 Superfluid jacket fill line heat sinks

In the previous iteration of the cell one of the major sources of heating was refluxing helium in the fill line for the superfluid jacket (see [115, §4.2] for details on the problem). This was a known issue, and the fill line was constructed so as to minimize the problem, with custom pinhole gaskets in three locations to minimize helium movement and a heat sink at the only intermediate temperature available (the 1K pot) [89, §5.3]. Even so, shaking the dewar to disrupt superfluid film flow in the fill line led to a reduction in the heat load on the ^{3}He refrigerator and a corresponding decrease in temperature. Fortunately, the new dilution refrigerator offers additional points for heat sinking to completely resolve the problem. The key ingredient is a heat sunk pinhole gasket attached to a point on the refrigerator that is cold enough to re-condense any refluxing helium vapor (< 300 mK) yet still has a significant cooling power. The so-called 50 mK plate on the new refrigerator provides a perfect location for such a heat sink; we also added a similar gasket heat sunk to the still, resolving the reflux problem.

3.3.3 RF discharge coil

In the previous iteration of the experiment the coil used to ignite the RF discharge was wrapped on a form that fit around the cell, just inside the IVC wall. This was done to minimize the amount of heat added to the cell while firing the discharge. However, the cell could still be warmed dramatically if the coil was left on for more than a brief moment, once boiling off half of the helium in the superfluid jacket when left on for just a few seconds. Also, the coil performance suffered due to its proximity to the electrically conducting IVC.

Since there was not a clear advantage to having the coil on a separate form, we elected to shift the coil to the cell itself rather than having it share a form with the current leads for the QUIC trap. It was hoped that moving it away from the IVC wall would improve the discharge efficiency, and since operating the experiment only requires igniting the discharge for < 1 ms at a time heating is not a significant issue. Furthermore, this simplified the electrical connections for the coil, since electrical feedthroughs in the dewar are located in the upper region of the IVC, whereas the coil form was in the lower IVC. The new coil consists of roughly 10 turns of 26 gauge enamel coated copper wire with a 1 turn/cm spacing, wound around the full-diameter region of the trapping chamber and affixed with Mylar tape. At low temperature the coil operates most efficiently at frequencies near 70 MHz.

3.3.4 RF evaporation coil

In addition to the RF discharge coil, a second coil was added to the cell to be used for RF-induced evaporative cooling after the atoms were transferred to the QUIC trap. By using a second, smaller coil we can reduce the range of fringing fields, minimizing eddy current heating in the refrigerator. Also, the use of superconducting wire prevents resistive heating.

Because RF currents will only travel in a thin skin on the surface of a conductor [116, §5.18], ordinary copper clad Nb:Ti wire cannot be used, as the current would not flow in the superconducting filaments. As such, the coil is wound from 0.003" diameter pure Nb:Ti wire ensuring the current flows in the superconductor. The coil consists of a matched Helmholtz pair of coils with 5 turns in each. The coils are wound into channels cut around the outer wall of the cell extension, and are centered about the location of the QUIC trap minimum. The field coils create an oscillating magnetic field, polarized appropriately to couple well to atoms oriented along the bias field in the trap minimum (see appendix B for details). After exiting the coil the superconducting wire passes up the side of the cell, affixed via Mylar tape, and connects to an SMA cable in the upper region of the IVC. Because superconductors are exceptionally poor thermal conductors [102, §3.3.4], the superconducting wire also serves as a thermal break, making heat-sinking of these leads straightforward.

3.4 Optical system

In keeping track of our progress towards BEC while evaporatively cooling our ^{4}He* we are principally interested in monitoring two quantities that describe our atom cloud: phase-space density and atom number. This requires the simultaneous measurement of the density and temperature of the trapped atoms. Depending on the temperature of the atom cloud in question, we either probe the atoms spectroscopically or by imaging the cloud onto a charge-coupled device (CCD) camera.

3.4.1 ^{4}He* optical transitions

As introduced in section 2.2, ^{4}He* has two transitions which are readily accessible for atom detection: the $2^3S_1 \rightarrow 2^3P_{0,1,2}$ transition at 1083 nm, and the $2^3S_1 \rightarrow 3^3P_{0,1,2}$ transition at 389 nm (see appendix A for details). Although both transitions were used for the work described in [89], the present experiment used the 1083 nm transition exclusively. This is for two main reasons. First, the 1083 nm transition is preferred for probing warm, low density atom clouds, scattering $\sim$ 8 times more light than the 389 nm transition due to the λ^2 scaling of the photon absorption cross-section. Second, due to the failure of the 389 nm diode laser following its use in [89], frequency doubling was the only option for generating light to probe the blue transition. Since

IR laser diodes are readily available, probing the atom cloud using the 1083 nm transition is technically less challenging.

3.4.2 Diode laser and optics

The 1083 nm optical system used for ^{4}He* detection consisted of three main components: the diode laser itself, optics used for referencing the laser frequency to the ^{4}He* transition, and photodiodes or a CCD camera used for the detection of laser light after it has interacted with trapped ^{4}He*. The optical system is pictured in figure 3.9. Light is first generated using a Toptical DL100 diode laser [117]. The DL100 has a short-term linewidth of about 200 kHz, and produces > 10 mW of IR light. This light is split into two paths. One path, the "reference beam," contains about 20% of the laser power. It is sent via a double-passed acousto-optic modulator (AOM) [118] to a saturated absorption cell. For spectroscopy this cell serves as a frequency reference with precision superior to that offered by a wavemeter. However, using a lock-in amplifier and a PID loop this reference can also be used to frequency stabilize the laser at the few-hundred kHz level for imaging applications where low frequency drift is required. The saturated absorption cell and frequency stabilization scheme are described in appendix C. The second path, a "probe beam" containing the remaining 80% of the power, double-passes an identical AOM before continuing on towards the cryostat via a variable neutral-density filter to adjust detection laser power.

Under the cryostat the probe beam passes through assorted beam sizing lenses and then strikes a large wedged glass beamsplitter, reflecting $\sim$5% of the power up into the dewar while passing about 90%. The transmitted light is collected by a 5 cm lens and focused onto a photodiode to be used as a reference beam to normalize

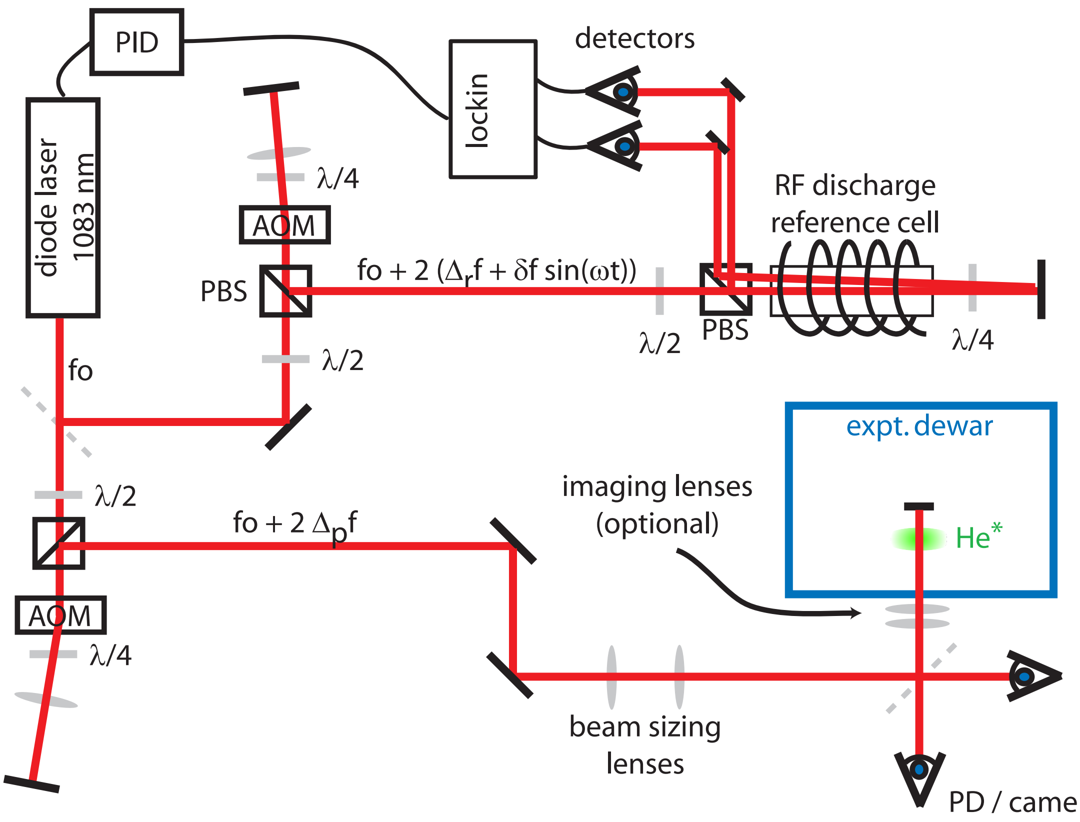

Figure 3.9: The 1083 nm optical system used for detection of ^{4}He*. 1083 nm light is produced by a diode laser, frequency stabilized as needed by locking to a saturated absorption reference cell, and passed through the atom cloud onto either photodiodes (for absorption spectroscopy) or a CCD camera (for imaging).

data against laser intensity fluctuations. The dewar beam travels into the cryostat, retroreflecting off of a mirror at the top of the cell trapping chamber before passing back out of the dewar and through the large beamsplitter before being detected.

For spectroscopy the beam is focused onto a photodiode using a 5 cm lens. To image the atoms, however, a pair of 40 cm lenses is added to the beam path immediately before the beam enters the dewar. This creates an image of the atom cloud beyond the large beamsplitter. By suitably locating a CCD camera at the image focus, this image can be recorded and information about about the atom cloud obtained based on the image size and contrast. Unfortunately, imaging in the IR is challenging; one faces the choice of using silicon based CCD cameras with low (1% or less) quantum efficiencies or expensive Ge or InGaAs based cameras with improved quantum efficiency but significantly poorer noise specs and complicated cooling requirements. Our images are collected using a Pixis 1024BR CCD camera [119] for which we measured a quantum efficiency of slightly better than 1%.

Nearly all of the optical elements are coated appropriately for our 1083 nm wavelength. Mirrors are all broadband coated for NIR (700-1100 nm), and lenses are broadband anti-reflection coated for a similar wavelength range. However, a few elements have narrowband coatings to reduce cost where broadband coatings were prohibitively expensive. In particular, broadband polarizing elements are quite costly. As such, the polarizing beamsplitters, quarter waveplates, and half waveplates used are laser-line coated for the 1064 nm YAG transition. Fortunately this coating is still sufficiently broad to perform well at 1083 nm while offering a significant savings. Unfortunately, the anti-reflection coatings on the dewar windows are incorrect for 1083 nm (for legacy reasons), and thus reflect approximately 8% per face.

3.4.3 532 nm YAG laser and optics

In addition to the 1083 nm laser system, the experiment also utilizes a frequency doubled pulsed YAG laser operating at 532 nm. Pulsed YAG lasers are often useful for buffer-gas experiments for production of gaseous samples to be trapped; for example, the chromium experiment described in section 2.1.1 used a laser pulse to ablate a metallic chromium target, producing more than 10^{12} Cr atoms. For producing metastable helium a laser is not required in the same way, since ^{4}He* is produced using a RF discharge. Despite this, ablation can still be useful for ^{4}He* production. RF discharges require a "trigger," often in the form of a cosmic ray, to ignite. This trigger creates ions that feel the RF fields and collide with gas particles, igniting the discharge. To force the discharge to start on demand, however, it is convenient to provide a suitable trigger coincident with the delivery of the RF current to the discharge coil. Since ablation produces ions in addition to neutral particles, a fairly weak laser ablation pulse is an ideal trigger.

To start our discharge we utilize a Continuum Surelite laser [120] capable of producing 200 mJ 532 nm pulses of < 10 ns duration at a 15 Hz repetition rate. For our purposes we require single pulses of significantly less energy (about 1 mJ), so we trigger the laser externally using timers synchronized with the RF discharge current. After exiting the laser, pulses pass through a telescope to expand them spatially and reduce the likelyhood of mirror damage. These pulses travel to the cryostat via 532 nm laser-line mirrors and are then focused onto a convenient metallic target inside the cell using a 50 cm lens. The choice of target is relatively unimportant, but ordinarily a brass screw that secures the cell mirror is used. Brass is composed almost entirely of copper, zinc, and sometimes lead, all of which have a magnetic moment of 1 μ_B or less, making it unlikely that the products of the ablation pulse contaminate the trap at long times.

Chapter 4

Production and surface evaporation of metastable helium

Having modified and updated the cryostat and optical system, we were ready to focus on evaporative cooling of ^{4}He* in the new QUIC trap, pushing below the few mK temperatures reached in the preliminary work described in section 2.2. Work proceeded in stages as we learned how to best produce ^{4}He* while achieving good vacuum in the modified cell and then characterized the new trap and RF evaporation coil. This chapter describes the exploration of metastable helium production and thermal isolation in the improved experimental apparatus as well as the initial stages of evaporative cooling in the modified cell.

4.1 RF discharge and cell vacuum

As a result of the addition of the dilution refrigerator we hoped it would no longer be necessary to produce ^{4}He* from the thin film used in previous experiments, hopefully improving the number of ^{4}He* produced and trapped. We began by investigating

^{4}He* production with the valve closed and the cell filled with helium gas. By igniting the discharge in the presence of a significant helium density we were able to produce much more ^{4}He* with the cell filled with gas than we could using the valve-open loading described section 2.2.2. Unfortunately, the dilution refrigerator did not solve the background gas problem without additional cell preparation, thus we were forced to return to valve-open loading from a thin film on the cell walls.

4.1.1 Production of ^{4}He* from a saturated vapor

As in previous work, helium is excited up to the long-lived metastable 2^3S_1 state using a RF discharge. To begin, the valve separating the trapping chamber from the pumping chamber is closed and helium is introduced into the cell by applying a brief heat pulse to a heater on the waiting room sorb, usually delivering about 500 mW for 1 sec. The strength of this heat pulse can be used in combination with the cell temperature to set an arbitrary buffer gas density in the cell, helping to tune the discharge performance. After adding helium to the trapping chamber, the discharge is ignited by passing RF current through the discharge coil coincident with the arrival of a 1 mJ pulse from a 532 nm pulsed YAG laser. After finding a suitable frequency using a RF signal generator the RF signal is generated using a voltage controlled oscillator (Mini-Circuits ZX95-100-S+ [121]) and amplified using an ENI 325LA 50 dB 25 Watt amplifier [122], and is delivered for 200 μsec. Significantly shorter on-times do not reliably produce ^{4}He*, while longer ones do not lead to increased production. In the interest of producing as much ^{4}He* as possible we began by firing the discharge with the cell well filled with helium, using cell heater pulses to a particular cell temperature to set the buffer-gas density according to the helium vapor pressure curve.

To determine the number of ^{4}He* produced in this way we probe the discharge at zero magnetic field using absorption spectroscopy. Light from a diode laser is reflected off of the cell mirror (see figure 3.9), and absorption is measured as the laser frequency is tuned across the atomic resonance. Atom number and temperature can be determined from the transmitted light intensity according to

$$I(\omega, T) = I_o e^{-\sigma_o \int n(z) f(\omega,T,z)\, dz} \tag{4.1}$$

where I_o is the incident intensity, n_o is the central atom density, σ_o is the resonant photon absorption cross section, $f(\omega, T, z)$ is a lineshape function, and the integral is carried out over the optical path. For measurements with no magnetic field the atom density is approximately constant throughout the cell, so this simplifies to

$$I(\omega, T) = I_o e^{-n_o \sigma_o f(\omega,T) L} \tag{4.2}$$

where n_o is the atom density and L is the length of the optical path through the cell. The quantity $n_o \sigma_o f(\omega, T) L$ is generally referred to as the optical depth, or OD. Most generally $f(\omega, T)$ is a Voigt profile, but at our loading temperatures it may be well approximated by a Gaussian since broadening due to the natural linewidth is negligible (see [123, §3.2], appendix A for more details).

One minor complication for measurements at zero field is that immediately after the discharge is ignited and before the atoms have had an opportunity to diffuse to the cell walls the OD is generally large enough that essentially all of the incident light is absorbed when the laser is on resonance. While it is possible to determine the peak OD (and thus the atom density) from the off-resonant wings of such a spectrum, doing so can be challenging in situations where the temperature is not well known. In our case, then, it is more convenient to measure the absorption as a function of time; assuming atom loss due to diffusion we can fit an exponential decay to the OD and infer the $t = 0$ value from data at later times, as in figure 4.1. From this data

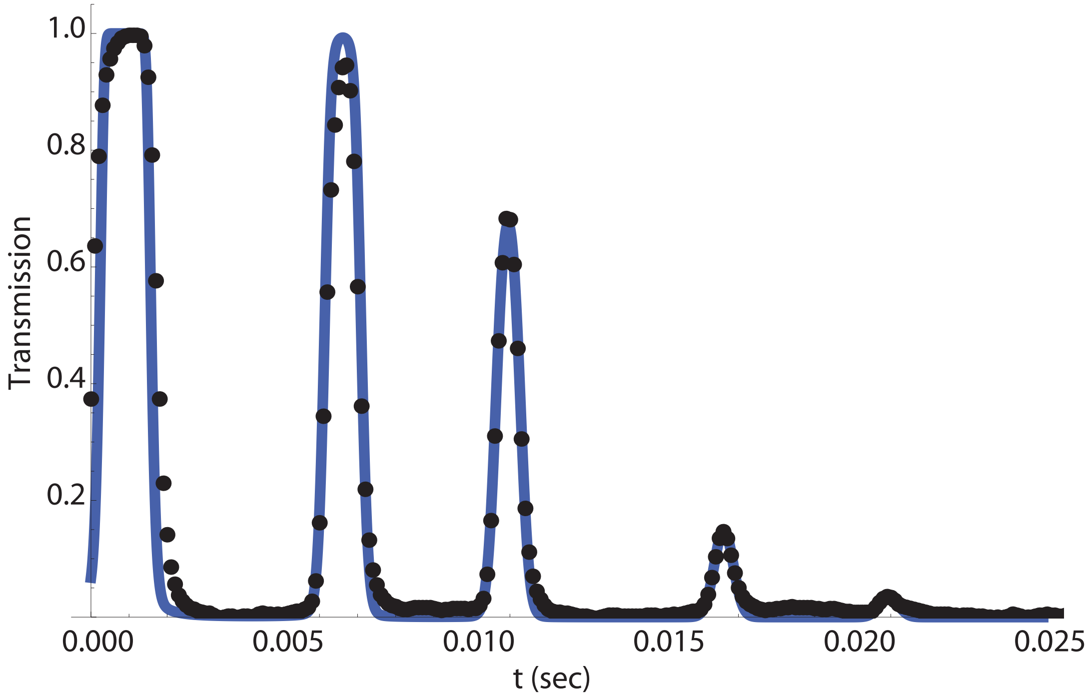

Figure 4.1: Decay of ^{4}He* due to diffusion to the cell walls, measured at zero magnetic field. Scans are taken at 100 Hz over the $2^3S_1 \rightarrow 2^3P_2$ line at 1083 nm, with $T_{\text{cell}} \sim 650$ mK. The solid line is a fit of Voigt profiles to the data, yielding $n_o = 2.2 \times 10^{10}\text{cm}^{-3}$ and $T = 2.6$ K, and $\tau = 2.9$ msec. The discrepancy between the fitted and cell temperatures is likely due to Zeeman broadening caused by trapped flux in the anti-Helmholtz magnet.

we calculate a total number of ^{4}He* produced of approximately 10^{13}. Assuming an initially equal distribution between the three m_S states we might reasonably hope to trap more than 10^{12} of these atoms — more than an order of magnitude greater than were trapped in the preliminary ^{4}He* work using valve-open loading.

Unfortunately, although igniting the discharge from a saturated film led to the production of a large number of ^{4}He*, our efforts to evaporatively cool a sample produced in this way were unsuccessful. As with the experiments described in [88, 89], opening the valve allowed the charcoal sorb to pump out the majority of the buffer gas, but a film remains on the cell walls. We had hoped that the significant cooling of the cell between heater pulses to 400-600 mK used for loading and the < 200 mK base temperature made possible by the new dilution refrigerator would bind the remaining film tightly to the walls, leading to good vacuum. However, we observed two signs of inconsistent or poor vacuum quality when loading from this setup. First, the number of atoms we were able to evaporatively cool to temperatures < 10 mK was variable (and often barely detectable) despite loading comparable numbers of ^{4}He* atoms into the trap initially and using identical magnet ramps. Second, the evaporative cooling efficiency depended strongly on ramp duration with slower ramps producing fewer atoms, whereas one expects that in the absence of loss processes slower ramps should be more efficient [37]. While Majorana and two-body losses contribute to this behavior, during the early stages of evaporative cooling in our anti-Helmholtz trap the cloud is neither small nor dense enough for these processes to explain the inefficient cooling. This leaves background gas collisions as the likely culprit.

Ideally, of course, we would simply measure the density of background gas atoms in the cell during evaporative cooling. However, measuring the quality of the vacuum is a bit of a challenging problem, since gas pressures too low to register on standard vacuum gauges are still too large for efficient evaporative cooling. Indeed, the typical way of measuring very low pressures is to observe the influence of the background gas on a cloud of atoms held in a shallow trap. In this situation individual collisions with the (comparatively) hot background cause trap loss, leading to a lifetime which is inversely proportional to the background gas density:

$$\tau_{bg} = \frac{1}{n_{bg}\sigma_{bg-a}\overline{v}_{bg}}, \tag{4.3}$$

where n_{bg} is the background helium gas density, $\overline{v}_{bg}$ is the mean thermal velocity of the background gas atoms, and σ_{bg-a} is the collision cross section between background gas atoms and the trapped species (generally about 1×10^{-14} cm^{-3} [46]). For our experiment this is a bit of a paradox; since we can only prepare a cloud of atoms in a sufficiently shallow trap via forced evaporation, we are only able to quantitatively measure the vacuum quality in circumstances where it was adequate for evaporative cooling in the first place. As such we are largely limited to making binary measurements. Either the vacuum is good enough to observe cold, trapped atoms (given the duration of our evaporative cooling ramps this implies $\tau_{bg} \gtrsim 100$ sec, or $n_{bg} < 10^8$ cm^{-3}), or we fail to observe any evaporatively cooled atoms and conclude that the vacuum is poor ($n_{bg} > 10^9$ cm^{-3}).

4.1.2 Cell preparation and valve-open He* production

To try to improve the quality of the vacuum and corresponding evaporative cooling performance we were forced to return to using various bakeouts to prepare our cell and pumping sorb and then igniting the RF discharge with the valve open. Our first efforts centered on changing the temperature of the sorb. According to the literature it is possible for a sorb to become "clogged" even with with small amounts of gas if the sorb temperature is below a critical temperature such that adsorbed gas atoms are unable to move across the surface of the sorb. In this case gas atoms are unable to permate the charcoal grains into the myriad nooks and crannies inside, and the effective area of the sorb is the same as its apparent area[1], dramatically reducing its pumping capacity. For example, for Ne and H_2 the critical temperatures are 11 K and 13.5 K, respectively [124]. Further information on this topic can be found in appendix D.

Our sorb has an apparent surface area of about 650 cm^2; given the helium monolayer density of $\sim$ 0.115 Å^{-2} [125], this would give it a capacity of only about 8×10^{17} helium atoms - just one or a few times filling the trapping chamber with buffer gas. Bearing this in mind, we began heating the sorb to a temperature of 5-7 K in an effort to "bake-in" the helium, i.e. make it possible for it to find its way into the empty binding sites deep inside the charcoal grains. After such a bake-in the sorb was allowed to cool back to its $\sim$ 1.5 K base temperature so that sorbed helium would be tightly bound. This helped dramatically, leading to approximately a ten-fold improvement in the number of atoms evaporated to temperatures of a few mK. In time, however, this improvement seemed to fade, perhaps due to clogging of the sorb with other material etched off of the cell walls while operating the RF discharge. We began baking out the cell as well, hoping to thin the film in the trapping chamber to help get most of the helium onto the sorb while the charcoal was still warm enough for the gas to permate the grains. Temperature profiles from a typical bakeout are shown in figure 4.2. Assuming that the sorb is performing well such a bakeout dramatically improves the vacuum; since the helium film is now quite thin, remaining atoms are tightly bound to the walls once the cell cools.

After preparing the cell and allowing it to cool back down to its $\sim$ 200 mK base

---

[1] That is, the area one can readily "see" on the exterior of the charcoal, not including the the myriad niches inside each grain. See appendix D for more details.

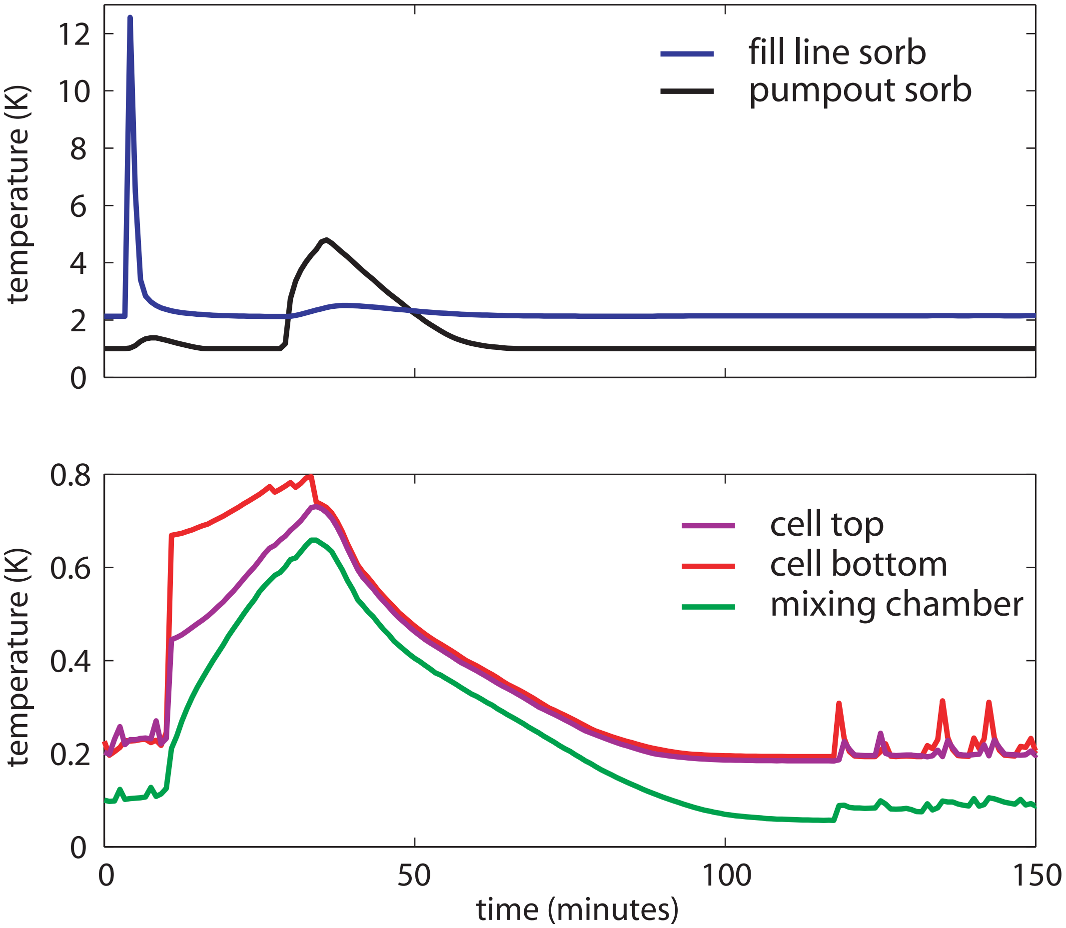

Figure 4.2: Temperature profiles for a typical cell and sorb bakeout. With the valve closed a heat pulse is sent to the fill line sorb to introduce helium into the trapping chamber. After opening the valve the cell is baked out to approximately 800 mK by applying current to the cell heating resistor, while the pumpout sorb is warmed to 5 K to increase permeation of ^{4}He into charcoal grains. The brief spikes in the cell temperature beginning at 120 minutes result from YAG and RF discharge pulses during ensuing ^{4}He* production.

temperature, helium atoms are excited to the metastable 2^3S_1 state using the RF discharge coil and 532 nm YAG laser pulse described above. In this case, however, we produce fewer atoms since we are no longer working in a helium-rich environment. Instead, the discharge must be ignited in the small amount of gas that is desorbed from the thinned film by the laser pulse (it is likely that the discharge itself may etch additional helium out of the film while it is lit). Having thinned the film with a bakeout the entire cell now acts as a cryopump, so as soon as the current to the discharge coil is turned off the helium remaining in the ground state rapidly adsorbs onto the walls. This means that we are no longer able to measure the zero-field spectrum of the ^{4}He* produced, since the lifetime of ^{4}He* atoms in the cell is set by the roughly 1 ms pumpout time to the cell walls. This is no problem, however; by energizing the anti-Helmholtz magnet we can utilize its confinement to trap that ^{4}He* which is in the $m_S = 1$ Zeeman sublevel and measure the absorption spectrum of the trapped cloud, as in figure 4.3. Fits to the spectrum indicate temperature and density (see appendix A). Using the cell preparation here described and igniting the RF discharge with the valve open generally leads to the trapping of 5×10^{10} to 2×10^{11} ^{4}He* atoms. The trapped distribution initially implies a temperature of nearly 600 mK, much warmer than the cell base temperature. This may be because the buffer gas is pumped away to the cell walls before the atoms can completely cool from the elevated temperatures present in the RF discharge. Spectra taken at later times fit to lower temperatures, presumably due to loss of hot atoms over the trap edge as the cloud evaporatively cools to its equilibrium temperature.

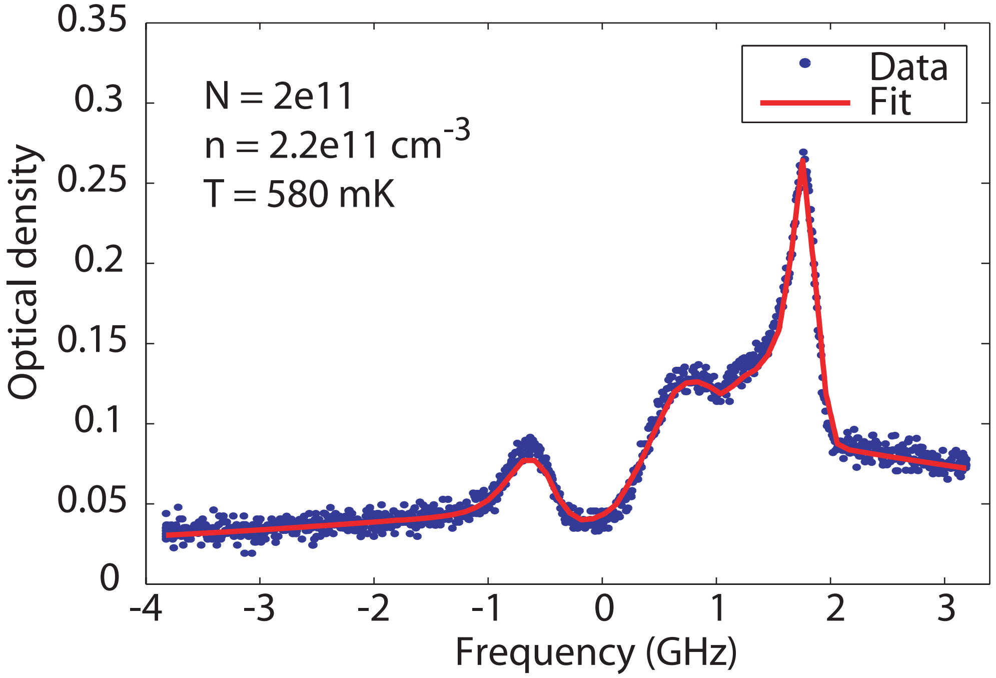

Figure 4.3: An absorption spectrum of trapped ^{4}He* taken within 200 ms of the RF discharge pulse.

4.2 Surface evaporation in the modified cell

Having now trapped ^{4}He* we can proceed with forced evaporative cooling using the same surface adsorption technique described in section 2.2.3. However, we cannot follow the previous cooling trajectory described in references [2, 89] for two reasons: a different cell wall geometry, and the need to completely turn off the anti-Helmholtz magnet so as to trap the atoms in the QUIC trap for further cooling, thus preventing Majorana losses.

In the previous work our goal was simply to evaporatively cool the ^{4}He* to as low a temperature as possible. Evaporative cooling is driven by elastic collisions between the trapped atoms; as the high-energy tail of the thermal distribution is removed by atoms adsorbing onto the cell wall, the remaining atoms must exchange energy via collisions to assume a new equilibrium distribution, now at a lower temperature. As such the rate at which the cooling process can proceed is limited by the density of the cloud, which determines the collision rate. Approximating the anti-Helmholtz field as a spherical quadrupole we can calculate the spatially averaged collision rate according to [126, §5.2]:

$$\Gamma_{el} = \frac{1}{8} n_o \sigma_{el} \overline{v} \sqrt{2} \tag{4.4}$$

where $\overline{v} = \sqrt{\frac{8k_BT}{\pi m}}$ is the mean thermal velocity and σ_{el} the two-body collision cross section. In contrast, our losses were dominated by Majorana losses, for which the loss rate is [87, §D]

$$\Gamma_{Maj} \propto \frac{\hbar\,\mu}{m\Delta\mu} R^2. \tag{4.5}$$

Since evaporative cooling is characterized by atom loss following

$$\frac{N}{N_o} \propto \left(\frac{T}{T_o}\right)^{1/\alpha} \tag{4.6}$$

and in a linear potential $R \propto T$, we can conclude that the collision rate will increase faster than the Majorana loss rate for all $\alpha > 1$ even as the cloud cools and shrinks. We thus expect cooling to be most efficient if we use a tightly confining potential, allowing for rapid evaporation and thus avoiding losses. With this in mind the previous work maintained significant currents in the anti-Helmholtz magnet and forced cooling by pushing the trap minimum close to the adsorbing surface (the cell window).

In the current work this technique is impossible. Although evaporation is most efficient in a tightly confining trap, we now have the additional constraint of needing an evaporative cooling trajectory in which milliKelvin temperatures and rapid Majorana loss do not occur until the anti-Helmholtz coil currents are near zero, at which point atoms can be transferred into the quadrupole-Ioffe configuration trap. Unfortunately, we can only energize the QUIC trap without the risk of quenching it when the anti-Helmholtz fields are fairly small (empirically determined to mean fewer than 5 A in the bottom coil). Also, it is preferable to pursue evaporative cooling in the QUIC trap with the anti-Helmholtz current supplies switched entirely out of the magnet circuit, thus eliminating a source of magnetic field noise; given the limited ramp rates possible for the large anti-Helmholtz coils, this requires most of the current be out of the magnet before we switch to the QUIC trap.

To incorporate this new constraint while forcing evaporative cooling by ramping the anti-Helmholtz magnet we now pursue a two-stage trajectory. After buffer-gas loading ^{4}He* into the trap with 100 A in both magnet coils we initially ramp the two coils uniformly to 10 A. This cools the atoms by an order of magnitude, but more importantly it removes the majority of the current from the magnet without changing the size of the atom cloud, maintaining a long Majorana lifetime of hundreds of seconds and minimizing losses. Although this does reduce the density of the cloud, since our initial collision rate is rapid — of order 1 kHz[2]— we are able to tolerate the loss of atoms without impacting the evaporation efficiency too strongly. We then proceed to reduce the current in the bottom coil only, shifting the trap minimum towards and then into the extension to the trapping chamber, eventually reaching 10/3 A[3]. This shrinks the cloud, boosting the density, and also locates it appropriately for transfering it into the QUIC trap. Magnet ramps for this part of the evaporative cooling are shown in figure 4.4.

---

[2] Collision rate is estimated using equation 4.4 and the low T limit for the scattering cross section, based on the ^{4}He*-^{4}He* scattering length from [127].

[3] Notation, not division; currents for the anti-Helmholtz magnet written as I_{top}/I_{bot}, where I_{top} and I_{bot} are the top and bottom coil currents, respectively

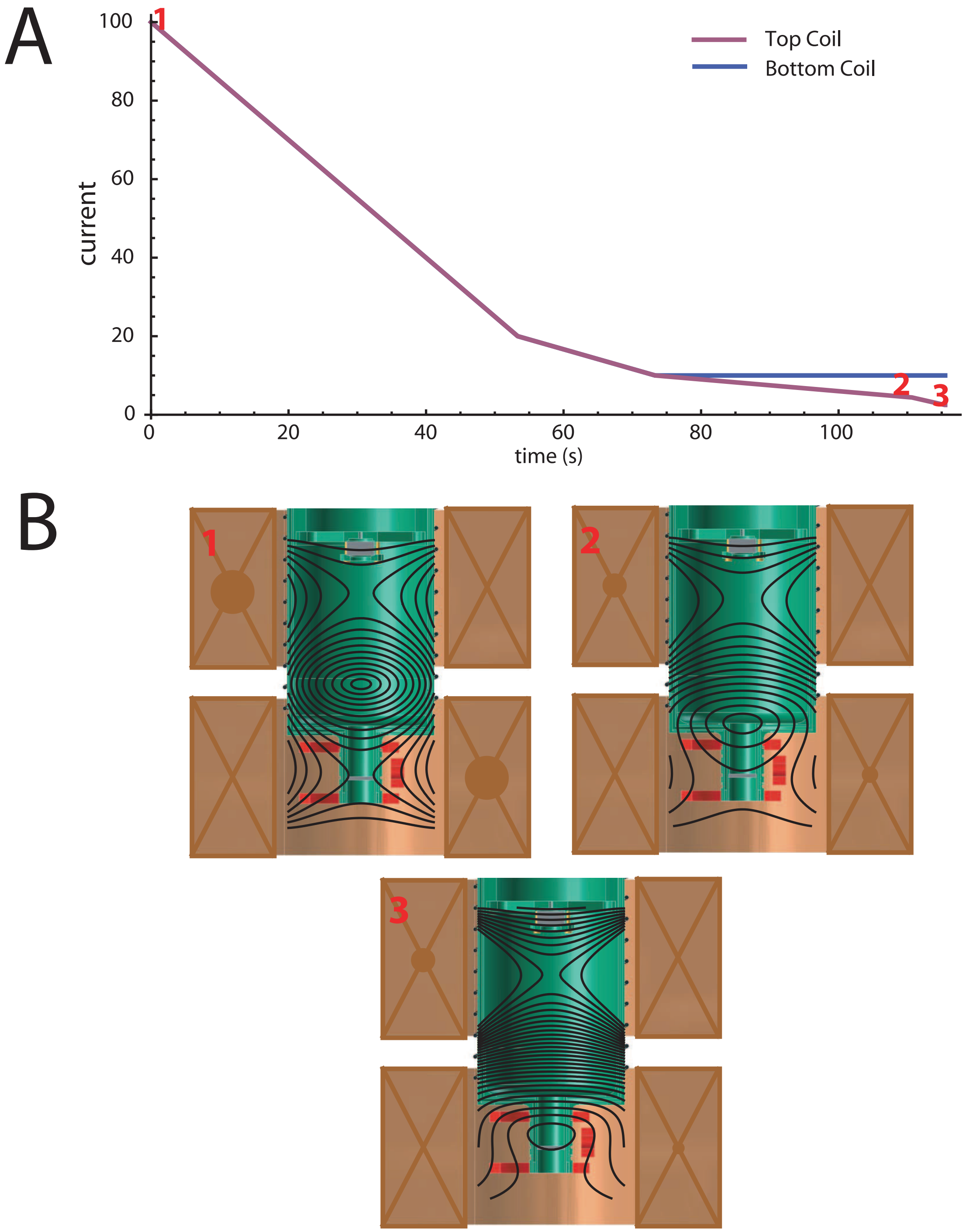

Figure 4.4: Currents and corresponding fields for surface evaporation. (A) shows the current ramps used for the anti-Helmholtz magnet. (B) displays the fields corresponding to points 1, 2, and 3 from (A). Contours every 5000, 500, and 250 G, respectively.

4.2.1 Spectroscopic detection

Just as we had while determining the number of atoms initially trapped, we detect the atoms using absorption spectroscopy, scanning the frequency of the 1083 nm laser back and forth across the atomic line. Because the various spectral features are magnetic field dependent, we can use the Zeeman broadening as a thermometer to determine the temperature of the atom cloud (see appendix A). Generally speaking, this broadening results from the different Zeeman shifts of the various magnetic sublevels of the ground and excited electronic states of the $2^3S_1 \rightarrow 2^3P_1$ transition. Because atoms at different temperatures have more or less kinetic energy, they "slosh" different distances up the walls of the confining potential and therefore experience different magnetic fields. Warmer atoms make orbits into the larger fields, so the presence of spectral components at large Zeeman shifts indicates greater temperatures. The width of the spectrum thus makes an excellent thermometer so long as the Zeeman broadening is larger than the natural linewidth of the transition.

Probe beam centering

In addition to providing information about the density and temperature of the atom cloud, spectra also give information about the position of the probe beam relative to the minimum of the quadrupole trapping field. For warm clouds this positioning is not especially important; the presence of an offset between the beam and the trap center merely means we miss the coldest, densest region of the cloud. Since there are still many atoms making orbits to large radii the beam still interrogates many atoms, and simulations incorporating a beam offset can account for the effect of the offset on the observed spectrum. For colder clouds a beam offset poses more of a problem, however. The atom density is given by a spatial Boltzmann distribution,

$$n(x,y,z) = n_o \mathrm{Exp}[\frac{\mu B(x,y,z)}{k_B T}] \tag{4.7}$$

thus for lower temperatures very few atoms orbit far enough from the trap minimum to interact with a displaced probe beam. This makes detection challenging in the presence of any noise, since the measured optical depths will be small. To resolve this issue we prefer to probe the cloud with a well centered laser that travels up the symmetry axis of the trap.

Centering of the beam is easily achieved using a mirror in the beam path and the beamsplitter under the dewar, using observed spectra to guide corrections. Beam offsets give rise to two major spectral changes: eliminating spectral components at low frequency detunings since the beam no longer interrogates atoms at very low fields, and altering the relative heights of Δm = ±1 and Δm = 0 transitions due to their dependence on the angle between the atomic and probe laser polarizations[4] [90], as in figure 4.5. As such one can use the width of the zero absorption region in the center of the spectrum to judge the size of the offset (relative to the probe beam diameter), and the relative peak heights to learn the direction. This is made more practical by adding a $\lambda/2$ plate and a polarizer under the dewar. Δm = 0 transitions are maximally enhanced relative to Δm = ±1 transitions when $\phi = 0$, so by rotating the laser polarization to maximize this transition strength one can determine the direction

---

[4] The atoms precess about the local magnetic field, and thus have a polarization defined by $\hat{B}$. Defining the symmetry axis of the quadrupole field (and the laser propagation direction) as $\hat{z}$, the laser polarization as $\hat{x}$, and θ and ϕ as the polar and azimuthal angles of $\hat{B}$, then

$$f_{\Delta m=\pm1} = \frac{1-\sin^2\theta\cos^2\phi}{2} \qquad f_{\Delta m=0} = \sin^2\theta\cos^2\phi. \tag{4.8}$$

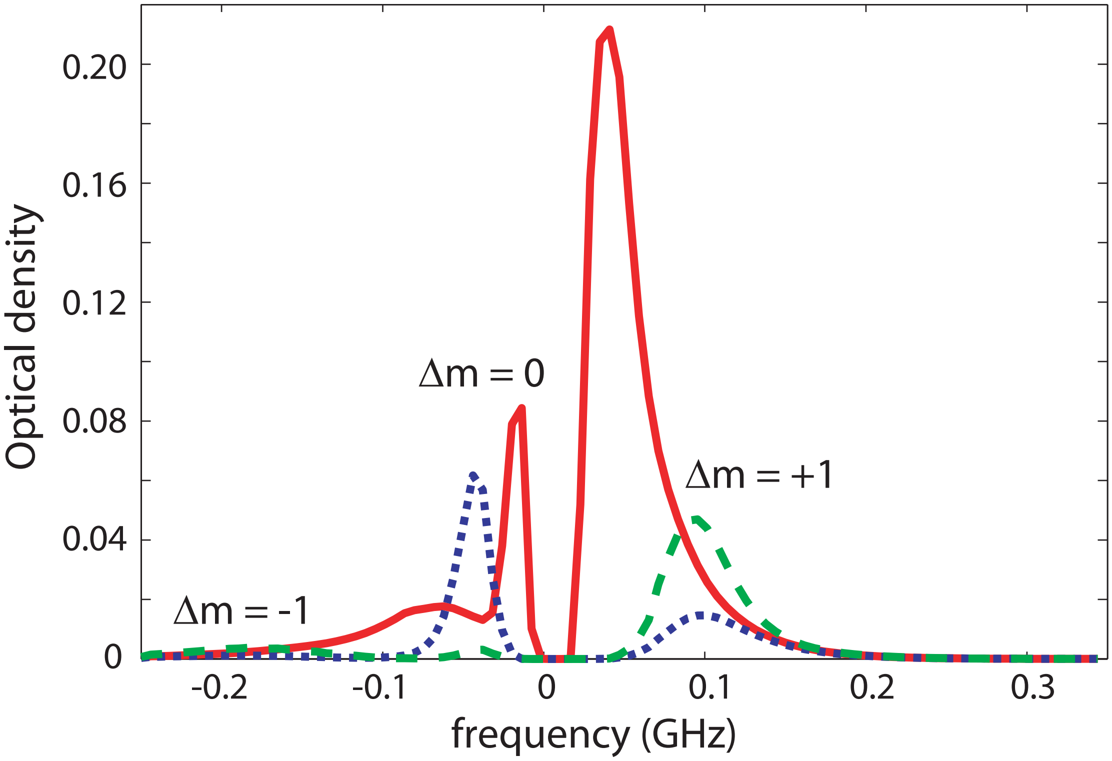

Figure 4.5: Simulated spectra with different beam offsets. The solid red line shows a spectrum assuming a centered probe beam, which is thus independent of the angle ϕ between laser and atom polarizations. In dashed green ($\phi = \pi/2$) and dotted blue ($\phi = 0$) are spectra offset by two probe beam diameters, displaying the "missing" absorption at small frequency detunings as well as the dependence on ϕ. For this simulation $T = 3$ mK and $n_o = 3 \times 10^{10}$ cm^{-3}, with anti-Helmholtz currents of 10 and 3 A.

along which to translate the probe beam to bring it to the center of the trap. In principle spectra of the atoms at any temperature provide this information. However, we usually use evaporatively cooled atoms for this purpose since the absence of level crossings and mixing due to the Paschen-Back effect for atoms in small magnetic fields simplifies interpretation of the spectra. For this purpose it is only necessary that the atoms be fairly cold (currents in the anti-Helmholtz magnet need not also be small since we are not transferring into the QUIC trap), so it is convenient to use ramps to 75/22 A in the top and bottom coils, respectively. This pushes the atoms deep into the cell extension and thus provides trap depths of about 200 mK and atoms at about 20 mK, but takes less time than ramps to 10/3 A and thus is less dependent on the quality of the vacuum.

Cell mirror vibration compensation lenses

Absorption spectra can also be improved by reducing noise that remains in the signal after dividing out intensity fluctuations which are common mode between probe light passing through the atoms and a reference beam sent directly to a photodiode without entering the dewar. The dominant source of this noise is mechanical jitter of the cell mirror off of which the probe beam reflects before exiting the dewar. This jitter is partly managed by reducing the vibrations themselves (for example, the cryostat support structure is filled with lead shot to reduce motion), but in the end it is difficult to eliminate vibrations well enough to do sensitive absorption measurements by reflecting a laser off of what is effectively a 1.5 m long pendulum. However, vibrations can be further mitigated by effectively canceling them at the photodetector by imaging the mirror onto the detector. Placing a lens such that its focus is located at the cell mirror turns mirror vibrations into parallel translations of the reflected

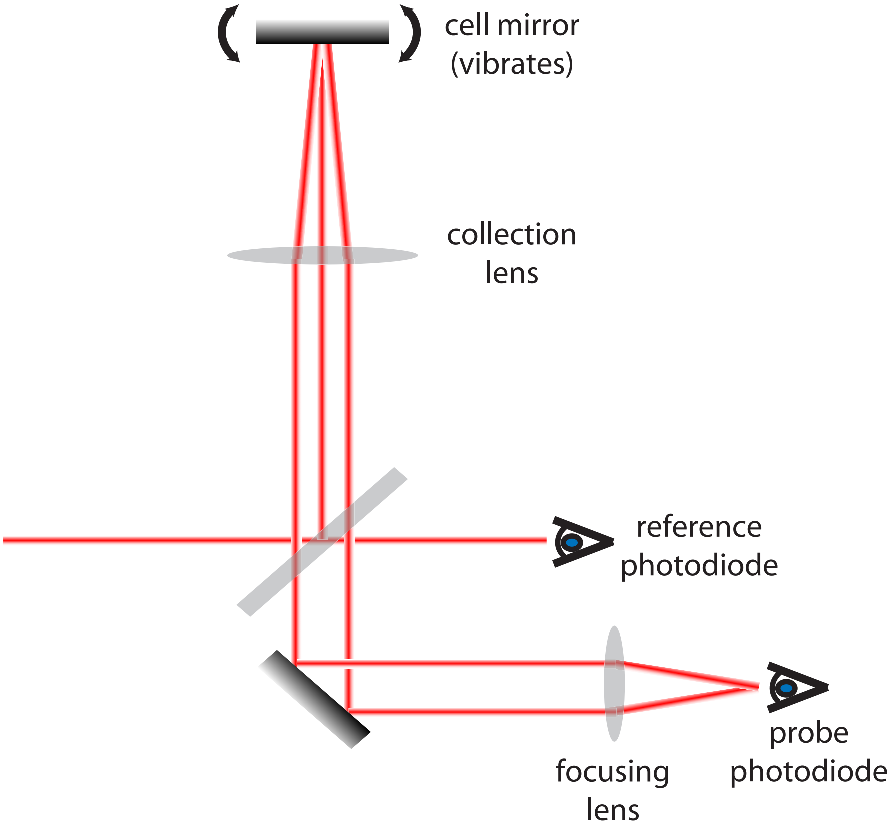

Figure 4.6: A two-lens set-up to minimize noise resulting from cell mirror vibrations.

beam, which can in turn be focused onto a photodiode using a second lens, as in figure 4.6. This helps significantly in reducing intensity fluctuations that result from the reflected probe beam wandering on and off of the detector as the mirror vibrates.

Measured spectra

With the laser probing the atoms through the middle of the cell and the vibration compensation lenses in place it is straightforward to take high quality absorption spectra. Figure 4.7 shows atoms evaporatively cooled to 19 and 3 mK in traps of 75/22 A (used for beam centering purposes) and 10/3 A (ready to be transferred into the QUIC trap). These spectra are both taken with a probe beam with a diameter of

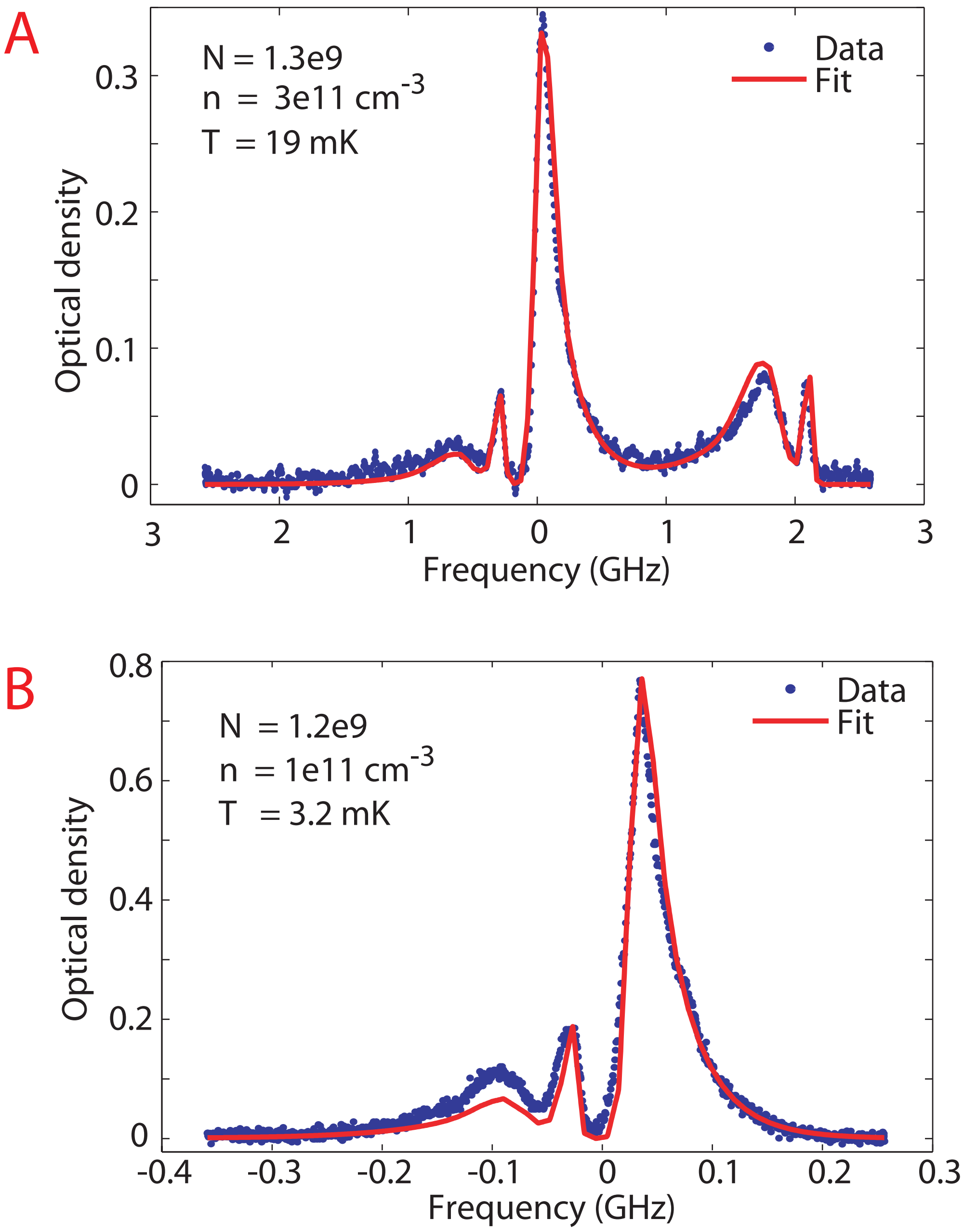

Figure 4.7: Spectra of evaporated ^{4}He*. (A) shows a spectrum of atoms evaporated to anti-Helmholtz currents of 75/22 A in the top and bottom coils, respectively. The features centered near zero GHz detuning result from absorption on the $2^3S_1 \rightarrow 2^3P_2$ line. Features near 2 GHz detuning are from the $2^3S_1 \rightarrow 2^3P_1$ line, thus the $\Delta m = +1$ transition is absent. In (B) the atoms have been evaporated to 10/3 A, and only the $2^3S_1, \rightarrow 2^3P_2$ transition is shown.

approximately 0.5 mm at the location of the atom clouds, well overlapped on ingoing and outgoing passes through the cloud, and within about 0.5 mm of the trap center.

4.2.2 Absorption imaging

As noted above, absorption spectroscopy ceases to be a useful probe of atom temperature once the Zeeman broadening becomes comparable to the natural linewidth of the transition used to interrogate the atom cloud. For the strongest $\Delta \mathrm{m} = +1$ excitation to the $2^3\mathrm{P}_2$ state the Zeeman broadening is $\mu_B \Delta B/h$, while the atoms sit in a typical field of order $B = k_B T/2\mu_B$. As a result, we expect spectroscopy to become a poor thermometer at temperatures such that

$$T \lesssim \frac{2h\Gamma}{k_B}, \tag{4.9}$$

or about 150 μK.

Fortunately, another straightforward option for thermometry exists, namely imaging the entire atom cloud onto a camera. Assume the atoms are orbiting about a potential $U(r) = ar^p$. Clouds of atoms in this potential will have a characteristic size R based on their temperature, with

$$R = \left(\frac{k_B T}{a}\right)^{1/p}. \tag{4.10}$$

Thus if we understand our confining potential, we can use the size of an imaged cloud as an accurate gauge of its temperature. Absorption images offer an additional attractive feature, namely that by imaging the entire cloud we can glean much more information about it than we can from simple spectroscopic detection, keeping track of its size, shape, and location. This makes images significantly more useful for troubleshooting when problems arise.

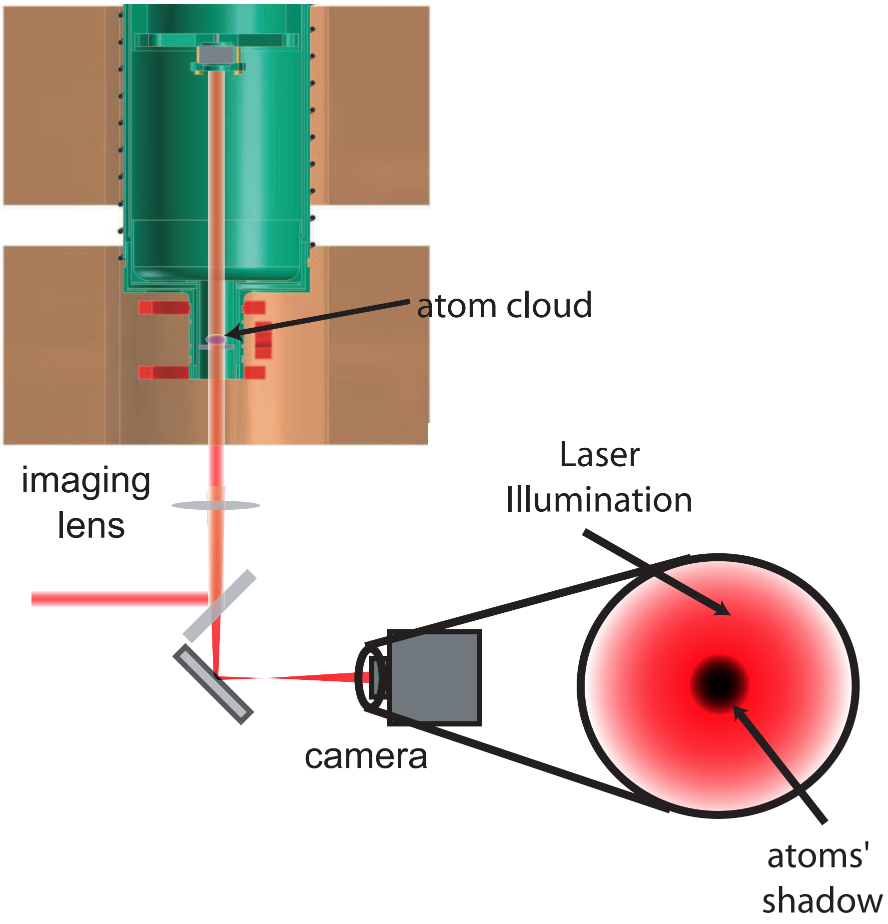

Figure 4.8: The optical set-up used for absorption imaging.

Many different techniques exist for imaging a cloud of atoms, including absorption, fluorescence, dark-ground, phase-contrast, and polarization contrast techniques [112]. Absorption imaging is the simplest of these; it works in much the same way as absorption spectroscopy, only a CCD camera takes the place of a photodiode to measure the light transmitted by the atom cloud. By incorporating a suitable lens into the beam path the cloud may be focused onto the face of the camera. Each of the individual camera pixels measures the transmitted light of a tiny component of the beam, thus the absorption by the atom cloud appears as a “shadow” on the camera face, as in figure 4.8.

Useful images of the atom cloud actually consist of four individual sets of data collected by the CCD camera, combined in such a way as to isolate the actual absorption by the atoms. Generally speaking a particular absorption image from the camera may be written as [112]

$$F_I(x,y) = A_I\,[P(x,y)\ \mathrm{Exp}[-OD(x,y)] + S(x,y)] + N(x,y) + C(x,y), \tag{4.11}$$

where A describes the strength of the probe beam, $P(x,y)$ gives the normalized profile of the laser beam, $OD(x,y)$ is the actual optical density of the atom cloud, $S(x,y)$ gives a normalized representation of light scattered out of the probe beam following its interaction with the atoms, $N(x,y)$ gives other sources of background light striking the camera, and $C(x,y)$ represents dark counts on the camera. The presence of S, N and C and the fact that P is generally not a well behaved Gaussian profile due to interference effects, etcetera, means that extracting the OD from F directly is not practical. As such, we take a sequence of images as follows:

- An initial image to “clean” the camera, F_C, for which the laser is shuttered. This is to reset the the dark counts on each pixel to zero, since they accumulate slowly between images, but is not directly involved in later image processing.
- A “dark” image, F_D, where the laser is once again shuttered.
- An absorption image, F_A, in which the atom cloud is illuminated by the probe laser.
- A “bright” image, F_B, with the laser on but the atoms now gone from the trap such that there is no absorption.

These images are combined as follows to form a transmission image $T(x, y)$:

$$T(x,y) = \frac{F_A(x,y) - F_D(x,y)}{F_B(x,y) - F_D(x,y)} \tag{4.12}$$

$$= \frac{A_A}{A_B} \frac{P(x,y)\mathrm{Exp}[-OD(x,y)] + S(x,y)}{P(x,y) + S(x,y)} \tag{4.13}$$

Generally the overall light level is fairly constant from shot to shot, such that $A_A \approx A_B$, but if not the images may be independently normalized to one another by comparing light from a small region in which there is no absorption. Thus for small $S(x, y)$ and fairly small optical densities we can write

$$T(x,y) = \mathrm{Exp}[-OD(x,y)]. \tag{4.14}$$

Images are triggered on the camera by a TTL pulse. The camera shutter opens coincident with the trigger pulse and remains open for a duration set in software, usually 20 ms. However, the actual image is largely independent of this shutter duration, as the camera is well shrouded from room light, hence very few counts are recorded in the absence of the probe laser. As such, the effective exposure length that sets the light level for each image is defined by using an acousto-optic modulator (AOM) to switch the laser on and off. The AOM permits rapid switching (1 μs) and is placed in series with a mechanical shutter to eliminate unwanted effects from the small amount of light passed by the AOM even when it is “off.” Typical exposures ranged from 50 μs to 1 ms of illumination, selected based on atom temperature, probe laser intensity, and frequency detuning.

Focusing the camera

One important consideration for taking crisp absorption images is making certain that the camera is located at the focus of the imaging system. As a starting point one can simply rely on the lens formula from introductory optics,

$$\frac{1}{f} = \frac{1}{d_o} + \frac{1}{d_i}, \tag{4.15}$$

where f, d_o and d_i are the lens focal length, object distance, and image distance, respectively. In our case we are using a pair of 2 in. diameter, 40 cm focal length lenses located approximately 35 cm from the atom cloud and separated by about 3 cm. This yields an object distance of about 46 cm. To improve upon this estimate, however, we can use the images themselves, shifting the camera towards or away from the dewar in pursuit of clearer images. To make this simpler the camera was mounted on a large translation stage with approximately 10 cm of travel. The best focus is achieved by looking at very small objects which are below the resolution limit of the imaging system and adjusting the camera position to minimize their apparent size. However, one can also use larger objects so long as they have sharp features. Our preliminary focus was achieved by imaging clouds evaporated to 75/22 A at temperatures of ~ 20 mK. In this trap the field gradient is approximately 500 G/cm and the atoms have a Doppler width of about 6 MHz, so we expect an absorptive shell to have a FWHM of only about 80 μm. As such, any image in which absorptive shells are broader than this distance must be poorly focused. While this is not quite the resolution limit of the imaging system (about 10 μm), it is a starting point from which future focusing with very small atom clouds may begin.

Measuring the camera magnification

As with the camera focus, and estimation for the magnification can be easily calculated using introductory optics: $m = d_i/d_o$. However, just as it is necessary to fine tune the focus, it is important to measure the magnification. This can be done in either of two ways. If one understands the magnetic field gradient in the anti-

Helmholtz confining potential and knows the detuning of the probe laser from the zero-field transition, the size of the absorption image is calculable. Using this value and the size of the cloud as measured in pixels on the CCD camera one can determine an effective pixel size in μm/pixel. Alternatively, one can insert an auxiliary mirror into the imaging system to place the camera focus in free space, making it possible to image an object of known size. Imaging a transparent grid with known spacing (printed on a transparency, for example) makes it straightforward to determine the camera magnification, and also to check for distortions in the image. Using this second method we measured the magnification to be 1.09, yielding an effective pixel size of 11.9 μm. This disagrees with the trivially calculated value by about 20% but is in rough agreement from a measurement based on the calculated trap gradient and measured resonant shell size in a 75/22 A trap.

Absorption images in the quadrupole field

Although absorption imaging is most useful for troubleshooting and thermometry at low temperatures, it is also possible to take absorption images of warmer atoms. This can make the images somewhat more challenging to interpret, since in addition to local atom density and laser polarization the measured absorption becomes a function of laser detuning because the trapping potential can Zeeman shift the atoms in and out of resonance (see appendix A)[5]. However, these images do provide a vivid visualization of the dependence of the absorption on polarization factor, and are thus interesting in and of their own right. Figure 4.9 shows an example of how laser polarization and detuning can affect an absorption image for warm atoms in a quadrupole trapping

---

[5] Optical rotations induced by the light-atom interaction can also complicate interpretation of the image, but at the relatively low optical depths present in our anti-Helmholtz trap this effect is small.

field.

One complexity of our imaging system which presents itself in these images is the fact that the probe laser must enter and exit the cryostat via the same port. Unfortunately, this means the laser passes through the atom cloud twice — once on the way in, and again upon exiting after reflecting off of the cell mirror. This means that the exiting probe laser actually contains two images of the atom cloud superimposed on one another, one of which must necessarily be out of focus since the imaging lens only focuses a single object plane clearly onto the camera. For example, in figure 4.9b the outermost rings are the focused image of a resonant shell of atoms, while the inner "bullseye" pattern arises from the out-of-focus image. We select the image from the second pass through the atoms as the laser exits the cryostat to be in focus, since it is less distant from the lens and thus affords slightly superior imaging resolution.

Fortunately, for smaller objects we can deconvolve the two images by slightly misaligning the laser such that the entrance and exit beam paths do not perfectly overlap. In this way a different part of the probe beam interacts with the atom cloud on the two passes, leading to spatial separation between the images on the camera, as in figure 4.10. We perform essentially all of our imaging of evaporatively cooled atoms on the $2^3\mathrm{S}_1 \rightarrow 2^3\mathrm{P}_2$ $\Delta m = +1$ transition. This transition is closed, allowing each atom to scatter many photons to give strong signal levels and good signal-to-noise. However, because the trap geometry does not permit the use of purely σ_+ light for probing the atoms there is off-resonant optical pumping of atoms on the nearby $\Delta m = 0, -1$ transitions, so exposure lengths are generally made only long enough to limit the influence of shot noise and the read noise of the camera.

Simulation of absorption for images of atoms at these temperatures (low enough

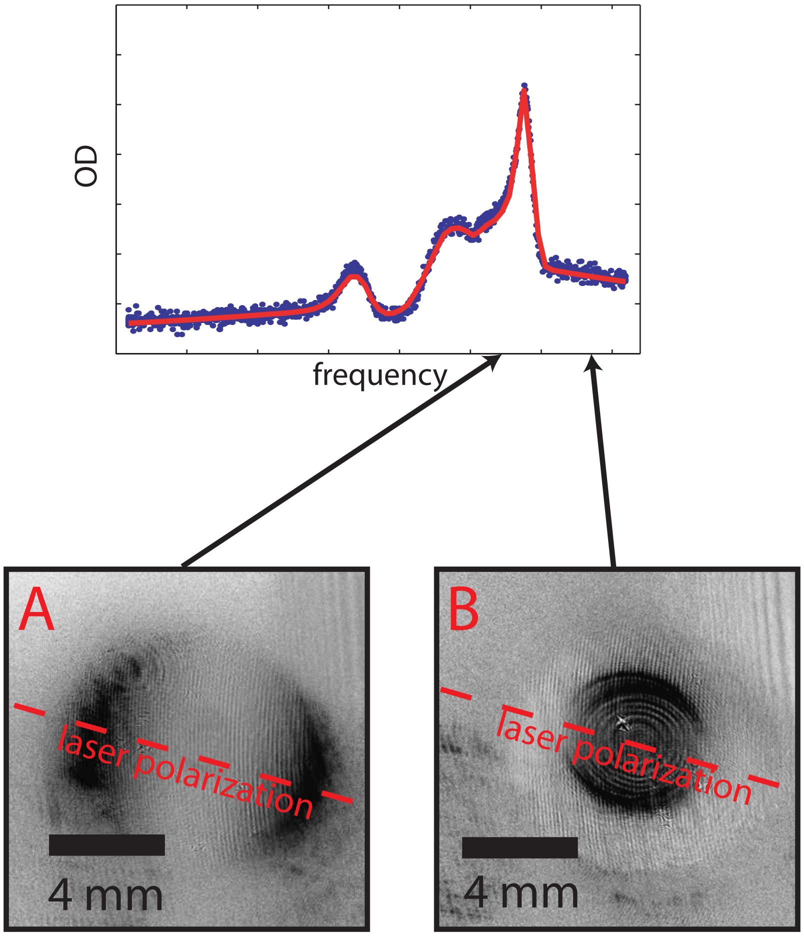

Figure 4.9: Images of atoms trapped with the anti-Helmholtz magnet fully energized. The laser polarization is as indicated in the figure, and laser detunings are as refereneced to the absorption spectrum. At these magnetic fields mixing between 2^3P_2 and 2^3P_1 states makes assigning the absorption to a particular transition impossible, but (A) has $\Delta m = 0$ character, and (B) $\Delta m = +1$ character. The true $1/e$ radius of the cloud in these images is approximately 3.5 mm. Circular fringes in (B) result from the superimposed out-of-focus image (see text).

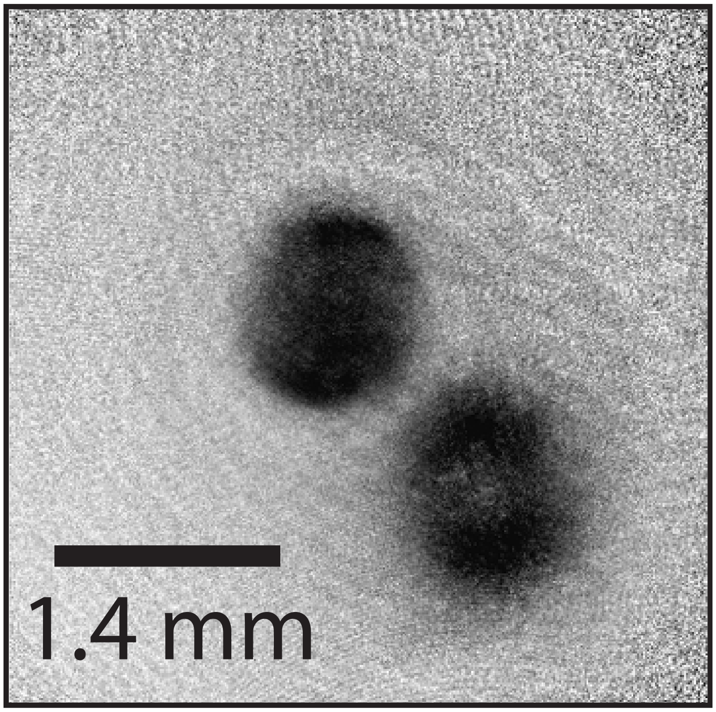

Figure 4.10: An absorption image of atoms evaporated to ~ 3 mK at 10/3 A on the $2^3\mathrm{S}_1 \rightarrow 2^3\mathrm{P}_2$ $\Delta m = +1$ transition. The laser is detuned from the zero-field transition by approximately +20 MHz. Here the paths of the laser as it enters and exits the cryostat are not completely overlapped, so the entrance and exit images of the atom cloud are spatially separated. The central image is well focused, while the image offset to the lower right is out of focus. The true $1/e$ radius of the cloud is approximately 1 mm.

that there is no mixing of Paschen-Back mixing of the excited states) is straightforward, and is discussed in appendix A. However, determining an atom number from a single image is not possible, since the measured column density at a particular magnetic field (spatial location) depends on both the cloud density and the Boltzmann factor. It is thus necessary to take a series of images at different laser detunings and compare the measured column densities at different spatial locations in the trapping potential to ascertain the number and density of the trapped atom cloud.

Chapter 5

Evaporative cooling in the ultracold regime

Having evaporatively cooled to few mK temperatures using surface evaporation and shifted the atom cloud into the cell extension, the cloud size has been reduced by the ratio of the radii of the wide and narrow portions of the trapping chamber[1]. Since the Majorana-limited lifetime of the trapped atoms scales as r^2_{cloud}, continued evaporative cooling in the anti-Helmholtz trap will soon lead to unacceptable atom loss. Here we describe the transfer of atoms into the new quadrupole-Ioffe configuration trap, solving the Majorana problem, as well as further evaporative cooling and imaging in the new trap as we made stepwise progress towards quantum degeneracy.

---

[1] This assumes that η, the ratio of the atom temperature to the trap depth, remains constant. Since the collision rate in the trapped cloud is large enough to rapidly return the cloud to an equilibrium thermal distribution after the cessation of evaporative cooling, this is a good assumption.

5.1 Using the QUIC trap

5.1.1 Transfering the atoms

As introduced in section 3.2, transfering the atoms from the anti-Helmholtz trap into the QUIC trap may be achieved quasi-statically through a suitable choice of current ramps of the various coils (see figure 3.5). These ramps must avoid several pitfalls:

- The QUIC quadrupole pair is centered well off-axis from the cell. Allowing the trap to be pulled too far towards the center of these coils will bring the cloud up against the cell wall, causing rapid loss of atoms.
- A second quadrupole-style field minimum is formed during the transfer process, and is initially located near the Ioffe coil, outside of the cell. As this minimum merges with the original anti-Helmholtz minimum and the atoms spill into it, there must be sufficient confinement to prevent the atoms from striking the cell wall near the Ioffe coil
- As the minima merge there is briefly a large “hole” via which Majorana loss can occur, making it important to merge them quickly.

In avoiding these dangers one can follow the general guideline that until the two field minima merge and an Ioffe-Pritchard trap is formed, adding current in the QUIC quadrupole pair will pull the atom cloud towards their center, whereas adding current to the Ioffe coil will pull them in the opposite direction. Unfortunately, simulating the fields during the transfer to determine the finer details of what current ramps to program into the power supplies is challenging, as the large inductance of the anti-Helmholtz coils leads to hysteretic effects that are difficult to quantify.

Fortunately, the atoms provide a simple method for troubleshooting; by imaging the atom cloud as the fields are modified from a quadrupole geometry to a QUIC trap one can determine the location, spatial extent, temperature, and number of atoms remaining. Given a known starting point (10/3 A in the anti-Helmholtz magnet, no current in the QUIC trap) and ending point (a ratio of about 2.65 between the QUIC quadrupole and Ioffe circuit currents and no current in the anti-Helmholtz coils), one can simply explore the parameter space between them to maximize the transfer of atoms between the two trapping geometries. Images of the atom cloud at various points in the transfer are shown in figure 5.1. As the transfer proceeds the atoms are initially pulled towards the QUIC quadrupole pair as it adds to the anti-Helmholtz minimum and shifts it in the $-\hat{z}$[2] direction. As the anti-Helmholtz current drops and the Ioffe current rises, the atoms are pulled back to the center of the cell. Meanwhile, the cloud gradually assumes an elongated cigar-shape as the quadrupole minimum is distorted into the harmonic QUIC minimum. After the currents have all been ramped to their final values the current supplies for the anti-Helmholtz magnet are switched out using solid state switches. This is important for field stability for two reasons. The 100 A supplies are switching supplies and therefore somewhat noisy, though the large inductance of the coils tends to reduce the problem. More importantly, the supplies do not zero very well, such that from one ramp to the next there tends to be an arbitrary offset current of order 100 mA, making the details of the QUIC trapping field irreproducible while the anti-Helmholtz supplies remain connected.

---

[2] $\hat{z}$ defined as in figure 5.1

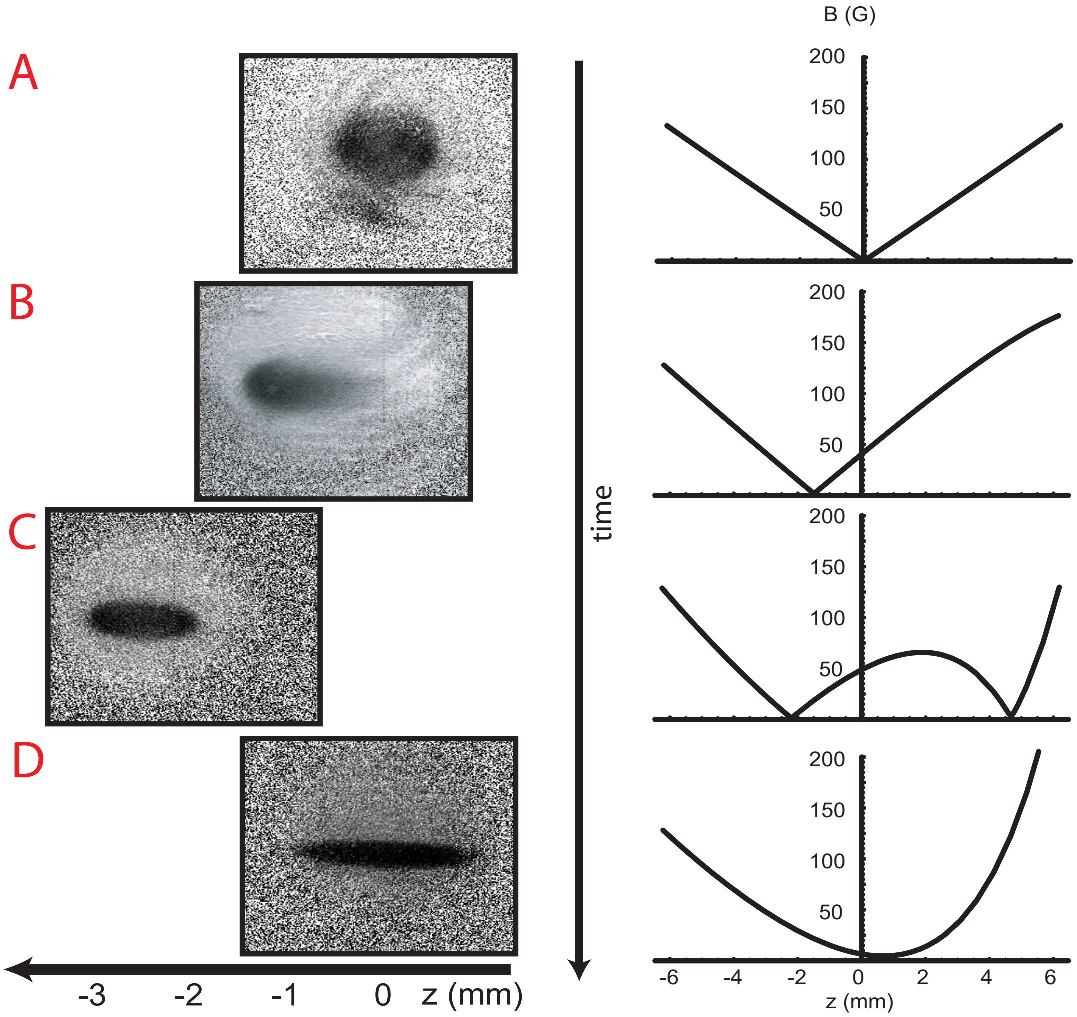

Figure 5.1: Transferring the ^{4}He* atoms from the anti-Helmholtz trap to the QUIC trap. The left column shows images of the atom cloud at various times during the transfer, while the right shows a plot of $B(z)$ at the time corresponding to each image ($\hat{z}$ points along an axis through the center of the Ioffe coil). Note that in (C) a few atoms may have already spilled into the minimum centered at $z = 5$ mm, (not imaged). Cell walls are located at approximately $z = \pm 6$ mm. Laser detuning is +15 MHz, and the QUIC bias field is approximately 2 G.

5.1.2 Transfer efficiency and atom loss

In principle this transfer can be nearly 100% efficient, limited only by whatever Majorana loss takes place during the time it takes to complete [100]. Given that the Majorana loss time when we begin the process is approximately 30 s and simulations of the integrated loss as the shape of the Majorana hole changes throughtout the transfer imply good efficiency, we would hope to transfer nearly all of our atoms. Unfortunately, this did not prove to be the case; whereas we generally started started with $\sim 2 - 5 \times 10^8$ atoms at about 2 mK in the anti-Helmholtz trap at 10/3 A, matching simulations to the images of atoms in the QUIC trap indicated only about 2×10^7 atoms remaining, now at a temperature of 500 μK. The reduced atom number along with the reduced temperature suggests two possibile problems, both related to loss of atoms due to the cloud interacting with the cell wall or window.

One possibility is that at some point during the ramp the trap depth drops suddenly, leading to all of the warm atoms effectively being "skimmed" out of the trap, their loss taking place too rapidly for collisional rethermalization of the cloud, preventing proper evaporative cooling. The most likely places for this to occur would be when the cloud is at its most extreme position in the $-\hat{z}$ direction or due to a lack of confinement on the $+\hat{z}$ side of the second minimum as atoms spill into it from the original minimum. Further investigation by imaging the atoms as they moved to their extreme position in the $-\hat{z}$ direction and back indicated no losses. Similar probing of the atoms as the minima merge is challenging, since this corresponds both to the point at which the field configuration is changing most rapidly as the coil currents change, and also to the situation with the most severe Majorana loss. However, given that a small displacement of the cell wall would cause a significant change in the trap depth at this point (see figure 5.1C), it is not unlikely that this could be the problem. A related problem might occur if misalignments of the QUIC trap coils led to "leakage" of atoms into the cell window during the trap transfer. Because this would correspond to atom displacement in the integration direction of the images, it is essentially impossible to diagnose.

We made two efforts to resolve the poor transfer efficiency. With either of these problems, one might hope to resolve the situation simply by ramping more slowly through the problem area. This would allow for collisional rethermalization and evaporative cooling rather than merely skimming away the warm atoms. In hopes of a more efficient transfer we tried a wide variety of ramp rates. For very slow rates we found that we transferred even fewer atoms, presumably due to additional Majorana loss, but at no intermediate rate did the transfer efficiency improve. It may be that skimming is the problem, but that by evaporatively cooling the atoms during the transfer we reduce the cloud size, thus causing increased Majorana loss and canceling out any gains in efficiency.

In a second effort to improve transfer efficiency we to sought to uniformly increase the trap depth by operating the QUIC trap at greater currents, thus increasing the temperature and reducing the number of atoms that might be skimmed out of the cloud. Unfortunately, this proved impossible, as in testing the trap we discovered that we could not increase the currents significantly without causing the trap to quench. These quenches did not occur immediately, but rather after about a second of operation at the increased currents. This behavior suggests gradual heat propagation to the coils originating from the resistive copper vacuum feedthroughs that carry current from the leads in the helium bath into the IVC. As the coils warm, their current carrying capacity drops, making a quench inevitable even though they are still being operated at well below their 4 K critical current. Given that the copper feedthroughs were already being operated at twice their room temperature current ratings, that they would contribute to quenches at still higher currents is perhaps unsurprising.

5.1.3 Parameterization of the QUIC trap

Having successfully transfered atoms into the QUIC trap, albeit only a small fraction of them, we could now use the atoms to measure the trap characteristics. As described in section 3.2, the field in an Ioffe-Pritchard trap is well described near the minimum by only three parameters: the bias field B_o at the trap minimum, the radial field gradient B', and the axial curvature B'', each of which can be measured fairly easily using the atoms.

The simplest of these parameters to measure is B'. As with the anti-Helmholtz trap, the temperature of the atom cloud upon loading into the QUIC trap is sufficiently high that atoms orbit through a large range of magnetic fields with a corresponding range of Zeeman shifts. As such the apparent size of the cloud in absorption images is dependent on the probe laser detuning. By imaging the cloud with known detunings one can determine the cloud size vs. Zeeman shift. This yields the magnetic field gradient according to

$$B' = \frac{d\, w_r}{d\, \delta} \times \frac{\mu_B}{h}, \tag{5.1}$$

where w_r is the radial half-width of the cloud and δ is the probe laser detuning. Applying this calculation to the values determined from images such as those in figure 5.2, we arrive at an estimate for B' of 500 G/cm. This measurement suffers from several possible sources of error, however, such as uncertainty in the relative laser frequencies and the difficulty in determining widths from the images, particularly for larger detunings with limited absorption.

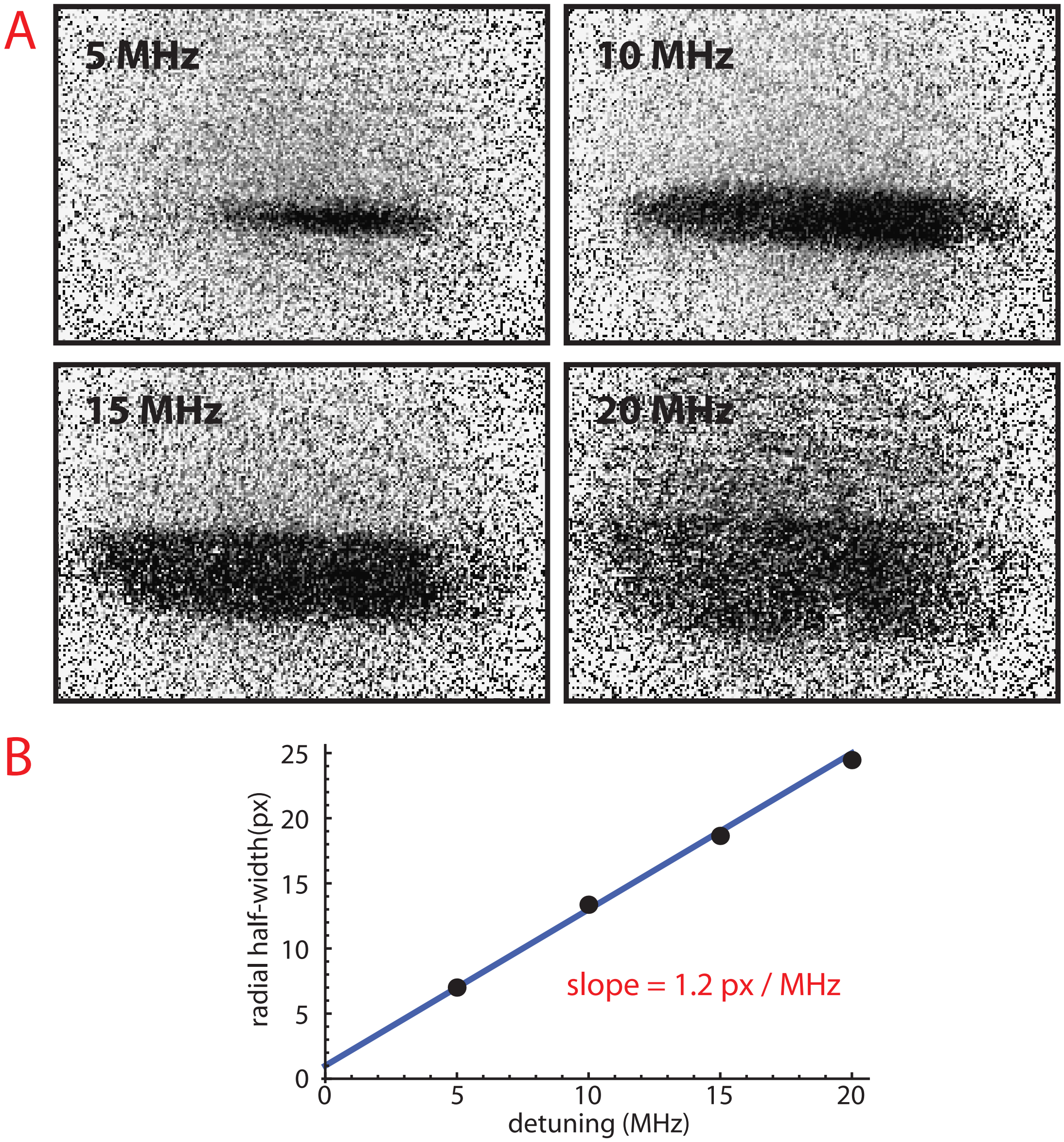

Figure 5.2: (A) Absorption images of atoms as initially loaded into the QUIC trap with trap currents of 7.35 and 20.4 A in the quadrupole pair and Ioffe coils, respectively. (B) A plot of radial half-width vs. probe laser detuning for the images in (A). The slope may be used to calculate the radial gradient B' in the QUIC trap.

Measurement of B_o is achieved most easily by using the RF evaporation coil to induce magnetic field dependent atom loss. By introducing a radio-frequency current to the coil we create a rapidly oscillating magnetic field at the location of the trapped atoms. By tuning the frequency of these oscillations they can be matched to the $\Delta\mathrm{m} = -1$ transition between ground state Zeeman sublevels to the magnetically neutral $m_S = 0$ state; the same frequency can also drive consecutive transitions to reach the anti-trapped $m_S = -1$ state. Arriving in either state causes the atom to be lost, since the trapping potential does not prevent these states from striking the cell walls. However, for atoms in the QUIC trap there exists a minimum frequency at which RF transitions may be driven resonantly,

$$\omega_{min} = \Delta\mu \, B_o, \tag{5.2}$$

where for ^{4}He* $\Delta\mu = 2\mu_B$. Since these RF-induced transitions are extremely narrow, if the field oscillates at a frequency below ω_{min}, the field is non-resonant and no loss is induced. As such, by gradually tuning the oscillation from low to higher frequencies while observing the atom cloud, we can note the frequency at which the atoms are suddenly lost from the trap and thus determine the value of B_o. Since there are some circular orbits which do not pass directly through the trap minimum, B_o may be determined more precisely by using colder atoms (which reside only near the minimum). This is easily achieved by evaporatively cooling the atoms to below the QUIC trap loading temperature before attempting to measure B_o, as described below in section 5.3. We usually evaporate to approximately 70 μK, more than adequate to give few mG resolution on B_o, but this choice was fairly arbitrary. Different values of B_o were used during the experiment, but typical values were around 1.5 G.

The process for determining B'' is a bit more involved than that for either of the other two trap parameters. In principle one could map out the spatial extent of the atom cloud as a function of probe laser frequency, as with B'. In practice, however, this is less practical due to the larger spatial extent of the cloud in the axial dimension, limiting the number and range of distinct laser frequencies which may used in the determination without using a very large laser beam and introducing image distortion from interference effects. Fortunately, a very accurate determination may be made using a second method that utilizes the parabolic nature of the potential in the axial dimension. Recalling from section 3.2 that $B_z = B_o + \frac{1}{2}B''z^2$, one can see that an atom's motion in this dimension should be harmonic, with

$$\omega_z = \sqrt{\frac{B''}{m}}. \tag{5.3}$$

If we drive an oscillation of the minimum of the magnetic trapping potential at ω_z, we should be able to drive the atoms' center-of-mass motion, imparting additional energy and heating the atoms out of the trap[3]. Imaging the cloud while tuning the driving frequency thus provides a map of atom loss from which ω_z can be determined, as in figure 5.3. Because the trap becomes more anharmonic at greater distances from the minimum (larger temperatures), cleaner measurements of the trap frequency may be performed by first evaporatively cooling the atom cloud to lower temperatures, as with measurement of B_o. The data in figure 5.3 was collected by driving a 5% oscillation on the Ioffe coil current. This causes a "shaking" of the trap minimum in the z direction at the driving frequency, since increasing $\mathrm{I}_{\mathrm{Ioffe}}$ strengthens the field near the Ioffe coil and pushes the trap minimum away from it.

With this method it is also possible to determine B''_ρ and ω_ρ according to equations 3.4 and 5.3. Since in the end we expect to cool the atoms to the point that the trap is harmonic in all three dimensions, we are arguably more interested in these

---

[3] Oscillations at multilples of ω_z can also cause heating, especially $2\omega_z$ — see section 5.5.

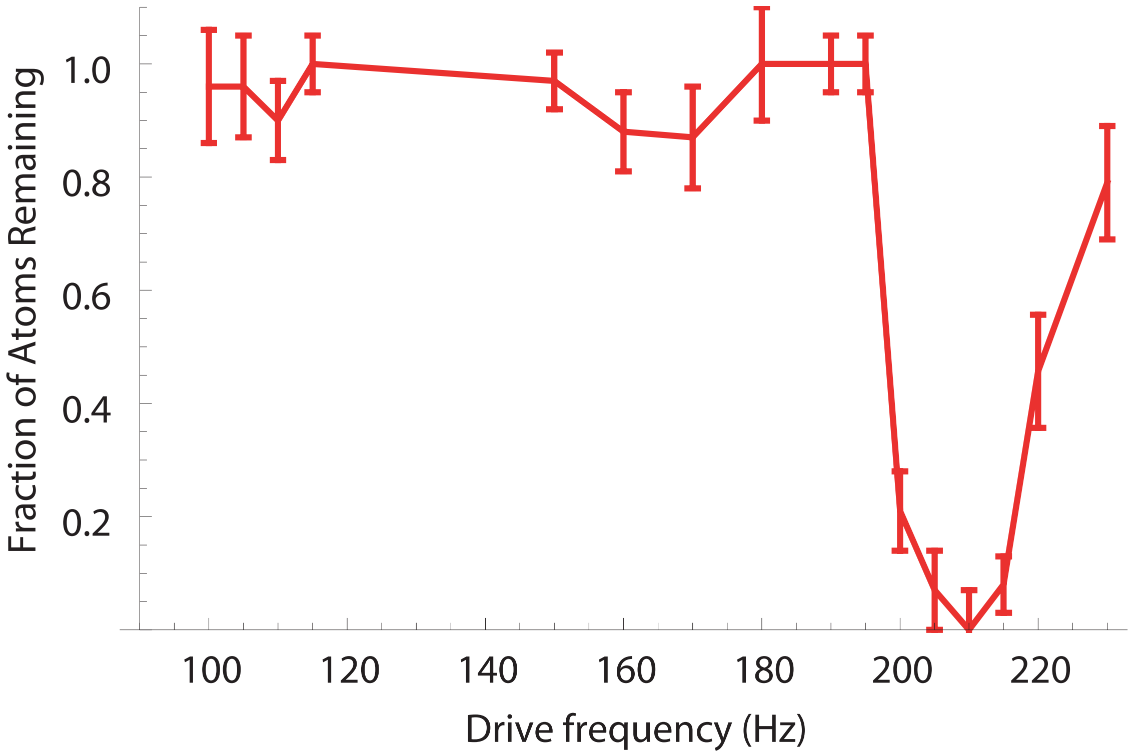

Figure 5.3: Atom loss due to driving of axial oscillations. The resonant atom loss near 210 Hz indicates the axial trap frequency ω_z.

values than in the radial gradient B'. Ideally we would measure ω_ρ directly as with ω_z, but the inductance of the QUIC trap coils makes driving the trap at the (larger) radial frequency impossible with our power supplies. Instead, ω_ρ is best inferred from the measured value of ω_z and the aspect ratio of clouds trapped at temperatures low enough that the trap is fully harmonic (see section 5.4.3), with

$$\omega_\rho = \epsilon\, \omega_z \tag{5.4}$$

ϵ representing the aspect ratio; for our trap $\epsilon = 12 \pm 1$.

5.2 Atom lifetime in the QUIC trap

Having loaded atoms into the QUIC trap and thus prevented Majorana flopping of atoms in the trap center, we expect the atom loss to be significantly reduced as compared to the $\sim$ 30 s lifetime at the end of the surface evaporation in the anti-Helmholtz trap. Two major sources of atom loss remain: two/three-body loss from He*-He* collisions and one-body loss due to collisions with background gas. Rates for binary and ternary collisions of metastable helium have been measured [128] to be $\beta = 2(1) \times 10^{-14}$ cm^{3}s^{-1} and $L = 9(3) \times 10^{-27}$ cm^{6}s^{-1}. These contribute to loss according to

$$\dot{n}(t) = -\frac{\beta\, n^2}{2\sqrt{2}} - \frac{L\, n^3}{3\sqrt{3}} \tag{5.5}$$

where the factors in the denominator result from spatially averaging the loss rate throughout the trap[4]. Solutions to this equation must be computed numerically, but at the $\sim 10^{11}$ cm^{-3} density upon initial trap loading the contribution from ternary

---

[4] These factors assume a 3D harmonic potential. In a QUIC trap this is only strictly accurate for temperatures below $\mu B_o/k_B$, but the correction for the real trap potential is of order unity.

collisions is negligible, and the result is the familiar one for two-body decay:

$$n(t) = n(t=0)\left(1 + \frac{\beta\, n(t=0)\, t}{2\sqrt{2}}\right)^{-1}. \tag{5.6}$$

At the QUIC trap loading density we thus expect binary collisions to cause a decrease to $1/e$ of the initial atom number over approximately 1000 s; however, the two-body lifetime scales as 1/n, so the denser clouds resulting from evaporative cooling will have significantly shorter lifetimes.

Trap loss from background gas collisions is significantly harder to predict, particularly given the complications from helium films and the variability in bakeouts and sorb performance detailed in section 4.1.2. However, now that the atoms are trapped without Majorana losses it is straightforward to simply measure their lifetime, as in figure 5.4. As is evident from the figure, with suitable cell preparation to achieve good vacuum, atom loss is negligible over a five minute timescale, so we set a lower limit of ten minutes on the trap lifetime. Presumably for $T_{He^*} < 1$ mK essentially every collision with a 2-300 mK background gas atom will eject an atom from the trap, allowing us to use equation 4.3 to estimate the background gas density. Assuming a collisional cross section of 1×10^{-14} cm^2, we set an upper bound of $n_{He} < 5 \times 10^{7}$ cm^{-3}.

5.3 Evaporative cooling using a radio-frequency knife

From the conditions upon loading the QUIC trap ($T \approx 550\mu$K, $n \approx 2 \times 10^{11}$ cm^{-3}, $n\,\lambda_{dB}^3 \approx 10^{-5}$, we still have five orders of magnitude of phase-space density to traverse. Fortunately, with the long lifetimes afforded by the new trapping geometry there is no problem in proceeding with further evaporative cooling. While it is possible to use surface evaporation all the way to BEC [95], there are some drawbacks to this

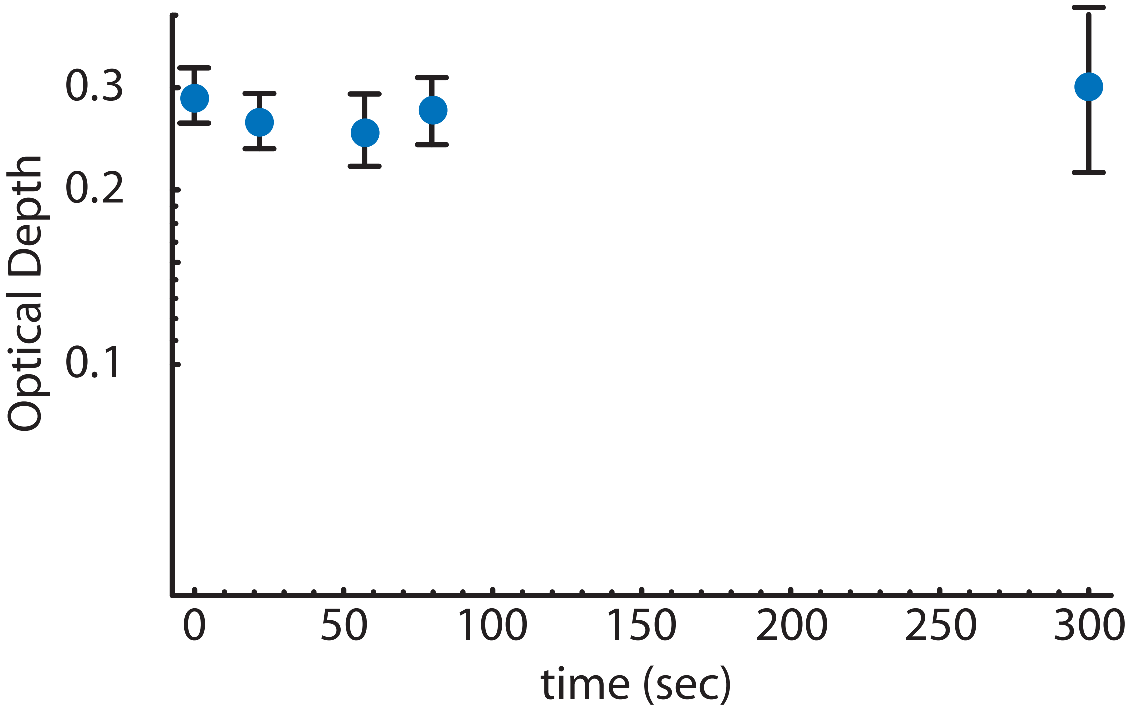

Figure 5.4: Atom loss (or lack thereof) for QUIC trapped atoms. $t = 0$ is a few seconds after transferring the atoms into the trap to allow for thermalization of the cloud from any non-equilibrium conditions caused by the magnet ramps.

technique. One issue is that the atoms are removed from the cloud at only a single point, allowing many orbits with more energy than the trap depth to persist until they are scattered into an orbit that strikes the wall. With a large elastic collision rate constantly mixing orbits this is probably not be a major concern. However, surface evaporation is also extremely susceptible to variation in the relative separation between the adsorbing surface and the location of the magnetic field minimum. This makes surface evaporation extremely susceptible to cell vibration and magnetic field noise. For example, for a 500 G/cm field gradient (the rough estimate for the the QUIC trap radial gradient made in section 5.1.3), a 10 μK change in the trap depth results from a vibration of less than 2 μm. While the harmonic nature of the low field region in the trapping potential relaxes this constraint somewhat since the gradient is weaker near the center of the trap, surface evaporation all the way to BEC is a daunting task given that the cell is free to vibrate independently of the QUIC trap.

To avoid these concerns evaporative cooling in the QUIC trap is accomplished in an entirely different way, using RF fields as a "knife" to selectively remove hot atoms from the trapped cloud. As with the measurement of the trap bias field B_o described above, we drive $\Delta m = -1$ transitions between Zeeman sublevels, transfering atoms to untrapped states which can strike the cell walls and be adsorbed. Whereas the knife frequency was tuned up from below ω_{min} (equation 5.2) to cut atoms out of the center of the trap in measuring B_o, we now begin at a large knife frequency and sweep down, addressing energetic atoms making orbits far from the trap minimum through a shell resonant with the knife. This technique would actually be preferable to the use of surface evaporation in the anti-Helmholtz trap as well; however, the frequency and RF power necessary for evaporating 300 mK atoms are challenging to implement.

5.3.1 Generating the RF ramp

Since in ^{4}He* the $\Delta m = -1$ transition that we drive takes the atoms directly from the trapped state to a magnetically neutral state, the desired cut frequency is related to the atom temperature according to

$$\hbar\,\omega_{RF} = 2\mu_B\,B_{cut} \tag{5.7}$$

$$= \eta\,k_B\,T + 2\mu_B\,B_o. \tag{5.8}$$

The actual value of η during the ramp will be related to a combination of the atoms' collision rate and the knife frequency sweep rate. By ramping more slowly the atoms undergo more collisions per fractional change in the trap depth, keeping them closer to their equilibrium temperature and increasing η. Higher values of η lead to more efficient evaporation in the absence of other losses since cuts at larger η mean that each evaporated atoms carries away more energy. Referring back to the α in equation 4.6, for a 3D harmonic potential in the absence of losses [37]

$$\alpha = \frac{\eta + 1}{3} - 1. \tag{5.9}$$

Of course, the slower ramp rates that correspond to larger values of η and therefore α also afford more time for loss due to inelastic processes or background gas collisions, thus placing a practical limit on evaporation efficiency; myriad experiments with alkali atoms tend to operate in the regime of $\alpha = 3/2$, implying $\eta \approx 7$.

In light of our long initial trap lifetimes we choose a starting frequency of $\omega_{RF} = 2\pi \times 140$ MHz, corresponding to $\eta \approx 12$. This is probably larger than necessary, but by starting high we also ensure that we also allow for errors in our initial determination of the atom temperature. End frequencies are selected based on the desired final temperature of the evaporated atoms. The RF fields are generated using the evaporation coil described in section 3.3.4 by sending an oscillating waveform to them from a

RF signal generator. Two different RF sources are used. To generate the > 100 MHz frequencies required for the beginning of the ramp we use a HP (now Agilent) 8647A signal generator [129] capable of generating frequencies from 250 kHz to 1 GHz and powers as great as 10 dBm. This signal generator can only be controlled by GPIB, limiting frequency updates to 5 Hz. For more precise control at lower temperatures we switch to a Tektronix AFG3022B arbitrary function generator [130] as we ramp below 24 MHz, with frequency updates performed at 1 kHz.

5.3.2 RF power limitations

The rate of the frequency sweep for the RF knife is set empirically to maximize the number of atoms remaining at a particular temperature. The sweep is broken into linear segments, each of which reduces the atom temperature by a factor of 2 or 3. Ideally the frequency sweep rate should be matched to the atoms' elastic collision rate. The ramp must permit enough collisions to keep repopulating the high-energy tail of the thermal distribution as the atom temperature drops, yet not so many as to suffer from excessive inelastic losses. For a constant collision rate this would lead to an exponential sweep. Because the density of the atom cloud increases as evaporation proceeds, however, the collision rate is also increasing, hence an ideal ramp has a gradually increasing logarithmic derivative.

Using this sort of idealized ramp relies on effective ejection of atoms from the trap each time they cross the shell where they are resonant with the RF knife. If the knife does not remove all of the atoms making orbits resonant with a particular cut frequency before being swept to a lower frequency, however, the cooling will not be efficient; as the frequency is reduced the knife will begin to remove atoms from the center of the distribution rather than just the high energy tail. While this problem can be remedied by increasing the RF power applied to the evaporation coil such that an atom will be ejected in a single pass through the resonant shell, for real experiments there are often practical limitations to the useable power. In this case one must reduce the knife frequency sweep rate, giving energetic atoms an opportunity to make enough orbits through the resonant shell to be ejected from the trap.

Fortunately, measuring the time required to eject atoms is straightforward using technique similar to that used for measuring the QUIC trap bias field. In this case we tune the knife frequency a fixed value, resonant with atoms at fields slightly greater than B_o, so that it will eject essentially all of the atoms from the trap. By sending a pulse of RF to the evaporation coil and imaging the atoms that remain we can determine how effectively the knife is driving transitions. Varying the power and/or duration of the pulse allows us to determine the ejection rate, which can then be used in setting the frequency sweep rate for evaporative cooling. For our coil 10 dBm of RF power led to approximately a 10 ms $1/e$ time for ejecting atoms, corresponding to hundreds of passes through the resonant shell. Since RF powers above 15 dBM or so led to quenching of the superconducting RF evaporation coil, we were forced to tailor our ramps to this ejection rate in addition to the atoms' collision rate. This is done empirically, choosing varied rates for each new segment added to the ramp to maximize the number of atoms remaining.

5.3.3 Absorption imaging of RF evaporated atoms

Successful of evaporative cooling manifests itself as the removal of atoms making orbits far out from the center of the QUIC trap while also enhancing the central density of the cloud. This leads to a reduction in the size of the atom cloud, causing reduced absorption at large laser detunings and increased absorption for light resonant with the atoms at the trap minimum. As the atoms are cooled to temperatures below about 100 μK, their spectrum begins to be dominated by the 1.6 MHz natural linewidth and resonant light is absorbed by all of the atoms with equal probability. At this point it should be straightforward to calculate atom number and density directly from the resonant optical density of absorption images; increasing density should soon lead to 100% absorption in the center of the cloud.

Sadly, for our images of ^{4}He* this did not prove to be the case. As we evaporated to lower temperatures we observed essentially constant optical density at far less than 100% absorption. In many cases this indicates the presence of light striking the camera that did not interact with the atoms (either due to a stray reflection or the presence of non-resonant light from a multi-mode laser). However, the optical densities observed were often substantially below those seen in images of atoms in the anti-Helmholtz trap despite no changes being made to the imaging system, making this highly unlikely. More careful investigation indicated that the absorption imaging itself was at fault since decreased exposure times yielded larger optical densities, as in figure 5.5.

This behavior stems from optical pumping during the exposure. Because the bias field in the QUIC trap is small, tuning the probe laser such that it is resonant with atoms at the trap minimum means it is detuned by only about 3 MHz from the $\Delta m = 0$ optical pumping transition to the $2^3\mathrm{P}_2, m_J = 1$ state, so about a thirtieth of the photons absorbed cause atoms to be lost to the non-resonant $m_S = 0$ ground state sublevel. Consider the case of imaging at $.1 I_{sat}$, for which we expect a photon absorption rate of approximately $.1 \times \Gamma/2$, or 80 kHz. If we aim to pump fewer than 10% of the atoms we can only withstand 3 absorptions on average, leading to an exposure time of about 40 μs. Due to the limited ($\sim$ 10%) transmission of our

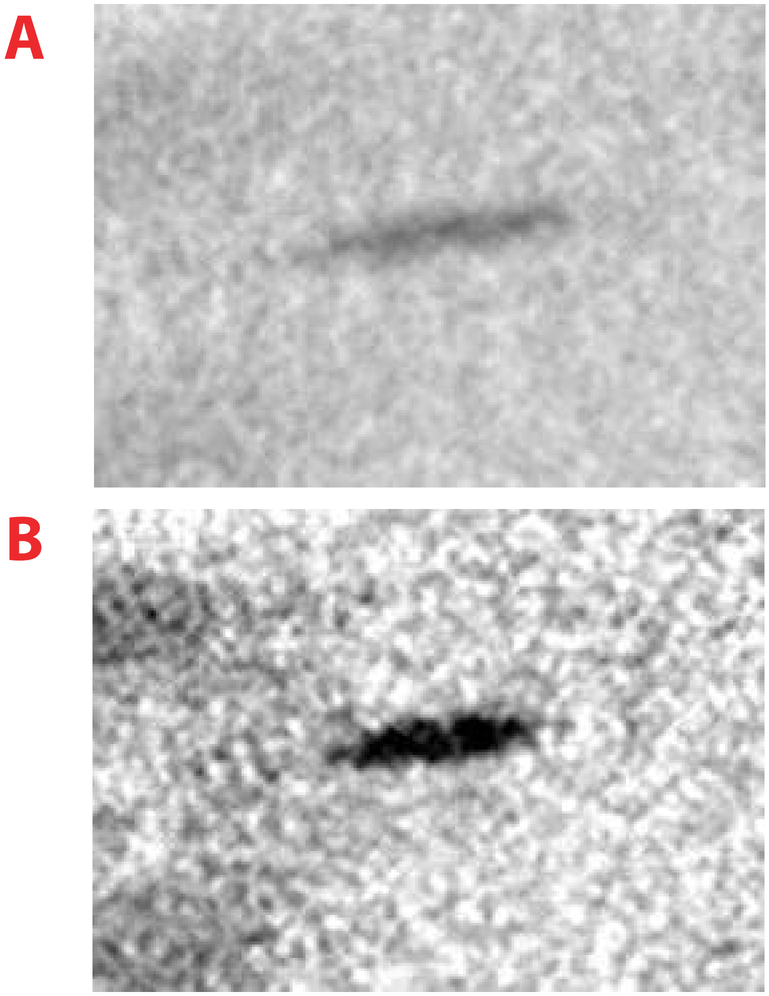

Figure 5.5: Near-resonant absorption images of atoms evaporatively cooled to approximately 100 μK displaying the dependence of absorption on exposure time. (A) and (B) show identically evaporated clouds imaged with 1 ms and 200 μs exposures, respectively, with apparent absorption doubling due to the shorter exposure. Peak absorption in (B) is 40%.

dewar optics and the 1% camera quantum efficiency this means we detect only 5 photons/pixel — an impossible task given the camera read noise.

Indeed, speaking generally ^{4}He* is a difficult atom to image. As discussed in section 3.4.2, the large transition wavelength leads to very low quantum efficiencies for silicon based CCD cameras when compared to shorter wavelength light. For example, our PIXIS 1024BR camera has a QE of about 1% at 1083 nm, while at 780 nm (one of the Rb D lines) the quantum efficiency is 94%. The $1/\lambda^3\,\tau$ dependence of the saturation intensity also makes the long wavelength[5] a hindrance, since lower light intensities means longer exposure times for the same number of counts, allowing photon-recoil kicked atoms to travel further during an exposure, blurring images. Finally, helium's small mass gives it a large recoil velocity in spite of the small momentum carried by 1083 nm photons, further exacerbating the blurring problem.

5.4 Detuned imaging

Considering the difficulties of absorption imaging (optical pumping, photon recoil induced heating, lack of spatial contrast for images with large optical densities, and photon counting statistics limited by the need keep the illumination below I_{sat}), a simple solution presents itself: detune the probe laser. Since absorption scales as $1/\delta^2$, increasing the detuning reduces absorption and thus decreases optical pumping [6] and recoil heating while allowing for the use of additional light without saturating the transition, improving counting statistics.

Detuned absorption imaging has been used for ultracold atoms [99, 109], but only

---

[5] and the long excited state lifetime — nearly 4 times longer than Rb and 6 times longer than Na

[6] at the expense of a poorer branching ratio due to reduced frequency selectivity

for atom clouds large enough to be well resolved by the imaging systems used. Due to the tight confinement offered by our superconducting trap and the considerable distance between the trapped atoms and the first imaging lens this is not the case for our imaging system; the radial dimension of clouds in our trap can shrink to and beyond our resolution. This creates a problem for detuned imaging; detuned light is phase-shifted as it passes through the cloud, and for small clouds the resulting steep phase gradients can refract light out of the imaging system and create spurious absorption signals.

5.4.1 The atom-light interaction

(This next two sections closely follow the treatment in [112, §3] except where otherwise noted)

The atom-light interaction can be described by the complex index of refraction. In the rotating wave approximation we can write (assuming a weak probe laser)

$$n_{ref} = 1 + \frac{\sigma_o\, n\, \lambda}{4\pi}\left(\frac{i}{1+\delta^2} - \frac{\delta}{1+\delta^2}\right) \tag{5.10}$$

where σ_o is the on-resonant photon absorption cross section ($\sigma_o = \frac{3\lambda^2}{2\pi}$ for a two-level atom), λ is the transition wavelength, n is the atomic density, and $\delta \equiv (\omega - \omega_o)/(\Gamma/2)$ is the detuning from resonance measured as a fraction of half the natural linewidth. For an electric field propagating along $\hat{z}$ through an atom cloud where the density $n = n(z)$ is a function of z and assuming the cloud is thin such that the light enters and exits at the same (x, y) coordinate [131, §5.5],

$$E(z) = E_o \,\mathrm{Exp}\left[i\, k \int_0^z n_{ref}(z')\, dz'\right], \tag{5.11}$$

where $k = 2\pi/\lambda$ as usual. Thus the atoms attenuate and phase shift the light, such that

$$E_{trans} = tE_o\, e^{i\phi}, \tag{5.12}$$

where t is the transmission coefficient and ϕ is the phase shift imparted on the transmitted light. From equations 5.11 and 5.12 it is clear that the attenuation results from the imaginary part of the index of refraction and the phase shift from the real part:

$$t = \; e^{-\tilde{D}/2} = \mathrm{Exp}\left[-\frac{\tilde{n}\sigma_o}{2}\frac{1}{1+\delta^2}\right] \tag{5.13}$$

$$\phi = -\delta\,\frac{\tilde{D}}{2} = -\frac{\tilde{n}\sigma_o}{2}\frac{\delta}{1+\delta^2}. \tag{5.14}$$

where $\tilde{D} = \tilde{n}\sigma_o/(1+\delta^2)$ is the off-resonant optical density and $\tilde{n} = \int n(z)\,dz$ is the column density of the cloud.

Now, consider detuned absorption imaging of a dense cloud, with resonant optical density $\tilde{D}_o = \tilde{n}\,\sigma_o \gg 1$. The best contrast for absorption imaging is achieved for clouds that absorb roughly half of the incident light ($\tilde{D} \approx 1$). This requires a detuning of $\delta = (\tilde{D}_o)^{1/2}$. Note, however, that for this detuning the phase imparted to light traveling through the center of the atom cloud is still considerable, with $\phi \approx (\tilde{D}_o)^{1/2}$. This phase will cause significant distortion of the wavefronts across the cloud; a rudimentary estimate of the refraction angle suggests the light will be bent by an angle of $\lambda\phi/\pi d$ - significantly greater than due to diffraction alone. For imaging of near diffraction-limited clouds, then, refraction will cause light to be lost from the imaging system, distorting the image. Reducing refraction to the point that it does not dominate over diffraction requires further detuning to $\delta \approx \tilde{D}_o/\pi$, but for large $\tilde{D}_o$ this reduces absorption to negligible levels.

Fortunately, all is not lost; it is possible to take advantage of the benefits of detuned imaging if one is willing to use the phase imparted by the atoms as a tool rather than treating it as a nuisance. Arguably this is even preferable, given that what we are truly interested in is the density of the atom cloud. Whereas the logarithmic dependence of $\tilde{n}$ on t makes it difficult to determine for small t, ϕ is directly proportional to $\tilde{n}$. However, since photodetectors are sensitive to intensity rather than phase, detecting ϕ requries one to convert phase variation into intensity fluctuations through the clever use of interference.

5.4.2 Phase-contrast imaging

Introduced by Zernike in 1934 [132, 133], phase-contrast methods are based on the fact that one can separate light that has been phase-shifted (and thus scattered) by a transparent object from unscattered light, allowing the two components to be separately manipulated and interfered. This is most easily achieved in the Fourier plane of the imaging system; since the scattered and unscattered light follow distinct optical paths they come to a focus at different locations, making spatial filtering straightforward, as in figure 5.6. In phase-contrast imaging the spatial filter is a transparent phase-plate which imparts a $\pi/2$ phase shift for the unscattered light that passes through its center, allowing this light to behave like the local oscillator in a homodyne measurement.

To calculate the intensity of the interference pattern in the image plane, recall equation 5.12, rewriting the transmitted light in terms of scattered and unscattered parts according to

$$E = tE_o e^{i\phi} = E_o + \Delta E. \tag{5.15}$$

Phase shifting the unscattered light by $\pm\pi/2$ yields

$$E' = E_o e^{\pm i\pi/2} + \Delta E = E_o e^{\pm i\pi/2} + (E - E_o) = tE_o e^{i\phi} + E_o(e^{\pm i\pi/2} - 1). \tag{5.16}$$

Since the intensity is given by $\frac{1}{2}|E'|^2$, the time averaged intensity in the image plane

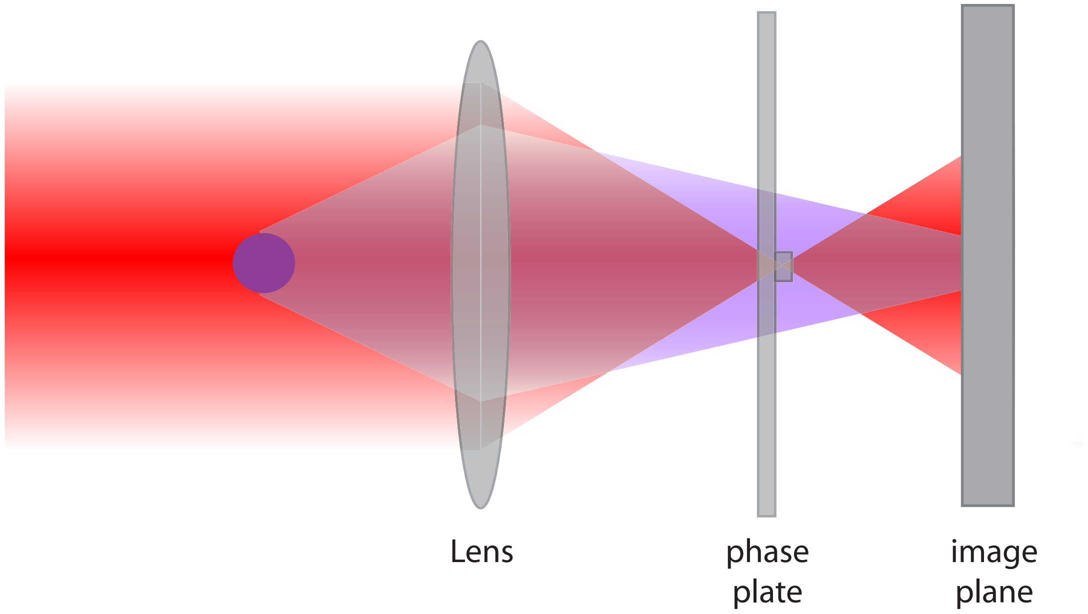

Figure 5.6: The general set-up for phase-contrast imaging. A probe laser (red) is dispersively scattered (purple) by an atom cloud. Unscattered light is phase-shifted by a phase plate in the Fourier plane of the lens, leading to interference between scattered and unscattered light in the image plane.

is thus

$$\langle I_{pc} \rangle = \frac{1}{2}|tE_o e^{i\phi} + E_o(e^{\pm i\pi/2} - 1)|^2 = I_o \left[t^2 + 2 - 2\sqrt{2}\, t \cos(\phi \pm \frac{\pi}{4}) \right]. \tag{5.17}$$

For large detunings δ such that $t \approx 1$ and the phase is small this is linear in ϕ,

$$\langle I_{pc} \rangle \simeq I_o(1 \pm 2\phi), \tag{5.18}$$

while for larger phases the intensity is periodic in ϕ, as in figure 5.7. Note that in addition to offering all of the advantages of imaging with large detunings, I_{pc} also benefits from an enhanced maximum contrast as compared to absorption imaging; whereas the transmitted light can vary only between 0 and 1, the phase-contrast signal can vary between 1 and nearly 6.

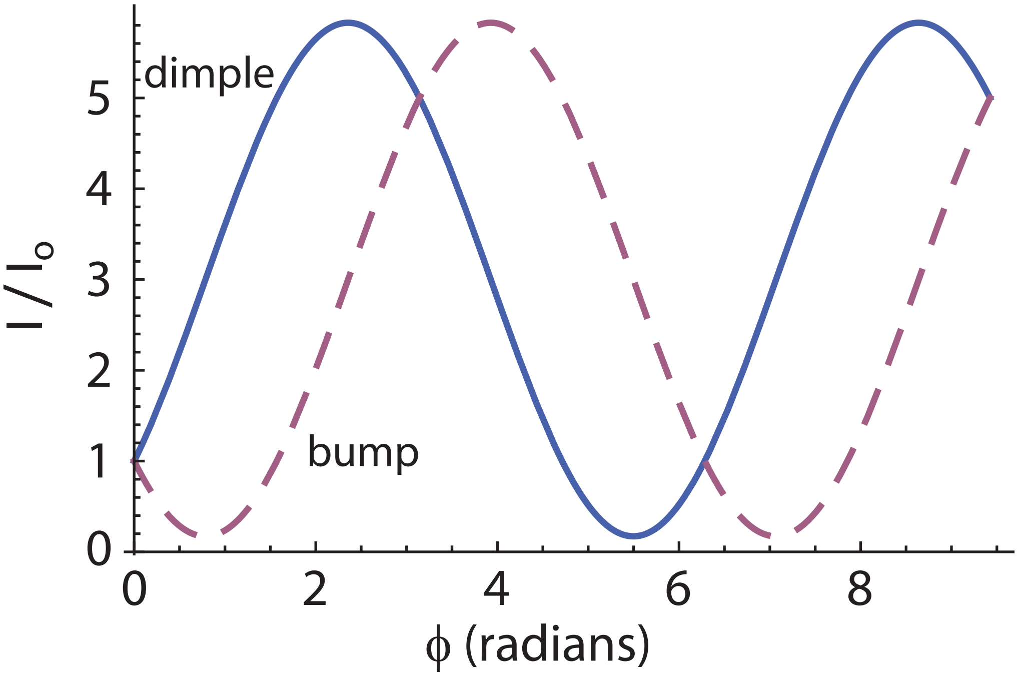

Figure 5.7: Phase-contrast signal vs. the phase ϕ imparted by the atoms for a phase plate that advances ("dimple") or retards ("bump") the phase of the unscattered light, assuming blue detuning.

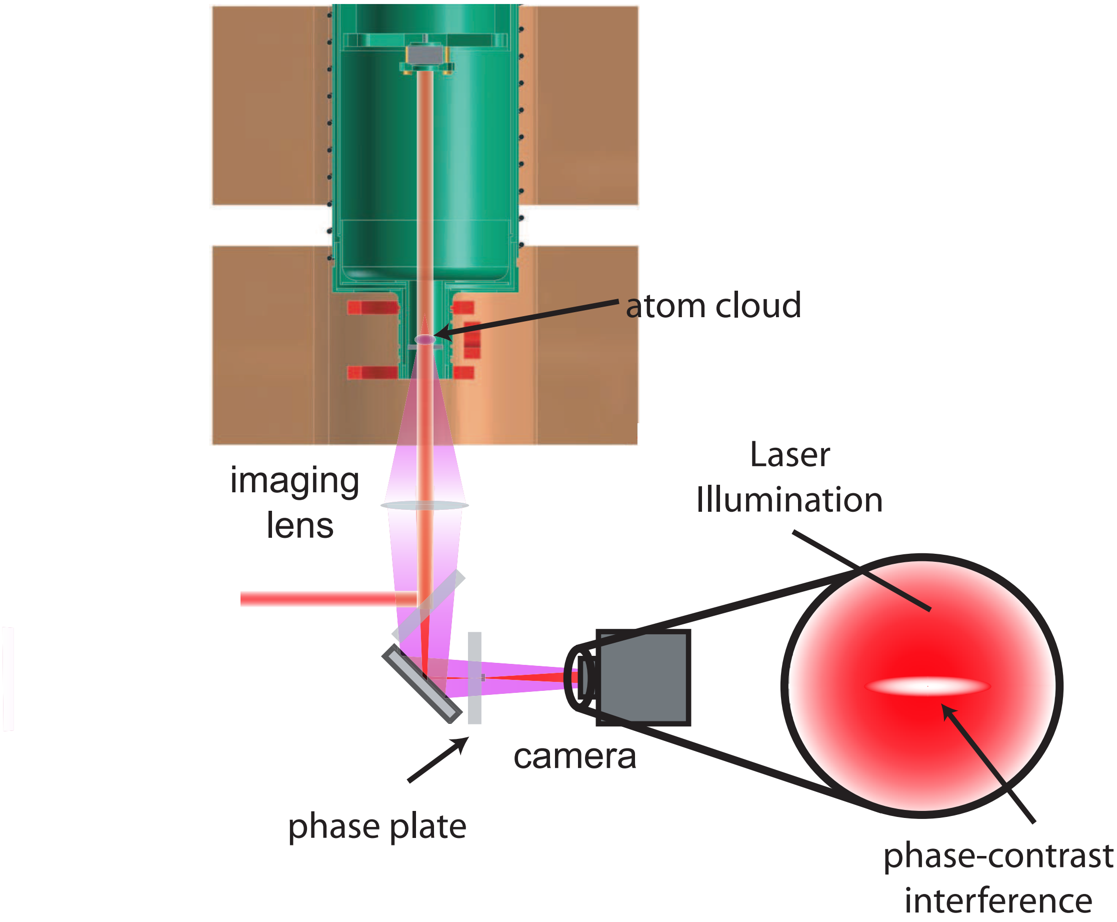

Figure 5.8: The optics set-up used for phase-contrast imaging.

5.4.3 Atom images in phase-contrast

Our set-up for phase-contrast imaging is identical to that used for absorption imaging excepting the addition of a phase plate to provide the required $\pi/2$ phase shift between scattered and unscattered light, as in figure 5.8. Our phase plate was manufactured from a stock 2” diameter × 3/8” thick plane parallel BK-7 window, coated with quartz everywhere excepting a small “dimple” in the center by ThinFilm Labs [134]. The quartz coating thickness was selected to give a $\pi/2$ relative phase shift for light passing through it vs. light passing through air,

$$t = \frac{\lambda}{4(n-1)}, \tag{5.19}$$

where n is the index of refraction of the coating ($n = 1.45$ at $\lambda = 1083$ nm). The diameter of the uncoated "dimple" was chosen to be 300 μm, selected as compromise between large spots that permit easy alignment and smaller ones that phase shift less of the scattered light that has interacted with the atoms[7]. To align the dimple with the laser focus we constructed a mask with a 500 μm hole in the center that could be fitted over the phase plate, providing a target for the beam. After getting close using the mask the alignment can be completed using the CCD camera to image the beam profile. Since the phase dimple imparts a $\pi/2$ relative phase shift, it causes interference that can be viewed on the camera if the laser is clipping the edge. By mounting the phase plate on a x-y translation stage it is straightforward to map out the edges of dimple and then center it on the laser focus.

The presence of the phase plate does complicate absorption imaging of atoms warm enough to experience Zeeman broadening due to the change in the sign and magnitude of ϕ for atoms that are red vs. blue detuned. This leads to images like 5.9, where absorptive and phase-induced interference effects compete. Fortunately, this problem is trivially resolved by shifting the phase plate such that the laser focus does not pass through the central phase dimple. With the phase plate mounted on a translation stage for alignment purposes the phase dimple can be shifted in and out of alignment with the laser in a reproducible manner, making it easy to switch between absorption and phase-contrast.

---

[7] This plate offered improved performance over a similar plate with a 500 μm dimple, while the laser focus would not have fit well through dimples smaller than about 200 μm.

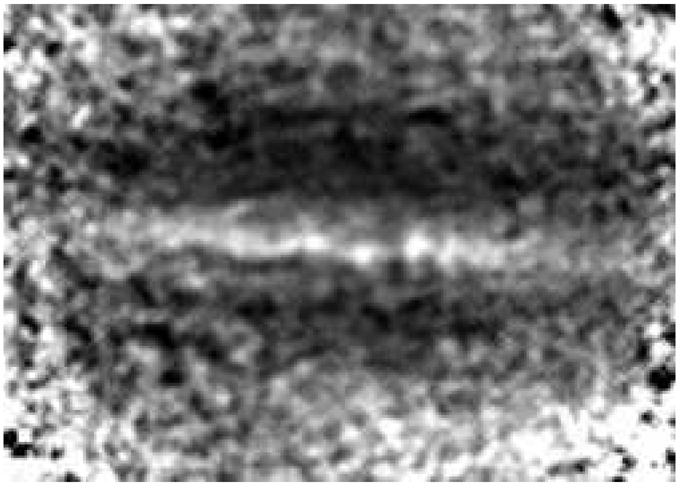

Figure 5.9: A phase contrast image of atoms immediately after transfer to the QUIC trap with $T \approx 550\ \mu$K, such that there is still considerable Zeeman broadening. Probe laser is detuned approximately 10 MHz above the trap bottom, and field of view is 1.7 mm x 1.2 mm. The central region is bright ($I \approx 1.5 I_o$) because it is dominated by the dense central core of the cloud for which the laser is significantly blue detuned, thus there is minimal absorption and significant phase. Outside of this region the atoms are close to resonance, hence ϕ is small while the absorption is greater, and the image is dark.

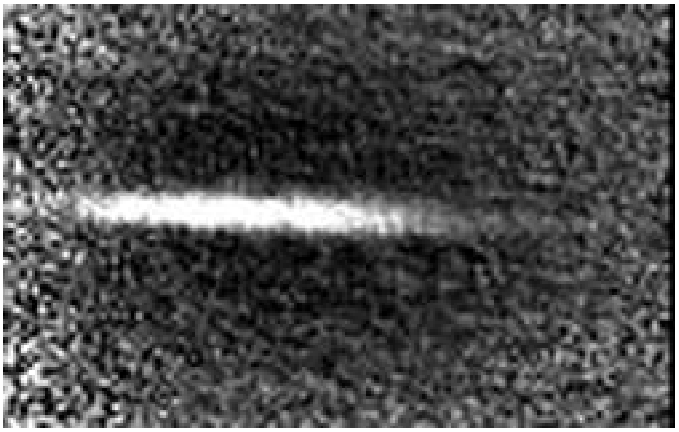

Figure 5.10: Phase-contrast image of approximately 5×10^6 atoms at $\sim 80\ \mu$K. Probe laser is detuned by 25 MHz, and field of view is 1.3 mm x 0.84 mm.

For colder clouds the Zeeman broadening is negligible, so the atoms share a common detuning and ϕ is proportional to $\tilde{n}$. Peak densities also increase as the atoms are evaporatively cooled, permitting the use of larger and larger detunings and thus steadily decreasing optical pumping and photon-recoil induced heating rates. Switching to phase-contrast imaging thus dramatically improves images of these colder clouds; these detunings also allowed for the use of significantly greater laser intensities without fear of saturating the transition. This improves counting statistics while permitting shorter exposures, minimizing blurring from any photon-recoils that do occur. We use blue detuned proble light exclusively to maximize the detuning from the $\Delta m = 0, -1$ optical pumping transitions. This gives images with excellent signal to noise in which the atoms appear as a cigar that is much brighter than the surrounding background, as in figure 5.10.

Unlike the absorption images for which it was difficult to determine how well the evaporative cooling was progressing, phase-contrast images clearly show increasing density as the end point of frequency ramp for the RF knife is lowered. The easiest way to determine this is by choosing a large detuning such that warmer clouds display

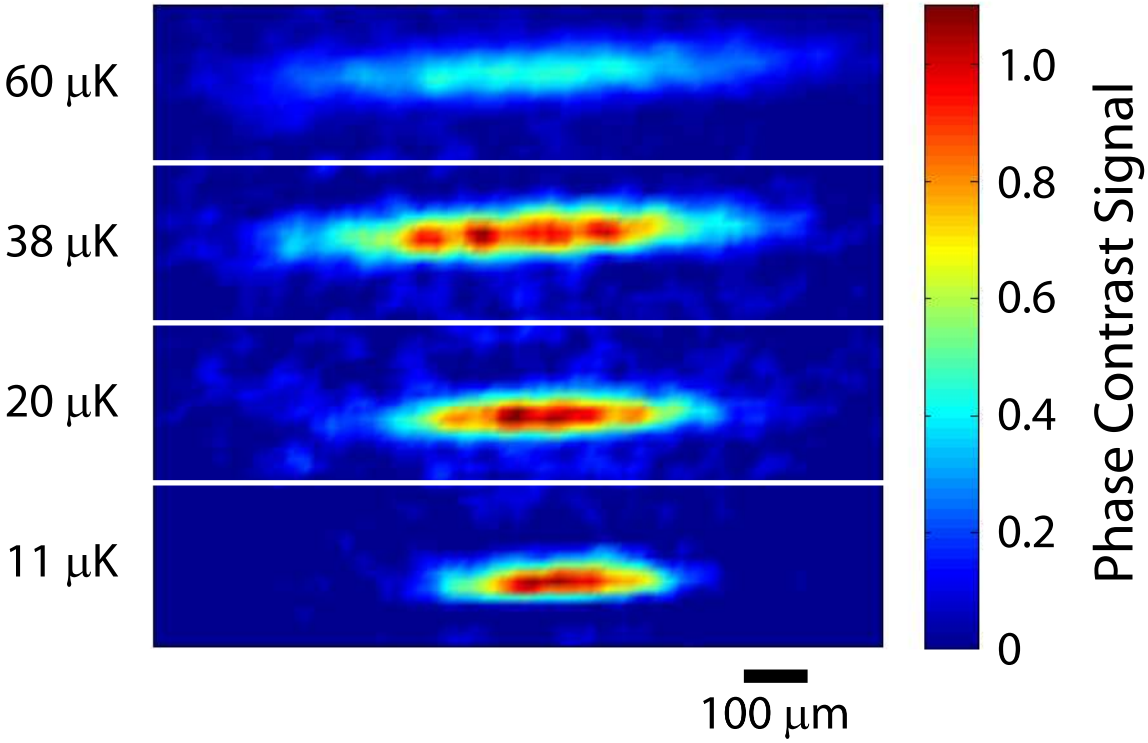

Figure 5.11: A sequence of false color phase-contrast images of atoms at progressively lower temperatures, taken at a constant laser detuning of 28 MHz above the trap bottom. Increasing brightness as the temperature is decreased indicates greater densities, the hallmark of successful evaporative cooling.

a small signal and then ramping to successively lower temperatures; increasing density appears as steadily increasing brightness, while a decreasing cloud dimensions indicate cooling. This is made particularly clear by plotting the phase-contrast images in false color, as in figure 5.11. Two dimensional fits to a sequential series of images taken at different temperatures also provide data from which one can extract a measurement of of the aspect ratio of the trapped cloud. Some caution is necessary; at higher temperatures the radial dimensions of the QUIC trap are predominantly linear, and at very low temperatures the radial dimension of images may be blurred by the resolution limit of the imaging system. However, by fitting for the aspect ratio in a sequence of images one can observe the ratio varying with temperature and account for these effects; we extract an aspect ratio for our trap of 12 ± 1, in reasonable agreement of the ratio inferred from the measured trap parameters described in section 5.1.3[8].

An additional sign of efficient cooling is given by the ratio η between the trap depth (measured in Kelvin) and the atoms' temperature. One expects that for continued cooling η should remain roughly constant; precisely speaking it should vary as approximately the logarithm of the ratio of elastic to inelastic collisions [126, §5.3]. At ultracold temperatures the inelastic collision rate is constant, while the elastic collision rate varies with the velocity, (following equation 4.3), so we expect

$$\eta \sim \frac{\log T}{2}, \tag{5.20}$$

representing a change of only 15% per order of magnitude change in temperature. Unfortunately, as we continued to evaporatively cool to ever lower temperatures we eventually found that the efficiency of the cooling began to drop, signaled by decreasing η, as in figure 5.12.

This decrease in measured η could come from two sources. One possibility is that the cooling is actually well behaved, but the cloud is being rapidly heated during the exposure time of the image due to absorption and associated photon recoils. This would cause the cloud to appear larger and warmer than it was prior to the exposure. Also, for a small bias field B_o the laser detuning is much greater than the frequency difference between the cycling and optical pumping transitions. As such absorption also suggests optical pumping, hence we would expect to be underestimating the number of atoms present before the image was taken. This is annoying, but resolveable

---

[8] The QUIC trap currents used for this data are $\sim 15\%$ smaller than those in 5.2, reducing B'

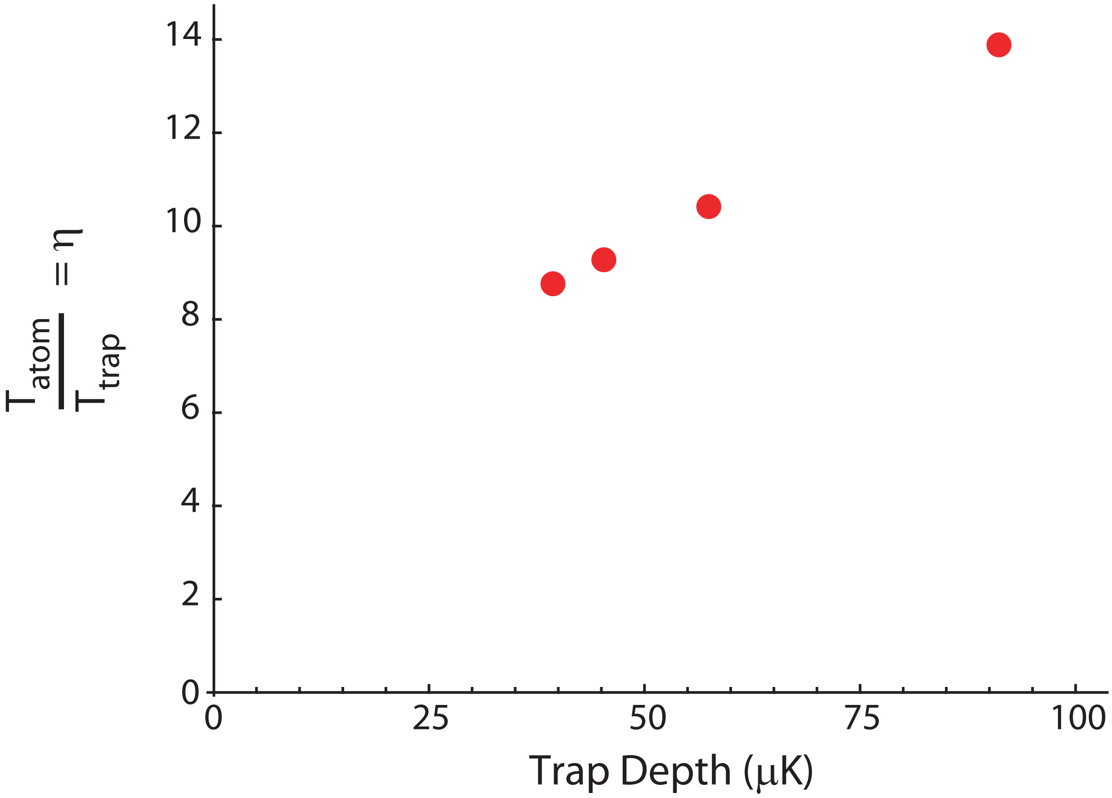

Figure 5.12: Stalling of evaporative cooling at low temperatures. As the trap depth dropped below approximately 100 μK ($T_{atoms} \approx 7$ μK), η began to drop precipitously, signalling inefficient evaporation.

with larger laser detunings or shorter exposures (at the expense of some signal to noise). A more nefarious possibility is that the cooling efficiency is dropping due to it having to combat a real heating rate, unrelated to the imaging and intrinsic to the magnetic trap itself, or that the trap depth is becoming poorly defined to to instability of the trap bias field. In our case we were suffering from both issues. Heating during imaging was resolved by improving the performance of of our phase-contrast set-up[9], and intrinsic heating from the trap was reduced by stabilizing the magnetic fields produced by our QUIC trap.

5.5 Stabilization of the magnetic trap

Heating of trapped atoms due to noisy trapping potentials is an obvious pitfall on the path to BEC and has received considerable study, ranging from mention as a factor limiting condensate lifetime in early BEC papers [8] to detailed investigation in magnetic [135] and far-off-resonant [136] traps.

5.5.1 Heating rates

Perhaps somewhat surprisingly, even at low temperatures trapped atoms are actually somewhat immune to noisy confining potentials. Because their orbits are oscillatory, white noise does not tend to cause heating since fluctuations are equally likely to cause excitation and damping of the motion. As such, significant heating is only caused by noise in particular frequency bands which can resonantly drive motion

---

[9] We had been (knowingly) using a phase plate with the wrong phase shift, having borrowed it from the Ketterle sodium BEC experiment. Switching to a new phase plate with the correct phase shift provided a 6x improvement in signal to noise, permitting larger detunings and shorter exposures

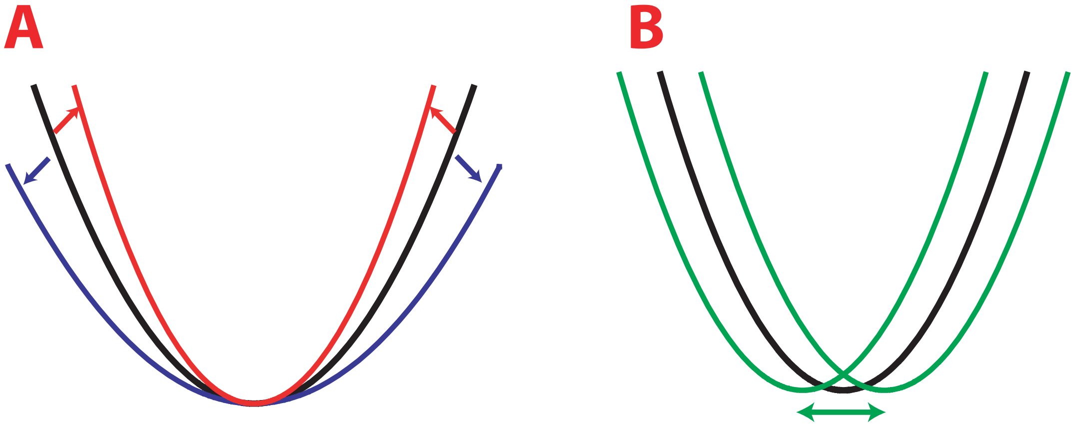

Figure 5.13: Schematic illustration of trap heating types. (A) Parametric excitation, in which the trap curvature is periodically varied at $2\omega_{trap}$. (B) Shaking of the trap potential, which directly forces the atom motion at ω_{trap}.

along one or more of the trap axes. For a harmonic potential this driving tends to occur in two ways: parametric excitation whereby the resonance occurs at twice the trap frequency, or directly forcing the motion at the trap frequency. These two types of heating can be understood in terms of periodic modulation of the trap curvature (changing the stiffness, or spring constant) or physical shaking of the entire trap, as in figure 5.13. These types of heating have been shown to have the following forms [136]:

$$\langle \dot{E} \rangle_{parametric} = \pi^2\, \omega_{trap}^2\, S_\epsilon(2\omega_{trap}) \langle E \rangle \tag{5.21}$$

$$\langle \dot{E} \rangle_{shaking} = \frac{\pi\, m\, \omega_{trap}^4\, S_\epsilon(\omega_{trap})}{2}, \tag{5.22}$$

where S_ϵ is the noise power spectrum. Given the behavior of η shown in figure 5.12, whereby the problem is only observed at lower temperatures, a constant heating rate is implied. This lends credence to shaking induced heating. Put another way, one can define the time required to double the energy of the trapped atoms as [136]

$$\frac{\langle \dot{E} \rangle}{\langle E(t=0) \rangle} = \pi^2 \omega_{trap}^2 \frac{S_x(\omega_{trap})}{\langle x^2 \rangle}, \tag{5.23}$$

meaning that as the cloud cools the doubling time decreases as $1/T$. This can be understood as the trap minimum shaking with a fixed amplitude, imparting more and more energy to the atoms relative to their intrinsic energy as the cloud size shrinks below the shaking amplitude.

Of course, the magnetic field coils naturally hate current noise due to their inductance. This makes it considerably more unlikely that dominant source of heating is due to noise on the quadrupole pair of the QUIC trap, since their larger size gives them an L which is roughly fifteen times that of the Ioffe coil. Similarly, given the much higher oscillation frequencies along the x, y axes of the trap it stands to reason that the heating is being driven along the z axis. This also agrees with the idea that the heating is due to shaking of the trap minimum, since it is known that the minimum is displaced by fluctuations in the ratio between I_{Ioffe} and $I_{quadrupole}$. With all of this in mind, we suspected noise on the Ioffe coil current with a component at or near the axial trap frequency of $\omega_z = 2\pi \times 210$ Hz.

5.5.2 Bias field stability requirements

In addition to our concerns about noise on the trapping fields at the trap frequencies, stabilizing the magnetic fields against white noise is also essential for maintaining the "sharpness" of the RF knife — that is, its energy selectivity. Recalling equation 5.7, the depth of the trap during evaporative cooling as set by the knife is proportional to the bias field B_o. If there is noise on B_o, the knife addresses atoms in a band of energy rather than at a specific energy, setting a minimum achievable temeprature limited by the peak-to-peak field fluctuations. Unfortunately, the wiring of our trap exacerbates this problem. Since the trap minimum is set by the vector addition of two large fields generated by the Ioffe and quadrupole coils, by putting the Ioffe and quadrupole coils on separate circuits we are far more sensitive to noise than we would be if they were operated in series off of a single power supply. In our case the bias field is formed by the $\sim$ 1 G difference between two fields of approximately 200 G. Supposing we have a 10^{-3} oscillation on the currents, we thus have a field fluctuation of $10^{-3} \times 200$ G, rather than a $10^{-3} \times 1$ G fluctuation if the coils were operated in series. As such if we seek trap depths which are steady at the 1 μK level, wiring the trap as we have increases our field stability requirement from $\sim 5 \times 10^{-3}$ to $\sim 2 \times 10^{-5}$, not met by most off-the-shelf power supplies.

5.5.3 Measured field stability

Since the magnetic field coils are inaccessible with the cryostat closed, field stability must be inferred from the noise on the QUIC trap currents. For large currents measurements are best performed with clamp-on Hall effect sensors which typically have 1-10 mA sensitivities. Unfortunately, this sensitivity is inadequate for measurements on the 10^{-5} level for 10 A currents. As such we are forced to perform a voltage measurement using a resistive shunt. This introduces significant added complexity; resistor choice must be a compromise between small R with low power dissipation and larger R with more dissipation but more easily measureable voltages. If the shunt is to be used as a reference it must also be temperature stable at the same level as the desired current stability — a tall order for a resistor susceptible to Ohmic heating.

We built two shunts, one for each of the Ioffe and quadrupole coil circuits. These were constructed out of sets of Riedon FNR 2-T227 0.5 Ω resistors [137] mounted in parallel. These resistors have very small inductances, and while nominally 15 ppm/K temperature stability they are designed such that near room temperature the stability is actually far better than this. The quadrupole (Ioffe) circuit has two (four) resistors, giving it a total resistance of 0.25 (0.125) Ω and a power dissipation of 5 (9) watts per resistor with the trap at normal 6.4 (17) A operating current . The resistors are connected via 0.125" thick copper plate[10] and individually heat sunk. Forced air cooling of the heat sinks keeps the resistors within a few degrees of room temperature.

Using the shunts to measure the current stability of the quadrupole and Ioffe circuits is straightforward. At full current the shunts produce DC voltages near 2 V, so a 10^{-5} measurement requires readings at the 20 μV level. This is easily achieved by amplifying the AC component of the signal; a low-pass filter at 10 kHz helps to reduce noise at frequencies too high to be reasonably passed by the inductive magnet coils. Measured noise (converted to current using Ohm's law) is shown in figure 5.14. The measured noise on the quadrupole coils is smaller than that on the Ioffe coil by roughly the ratio of the inductances, which is unsurprising since the two circuits are powered by similar supplies. However, the Ioffe coil shows noise at the 10^{-3} level. This is easily large enough to cause a problematic instability on the trap bias field, and also a problem for heating if there is any component near the trap frequency. It is also worth nothing that BNC cables are *not* immune to oscillating magnetic fields (as from transformers in the power supplies), hence proximity of control electronics to any large transformer (as in the power supplies themselves) can add 60 Hz noise.

5.5.4 Passive and active field stabilization

As a first step towards resolving the problem we aimed to remove higher frequency noise by adding capacitors in parallel with the magnet coils, passively shunting oscillatory signals past the magnets. The capacitances were selected to have an impedance

---

[10] Copper of course has significantly poorer thermal stability, but its contribution to the total resistance is small enough that its stability is irrelevant.

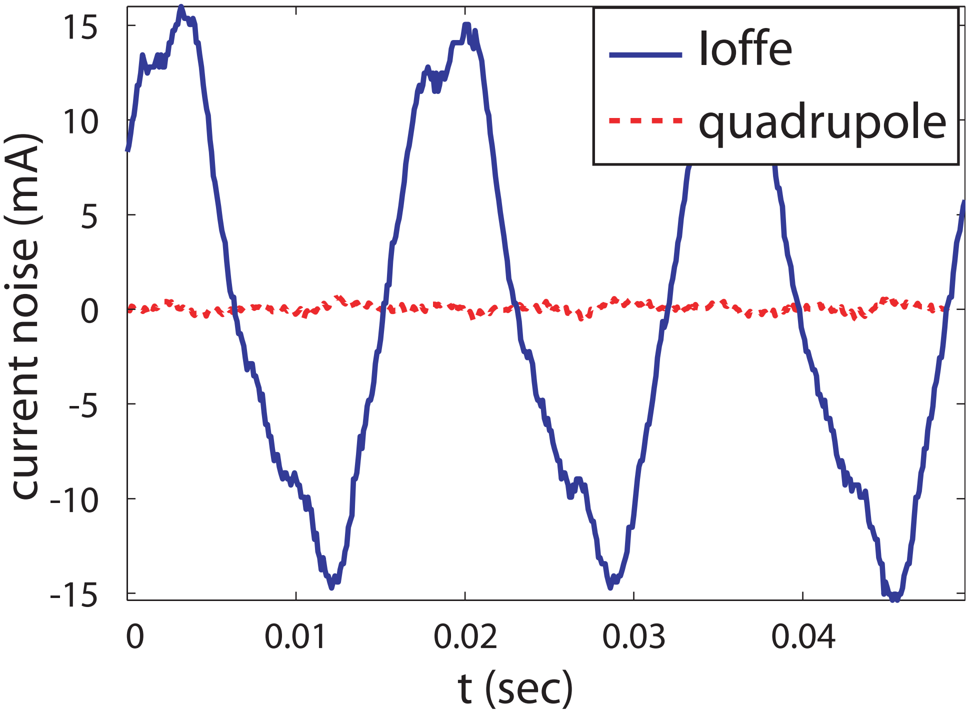

Figure 5.14: Current noise on the QUIC trap coils. The lower noise on the quadrupole coil is due primarily to its larger inductance.

at 10 Hz much smaller than that of the current path through the coil, $1/\omega C \ll \omega_L + R$. This dramatically reduced the 60 Hz noise visible in figure 5.14, but slow drifts of the currents on timescales of order 1 s remained. These drifts tend to be unidirectional, the current steadily decreasing in time probably due to Ohmic heating of the measurement resistors that are internal to the current supplies. To address these drifts we added active stabilization using feedback based on voltage measurements on the Riedon resistors.

In addition to the measurement resistors the active stabilization circuitry consisted of three distinct components: a PID controller, Howland amplifier, and a "humbucker." For PID control we used the SIM960 from Stanford Research [138], a 100 kHz PID controller with variable internally generated setpoints. The PID module accepts an error signal via a BNC terminal. The outer conductor on this terminal is grounded; although one side of the measurement resistor is also grounded we use a humbucker (a circuit built around an instrumentation amplifier) to allow the two grounds to float relative to one another. The correction signal generated by the PID controller is then sent to the Howland amplifier (a fast current source) and turned into a current which is injected into the magnet circuit. This active feedback reduced the slow drifts to an imperceptible level, leaving only the residual higher frequency fluctuations not removed by the capacitors. The residual current noise remaining after passive and active stabilization is shown in figure 5.15; both circuits achieved stability at about the 10^{-5} level.

5.5.5 Anti-Helmholtz magnet flux creep

After stabilizing the currents we observed one more problem with field stability which did not seem to be correlated to the current noise on the QUIC trap magnets. Using

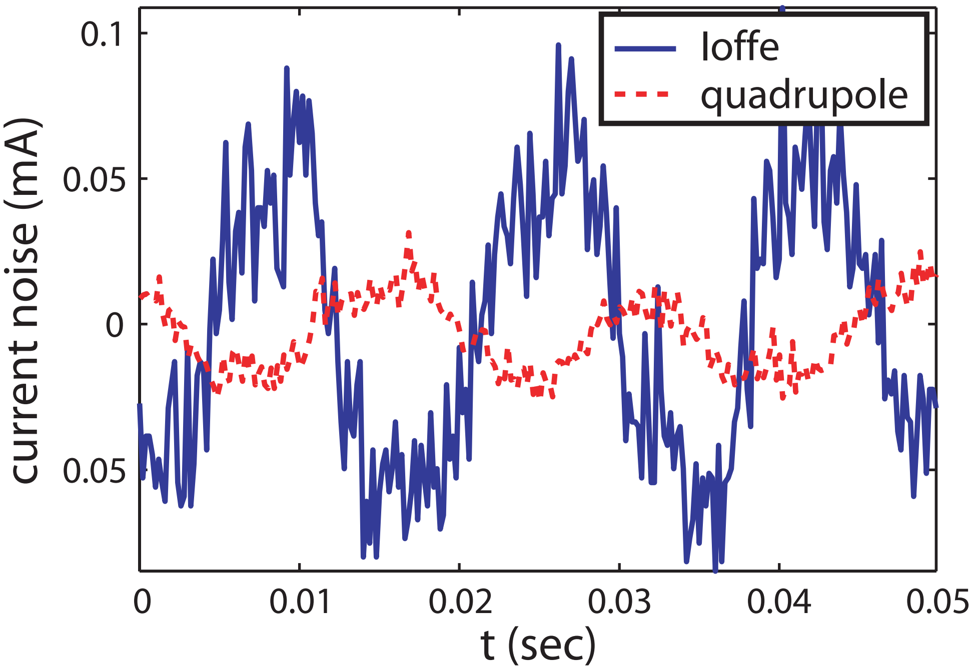

Figure 5.15: Residual noise after stabilization of the QUIC trap currents.

the atoms themselves as a measurement tool to determine B_o (as described in section 5.1.3 we noted that the bias field seemed to be varying by up to 100s of milliGauss over a period of hours. This sort of variation could not be caused by current noise, as it would have required slow drifts on the 10^{-3} scale which would be trivial to observe on our error signal. After making certain that neither the Riedon resistors nor the SIM960 setpoints were at fault we considered the fact that the anti-Helmholtz magnet might be causing the problem. Having totally divorced it from its power supplies the problem could not be related to current noise. However, due to the volume of superconductor in the magnet a considerable amount of flux is trapped, giving rise to a ~ 10 G residual field even when the magnet is not energized [88, §3.2]. If this field has some significant slowly time-varying component, it could cause effects of the size we observed.

This phenomenon is known as "flux creep," and it has received some attention from the accelerator magnet community, where long term stability of fields is critical to accelerator performance. Theoretical work has provided some explanatory models of thermally activated motion of flux quanta [139], but for our purposes it is more practical to consider experimentally observed behavior. Measurements of the time dependence of magnetic fields in Tevatron superconducting magnets [140] have shown variation of magnetic fields on time scales from seconds to hours. The size of long term changes tend to follow a $\log t$ behavior, but there are also changes on shorter time scales which are strongly dependent on magnet ramp history, including ramp rates and peak fields attained on both the most recent and other previous ramp cycles. Given that we perform nominally identical ramps of our anti-Helmholtz magnet again and again we would not expect the recent history to be a factor. However, dependence on past ramps might make variables such as the time since breaking for lunch important for understanding our flux creep.

Rather than eating at the same time each day we instead try to minimize the effects of trapped flux by removing them from the magnet, heating it to above the superconducting transition. Our magnet is equipped with resistive heaters for just this purpose. Measurements of the magnet resistance while passing current through the heaters indicate that R jumps from zero to a roughly constant value within about 1 s of applying current; presumably the high copper content of the magnet coils allows them to quickly reach thermal equilibrium. This value increases with applied current for currents up to 1 A and then is nearly independent of current for larger values, which we interpret as the magnet being entirely above T_c.

Observations of the QUIC trap bias field before and after heating the anti-Helmholtz magnet indicate a change of ~ 1 G, in agreement with the model that time variation of the trapped flux field is influencing B_o. While the stability of B_o is significantly improved, after this initial sudden change upon driving the anti-Helmholtz magnet normal some residual variation in B_o on the 10 mG scale does still remain. The source of this variation is unknown, but may result from small irreproducible movements of the magnetic field coils, perhaps due to flexing of the thin G-10 spacers via which the QUIC trap coils are affixed to the brass coil assembler (see figure 3.6). These fluctuations are inconsistent; sometimes the bias field will be stable for hours or days at a time, while at other times it varies more steadily. Because we are unable to predict these variations while collecting data we pause to re-measure B_o regularly, and account for any drift in later data analysis.

Chapter 6

Producing, detecting, and characterizing the condensate

With the QUIC trap stabilized and heating and bias stability issues resulting from magnetic field noise resolved, continued evaporative cooling towards quantum degeneracy is straightforward. By adding new segments to the RF knife ramp that end at ever lower temperatures and optimizing the frequency sweep rate for each one, evaporative cooling can proceed until one runs out of atoms or a new heating problem appears. Here we describe the detection of the Bose-Einstein condensate that forms following evaporative cooling to quantum degeneracy.

6.1 The Bose-condensed state

As one evaporates to lower and lower temperatures the cloud of atoms continues to shrink spatially while increasing in density. This contributes to a steady rise in the phase-space density and the chemical potential,

$$\rho_{psd} = n\,\lambda_{dB}^3 = n\left(\frac{2\pi\hbar^2}{mk_BT}\right)^{3/2} \tag{6.1}$$

$$\mu = U_o n, \tag{6.2}$$

where U_o is the mean-field interaction energy in the Gross-Pitaevskii equation [141, §6.1]

$$-\frac{\hbar^2}{2m}\nabla^2\psi(\vec{r}) + V(\vec{r})\psi(\vec{r}) + U_o|\psi(\vec{r})|^2\psi(\vec{r}) = \mu\psi(\vec{r}) \tag{6.3}$$

and is defined in terms of the scattering length, $U_o = 4\pi\hbar^2 a/m$. Bose-Einstein condensation occurs when $\rho_{psd} = \zeta(3/2) \approx 2.612$. At this point a macroscopic fraction of the atoms begin to collect in the lowest state of the potential, leading to a sudden and dramatic increase in the density at the center of the cloud as the condensate forms. The signal of BEC is thus the formation of a bi-modal density distribution, with a dense core (the BEC) surrounded by a more dilute normal component (the so-called thermal cloud).

The details of the bimodal distribution depend upon the density at which it is reached. The condensate is most easily considered in two limits based on neglecting either the mean-field or kinetic energy term in equation 6.3 — that is, comparing U_o to $\hbar\,\omega_{\rho,z}$. At low densities the interaction between atoms is insignificant (the ideal gas limit), hence we can neglect the interaction term and the condensate wave function is simply the harmonic oscillator ground state [112, §4.2],

$$n_c(r) = \frac{N}{\pi^{3/2}}\frac{1}{\rho_{rms}^2 z_{rms}}\,\mathrm{Exp}\left[-\frac{\rho^2}{\rho_{rms}^2} - \frac{z^2}{z_{rms}^2}\right], \tag{6.4}$$

where $\rho_{rms}, z_{rms} = \sqrt{\hbar\,\omega_{\rho,z}/m}$. At larger densities repulsion between atoms dominates the kinetic energy (the Thomas-Fermi limit), and one can imagine the atoms "filling up" the potential until they reach the chemical potential μ. In this case the condensate density mirrors the shape of the potential [112, §4.3]:

$$\begin{aligned} n_c(r) &= \max\left(\frac{\mu - V(\vec{r})}{U_o}\,, 0\right) \\ &= \frac{15}{8\pi}\frac{N}{\rho_o^2\, z_o}\max\left[1 - \left(\frac{\rho^2}{\rho_o^2} + \frac{z^2}{z_o^2}\right)\,, 0\right]. \end{aligned} \tag{6.5}$$

Here $\rho_o, z_o = \sqrt{2\mu/m\omega_{\rho,z}^2}$ are the condensate half-widths at which the condensate density drops to zero.

Bose enhancement also affects the thermal component, with a density given by

$$n_{th}(\vec{r}) = \frac{1}{\lambda_{dB}^3} g_{3/2}\left(\,\mathrm{Exp}[(\mu - V(\vec{r}))/k_B T\,]\,\right), \tag{6.6}$$

where $g_j(z) = \sum_i^\infty z^i/i^j$ is the Bose function. μ is again the chemical potential, simply defined in the Thomas-Fermi limit for a harmonic trap as

$$\mu = \left(N_c \omega_\rho^2 \omega_z a \frac{15\hbar^2 m^{1/2}}{2^{5/2}}\right)^{2/5}, \tag{6.7}$$

where μ depends on the condensate number $N_c = N\,(1 - (T/T_c)^3)$, scattering length $a = 7.5$ nm [127], and the trap frequencies. For analysis or fitting of only the wings of the thermal distribution it is often convenient to drop all but the first term in $g_{3/2}(z)$, particularly at larger temperatures. This is analogous to treating the normal component classically, as distinguishable particles.

Due to the large ^{4}He* scattering length and the large densities we anticipate having in the condensate we expect that for our trapping parameters ($\omega_z = 2\pi \times 210$ Hz, $\omega_\rho = 2\pi \times 2520$ Hz) condensates on the scale of $10^4 - 10^5$ atoms or more will be well into the Thomas-Fermi limit in both the axial and radial dimensions. This makes simulation of cloud density profiles and corresponding phase-contrast images straightforward, as in figure 6.1.

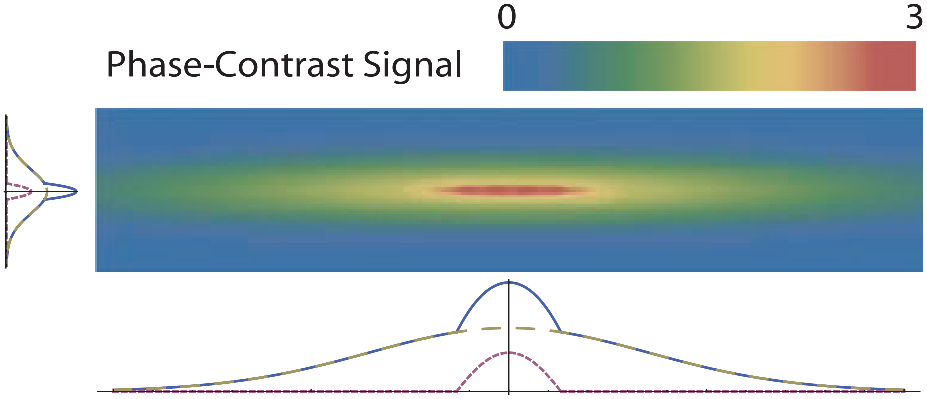

Figure 6.1: A simulated (false color) phase-contrast image of a BEC surrounded by a thermal cloud at slightly below $T_c = 5$ μK, with $N = 10^6$ atoms. Adjacent to the image are cross sections showing the contribution from thermal and condensed fractions. Field of view is 200 x 40 μm.

6.2 *In-situ* detection of Bose-Einstein condensates

Due to the benefits offered by dispersive imaging (low image-induced heating and signal proportional to the cloud column density $\tilde{n}$) it is possible to detect Bose-Einstein condensation of atoms while they remain trapped. As is described above, the onset of of BEC is signaled by the sudden appearance of a bright center to phase-contrast images of a trapped cloud. With large enough detunings this may be observed non-destructively, permitting repeated imaging of the same atom cloud to observe dynamic effects. In our case the poor quantum efficiency of our camera at 1083 nm requires we use large laser intensities for imaging, limiting us to one or at most two observations of clouds cold enough for condensate formation. Even so, we hoped to be able to observe the condensate *in-situ* with this destructive imaging.

Unfortunately, as implied to by equation 6.5 and figure 6.1, *in-situ* detection of a BEC places a stringent requirement on the resolution of one's imaging system. For a condensate with 10^5 atoms in our trap ρ_o is only about 5 μm and scales only as $N_c^{1/5}$, so imaging without blurring requires a resolution of only a few microns. With

$\sim$ 35 cm between our atom cloud and the first 2” aperture lens we expect a resolution of about 10 μm[1], so images of a trapped condensate should be significantly blurred in the radial dimension. Indeed, blurring starts to be noticeable even for thermal clouds well above T_c, as is evident from the changing of the apparent aspect ratio between colder images in figure 5.11 as the cloud begins to be blurred in the radial dimension.

For observing a condensate the effects of limited resolution are even worse than they are for a thermal cloud. For an object smaller than the resolution limit of the imaging system the signal in phase-contrast will remain spread over a width set by the resolution, d_{res}. This reduces the contrast C of the image by the ratio of the actual to blurred areas, which for a long, narrow condensate is given by ratio of the radial dimensions,

$$C_{image} = C_{true} \frac{\rho_o}{d_{res}}. \tag{6.8}$$

In our case this reduces the observed BEC contrast by a factor of nearly 3. As such, if the thermal cloud remains large enough to be clearly imaged and thus maintains its full contrast, the condensate is washed out into its surroundings. With adequate signal-to-noise the two components may still be distinguished, but in practice they become very difficult to separate, as in figure 6.2. In this case we have fit the data to a sum of two Gaussians for convenience — one for the condensate, and one for the thermal cloud. The widths of the two Gaussian components agree well with the expected condensate and thermal widths for $N \approx 10^6, T \approx 4$ μK, but the data fits nearly as well to a single Gaussian.

Two routes exist for increasing the condensate size to the point that it may be clearly imaged. The first is to simply relax the trapping potential, allowing the atoms to spread. Since the condensate half-width scales as $(1/\omega_\rho)^{3/5}$, opening the trap will

---

[1] Resolution measured to be $\sim$ 16 μm.

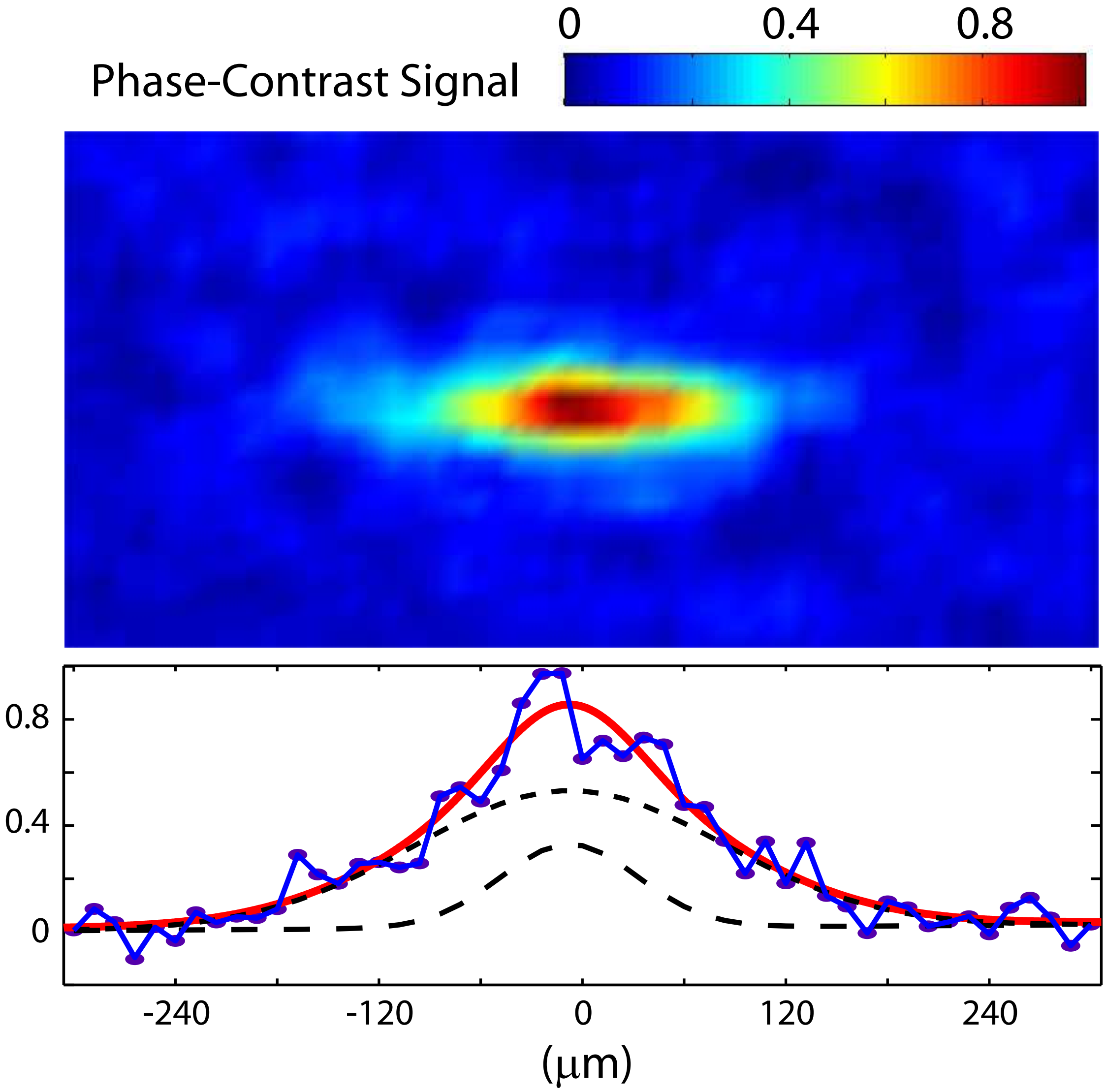

Figure 6.2: *In-situ* phase-contrast image of what is almost certainly a BEC surrounded by a thermal cloud. Blurring of the condensate reduces its contrast such that it is difficult or impossible to distinguish from the surrounding normal component. The dashed lines are the components of the solid line fit to two Gaussians (see text).

allow the condensate to expand along the radial axis. As is evident from equation 3.4, it is straightforward to relax the trap in the radial dimension by increasing the bias field B_o. Unfortunately, this is a two-edged sword; opening the trap spreads out the condensate, but also reduces the atom density, thus requiring lower temperatures before T_c is reached. Given that some residual magnetic field noise remains in our trap even after stabilization, evaporating to significantly lower temperatures to achieve BEC in a relaxed trap (or adiabatically expanding a condensate formed at higher temperatures) may not be possible. This led us to implement the second option: releasing the atoms from the trap entirely and imaging them in time-of-flight expansion.

6.3 Imaging BECs in time-of-flight expansion

Time-of-flight (TOF) expansion has been used to image dilute-gas BECs since the field's inception [7, 8] as a way of both improving spatial resolution and reducing the resonant absorption to the point that images yield useful information. By suddenly turning off the magnetic trap, the atom cloud is allowed to expand in all directions. This expansion proceeds according to the atoms' momenta at the moment the confining potential vanishes modified by any further acceleration resulting from inter-atomic interactions. This gives rise to different expansions for normal vs. Bose-condensed clouds, since they differ both in their *in-situ* momentum distributions as well as their mean-field interaction energies, which are proportional to density.

6.3.1 Expansion of normal and Bose-condensed clouds

Understanding expansion of thermal clouds is straightforward. Above T_c the cloud density can be written in momentum space as [141, §2.3]

$$n(\vec{p}) \propto e^{-p^2/2mk_BT}, \tag{6.9}$$

thus the momentum distribution is isotropic, and the cloud expands uniformly in all directions at a velocity $v = \sqrt{k_BT/m}$. For expansion times sufficiently long to ignore the initial size of the trapped cloud ($t_{expand} \gtrsim 1/\omega_z$) the ballistically expanding cloud is spherical, with a size given by

$$\rho_{RMS}, z_{RMS} = \sqrt{\frac{k_BT}{m}}\, t_{expand}. \tag{6.10}$$

For a BEC the expansion is somewhat more complicated, as the momentum distribution of the trapped cloud is no longer isotropic and the greater density of the condensate increases the strength of the mean-field interaction. As with the spatial density profile described above it is again convenient to consider the expansion in the ideal gas and Thomas-Fermi limits.

For a non-interacting condensate the density in momentum-space is given by the square of the momentum space wavefunction [141, §2.3],

$$n(\vec{p}) = \frac{N_c}{\pi^{3/2}\sigma_\rho^2\sigma_z}\, e^{-(p_\rho^2/\sigma_\rho^2 + p_z^2/\sigma_z^2)}, \tag{6.11}$$

where $\sigma_{\rho,z} = \sqrt{m\,\hbar\,\omega_{\rho,z}}$ are the RMS momenta. This is much like the classical Maxwell velocity distribution, excepting that here the width is set by unequal "temperatures" in different dimensions, $T_{\rho,z} = \hbar\omega_{\rho,z}/2k$. Put another way, since the momentum space and real space wavefunctions are related by a Fourier transform, a narrow spatial distribution implies a broad momentum distribution — just a restatement of the Heisenberg uncertainty principle. As such the condensate expands anisotropically; the velocity of the expansion is larger in the tightly confined radial dimension. One reaches a similar conclusion for a strongly interacting condensate in the Thomas-Fermi limit, where it has been shown that the condensate half-widths evolve in time as [112, 142]

$$\begin{aligned} \rho_o(t) &= \rho_o(0)\sqrt{1+\tau^2} \\ z_o(t) &= z_o(0)\left(1+\frac{\omega_z^2}{\omega_\rho^2}\left[\tau\arctan\tau - \ln\sqrt{1+\tau^2}\right]\right), \end{aligned} \tag{6.12}$$

where $\tau = \omega_\rho t$. This can be thought of a pressure-driven acceleration of the atoms away from the center of the trap, where the pressure results from the mean-field interaction. The density gradient, being steeper in the radial dimension, thus drives more rapid expansion in this direction.

For our condensate (fully in the Thomas-Fermi limit) we expect an expansion like that in figure 6.3. This reveals three regimes. Initially ($t < 1/\omega_\rho$) the condensate undergoes accelerating expansion in the radial dimension as the mean-field energy is converted into atomic motion. This is followed ($1/\omega_\rho < t < \omega_\rho/\omega_z^2$) by radial expansion with minimal axial expansion beyond the initial axial dimensions, and finally ($t > \omega_\rho/\omega_z^2$) expansion in both dimensions with a constant ratio of velocities $v_\rho/v_z = \pi\omega_\rho/2\omega_z$. This also defines a "sudden" shutoff of the trapping potential; although it is important to release the radial confinement in a time short compared to $1/\omega_\rho$, the axial dimension need be released only on a time fast compared to $1/\omega_z$ — a significantly weaker constraint.

The differences between the expansion of thermal clouds vs. condensates also gives an additional signature of condensate formation: inversion of the cloud aspect ratio for TOF greater than $1/\omega_z$. While both thermal clouds and BECs have the same aspect ratio *in-situ* — that of the cigar shaped trap, or about 12:1 in our case — their asymptotic expansions are very different. Up to $t_{expand} \approx 1/\omega_z$ both expand from a

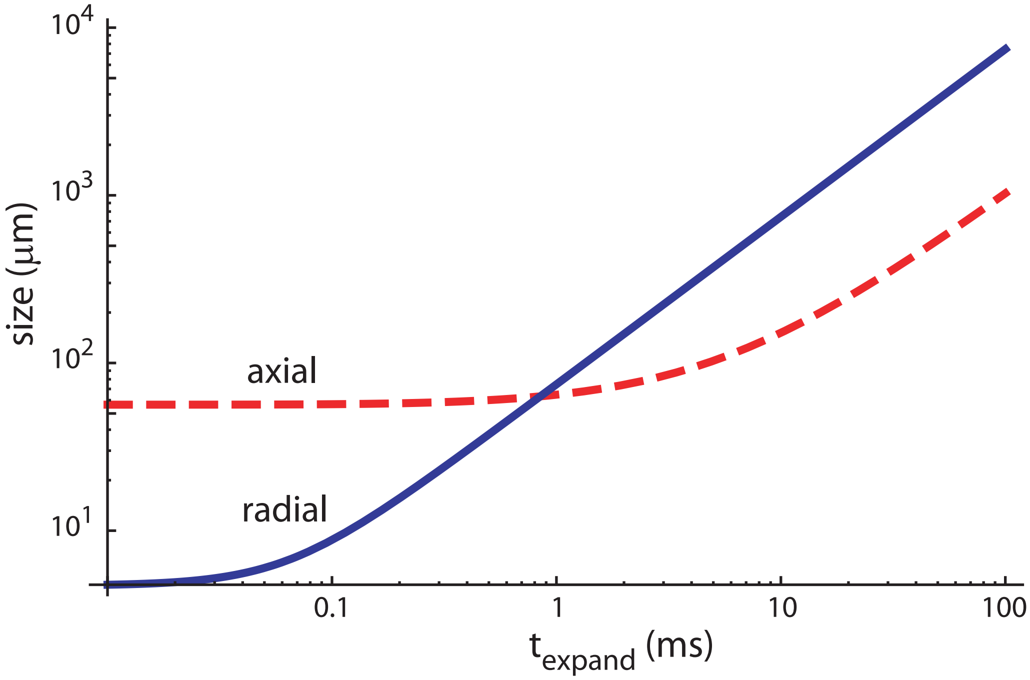

Figure 6.3: Simulated TOF expansion according to equation 6.12 for a condensate with parameters similar to those in our trap.

12:1 ratio towards 1:1 (spherical), but while thermal clouds then maintain this 1:1 ratio indefinitely, condensates continue to expand into a pancake shape, eventually reaching a ratio of about 1:8. Observing a complete inversion requires imaging after a long TOF, which can be difficult since the optical density of the cloud drops steadily throughout the expansion. However, images at intermediate times that show an aspect ratio notably below 1:1 strongly suggest the presence of a BEC[2].

---

[2] Collisions during the expansion can also contribute to an inverting aspect ratio, even for thermal clouds [143]. However, this requires a collision time $\tau_{col} \lesssim 1/\omega_\rho$, which does not occur in our trap except at densities where the cloud is Bose-condensed anyway.

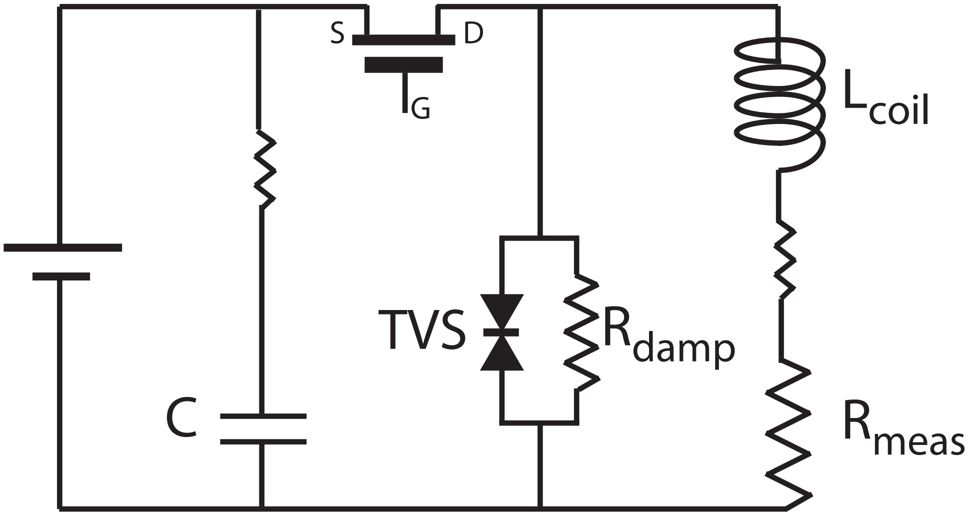

Figure 6.4: QUIC trap shutoff electronics schematic. The P-FET switches out the positive terminal of the power supply, forcing current to circulate through the TVS and damping resistor. The TVS sets the voltage at which the coil discharges, while the damping resistor prevents ringing as the last few percent of the current dissipates.

6.3.2 Trap shutoff and induced currents

We shut off our QUIC trap using P-channel MOSFETS (Fairchild FQA36P15 [144]) using the circuit shown in figure 6.4 (details in appendix E). The FETs switch out the positive terminal of the current supplies, forcing the coils to discharge across transient voltage supressors (Littelfuse 5KP series [145]) — essentially back-to-back Zener diodes that sap energy from the circuit at a fixed voltage, giving us a constant dI/dt. We were unable to find low resistance P-type FETs capable of switching at voltages higher than 150 V[3], limiting the shutoff time for the $\sim$ 15 mH quadrupole coils to about 600 μs. This is too slow for the shutoff to be considered sudden for the radial expansion; fortunately, because our quadrupole and Ioffe coils are on separate circuits we can achieve an effective shutoff for the radial direction which is much faster

---

[3] Unfortunately, the grounding of the coil enforced by the stabilization electronics made the use of higher voltage N-channel FETS impossible.

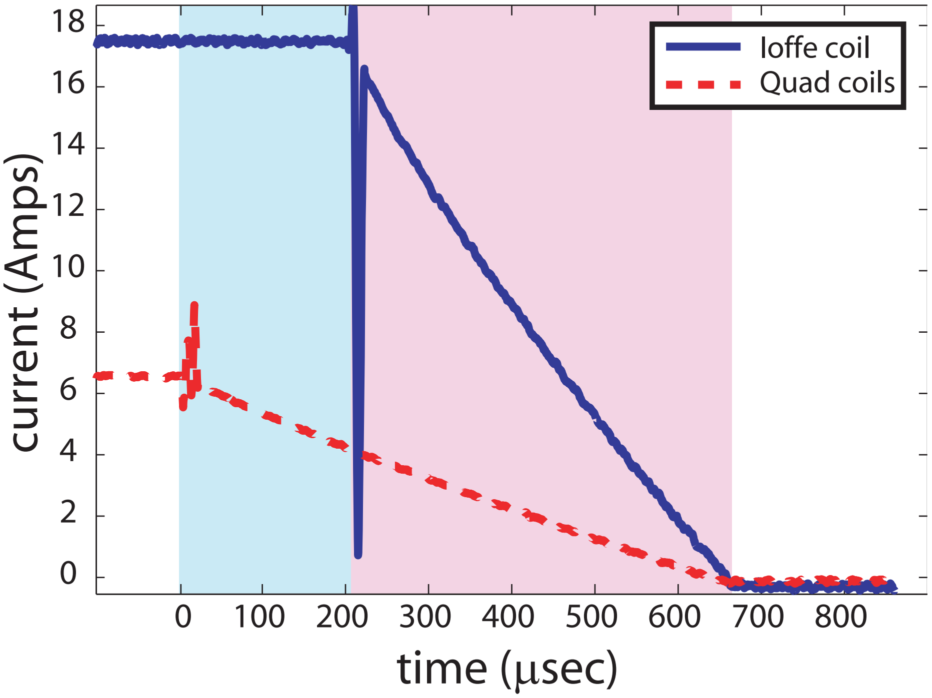

Figure 6.5: Shutoff of the QUIC trap magnet coils. For the first 200 μs we reduce the current in only the quadrupole coils, increasing the trap bias field B_o and relaxing the confinement in the radial dimension. For $200 < t < 600$ μs both coils are ramping down, uniformly lowering the relaxed potential.

by manipulating the trap bias field.

As described in section 5.5.2 the bias field is generated by the difference between the local fields generated by the quadrupole and Ioffe coils. As such if we modify the ratio of the current between the coils we can easily change B_o, leading to a change in the radial confinement as defined by equation 3.4. Since it takes only a small change in this ratio to achieve a large change in B_o and therefore B''_ρ, it is possible to open the trap very quickly in the radial dimension simply by beginning to turn off the quadrupole coils before the Ioffe coil, as in figure 6.5. This leads to an effective turn-off time of approximately 100 μs (the time required to significantly increase B_o). This satisfies the requirement for sudden shutoff in the radial dimension, but is still not quite so fast as we would prefer and must be considered for quantitative interpretation

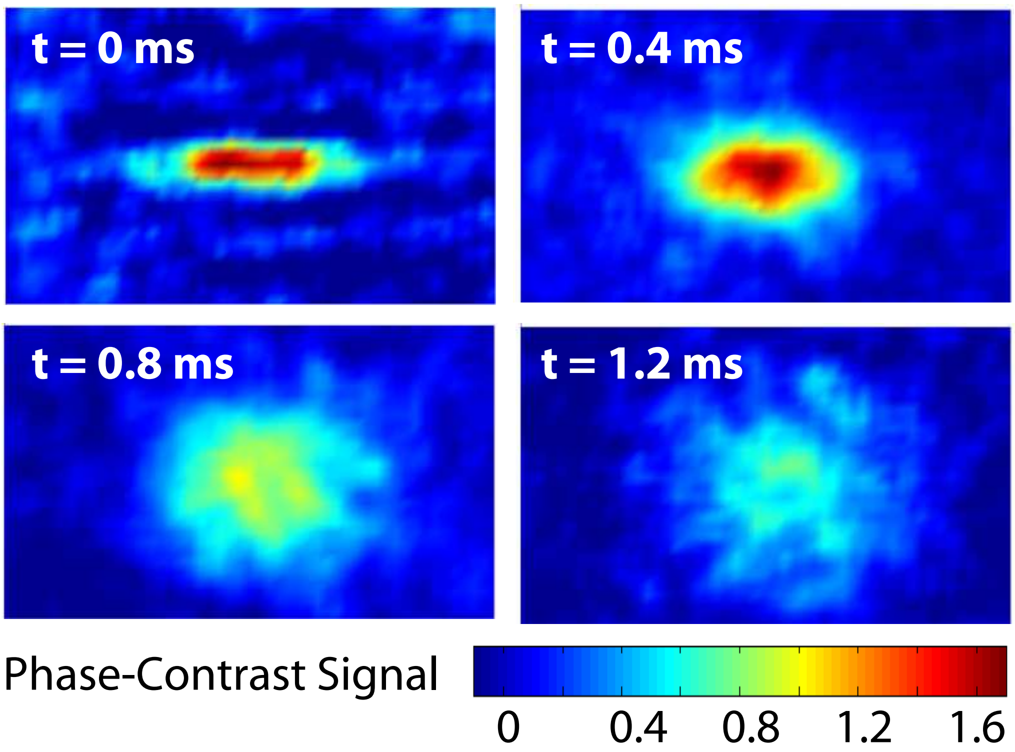

Figure 6.6: Thermal clouds ($T \approx 6\ \mu$K) at varying expansion times. The contrast in the 0.8 and 1.2 ms images has been amplified by a factor of two for clarity.

of radial TOF data.

Generally speaking the trap shutoff and ensuing expansion of the atom cloud works beautifully. The highest quality images are acquired with an expansion time long enough to allow the radial dimension to expand beyond the diffraction limit yet brief enough that the axial expansion is minimal, preserving optical density and image contrast. In our trap this corresponds to between 0.6 and 1 ms, as in figure 6.6. However, one unexpected challenge did arise for collecting images in time-of-flight. Due to the rapidly changing magnetic fields permeating the brass QUIC trap coil assembler (refer to section 3.2.4) the trap shutoff induces considerable eddy currents, creating a magnetic field of several tens of Gauss that varies on the same timescale as our selected expansion times. This field Zeeman shifts the $\Delta m = +1$ detection transition to higher frequencies, thus we must select a different probe laser detuning for each expansion time to compensate for the Zeeman shift. Furthermore, it mandates that we image with brief exposure times, as otherwise the effective detuning can change during the exposure, making calibrating phase-contrast signals difficult. Also, the field is not uniform, but rather applies a force to the atom cloud that tends to accelerate it towards the Ioffe coil.

To try to understand how these eddy currents might impact our images we constructed a simple model of this induced field based on the dominant current loops present in the coil assembler. Due to the contact resistance in the joint between the two halves of the assembler we assumed currents traveled only within each half. Since the currents are induced by a brief pulse of field they should be limited to flowing within a skin-depth of the surface of the brass, setting the resistance of the each loop and thus limiting the size of the induced current. The results of this model are in rough agreement with the observed Zeeman shifts, and indicate that the eddy-current field creates a magnetic field gradient with minimal curvature at the location of the atoms. This is important; a curvature would tend to deform the cloud during time-of-flight, whereas the gradient merely pushes the cloud without deforming its structure. It should also be noted that while a curvature would magnify the cloud (perhaps anisotropically), it could not create a bimodal distribution.

In two respects this gradient is actually somewhat convenient. Increasing the trap bias field (as we do at the beginning of turning off the QUIC trap) tends to shift the location of the trap minimum away from the Ioffe coil. As such, our shut-off proceedure initially accelerates the atoms in this direction. This leads to the cloud moving “up the hill” created by the eddy-current field, which slows its motion and reflects it back towards the Ioffe coil. By matching the details of the trap shut-off to the strength of the gradient we can vary the time at which the direction of the cloud's motion is changing — that is, when it is stationary — and match it to the expansion time at which we would like to image. This way we can take images of a stationary cloud and eliminate any motional blurring that would otherwise be caused by the shifting of the minimum during shut-off. Also, by Zeeman shifting the $\Delta m = +1$ transition away from the $\Delta m = 0, -1$ transitions optical pumping ceases to be an issue. This is particularly useful for imaging expanded clouds, as their reduced optical density means our imaging must take place at smaller detunings from resonance.

6.4 Time-of-flight images of Bose-Einstein condensates

With the problem of sub-resolution BECs solved by imaging in ballistic expansion it became much easier to distinguish between clouds with and without condensate fractions, as in figure 6.7. The BEC forms suddenly as the RF knife is ramped to within approximately 1 MHz of the trap bottom (trap depth of 55 μK), appearing as a significantly denser (brighter) region at the center of the phase-contrast images of the expanded cloud. The bimodal distribution is particularly clear along the axial dimension, where the widths of the BEC and thermal cloud are well separated.

Although the 1 ms TOF in figure 6.7 is not long enough to for the aspect ratio to approach its asymptotic value, it is clear that the condensate aspect ratio has already inverted beyond 1:1. We can also observe the aspect ratio as a function of time, yielding the data in figure 6.8. Here we see that at early times there is little distinction between thermal clouds and nearly pure condensates, while at longer times the aspect ratio of the BEC is consistently below that of warmer thermal atoms. Unfortunately,

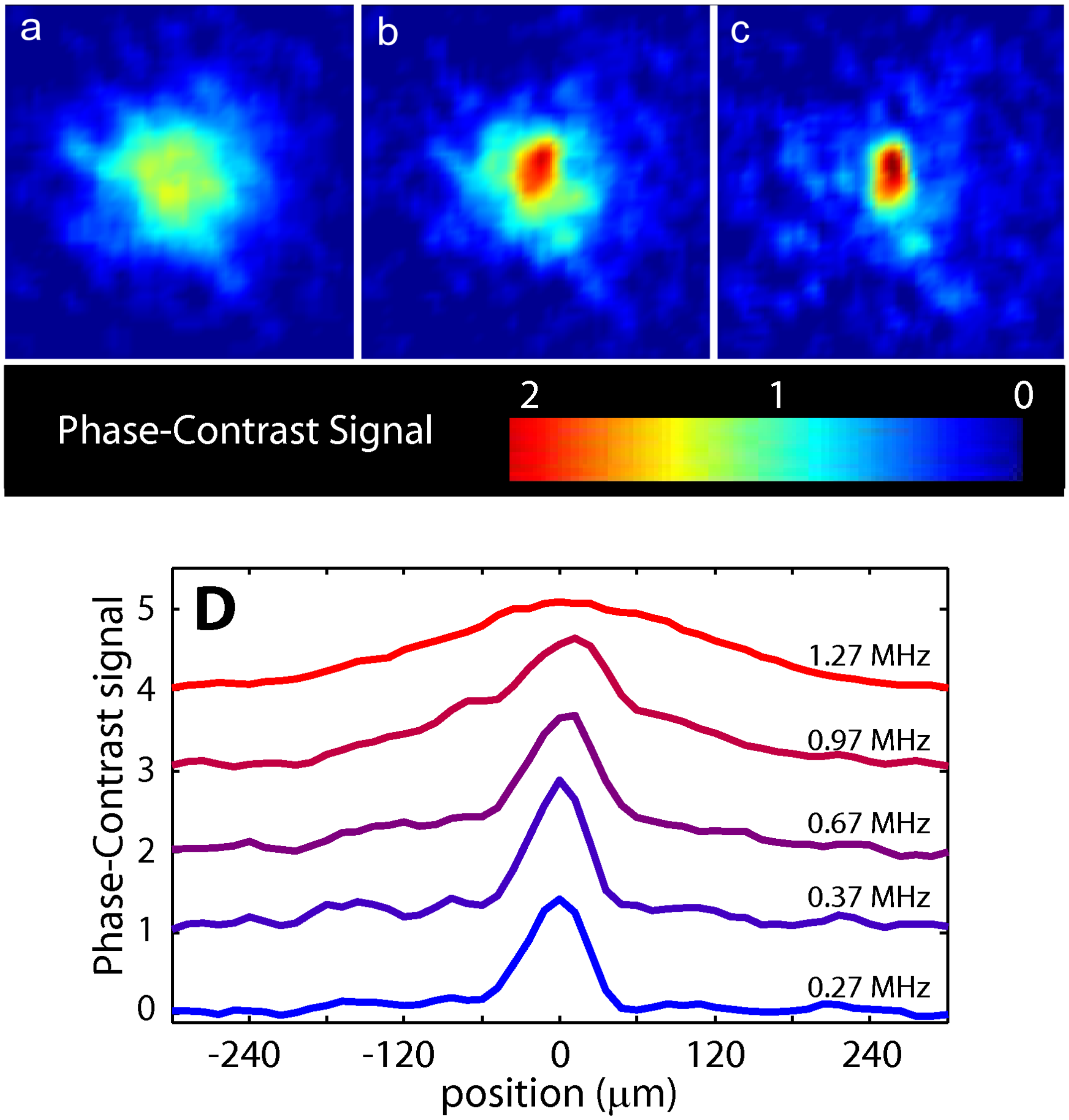

Figure 6.7: The BEC transition after 1 ms TOF. (A) A thermal cloud slightly above T_c. (B) Just below T_c the condensate appears, characterized by its increased density and slightly inverted aspect ratio. Further evaporative cooling yields a nearly pure condensate, as in (C). Field of view is 600 μm. (D) Axial cross sections showing the onset of the biomodal distribution characterizing the presence of Bose-condensed and thermal components. All data is in phase-contrast with a laser detuning of $7.5\times\Gamma/2$, averaged over three evaporation cycles.

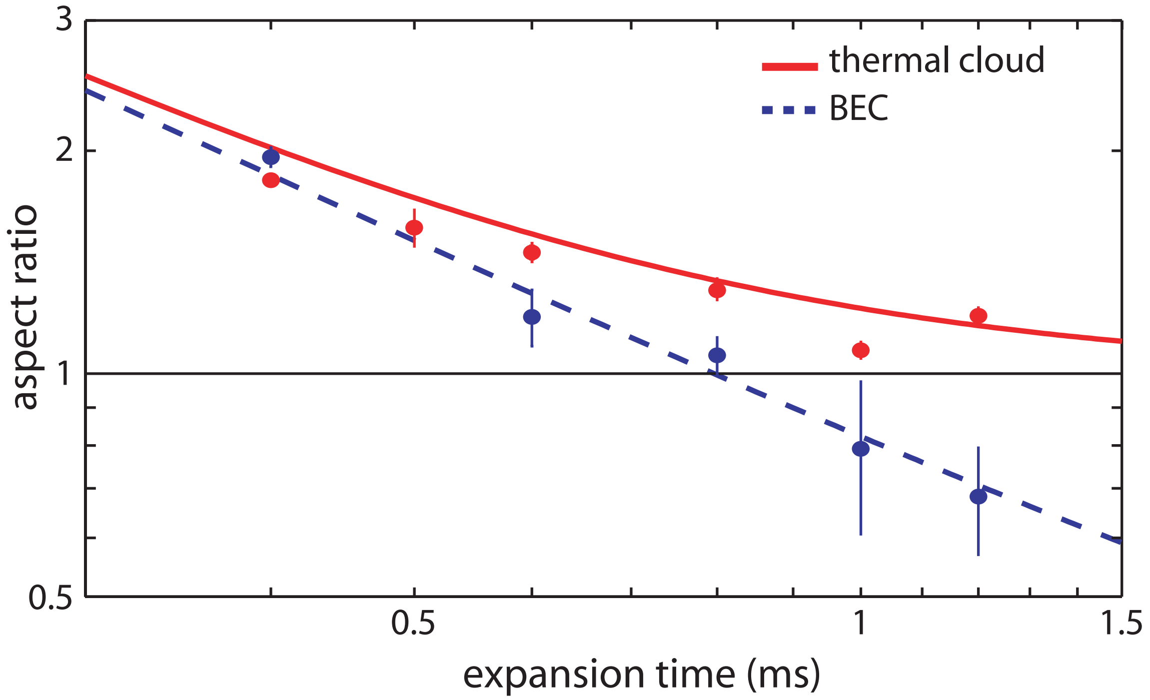

Figure 6.8: Aspect ratios as measured from 2D Gaussian fits. Thermal clouds evaporated to $T_{trap} \approx 100\ \mu$K, BEC samples to $T_{trap} \approx 30\ \mu$K. Solid lines are predictions based on equation 6.12.

it was not possible to observe the condensate long enough to see the aspect ratio fully invert. At expansion times greater than 1.5 ms the signal-to-noise is not adequate to obtain quality fits to the cloud, but the data for $t_{expand} < 1.5$ ms does agree fairly well with the expansion predicted by equation 6.12.

6.5 Determining N_{crit}, T_c at the BEC transition

The two critical parameters that describe the BEC are the number of atoms present at the transition temperature, N_{crit}, and the transition temperature itself, T_c. These in turn may be combined to yield the critical atom density for condensation, n_{crit}. Both parameters may be determined from images in a variety of ways.

6.5.1 Critical temperature

By repeatedly evaporatively cooling clouds of atoms to ever lower temperatures one can pinpoint the RF knife frequency at which the condensate first appears. This makes it it possible to determine T_c from TOF images by fitting for the RMS radial width in TOF of thermal clouds evaporated to knife frequencies just above the transition. Alternatively, one can fit to the thermal component of the bimodal distribution for a cloud just cold enough to contain a condensate in cases where the condensate and thermal widths are easily distinguished. In both cases the temperature is extracted from the width for these fits according to equation 6.10. These fits indicate a temperature of approximately 4-4.5 μK, but unfortunately suffer from some systematic uncertainty since our trap shutoff may not be truly sudden for expansion in the radial dimension. If the shutoff is too slow there can be a bit of adiabatic expansion and cooling during the first instant, slowing expansion at longer times and leading us to underestimate the true temperature.

An alternative estimate may be based on the dynamics of evaporative cooling and the expected ratio η between the atom temperature and the trap depth during evaporation. This parameter varies depending on the details of the evaporative cooling ramp and on the collisional parameters of the atom being cooled. Faster ramps permit fewer collisions for rethermalization, leading to lower values of η and reduced efficiency in the idealized case (see equation 4.6), but also lose fewer atoms to inelastic processes. For maximally efficient evaporation in real atoms η varies between about 5 and 12 [37, §2] depending on the ratio of elastic to inelastic collisions and other loss rates. ^{4}He* has excellent collisional parameters [128] and we expect η to be above 9 until BEC is reached and the increased density makes three-body inelastic collisions more probable. *In-situ* measurements of temperature at somewhat higher temperatures indicate $\eta \approx 12$.

One way of looking at the evaporation data that is particularly well suited to this sort of estimate for T_c is to plot the area of a 2D Gaussian fit vs. RF knife frequency, as in figure 6.9. For thermal clouds with $T > T_c$ the area, defined as $\sigma_x \times \sigma_y$ for the Gaussian fit, is expected to be proportional to T and therefore to the RF knife frequency[4]. However, with the onset of BEC many of the atoms collapse into the center of the trap, giving rise to a narrower distribution with a taller peak and correspondingly smaller area, and the area suddenly ceases to be proportional to the knife frequency. For our experiment this divergence from proportionality takes place at 1.05 MHz; assuming $\eta = 10$ yields a critical temperature of $T_c \approx 5$ μK.

---

[4] This assumes that η is constant throughout the temeprature range of interest, reasonable over an order of magnitude or so.

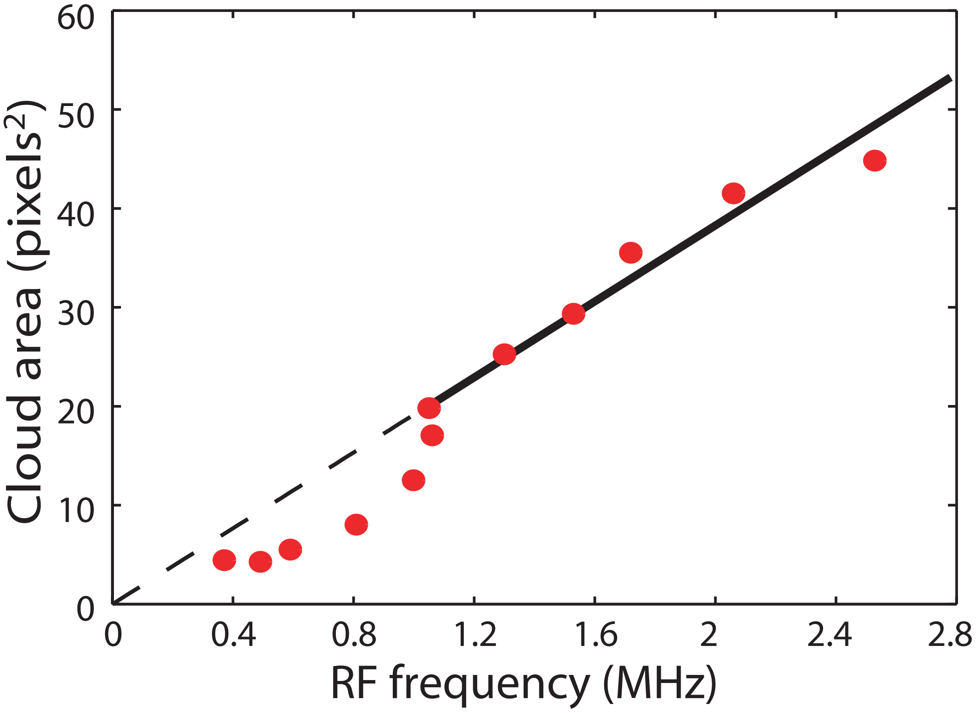

Figure 6.9: Cloud area in TOF, plotted as a function of the final RF knife evaporation frequency measured relative to the trap bottom. The divergence from a straight line near 1.05 MHz signals the onset of BEC.

6.5.2 Critical atom number

The atom number in TOF images may be determined most simply by combining equations 5.14 and 5.18 and integrating the phase-contrast signal over the image,

$$N = \frac{2(1+\delta^2)}{\delta\sigma_o} \iint_{-\infty}^{\infty} \frac{I_{pc}(x,z) - 1}{2I_o}\, dx\, dz. \tag{6.13}$$

This determination yields an atom number of $1.1 \times 10^6 \pm 10\%$ (statistical), but suffers from several systematic uncertainties. Our images are taken with significant light intensities, and it is possible that there are some effects due to saturation, despite being detuned from the transition. Furthermore, the measured atom number is roughly proportional to the laser detuning, which is uncertain. It both changes slightly during the image due to the time-varying eddy current field in which the atoms are located following trap shutoff and is susceptible to nonlinearities in the voltagae-to-frequency conversion for the voltage controlled oscillators that set the AOM frequency shifts. For 1 ms TOF images the detunings used are only $7.5 \times \Gamma/2$ — only a handful of MHz — so errors below the 1 MHz level will still be enough to dominate the statistical uncertainty.

Fortunately, as with the critical temperature we have an alternative way of determining N_{crit} based on a theoretical model. If one neglects the effects of interactions the number of atoms at the critical temperature can be calculated for a variety of different potentials [146]. For an axially symmetric harmonic potential such as our QUIC trap one can write

$$N_{crit} = 1.202 \left(\frac{k_B T_c}{\hbar \omega_z \omega_\rho^2} \right)^3 . \tag{6.14}$$

Using our measured trap frequencies and $T_c = 5\ \mu$K we estimate $N_{crit} = 1 \pm 0.2 \times 10^6$, where the error is from uncertainty in the trap frequencies. This is in surprisingly good agreement with the value determined by simply integrating the phase-contrast signal, suggesting the systematic uncertainties associated with our phase-contrast imaging are not too severe. Further evaporative cooling, such as that depicted in figure 6.7C, yields nearly pure condensates with $2 - 3 \times 10^5$ atoms.

From this critical atom number we can also calculate the critical density for condensate formation at T_c in our trap to be 2×10^{13} cm^{-3}. At this density we expect an instantaneous decay rate of approximately 1 Hz [128], dominated by three-body collisions, which is in agreement with observations of the cloud lifetime. However, once the condensate forms we expect the *in-situ* density at the center of the trap to be greater than 1×10^{14} cm^{-3}, corresponding to an instantaneous decay rate of 25 Hz, so our condensates must be short lived. Since the last bit of the evaporative cooling ramp takes only a fraction of a second this rapid loss rate never poses a problem, but for carrying out experiments with these condensates it might be necessary to relax the confinement so as to reduce the three-body collision rate.

Chapter 7

Conclusions and future directions

After a long research effort that began over a decade ago and entered its current iteration in 2007 we have created a buffer-gas loaded BEC, the world's first demonstration of a general path to Bose-Einstein condensation. Along the way we have surmounted a number of technical challenges: incorporation of a dilution refrigerator into the existing cryostat to lower the cell base temperature and development of a bakeout scheme to improve the quality of the cell vacuum, construction and stabilization of a tightly confining superconducting QUIC trap (the first of its kind) to prevent Majorana losses, and *in-situ* and time-of-flight imaging of trapped atoms despite limited optical access. With these improvements in place we were able to evaporatively cool all the way from $\sim$ 500 mK to quantum degeneracy, achieving Bose-Einstein condensation at $T_c = 5\ \mu$K with 1.1×10^6 atoms remaining.

Unlike the MIT hydrogen condensate, which relied upon the uniquely weak atom-surface interaction between ^{1}H and a superfluid helium coated wall, or the myriad laser-cooled BEC experiments, buffer-gas techniques are applicable to a comparatively wide array of paramagnetic atoms and molecules. Due to its ability to trap samples several orders of magnitude larger than achieveable via laser cooling, this new method promises to generate correspondingly larger condensates. While the current experiment has not yet realized these large condensates, a number of relatively straightforward modifications to the existing apparatus should make possible ^{4}He* condensates of approximately 10^8 atoms.

Extension of buffer-gas loading to new species should also be straightforward. Although the true range of species for which magnetic trapping followed by evaporative cooling is a viable path to degeneracy is unknown, research on the subject is ongoing both experimentally [80] and theoretically [147]. However, even for species in which the atom-atom collisional parameters are not suitable for evaporative cooling, sympathetic cooling with large buffer-gas loaded condensates or other large reservoirs of ultracold atoms may still be possible.

7.1 Generation of large metastable helium condensates

Despite producing upwards of 10^{13} ^{4}He* atoms at zero-field and starting with approximately 10^{11} trapped in good vacuum at dilution refrigerator temperatures, our condensate size is somewhat disappointing. The $\sim 10^6$ atoms remaining when we reach T_c is more than an order of magnitude smaller than largest ^{4}He* condensates produced using laser cooling [128], and over two orders smaller than the largest alkali condensates [148]. This occurs despite our evaporative cooling taking place fairly efficiently (particularly after loading atoms into the QUIC trap) largely due to a critical failure of our apparatus, namely the extremely poor transfer efficiency between the large anti-Helmholtz trap and the QUIC trap. The most important step towards producing larger condensates is to resolve this loss by implementing a few minor changes

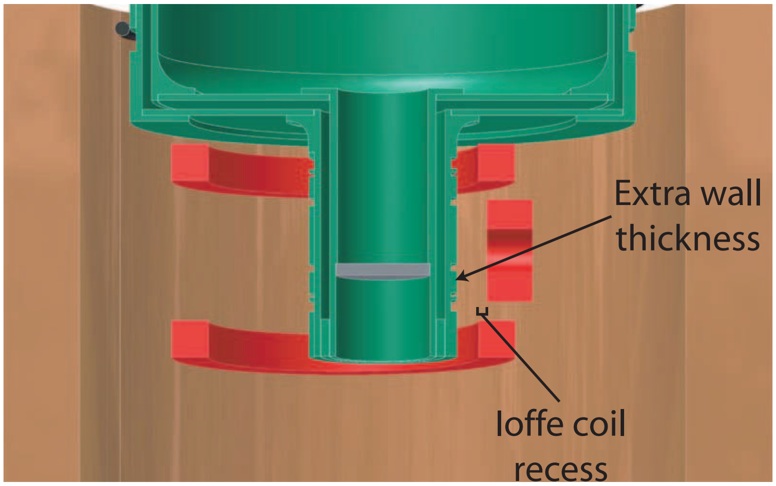

Figure 7.1: Resolveable problems with the existing cell—QUIC trap assembly.

to the cell and trap.

7.1.1 Cell and assembly modifications

Loss of atoms occurs due to the cell wall and/or window being too close to the trapping minimum, providing a place for energetic atoms to adsorb and setting a trap depth much smaller than that of the potential itself. In the case of the window this is easily resolved by merely lengthening the extension around which the QUIC trap is located. The existing short extension was designed to permit evaporation directly against the window, but this is not actually required to cool the atoms enough to permit transfer to the QUIC trap, thus the window merely serves as an artificial boundary on the trap depth. Increasing the trap depth at the cell wall is a more complicated proposition due to the need to maintain vacuum space between the 4 K trap coils and the 200 mK cell. However, at present the Ioffe coil is actually recessed back from the cell, and thus not even the surface which defines the vacuum space; also, the walls on the cell extension are thicker than necessary (see figure 7.1).

By removing the thickened region of outer extension wall where the RF evaporation coil wiring channels are cut, reducing both inner and outer extension wall thicknesses slightly, and bringing the Ioffe coil forward to match the inner diameter of the QUIC quadrupole coils, the Ioffe coil can be brought more than 2 mm closer to the center of the cell. This should be more than adequate to resolve the low trap depth. A second auxiliary measure to increase the depth of the QUIC trap upon initial loading would be to replace the existing 4 K vacuum feedthrough from the helium bath into the IVC. Made of copper and rated to only 15 A, heating in this feedthrough causes delayed quenching of the QUIC trap for Ioffe coil currents much above 20 A. Constructing a home-built feedthrough from Cu:NbTi wire surrounded by a G-10 sleeve and embedded in epoxy would allow for the use of larger currents without encountering this heating problem. With these changes it should be possible to transfer atoms into the QUIC trap with near unit efficiency, leading to condensates at least an order of magnitude larger.

Yet another factor of thirty in condensate size could likely be achieved if we were able to trap atoms in good vacuum after production from a saturated vapor, as in section 4.1.1. Given that the vapor pressure of ^{4}He at 200 mK is quite low, this should be possible by completely removing the cell pumpout sorb and returning to an apparatus similar to that described in section 2.1.1. Removal of the sorb and valve shaft should also significantly reduce the heat loads upon the cell and refrigerator; along with shortening and enlarging the diameter of the superfluid helium heatlink between the cell and mixing chamber this should allow for even lower base temperatures, further improving the quality of the vacuum. It might also be possible to further improve the number of ^{4}He* trapped if a set-up could be constructed with a more steady-state discharge at the edge of the cell, allowing metastable atoms to collect in the trap.

7.1.2 QUIC trap and RF evaporation coil modifications

If the cell were modified as described above, leading to the trapping of 100x larger numbers of ^{4}He* atoms in the QUIC trap, it would likely also be necessary to improve the QUIC trap itself. Due to the large two- and three-body inelastic rates for metastable helium collisions, the lifetime of trapped clouds decreases rapidly as densities increase. To prevent unacceptable loss of atoms it will likely be necessary to steadily relax the trapping confinement as the atoms are evaporatively cooled, reducing the increase in density as the atom temperature drops.

Due to the independent wiring of the quadrupole and Ioffe coils in the existing QUIC trap it is difficult to make this sort of smooth change in the trapping potential. To simplify adiabatic expansion of the cloud during evaporative cooling it would be preferable to operate the trap with the coils in series, powered by a single supply. This would require re-winding the trap with the number of turns selected to match I_{quad} to I_{Ioffe}. By running the trap with four leads and joining the two circuits at 300 K it would still be possible to use distinct current ramps while transferring atoms from the anti-Helmholtz trap, followed by switching to a single supply after the atoms are QUIC trapped. This would also significantly improve the trap stability, and by winding a secondary coil of perhaps 5% as many turns on the Ioffe coil form it would be possible to modify the bias field using an auxiliary current supply.

Unnecessary inelastic losses during evaporative cooling can also be mediated by carefully matching the cooling rate to the elastic collision rate. This is impossible with the existing RF knife, as the larger RF power necessary to evaporate quickly causes the small superconducting wire making up the evaporation coil to quench. This should be easily resolved by using a larger gauge NbTi wire for the evaporation coil. Larger powers might also cause unacceptable eddy current heating, but coil windings designed to reduce fringing fields [149] should keep such heating to a tolerable level.

7.2 New ultracold gases

While the production of large condensates and degenerate Fermi gases of He* offers opportunities for new hydrodynamic studies and improved or novel experiments in atom optics, the true power of buffer-gas methods is their applicability to new species that have not yet been brought to the ultracold regime. Of particular interest is the creation of large samples of ultracold, polar molecules of varied elemental composition. To date such molecules have only been assembled from pre-cooled atoms [150, 151], limiting the molecules available for research to only a handful of possibilities.

An alternative path is to directly cool a bound molecule; while the many collisional channels in molecules make ordinary evaporative cooling challenging or impossible, sympathetic cooling with an atomic collisional partner remains a possibility. Such a partner should ideally be a spherical atom with a small C_6 coefficient and low mass, making for large centrifugal barriers in collisions that can eliminate inelastic channels [152]. These atoms are necessarily difficult to laser cool since small C_6 coefficients are associated with short transition wavelengths, but are well suited to buffer-gas methods. Two such partners are atomic nitrogen and atomic silver; here we describe prospects for evaporatively cooling these atoms with an eye towards sympathetically cooling NH.

7.2.1 Atomic nitrogen

Nitrogen is a natural choice for new studies in the cold and ultracold regime, where low temperatures and high densities provide an avenue to study collisional physics present in astronomical systems such as interstellar gas clouds. N also has a 3 μ_B magnetic moment, making it straightforward to magnetically trap, and theoretical studies have indicated it has adequate collisional parameters for evaporative cooling [153]. The first E1 allowed transition in nitrogen is in the VUV at 120 nm, making laser cooling essentially impossible with current laser technology; this also forces detection to be accomplished via two-photon laser-induced fluorescence [154].

Despite these difficulties, trapping and detection of more than 10^{11} atoms via buffer-gas loading has already been demonstrated [153], and is described in Matthew Hummon's PhD thesis [155]. This work was carried out using an atomic beam generated by an RF plasma source, but it should be possible to dissociate N_2 directly from ice frozen on the walls of a cell at dilution refrigerator temperatures using an RF discharge coil like that used for ^{4}He* production. Using such a set-up would permit trapping of large numbers in an environment that can achieve UHV conditions, allowing for evaporative cooling exactly as with metastable helium. Atomic nitrogen is also a natural choice for sympathetic cooling of NH. Buffer-gas loading by igniting an RF discharge from ammonia (NH_3) or N_2 and H_2 ice would lead to co-trapping of N and NH. Finally, Nitrogen is also expected to be a good collisional partner for sympathetic cooling; the same 120 nm transition that makes it so difficult to detect gives it a very low polarizability [71] and C_6 coefficient, 20 and 40 times smaller than Na and Rb, respectively. Preliminary theoretical calculations indicate σ_{el}/σ_{in} for N — NH collisions to be on the order of 800 in the temperature range of interest [147], with further investigation ongoing.

7.2.2 Atomic silver

Silver is also an intriguing candidate for new trapping and cooling experiments. Atomic silver has a narrow (0.8 Hz) $^2S_{1/2} \rightarrow ^2D_{5/2}$ line which has been proposed as an optical frequency standard. The alkaline earths have received more attention among neutral atom candidates; however, the narrowness of the silver transition makes it unique in its ability to benefit from the long interaction times offered by atomic fountains [156]. Silver has been trapped in a MOT at 328 nm [156], but only in small numbers compared with alkali atoms due to both the difficulty in generating enough laser power to adequately saturate the cooling transition and to silver's low vapor pressure.

Silver has already been studied in a buffer-gas set-up [90, 157], with up to 10^{13} atoms trapped at approximately 500 mK. As an S state atom with a small magnetic moment it is plausible that silver will have favorable collisional parameters for evaporative cooling, making it possible to cool to the quantum degenerate regime. However, in addition to its application as frequency standard, silver may also be almost uniquely suited for use as a sympathetic coolant. Though not as small as that of nitrogen, silver has a polarizability much less than that of the alkalis [158], making it likely to be a good collisional partner. For sympathetic cooling of NH, silver may be preferable to nitrogen due to its smaller 1 μ_B magnetic moment, allowing silver to be preferentially evaporated from the trap without loss of the more deeply trapped NH molecules. Additionally, co-trapping of Ag and NH followed by laser cooling of Ag in the magnetic trap may be a very efficient way to quickly cool large numbers of NH molecules with minimal losses. Silver also offers vastly simpler diagnostics in comparison to nitrogen since it may be easily detected via absorption spectroscopy/imaging of the trapped cloud on the 328 nm cooling transition.

Trapping and evaporative cooling of silver using buffer-gas methods will be significantly more challenging than ^{4}He* due to silver's smaller magnetic moment and correspondingly weaker trap depths. The difficulty stems from the antithetical requirements on the buffer-gas density for initially loading the trap ($n_{He} \gtrsim 10^{15}$ cm^{-3}) and evaporative cooling ($n_{He} \lesssim 10^8$ cm^{-3}). Evacuating the buffer gas to allow for evaporation requires traversing a buffer gas density at which the lifetime of atoms in the trap exhibits a minimum (the "valley of death" [90, §2.2]), where collisions with the residual background gas are still frequent but the gas density is too low for diffusion to extend the trap lifetime. Maintaining a minimum trap lifetime of > 1 s while removing the buffer gas requires a trapping $\eta \gtrsim 10$, which for the ~ 2.7 K/μ_B trap depths of our existing Nb:Ti magnets means $T_{atom} < 270$ mK.

In [90] this challenge was met through the use of a ^{3}He buffer gas. However, the large low temperature ^{3}He vapor pressure complicated removal of the buffer gas for evaporative cooling, since for ^{3}He cell temperatures of $\lesssim 100$ mK are necessary to achieve $n_{He} \lesssim 10^8$ cm^{-3}. However, three paths may be pursued to improve on the work in [90] to permit trapping and evaporative cooling of 1 μ_B species such as silver. First, by completely removing the pumping sorb and its associated mechanical connections it should be possible to reduce heat loads on the trapping cell, which may make pursuing the "cold-loading" techniques described in [90] feasible without any additional changes. Second, construction of a Nb_3Sn trapping magnet should be pursued. Preliminary investigation indicates that the higher critical field offered by Nb_3Sn should afford a 40% increase in trap depth, which would simplify trap loading by permitting the use of ^{4}He buffer gas. Finally, it may be possible to load with ^{4}He using our existing magnets by briefly desorbing buffer gas from a very thinly coated cell wall, as in the ^{4}He* work described in this thesis. This technique has also been used for loading heavier (albeit more magnetic) atoms in the work described in [80], and may be extendable to silver.

Appendix A

Simulation of metastable helium spectra

^{4}He* is a simple atom, having zero nuclear spin and a symmetric $^3S_1$ ground state, and its spectrum is easily understood. Even so, there are some complexities associated with simulating the interaction between the fine structure levels of the excited state manifold in the presence of a magnetic field. Here we list the relevant spectroscopic parameters for the $2^3\mathrm{S}_1 \rightarrow 2^3\mathrm{P}_J$ transitions and describe simulation of the absorbtion spectrum at zero-field and in the anti-Helmholtz trap as well as simulation of absorption images.

A.1 Spectrum simulation at zero-field

The $2^3S_1 \rightarrow 2^3P_J$ transition in ^{4}He* consists of three fine structure lines, one for each of the $J = 0, 1, 2$ excited states, with properties as in table A.1 and Clebsch-Gordan coefficiencts in figure A.1. These lines are split by 2.29 GHz ($^3\mathrm{P}_1$–$^3\mathrm{P}_2$) and 29.62 GHz ($^3\mathrm{P}_0$–$^3\mathrm{P}_1$). At zero-field these lines are unmixed and the atoms are

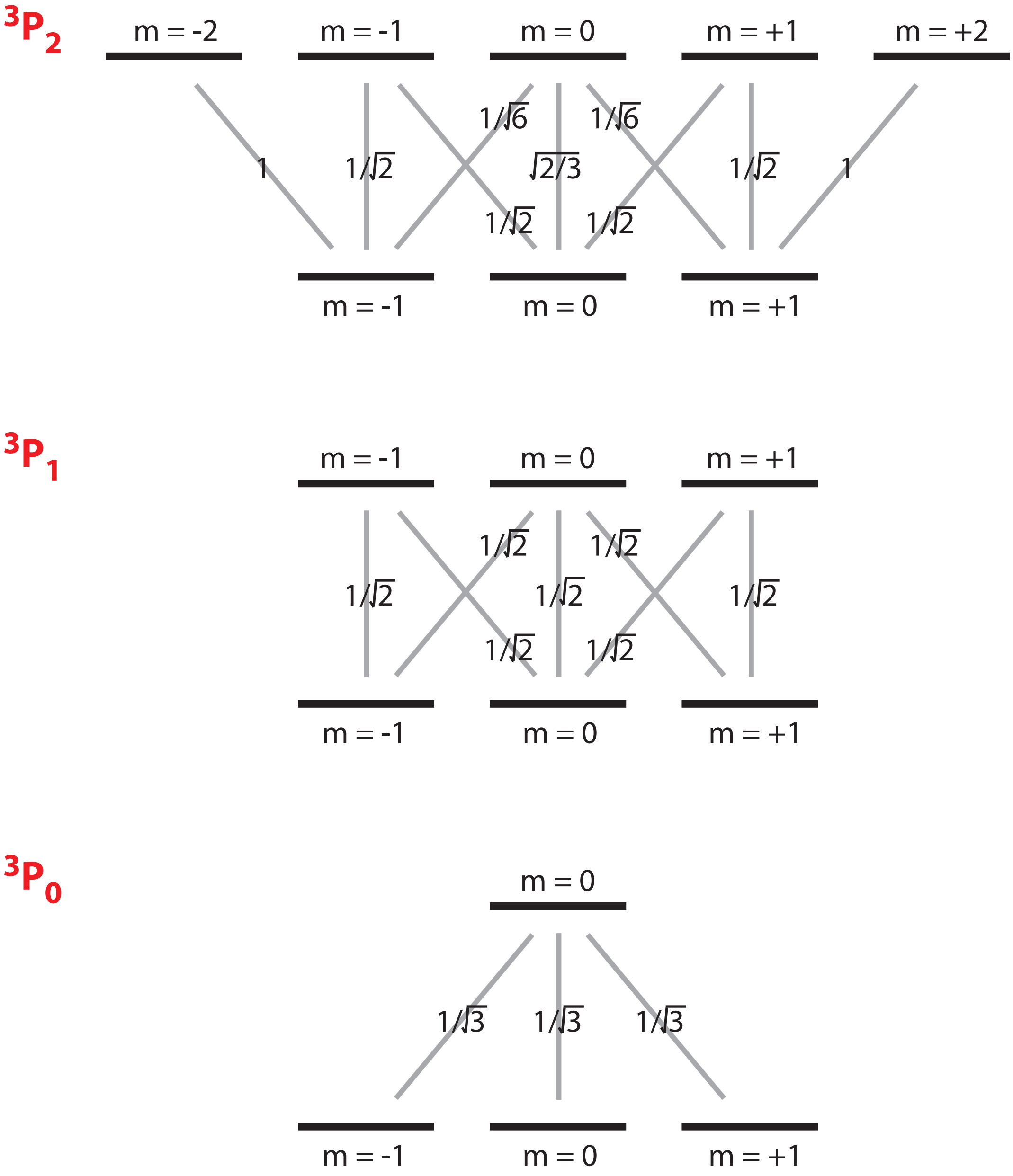

Figure A.1: Clebsch-Gordan coefficients for the ^{4}He* $2^3S_1 \rightarrow 2^3P_J$ transitions.

Table A.1: Assorted ^{4}He* $2^3S_1 \rightarrow 2^3P_J$ transition information.

Property	Symbol	Unit	Value
Vacuum wavelength	λ_o	nm	1083.33[1]
Atomic mass	m	amu	4.0026
Natural linewidth	$\Gamma/2\pi$	MHz	1.63[1]
Saturation intensity	I_{sat}	μW/cm^2	167
Recoil velocity	v_{rec}	cm/s	9.2

unpolarized, so each line gives rise to a cross section of the form

$$\sigma(\omega, \Gamma, \Delta) = \frac{\lambda_o}{2\pi} \frac{d_e}{d_g} f(\omega, \Gamma, \Delta), \tag{A.1}$$

where d_e and d_g are degeneracies of the excited and ground states [87], and $f(\omega, \Gamma, \Delta)$ is a lineshape profile. Most generally $f(\omega, \Gamma, \Delta)$ depends on a Lorentzian FWHM Γ and a Gaussian FWHM Δ , where Γ is usually dominated by the transition natural linewidth[2] and Δ by the Doppler width. In this case for a transition centered at ω_o the Gaussian width is

$$\Delta = \frac{\omega_o}{c} \sqrt{8 k_B T \ln(2)/m}, \tag{A.2}$$

and we find that $f(\omega, \Gamma, \Delta)$ is given by a convolution of Lorentzian and Gaussian components [123, §3.2]:

$$f(\omega, \Gamma, \Delta) = \frac{(\Gamma/2)^2}{\Delta\sqrt{\pi/4\ln(2)}} \int_{-\infty}^{\infty} \frac{\mathrm{Exp}[-\frac{4\ln(2)(\omega_o - \omega')^2}{\Delta^2}]}{(\omega - \omega')^2 + (\Gamma/2)^2}\, d\omega' \tag{A.3}$$

where the convolution accounts for the fact that for individual velocity classes of atoms at Doppler shift ω' the absorption will be broadened by the natural linewidth Γ. This lineshape is known as a Voigt profile, and is shown in figure A.2 for the case of $\Gamma = 10$ MHz and $\Delta = 30$ MHz.

---

[1] Data from [159].

[2] Pressure broadening also contributes to the Lorentzian width, but is generally negligible for strong transitions and buffer-gas densities used in cryogenic trapping experiments [123, §3.3].

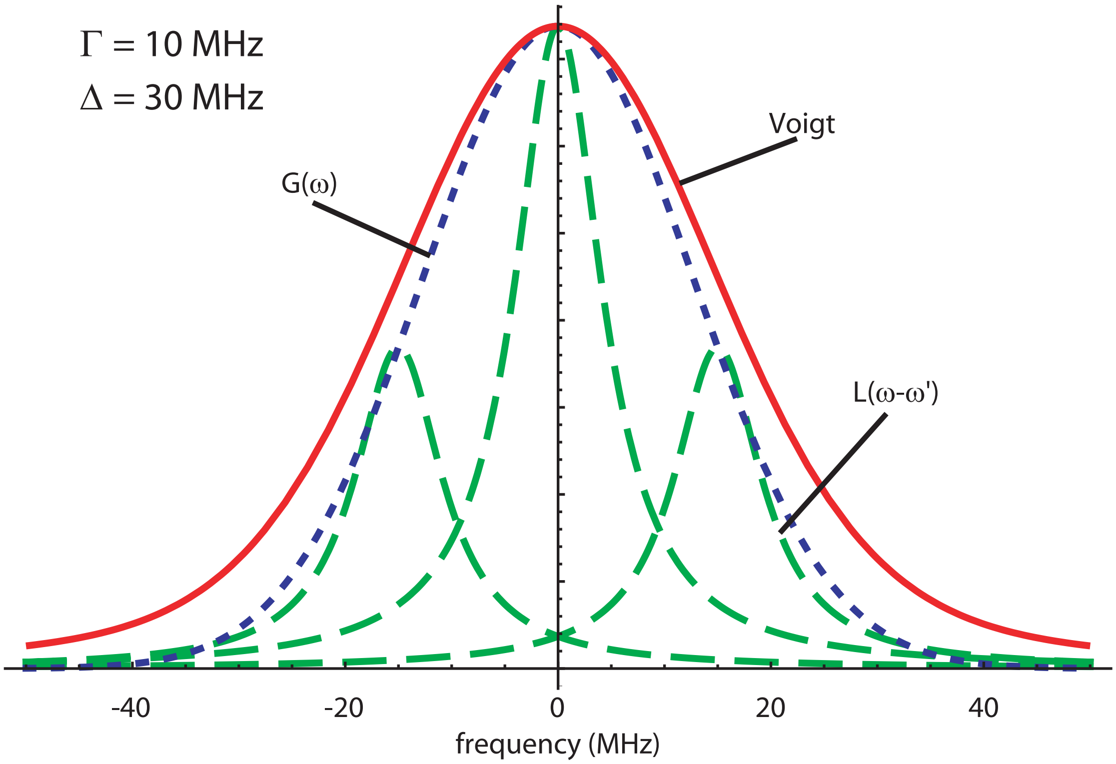

Figure A.2: A Voigt profile for $\Gamma = 10$ MHz and $\Delta = 30$ MHz. Example Lorentzian profiles and their Gaussian envelope are also shown for comparison.

This integral does not have a simple analytic closed form, hence computation of Voigt profiles must be performed numerically. For some situations one can utilize the limiting behavior of $f(\omega, \Gamma, \Delta)$ to simplify calcuations, treating either the Lorentzian or Gaussian components as a δ function. For example, at low T the Doppler width is negligible, and

$$f(\omega, \Gamma, \Delta) \approx \frac{(\Gamma/2)^2}{(\omega - \omega_o)^2 + (\Gamma/2)^2}, \tag{A.4}$$

and at high T the lineshape assumes a Gaussian profile:

$$f(\omega, \Gamma, \Delta) \approx \frac{\mathrm{Exp}[-\frac{4\ln(2)(\omega-\omega_o)^2}{\Delta^2}]}{\Delta\sqrt{\pi/4\ln(2)}}. \tag{A.5}$$

For ^{4}He*, these limits are for temperatures $T \lesssim 10\ \mu$K and $T \gtrsim 25$ mK, thus it is reasonable to use the high T limit for typical zero-field spectra at a ~ 1 K temperatures. For most atoms, however, larger masses and natural linewidths mean that zero-field spectra must be simulated and fit using the full convolution integral. Figure A.3 shows Lorentzian, Gaussian, and Voigt profiles of equal FWHM and integrated areas for comparison purposes.

Fortunately, simulation of the Voigt profile can be straightforward if one has access to appropriate special functions. Take the generalized form of the Voigt profile to be

$$K(x, y) = \frac{y^2}{a\sqrt{\pi}} \int_{-\infty}^{\infty} \frac{\mathrm{Exp}[-(\frac{t}{a})^2]}{y^2 + (x - t)^2}\, dt. \tag{A.6}$$

It has been shown that if one defines a complex number z such that

$$z = x + iy, \tag{A.7}$$

then the complex error function of z, $W(z)$, can be written in terms of the $K(x, y)$ and an additional function $Q(x, y)$ that is not of interest here [160–162]:

$$W(z) = \mathrm{Exp}[-z^2]\mathrm{Erfc}[-iz] = K(x, y) + iQ(x, y). \tag{A.8}$$

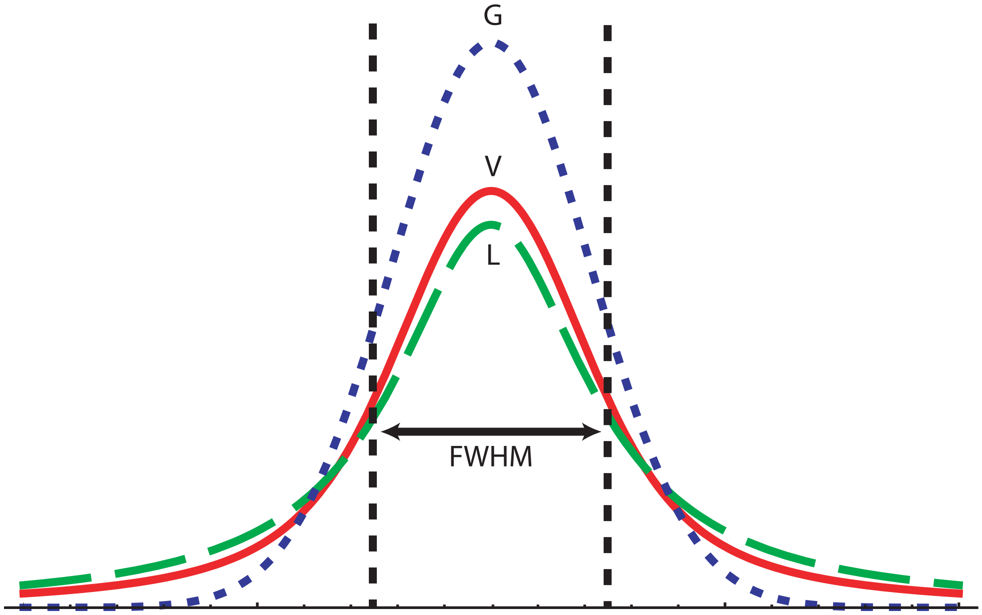

Figure A.3: Lorentzian (L), Gaussian (G), and Voigt (V) lineshapes. Each has the same FWHM, and is normalized to the same integrated area. For the Voigt profile $\Gamma = \Delta = \mathrm{FWHM}_{\mathrm{L,G}}/1.64$.

Making the change of variables

$$x = 2\sqrt{\ln(2)} \times \frac{(\omega - \omega_o)}{\Delta}, \qquad\qquad y = 2\sqrt{\ln(2)} \times \frac{\Gamma/2}{\Delta}, \tag{A.9}$$

we can define our specific Voigt profile with Lorentzian and Gaussian widths in terms of $W(z)$ as

$$f(\omega, \Gamma, \Delta) = \mathrm{Re}[W(z)]. \tag{A.10}$$

Since the complementary error function, Erfc$[z]$, is defined in *Mathematica* and *MATLAB*, this makes simulation and fitting of Voigt profiles a simple exercise. Figure A.4 shows a simulated spectrum of ^{4}He* at 300 K, as one might expect to see in a room temperature RF discharge cell like that described in appendix C. Since the ^{4}He* lines are well resolved even at room temperature, colder spectra look very similar but with narrower lines.

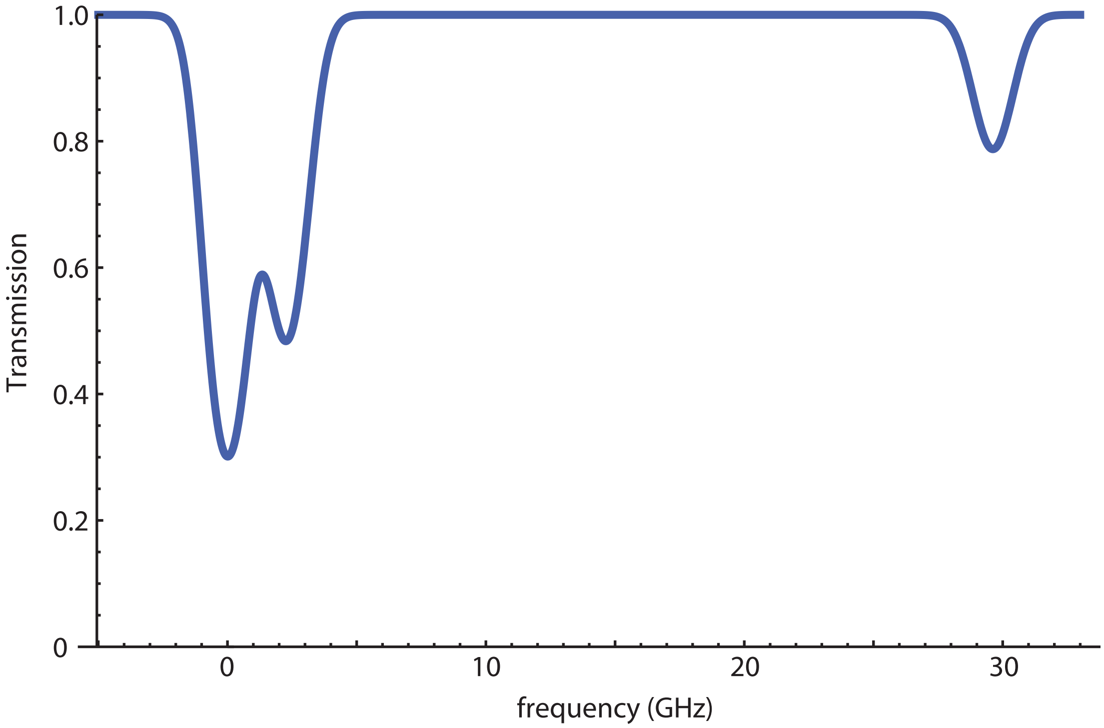

Figure A.4: A 300 K ^{4}He* zero-field spectrum simulated using the method described in appendix A.1.

A.2 Spectrum simulation in a magnetic field

The presence of a magnetic field adds complexity to simulating the ^{4}He* spectrum in the form of an additional spatially dependent Zeeman shift to the energy levels in both the ground and excited states,

$$\mathcal{H}(B) = \mathcal{H}_o + \mathcal{H}_Z(B) \tag{A.11}$$

where $\mathcal{H}_o$ is the field-free Hamiltonian and $\mathcal{H}_Z(B)$ is the Zeeman term. In small magnetic fields this is straightforward; the contribution from the Zeeman term is small compared to the fine-structure (part of $\mathcal{H}_o$; see [33, 90]), so j is a good quantum number, and the Zeeman term may be written as

$$\mathcal{H}_Z(B) = g_j \mu_B \vec{B} \cdot \vec{\mathbf{J}} \tag{A.12}$$

$$g_j = 1 + \frac{j(j+1) - l(l+1) + s(s+1)}{2j(j+1)}. \tag{A.13}$$

In this case $\vec{J}$ tends to precess about $\vec{B}$, so $\vec{B} \cdot \vec{\mathbf{J}} = m_J B$.

Since the strength of the Zeeman interaction is proportional to B, however, at larger fields it can become comparable to (or larger than) the fine-structure interaction, and levels of different j are mixed (The Paschen-Back effect). For many atoms this does not occur in reasonable laboratory fields due to large fine-structure splittings. In ^{4}He* this is the case for the well isolated ground $2^3\mathrm{S}_1$ state, but the excited $2^3\mathrm{P}_J$ states are close enough to one another to be mixed. In particular, the small 2.29 GHz $2^3\mathrm{P}_2 - 2^3\mathrm{P}_1$ leads to mixing at fields of only a few hundred Gauss, as in figure A.5; however, all three states are mixed when the anti-Helmholtz trap is fully energized. In this case the Zeeman term is most easily included by writing the Hamiltonian in the $|l m_l s m_s\rangle$ basis, rewriting the $|j m_j\rangle$ states in terms of Clebsch-Gordan

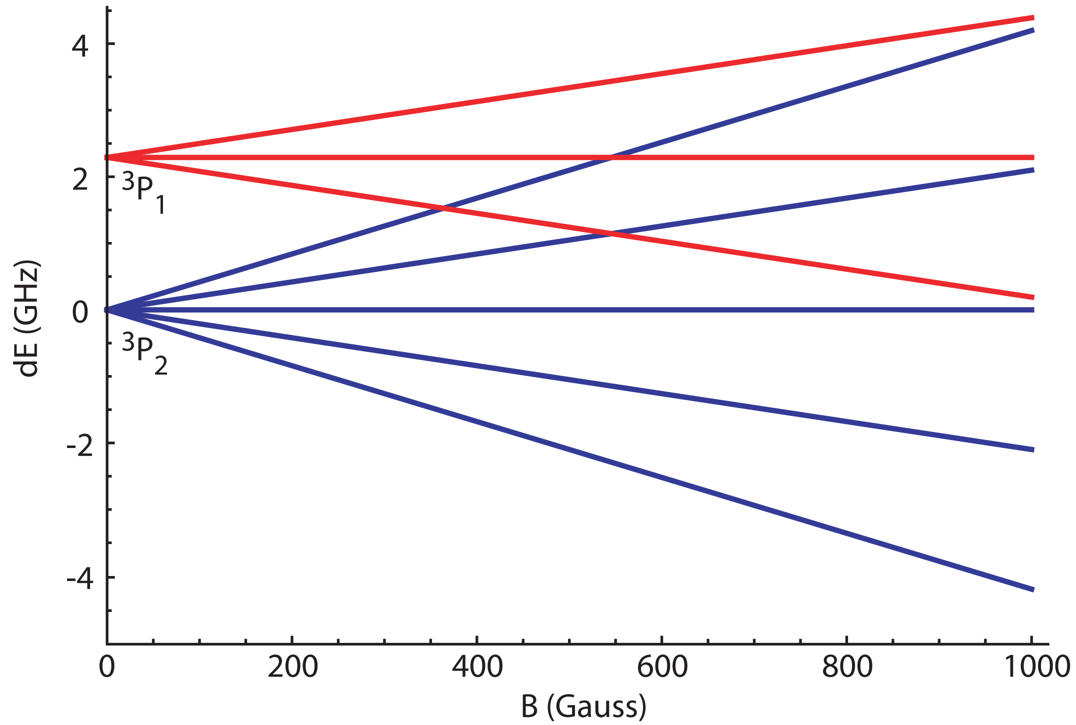

Figure A.5: Zeeman shifts of the 2^3P_2 and 2^3P_1 lines in $^4He^*$, neglecting Paschen-Back effect mixing.

coefficients as

$$|jm_j\rangle = \sum_{m_l,m_s} a_{jm_jm_lm_s}|lm_lsm_s\rangle. \tag{A.14}$$

For some atoms (e.g. H and Li) writing the $\mathcal{H}_{fs}$ in the $|lm_lsm_s\rangle$ is fairly straightforward, as one can write

$$\mathcal{H}_{fs} = f\vec{\mathbf{L}}\cdot\vec{\mathbf{S}}. \tag{A.15}$$

Unfortunately, this Hamiltonian does a very poor job of reproducing the ^{4}He* fine structure, producing a ratio of 2 for the ^{3}P$_2$-^{3}P$_1$ to ^{3}P$_1$-^{3}P$_0$ splittings rather than the observed ratio of nearly 13, perhaps due to spin-spin coupling between the two electrons. Rather than adding a term to the Hamiltonian based on a first-principles understanding, however, we instead build a "custom" term for the Hamiltonian based on the known splittings. This is done by setting the f in equation A.15 to reproduce one of the splittings (the ^{3}P$_2$ - ^{3}P$_1$ splitting was arbitrarily selected, so $f = -\frac{h}{2}\cdot$ 2.29 GHz) and then adding additional terms as needed to offset the ^{3}P$_0$ state energy appropriately.

Determining this additional term for the Hamiltonian is not too difficult. With the $j = 2, 1$ states taken care of we can build $\mathcal{H}'_{fs}$ following [90, §A.1] subject to the constraints that

1. $\mathcal{H}'_{fs}$ is Hermitian.
2. $\langle jm_j|\mathcal{H}'_{fs}|jm_j\rangle = E_{offset}$ for $j = 0$; $= 0$ for $j = 2, 1$ with $|jm_j\rangle$ converted to the $|m_lm_s\rangle$ basis.
3. $\mathcal{H}'_{fs}$ commutes with $\mathbf{J}^2, \mathbf{J}_z$.

Since we write the ^{3}P$_0$ state as

$$|2,0\rangle = \frac{1}{\sqrt{3}}|1,-1\rangle - \frac{1}{\sqrt{3}}|0,0\rangle + \frac{1}{\sqrt{3}}|-1,1\rangle, \tag{A.16}$$

applying constraint (1) gives us a Hamiltonian with six unknowns. Applying constraints (2) and (3) yields a system of equations with which we can solve for $\mathcal{H'}_{fs}$. Definining a basis of the form $|m_l m_s\rangle = |1,1\rangle, |1,0\rangle, \ldots |-,-1\rangle$ and solving the equations we find that

$$\mathcal{H'}_{fs} = \begin{pmatrix} 0 & 0 & 0 & 0 & 0 & 0 & 0 & 0 & 0 \\ 0 & 0 & 0 & 0 & 0 & 0 & 0 & 0 & 0 \\ 0 & 0 & A & 0 & B & 0 & A & 0 & 0 \\ 0 & 0 & 0 & 0 & 0 & 0 & 0 & 0 & 0 \\ 0 & 0 & B & 0 & A & 0 & B & 0 & 0 \\ 0 & 0 & 0 & 0 & 0 & 0 & 0 & 0 & 0 \\ 0 & 0 & A & 0 & B & 0 & A & 0 & 0 \\ 0 & 0 & 0 & 0 & 0 & 0 & 0 & 0 & 0 \\ 0 & 0 & 0 & 0 & 0 & 0 & 0 & 0 & 0 \end{pmatrix}, \tag{A.17}$$

where $A = -B = E_{offset}/3$ and $E_{offset} = h \cdot 28.47$ GHz.

After adding this term to the Hamiltonian, the ^{4}He* level structure and spectra can be simulated for any magnetic field configuration by integrating the absorption along the probe laser's path. Simulations are performed using the *MATLAB* code described in Nathaniel Brahm's thesis [90, §A]. The results of the simulation for the magnetic field dependence of the ground and excited state levels are shown in figure A.6.

A.3 Absorption image simulation in small fields

In addition to simulating the spectrum of ^{4}He* as detected in absorption spectroscopy, it is also useful to simulate the absorption images we detect in both the anti-Helmholtlz and QUIC trapping fields. In this case we simulate the absorption

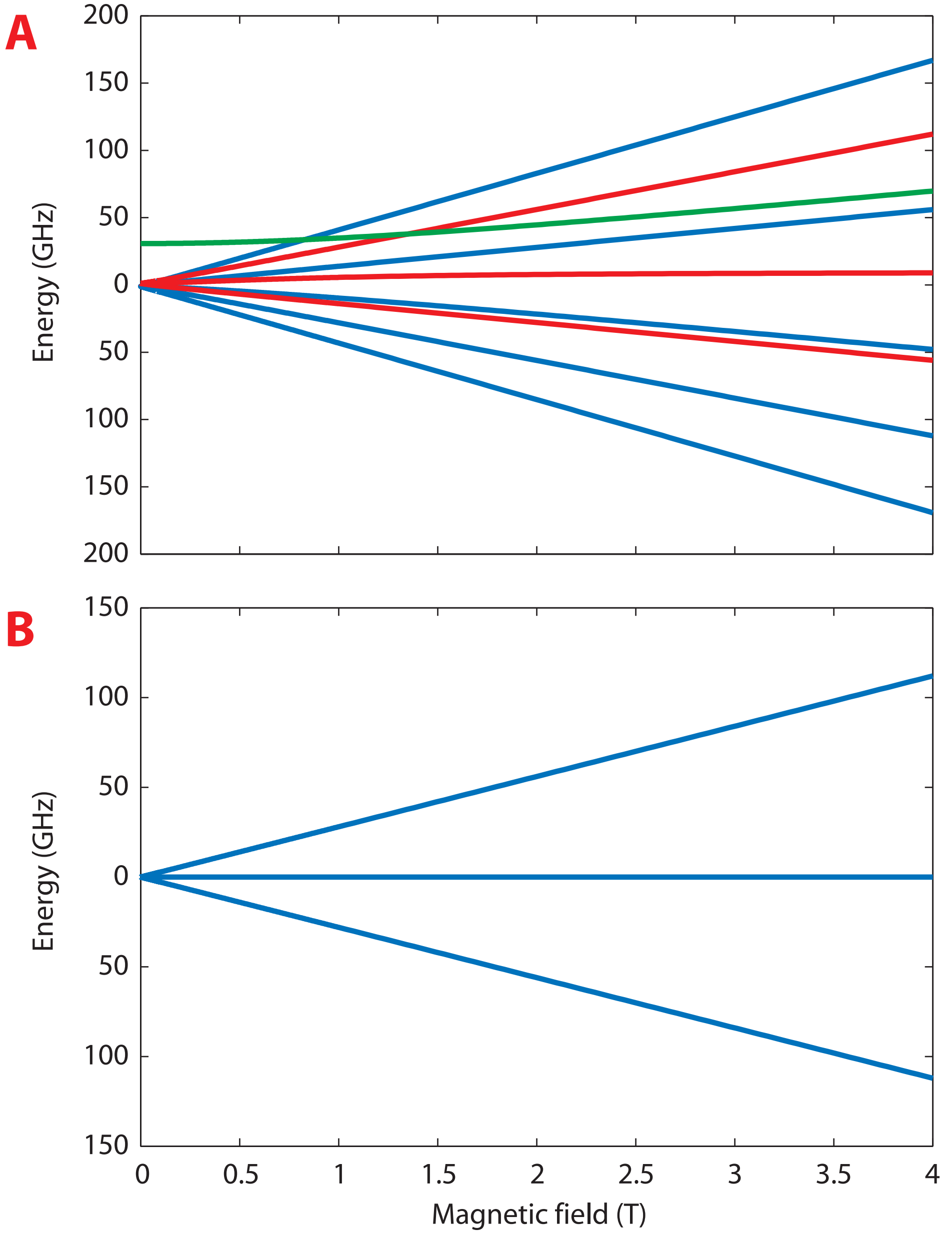

Figure A.6: The Zeeman structure of ^{4}He* for the 2^3P_J (A) and 2^3S_1 (B) states. In (A) states identified as $j = 0, 1, 2$ at low field are identified in green, red, and blue, respectively. At high field the good basis is $|m_l, m_s\rangle$ and the states are (from high to low energy): $|1,1\rangle, |0,1\rangle, |-1,1\rangle, |1,0\rangle, |0,0\rangle, |1,-1\rangle, |-1,0\rangle, |0,-1\rangle, |-1,-1\rangle$. In (B) the states are defined entirely by m_S, with $m_S = 1, 0, -1$ from high to low energy.

as a function of spatial position at fixed frequency rather than integrating over the polarization factor and spatial coordinates within the laser beam. While determining atom number and density from single images is difficult unless the atoms are sufficiently cold that the linewidth is dominated by Γ_{nat}, these quantities can be used by comparing images of the same cloud at several different laser frequencies with corresponding simulations. Since we use absorption imaging to probe the atoms primarily at low temperatures, the atoms do not experience magnetic fields large enough to mix states of different j. As such j remains a good quantum number and we can simulate the absorption using the $|jm_j\rangle$ basis. Combined with the fact that we need consider only a single laser frequency this makes the calculation much more straightforward than that for an entire spectrum.

Defining the laser propagation direction to be along $\hat{z}$, we can write the transmission $\mathcal{T}$ at a single (x, y) coordinate in the probe beam as

$$\mathcal{T}(x, y, T) = 1 - e^{-OD(x,y,T)} \tag{A.18}$$

where $OD(x, y, T)$ is the optical density, also a function of the atom temperature T. In this case the optical density is defined as

$$\begin{aligned} OD(x, y, T) = \sigma_o C_m \int_{-\infty}^{\infty} C_p(x, y, z)\, n(x, y, z, T) \times \\ \times f(\omega - \omega_{res}, \Gamma, \Delta(T))\, dz. \end{aligned} \tag{A.19}$$

Here $\sigma_o = 3\lambda^2/(2\pi)$ is the resonant absorption cross section and C_m is the Clebsch-Gordan coefficient for the particular transition being excited, neither of which depend on the magnetic field configuration. $C_p, n,$ and f are the polarization factor, atomic density, and lineshape function, each of which does depend on the magnetic field.

C_p arises directly from the matrix element $\left|\langle e|\vec{\mathbf{E}} \cdot \vec{\mathbf{r}}|g\rangle\right|^2$ that is present in formula for atomic transition rates [90, 123]. For a $\Delta m = 0$ transition this dot product is proportional to $(\hat{\mathbf{E}} \cdot \hat{\mathbf{J}})^2$, while for the $\Delta m = +1$ transitions in which we are most interested it scales as $1 - (\hat{\mathbf{E}} \cdot \hat{\mathbf{J}})^2$. Since in low fields where j is a good quantum number the atom precesses about the local magnetic field, we can replace $\hat{\mathbf{J}}$ with $\hat{B}(x, y, z)$. If we define the (linearly polarized) probe laser as $\vec{E} = E_o \hat{x}$, then we can define C_p entirely in terms of magnetic field components as

$$C_p = 1 - \left(\frac{B_x(x, y, z)}{B(x, y, z)} \right)^2 . \tag{A.20}$$

$n(x, y, z, T)$ and $f(\omega - \omega_{res}, \Gamma, \Delta)$ are also easily defined in terms of $B(x, y, z)$, where n is simply a spatial Boltzmann distribution, and f the Voigt function (see section A.1) with ω_{res} a field-dependent center frequency,

$$\omega_{res} = \omega_o + \frac{\Delta\mu \, B(x, y, z)}{\hbar}, \tag{A.21}$$

where $\Delta\mu$ is the difference between $g_J \, m_J$ of the excited and ground states. In this case we are ignoring the influence of the atoms' optical activity on the polarization of the probe laser as it propagates through the atom cloud. This can be an important effect (see [112, §3.5]), but it did not significantly influence our images, probably due to the relatively low optical depths present. However, these effects could be included by making $\vec{E}$ a function of z with an amplitude and direction that varied as the laser passed through the cloud.

To generate an image, one simply calculates the optical density for an array of (x, y) points, tabulating the results from equation A.19. Inserting the results into equation A.18 gives transmission values that can be color-mapped to form an image using functions like *Mathematica's* `ListDensityPlot[]` or *MATLAB's* `pcolor()`, as in figure A.7.

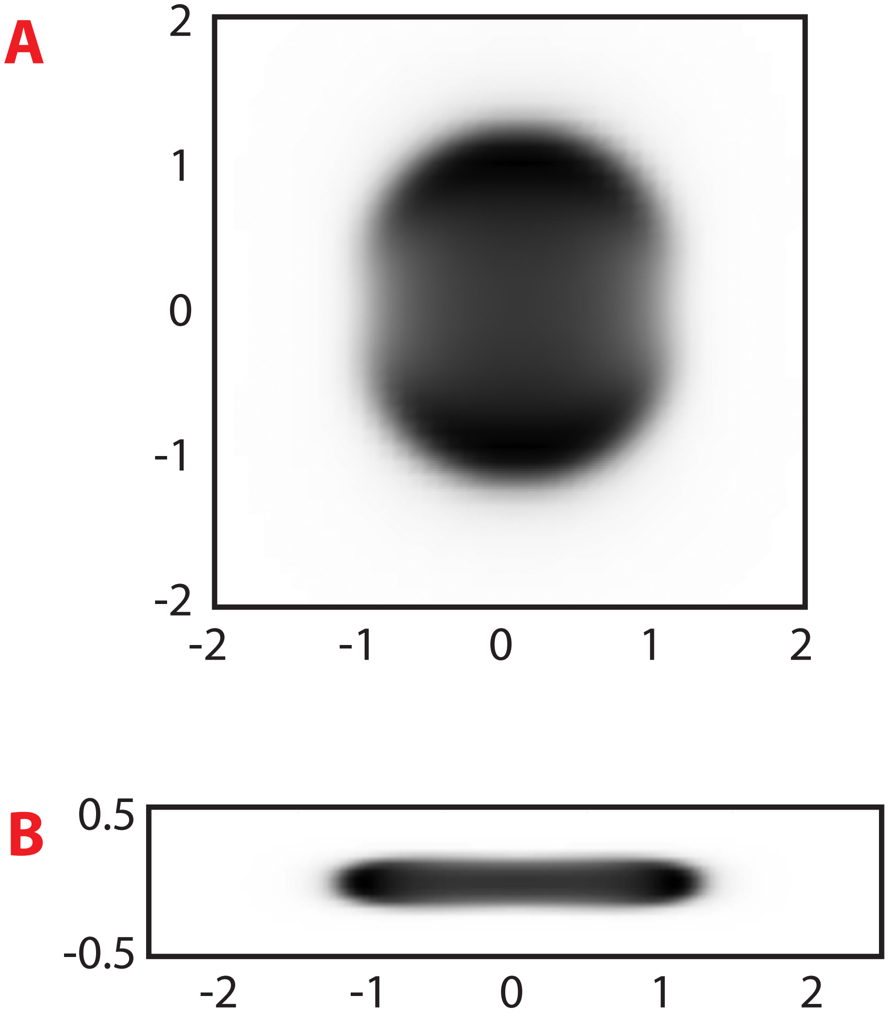

Figure A.7: Simulated absorption images excited on the $2^3S_1 \rightarrow 2^3P_2$ $\Delta m = +1$ transition. Dimensions in mm. (A) 10^8 atoms in a 10/3 A anti-Helmholtz field at 2 mK and 20 MHz detuning. The lineshape function and density profile give rise to a resonant shell of absorption, which causes to crescent shaped absorption when convoluted with the polarization factor. Probe laser is polarized along the horizontal direction, and peak absorption is 65%. (B) 10^7 atoms in the QUIC trap at 550 μK, detuned 7 MHz above the trap minimum. The bias field is oriented along the horizontal direction, while the laser is polarized along the vertical direction. Peak absorption is 55%.

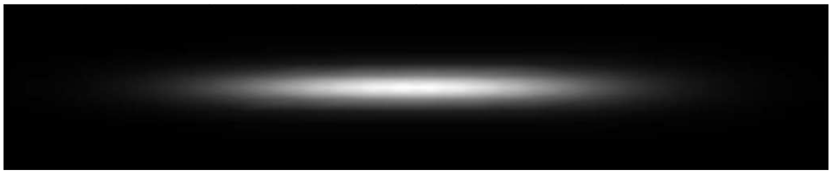

Figure A.8: A simulated phase-contrast image of 5×10^6 atoms at 100 μK with a laser detuning of 60 MHz. Peak signal is $4.8 I_o$, and field of view is 2 mm by 0.4 mm.

A.4 Phase-contrast image simulation

A complete simulation of phase-contrast images for a wide array of probe laser detunings, temperatures, and fields would be similar to the simulation of absorption images since the t^2 in equation 5.17 is the same as $\mathcal{T}$ from equation A.18 above. However, since we are principally interested in phase-contrast images of atoms after they have been evaporatively cooled with the RF-knife and have large optical densities, we can select detunings such that the $t \approx 1$, and thus ignore the effects of absorption. This allows us to drop the polarization factor C_p since for atoms at low temperatures the magnetic field in the QUIC trap is dominated by the bias field and essentially unidirectional, $\vec{B} = B_o \, \hat{z}$. Calculations are thus reduced to combining equation 5.14 with equation 5.17 for the case that $t = 1$ and numerically integrating the atom density along the laser propagation direction, producing images similar to that in figure A.8.

Appendix B

Radio-frequency evaporation and Landau-Zener transitions

Radio frequency evaporation can be understood in terms of a mixing between Zeeman sublevels of the ^{4}He* ^{3}S$_1$ ground state. Application of RF magnetic fields creates a resonant shell in which atoms can be adiabatically transferred to the $m_S = 0, -1$ states, allowing them to be lost from the trap. Calculating the transition probability requires the use of the Landau-Zener transition formalism [163], which has been worked out for RF evaporation with an arbitrary number of levels by Vitanov and Suominen [164]. We follow their treatment here for the case of three levels, as in ^{4}He*, with additional information added for clarification as necessary.

The atoms' magnetic moment can be written as

$$\vec{\mu} = \frac{e}{m_e c}\vec{\mathbf{S}}, \tag{B.1}$$

which in general couples strongly to the local magnetic field, such that $\hat{\mathbf{S}} = \hat{B}$; define $\hat{B} = \hat{z}$. As discussed in appendix A, the Zeeman shifts of the ^{3}S$_1$ magnetic sublevels are linear and proportional to the static trapping field, so we can write

$$\mathcal{H}_o = \begin{pmatrix} 2\mu_B B & 0 & 0 \\ 0 & 0 & 0 \\ 0 & 0 & -2\mu_B B \end{pmatrix}, \tag{B.2}$$

where B is the trapping field and is a function of the spatial coordinates. The atoms are also coupled to the applied RF field $\vec{B}_{RF} = B_{RF}\cos(\omega_{RF}t)\,\hat{e}_{RF}$ via their magnetic moment $\vec{\mu}$,

$$\mathcal{H}_{RF} = -\vec{\mu}\cdot\vec{B}_{RF}\cos(\omega_{RF}t), \tag{B.3}$$

giving rise to a total Hamiltonian $\mathcal{H} = \mathcal{H}_o + \mathcal{H}_{RF}$. If we want to induce a coupling between adjacent Zeeman sublevels, it is clear that we must couple to $\mathbf{S}_x$ and/or $\mathbf{S}_y$, hence our RF field must have components which are perpendicular to the local trapping field; classically this is can be thought of in terms of applying a torque to $\vec{\mu}$.

For RF evaporation in an Ioffe-Pritchard trap, then, the natural choice for the RF field is along the $\hat{\rho}$ direction. Defining that direction to be the $\hat{x}$ direction, we find that our coupling may be written as

$$\mathcal{H}_{RF} = \begin{pmatrix} 0 & \sqrt{2}\hbar\Omega(t) & 0 \\ \sqrt{2}\hbar\Omega(t) & 0 & \sqrt{2}\hbar\Omega(t) \\ 0 & \sqrt{2}\hbar\Omega(t) & 0 \end{pmatrix}, \tag{B.4}$$

where $\hbar\Omega(t) = \mu_B B_{RF}\cos(\omega_{RF}t)$. With this representation eigenstates and eigenenergies for $\mathcal{H}$ are easily found, as in figure B.1. From the figure it is quite clear how an atom can be lost from the trap as its state adiabatically morphs from trapped to anti-trapped.

In [164] it is shown that following a traversal of the RF resonance the probability of an atom being in each of the three sublevels (assuming it started in the $m_S = +1$

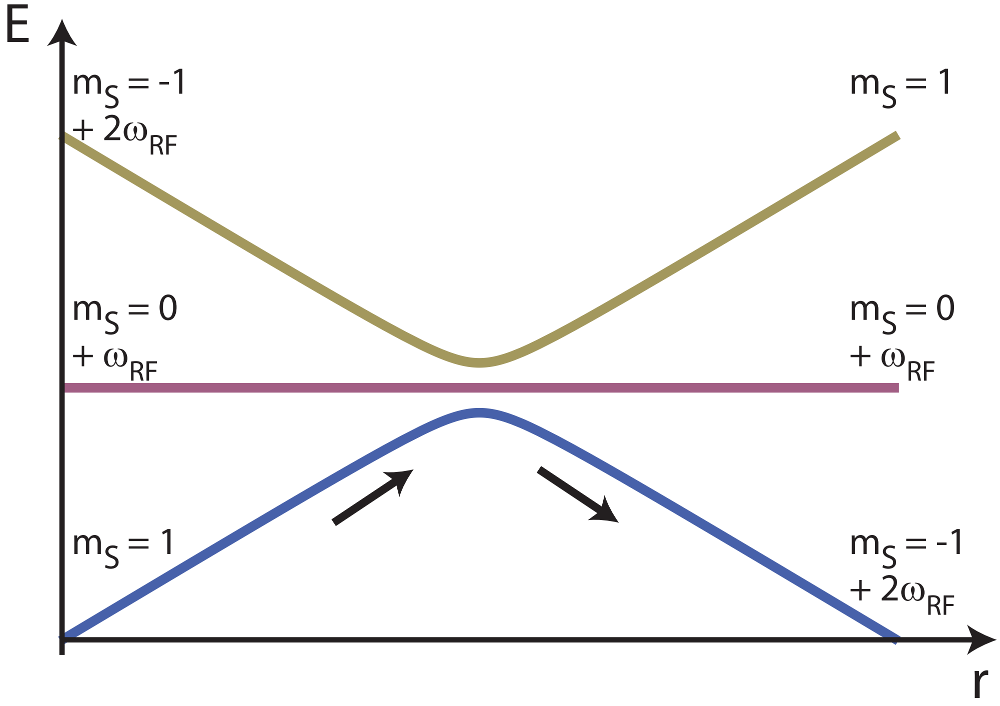

Figure B.1: A pictorial description of trap dynamics during RF evaporation. Atoms which are trapped in the $m_S = 1$ Zeeman sublevel can be adiabatically transferred to the $m_S = -1$ sublevel as they orbit through the region of the trap where the applied RF field is resonant, as indicated by the arrows.

state) is

$$\begin{aligned} P_{m_S=+1} &= (1-p)^2 \\ P_{m_S=0} &= 2p(1-p) \\ P_{m_S=-1} &= p^2, \end{aligned} \tag{B.5}$$

where p is the two-state transition probability given by

$$p = 1 - \mathrm{Exp}\left(-\frac{2\pi\Omega^2}{\dot{\Delta}}\right). \tag{B.6}$$

Here Ω is the Rabi frequency defined above, while $\dot{\Delta}$ is the time derivative of the detuning of an atom's Larmour frequency from the applied RF field as it orbits the trap. We can use this formula to arrive at an estimate for the RF field needed for maximally efficient evaporation by making some assumptions about the atoms' orbits. Since the RF transitions are narrow, the atoms will be in resonance for only a small region of magnetic field, hence we can assume that the fields vary linearly. As such we can write

$$\dot{\Delta} = 2\frac{\mu_B}{\hbar}\frac{dB_\rho}{d\rho}v \tag{B.7}$$

where $v = \sqrt{8k_BT/\pi m}$ is a typical thermal velocity. Ideally an atom would have a large chance of being successfully ejected in a single pass through the resonance, $(1 - P_{m_S=+1}) \gtrsim .5$. This is most difficult at our starting point for evaporation, when the trap gradient is steep and the atoms are moving quickly. For $\frac{dB_\rho}{d\rho} = 500$ G/cm and $T = 500\ \mu$K we find $B_{RF} \approx 30$ mG. However, a more relaxed constraint is that an atom be ejected within one collision time, during which it may traverse the resonance region many times. For a linear potential the atom passes through the resonance region once every quarter period,

$$\frac{t_{osc}}{4} = \frac{\sqrt{8k_BT/\pi m}}{2\mu_B\frac{dB_\rho}{d\rho}/m}. \tag{B.8}$$

Comparing this with the collision rate for a density of 1×10^{11} cm^{-3} indicates the atoms pass through the resonance approximately 30 times per collision, relaxing the RF field amplitude requirement to about 5 mG.

Appendix C

Frequency stabilization of the ^{4}He* detection laser

Diode lasers have been a boon for atomic physics, providing inexpensive, robust, reliable, tunable sources of coherent light for applications in spectroscopy and imaging. However, typical frequency “jitter” of 1-10 MHz over millisecond timescales and longer term drifts of hundreds of MHz/hr (see figure C.1) are inadequte for imaging ultracold atoms. Frequency stability at or below the level of the transition natural linewidth (1-10 MHz for the strong transitions usually used for detection) is required to avoid faulty determinations of atom number or refractive effects resulting from unstable laser detunings.

Fortunately, this is a solved problem. Frequency stabilized lasers have long had applications throughout atomic physics for spectroscopy and precision measurement. Stabilization requires two key elements: a stable frequency reference and a method for providing feedback. Over the years many references have been developed, ranging from general, wavelength independent all-optical techniques [165] useful in the absence of a convenient atomic or molecular reference, to ultra-narrow, high-finesse

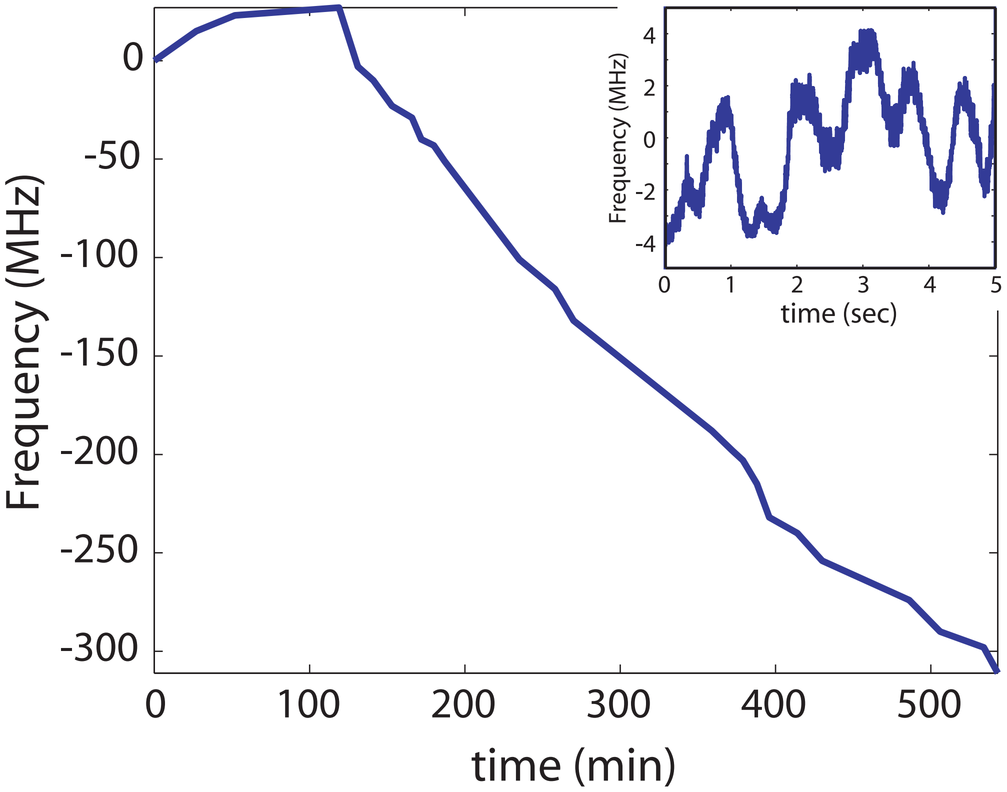

Figure C.1: Example frequency drift of 1083 nm diode laser prior to frequency stabilization.

optical cavities [166] used in stabilizing lasers for optical atomic clocks. For typical applications imaging ultracold atoms, however, a vapor cell of the atom itself probed using saturated absorption spectroscopy [167] often offers a suitable reference. This is especially true for the alkalis; since they have large vapor pressures at or near room temperature it is straightforward to create a reference with good signal-to-noise. After using such a reference to generate an error signal, frequency corrections are generated either via an acousto-optic modulator (AOM) or by feedback to the laser itself, usually via the current.

Saturated absorption spectroscopy is also a good choice for creating a ^{4}He* reference, particularly for the easily saturated 1083 nm transition. To stabilize our 1083 nm diode laser we used a room temperature RF discharge cell as a frequency reference and generated an error signal using a lock-in amplifier following the method described in [168]. This error signal is sent to a home-built PID circuit[1] which creates a correction signal for feedback via the diode laser's current controller.

C.1 Saturated absorption reference cell

The saturated absorption cell is constructed out of a Conflat vacuum assembly featuring a glass bulb approximately 1" diameter by 6" length (figure C.2). The bulb is wrapped with approximately 10 turns of bare 16 AWG copper wire to form an RF discharge coil. The coil is tapped near each end and driven with a 50 W ENI 550L ampflifier [122] sourced by an HP 8647A RF synthesizer [129]. To ignite a discharge we fill the cell with 200 mTorr of 99.999 % pure ^{4}He and drive the coil with $\sim$ 10 W at approximately 100 MHz. Usually it is necessary to initiate the discharge with a

---

[1] Based on a design by Jim MacArthur; see appendix E.

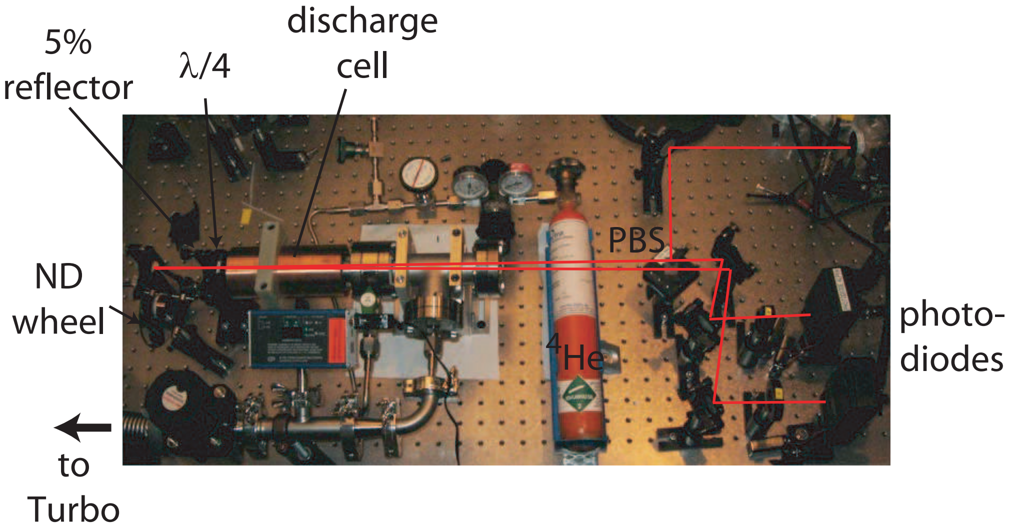

Figure C.2: RF discharge set-up for saturated absorption frequency reference. The laser enters from the upper left, is retroreflected through the cell, and collected on photodiodes in the lower right. The glass bulb of the discharge cell is hidden by the copper ground-plane that surrounds it.

spark to the glass bulb from a high-voltage piezo-electric "gun," but after this the discharge is self-sustaining. ^{4}He* density in the cell can then be varied by modifying the applied RF power and ^{4}He pressure.

^{4}He* density is also strongly dependent on the cleanliness of the discharge cell; the metastable density steadily declines with time if the cell is filled with a set pressure and sealed, presumably due to the discharge slowly etching impurities off of the glass. Methods to mitigate this problem by cleaning the cell through bakeouts [168] or etching with hydrofluoric acid exist, but instead we simply operate the cell with constant helium flow to clear away impurities. By connecting the cell to the ^{4}He bottle and a turbopump via valves and adjusting the valves appropriately we can set an arbitrary flow rate and cell pressure. Flow rates of less than 100 STP liters/month are adequate to keep the cell clean, so after finding suitable settings for the valves and RF discharge power we simply leave the discharge operating continuously.

C.2 Optics

The RF discharge cell is probed using the optical set-up shown in the upper-right quadrant of figure 3.9. A reference beam is created from a small fraction (1 or 2 mW) of the laser's output, split off using a polarizing beam splitter (PBS) and half-wave ($\lambda/2$) plate. This beam is double passed through an AOM [118] via a "cat's eye" retroreflector [169] to maintain beam alignment while tuning the AOM frequency shift, while a second PBS — $\lambda/2$-plate pair separates the input and double-passed beams[2]. After double passing the AOM the beam is collimated to 1 mm, now with a power of approximately 300 μW ($I/I_{sat} \approx 55$), and sent through the RF discharge cell via another PBS.

After passing through the cell and a quarter-wave ($\lambda/4$) plate the beam is retroreflected in two pieces. A glass wedge reflects $\sim 5\%$ of the intensity back through the $\lambda/4$ plate and the cell, directly along its original path. The remainder of the beam continues through a continuously variable neutral density wheel and then reflects off of a mirror and back through the optics and cell, misaligned from the original path. The $\lambda/4$ plate allows the retroreflected beams to be separated from the input beam via the PBS, and they are separately reflected onto photodiodes. Scanning them over the ^{4}He* transition yields spectra with and without Lamb dips, respectively, as in figure C.3. Care is taken to misalign the second beam only slightly so that the two spectra will be well matched outside of the Lamb dips.

---

[2] A second "compensation AOM" with an identical set-up shifts the frequency of the remainder of the laser's output to match, but is not involved in stabilization.

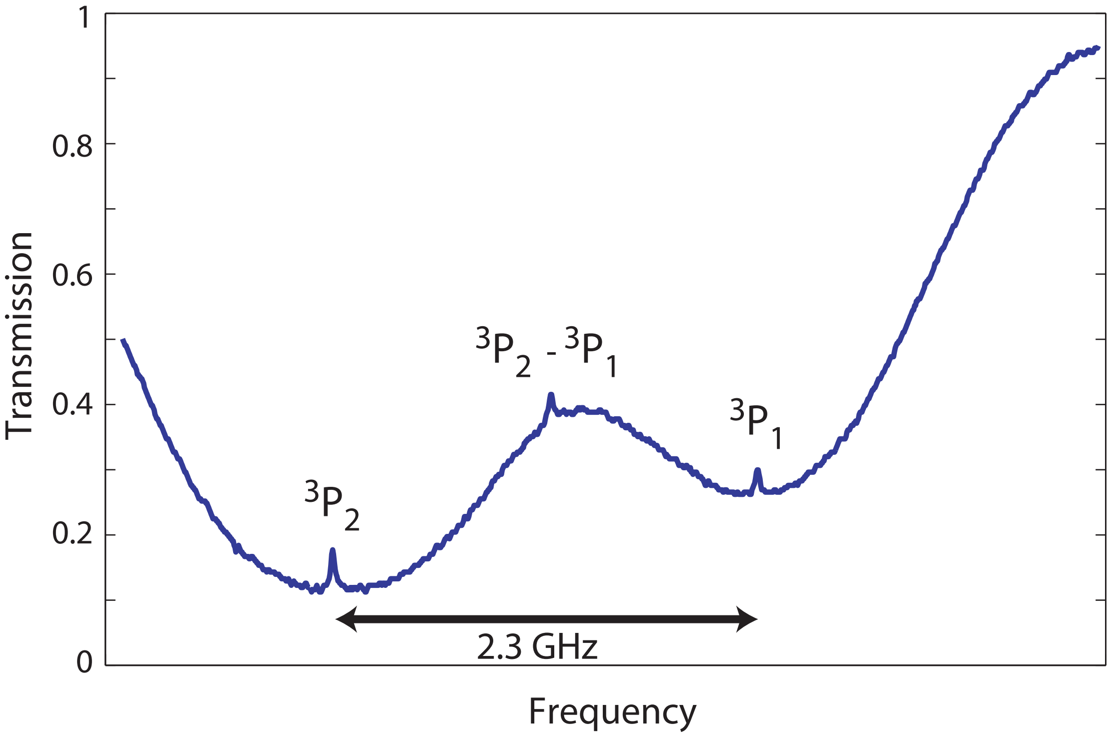

Figure C.3: Saturated absorption spectrum of ^{4}He*. ^{3}P$_2$ and ^{3}P$_1$ Lamb dips of reduced absorption occur where input and retroreflected beams address the identical $v = 0$ velocity class. The third ^{3}P$_2$ - ^{3}P$_1$ "crossover" dip occurs at the midpoint between the two transitions where the $v = v_o$ velocity class on one transition is optically pumped, reducing the ground state population available for excitation of the $v = -v_o$ class from the other transition (and vice versa). With a non-overlapping retroreflection the Doppler broadened spectrum is observed, without Lamb dips.

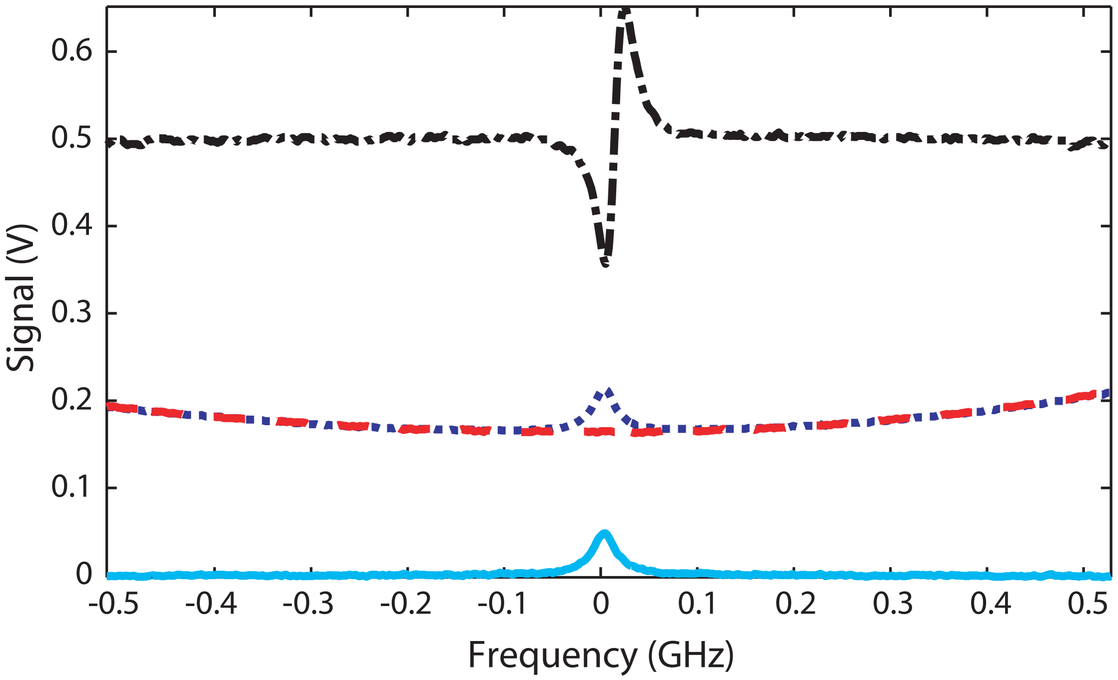

Figure C.4: Doppler-narrowed absorption spectrum and error signal used for laser locking. Curves are as follows: dashed — Doppler broadened $^3P_2$ line, dotted — $^3P_2$ with Doppler narrowed feature, solid — subtracted signal featuring only Doppler narrowed feature, dot-dashed — dispersively shaped error signal generated by lock-in amplifier.

C.3 Error and correction signal generation

By adjusting the neutral density wheel to match the size of the photodiode signals and subtracting the two spectra from one another a Doppler-narrowed spectrum may be generated. Dithering the AOM frequency (peak-to-peak modulation of 4 MHz, 20 kHz dither frequency) and then demodulating the subtracted signal at the dither frequency using a lock-in amplifier (SRS 830 [138]) yields a dispersively shaped error signal, as in figure C.4. This error signal is sent to a PID loop (derivative gain set to zero) which generates a correction signal to be added to the diode laser's current input. Due to noise and imperfect matching of the two Doppler broadened spectra the capture range of the error signal is only approximately ±100 MHz from the transition

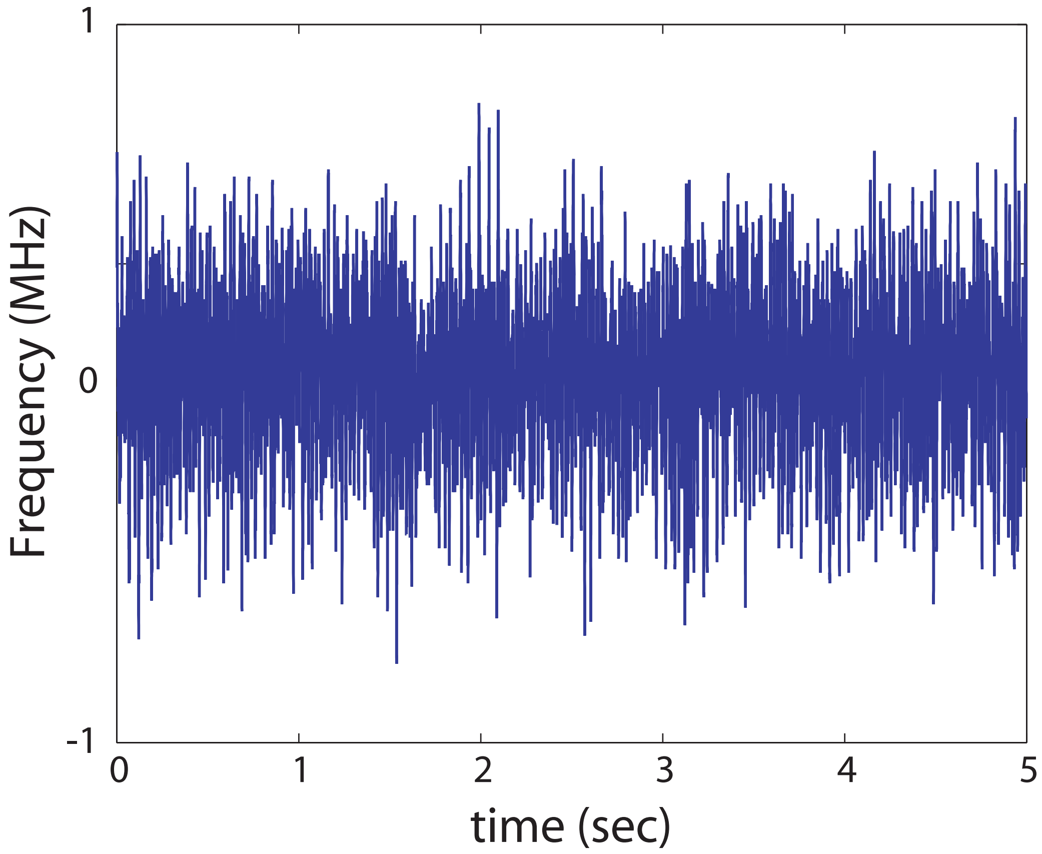

Figure C.5: Frequency noise on the stabilized diode laser. RMS noise is approximately 200 kHz with negligible long-term drift, to be compared to $\Gamma_{nat} = 1.6$ MHz.

center, so it is necessary to narrow in on the transition before activating the PID loop to ensure that the laser is locked to the main zero-crossing of the error signal. It was also necessary to add a “soft-on” feature to the PID circuit in the form of a variable voltage divider on the output to prevent an initial corrective “kick” from suddenly shifting the laser frequency outside of the capture range upon activating feedback.

C.4 Frequency lock performance

The performance of the frequency stabilized laser is shown in figure C.5. RMS noise is at the 200 kHz level, well below the 1.6 MHz natural linewidth and more than adequate for our purposes. The lock is extremely robust, maintaining the laser within this window indefinitely so long as temperature fluctuations in the lab are not so great ($>$ 1 C or so, causing long-term frequency drifts on the 400 MHz level) as to make the necessary correction signal larger than the maximum PID output signal. By monitoring the size of the correction signal and making occasional small corrections via the laser's piezo temperature fluctuations can also be tolerated. Larger drifts could also be followed directly by the PID at the expense of slightly poorer short-term stability by changing the gain.

It is worth noting that by modifying the center frequencies of the dither and compensation AOMs the portion of the laser sent to the experiment can be frequency stabilized to any value within approximately 100 MHz of the atomic line. These frequencies can be changed without compromising the lock, allowing for data collection at different precisely known detunings. 2x larger shifts are also possible by single passing or completely removing the compensation AOM. However, in single-passed configuration the beam is steered when the AOM frequency is shifted, so on-the-fly frequency shifts must be generated only by the dither AOM, reducing the dynamic range.

Appendix D

Cell vacuum and charcoal sorbs

High and ultra-high vacuum conditions are important for for a wide array of experiments in atomic physics. Unwanted background gas can scatter particles out of an atomic or molecular beam or cause losses from a trapped cloud. In typical room-temperature vacuum chambers the problem of background gas is dealt with in two ways: an initial high-temperature (100-200 C) bakeout of all chamber elements to reduce outgassing, and differentially pumped regions separating low and high vacuum sections of the chamber.

Low temperature experiments need not be concerned with outgassing, but are often still interested in differential pumping. This is particularly true when large loads of unwanted gases are present, as with carrier gases used for supersonic expansion. In these situations one often uses cryogenic sorption pumps to achieve large pumping speeds and low pressures. Charcoal is a commonly used cryosorbent, as it is inexpensive, offers a large surface area for adsorption, and can be easily regnerated by heating to refresh its pumping speed and capacity.

D.1 Sorbs in the buffer-gas BEC project

The buffer-gas BEC project presents a pumping challenge somewhat similar to that found in beam experiments using noble carrier gases. When operated as originally conceived the trapping chamber is periodically filled with helium buffer gas; after buffer-gas cooling a sample of interest the helium must be evacuated from the cell to provide good vacuum and to thermally disconnect the trapped sample from its environment. This provides an intermittent but large gas load that must be rapidly pumped away — a problem seemingly well suited to the large pumping speed and capacity offered by cryosorption.

As described briefly in section 2.1.2 and in detail in Robert Michniak's thesis [88, §5.7], this plan for achieving good vacuum did not achieve the performance desired. Data indicated that the sorb did effectively pump out the vast majority of the buffer gas on timescales short enough to permit trapping of weakly magnetic species, but that the ultimate vacuum was limited to densities of approximately $n_{He} = 10^{12}$ cm^{-3}. A model was developed to explain the poor vacuum quality based on the presence of a thin helium film coating the walls of the cell. Atoms in this film are bound to the wall with a continuum of binding energies ranging from > 100 K for the first monolayer [170] to approximately 4 K (the binding energy in bulk helium). The desorption time is assumed to behave in a way related to the Boltzmann factor,

$$t_D = t_o \mathrm{Exp}(E_b/k_B T_{wall}) \tag{D.1}$$

where E_b is the helium-wall binding energy and t_o is a constant of order 10^{-13} s [171, §4.3]. This suggests that weakly bound layers rapidly desorb and can be pumped away, while intermediate layers continue desorbing over the timescale of the experiment, poisoning the vacuum.

Based on this model a plan for managing the film was developed that mirrors the baking-out of room temperature vacuum chambers. After loading the atoms into the trap the cell temperature is deliberately elevated above its base temperature, desorbing more helium from the film such that it can be pumped to the sorb. After briefly holding the cell at the elevated temperature to allow the sorb to pump out the desorbed helium, the cell is allowed to cool; because weakly bound helium has been desorbed and pumped away, cooling the cell should lock remaining layers to the wall. Putting this plan into practice did significantly improve the vacuum in the cell [88], but some questions remained. In particular, given that the pumpout time for the cell could be measured in tens of milliseconds, bakeouts of order a few seconds should have been adequate, yet much longer bakeouts were necessary. Also, vacuum quality was inconsistent; on some days bakeouts seemed to lead to very low background gas densities, while on others they were less effective.

D.2 Adding a dilution refrigerator

Despite some uncertainty between the model and the actual cell vacuum, we elected to go ahead and add a dilution refrigerator to the apparatus with the expectation of dramatically improving vacuum quality and eliminating the need for bakeouts. Generally speaking we expected that loading the trap with the cell at several hundred milliKelvin and then letting it cool to < 200 mK would completely solve the film problem (the vapor density of ^{4}He at 200 mK is $\ll 10^{10}$ cm^{-3} — see figure 3.1). Combined with the rapid pumpout of the majority of the buffer gas to the sorb, this would make loading of weakly magnetic atoms straightforward, in keeping with the original goal of the valved buffer-gas cell.

Early reports were positive. At the very beginning of the first cooldown with the dilution refrigerator we were able to load the trap with ^{4}He* and efficiently evaporatively cool without any bakeout whatsoever. This performance rapidly degraded, however, and we began utilizing bakeouts, as described in section 4.1.2. Even with bakeouts the vacuum would degrade steadily with time over a period of a few weeks, but could be restored by baking out the pumping sorb to temperatures of order 20-30 K while pumping on the cell with a turbopump[1].

D.3 Sorb behavior at low coverages

Clearly this behavior is not in agreement with the simple model for cell vacuum described above, whereby a cold cell wall should have prevented helium desorption and led to superb vacuum. The shortcoming comes from treating the sorb itself as an essentially perfect pump. Naively we might assume it behaves according to the same model; the He-charcoal binding energy is large, and the sorb's enormous surface area should permit all of the helium to bind directly to the charcoal, eliminating the problem caused by the smaller binding energies in second, third, . . . monolayers. However, this is clearly not the entire story; much of the sorb's surface area is tucked deep inside the individual charcoal grains and is not directly accessible to incoming helium atoms, so for the naive model to hold an adsorbed helium atom must be able to somehow negotiate its way into the inside of the grain where it can find a tight binding site. After adsorbing helium onto the small amount of area this is directly accessible, then, sorb performance must become a question of surface mobility: how

---

[1] The vacuum also degraded over a much longer timescale (many months) in a way not healed by 30 K bakeouts, nor did a 150 K bakeout help. Warming up to room temperature and baking to 330 K while pumping overnight did solve the problem, which we attribute to epoxy or other cell materials slowly clogging the sorb as they were etched out of the walls by the RF discharge used to produce metastable atoms.

well can helium permeate the charcoal grains?

D.3.1 Studies of adsorbed helium

Perhaps somewhat surprisingly, this is a question which has received a startling amount of attention in the literature, both experimentally and theoretically [172]. Unfortunately, the system is decidedly difficult to understand theoretically, as behavior for adsorption onto nearly all real surfaces is dominated by the existence of surface inhomogeneities. On an idealized uniform, inert surface the ground state of adsorbed helium has been calculated to be a 2D liquid with a a lateral binding energy of only 0.6 K [173]. In contrast, experiments with ^{4}He plated onto copper indicated a lower limit for the lateral evaporation of the 2D solid phase to be 60 K [174], with the adsorbed helium behaving like a solid for all temperatures low enough to keep the majority of it adsorbed onto the surface.

In an effort to better understand the behavior of the adsorbed helium, extensive thermodynamic studies have been performed of helium adsorbed at sub-monolayer coverages onto Grafoil, a flexible exfoliated graphite sheet material [125, 175]. Evidently Grafoil consists almost entirely of basal-plane graphite, making it extremely energetically uniform across distinct adsorption sites, and thus providing a good experimental platform for comparison with theory. Whereas previous studies with other materials had seen only solid-like behavior, these studies indicate the presence of a a number of distinct phases for the adsorbed helium in different regimes of temperature and coverage.

At very low coverages solid behavior was still observed, presumably due to the adsorbed helium preferentially binding to a limited number of extremely tight binding sites, the behavior thus still being dominated by surface inhomogeneity. Similarly, at the lowest temperatures the helium forms ordered lattice gases, and at high coverages approaching a full monolayer the adsorbed helium forms a solid once enough of the adsorption sites are filled to limit surface mobility. However, for a wide range of coverages at temperatures above ~ 2 K the adsorbed helium is gas-like and able to move freely about the Grafoil surface. A more recent theoretical study that considers the effects of substrate corrugation agrees with the data, and confirms the role of surface inhomogeneities in enforcing the solid phase for most adsorbing materials.

D.3.2 Suggestions for future sorb use

What, then, does this mean for use of charcoal sorbs in evaporative cooling experiments? Clearly having helium form a solid phase strictly registered to the substrate is a problem. Without surface mobility helium will only find its way to adsorption sites within charcoal grains by gaseous diffusion. Since the pores in the charcoal are small this is necessarily a slow process, so the timescale for adsorption to "buried" tight binding sites will be slow and the ambient pressure will be set by sites with lower binding energies. This implies that the charcoal must be maintained at a relatively large temperature (perhaps 7 K) to enforce large tunneling rates between binding sites. Unfortunately, in this temperature range the desorption time (equation D.1) is short and the ambient pressure too great for evaporative cooling.

A better alternative might be to try to use a sorb with large binding energies but small surface corrugation. Grafoil is the obvious choice. While its surface area is not nearly so great as that for charcoal (20 m^2/g [125] as opposed to> 1000 m^2/g [176]), this still corresponds to a monolayer capacity of ~ 10 cm^3/g (STP). Such a sorb would clearly not be adequate for a beam experiment with large gas loads, but might perform well for an evaporative cooling experiment like the one described here. A sorb constructed out of Grafoil with mass similar to our existing sorb (30 g) would thus be adequate for approximately 1000 cell loadings; a multi-layer sorb might easily have 5x as much capacity and would only require regeneration once a month or so.

Appendix E

Circuit diagrams

A number of pieces of home-built electronics were used in performing the work described in this thesis, ranging from small RC filters to op-amp based analog adding circuits and VCO drivers for laser frequency stabilization AOMs. Some more complicated circuits for laser frequency stabilization (PID) and magnetic trap stabilization (Humbucker, Howland current amplifier) as well as for magnetic trap shutoff (optically isolated magnet quencher) were designed and built by Jim MacArthur in the Electronic Instrument Design Lab. These circuit diagrams are included here as figures E.1 through E.7.

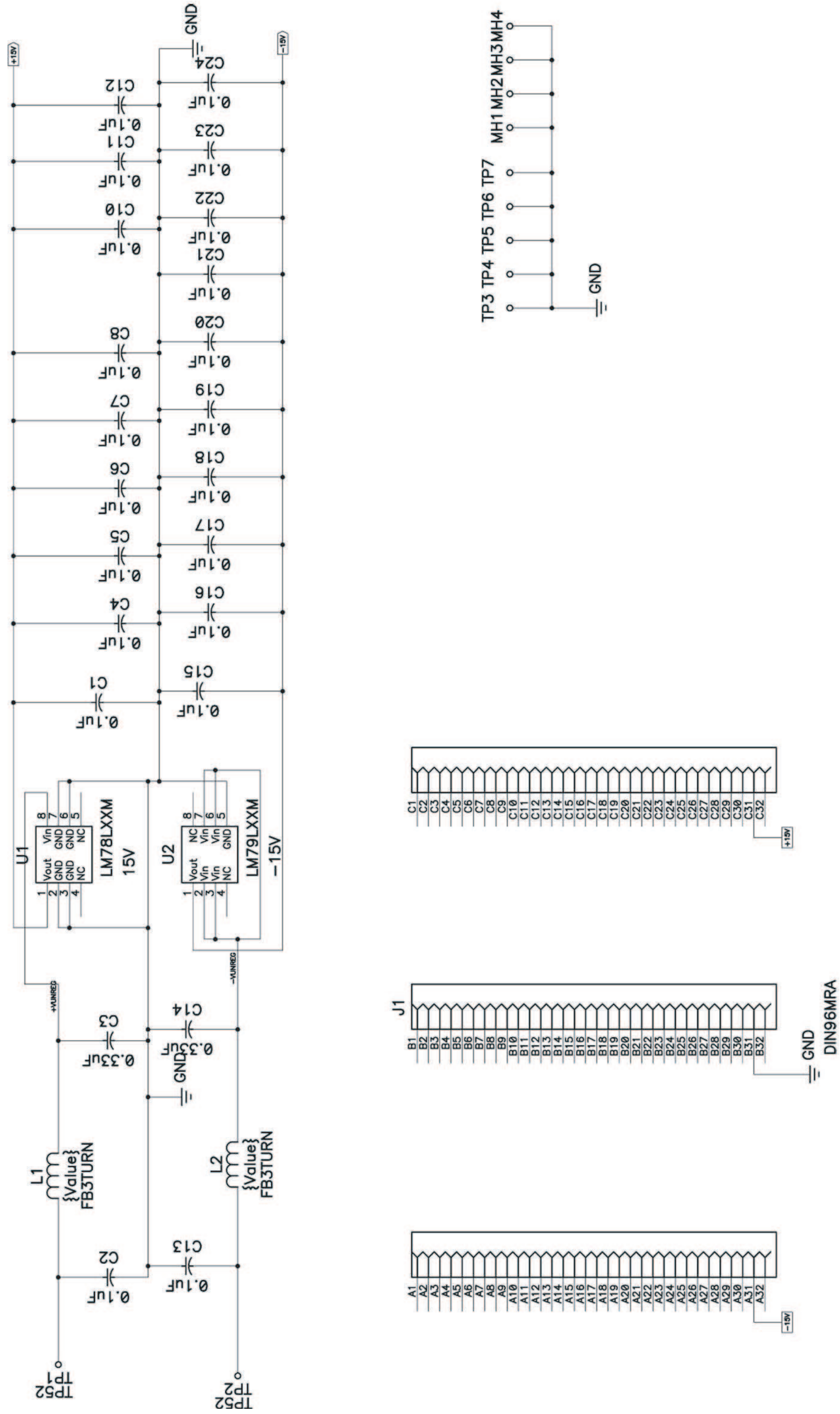

Figure E.1: Regulated ± 15 V supply for laser frequency stabilization PID.

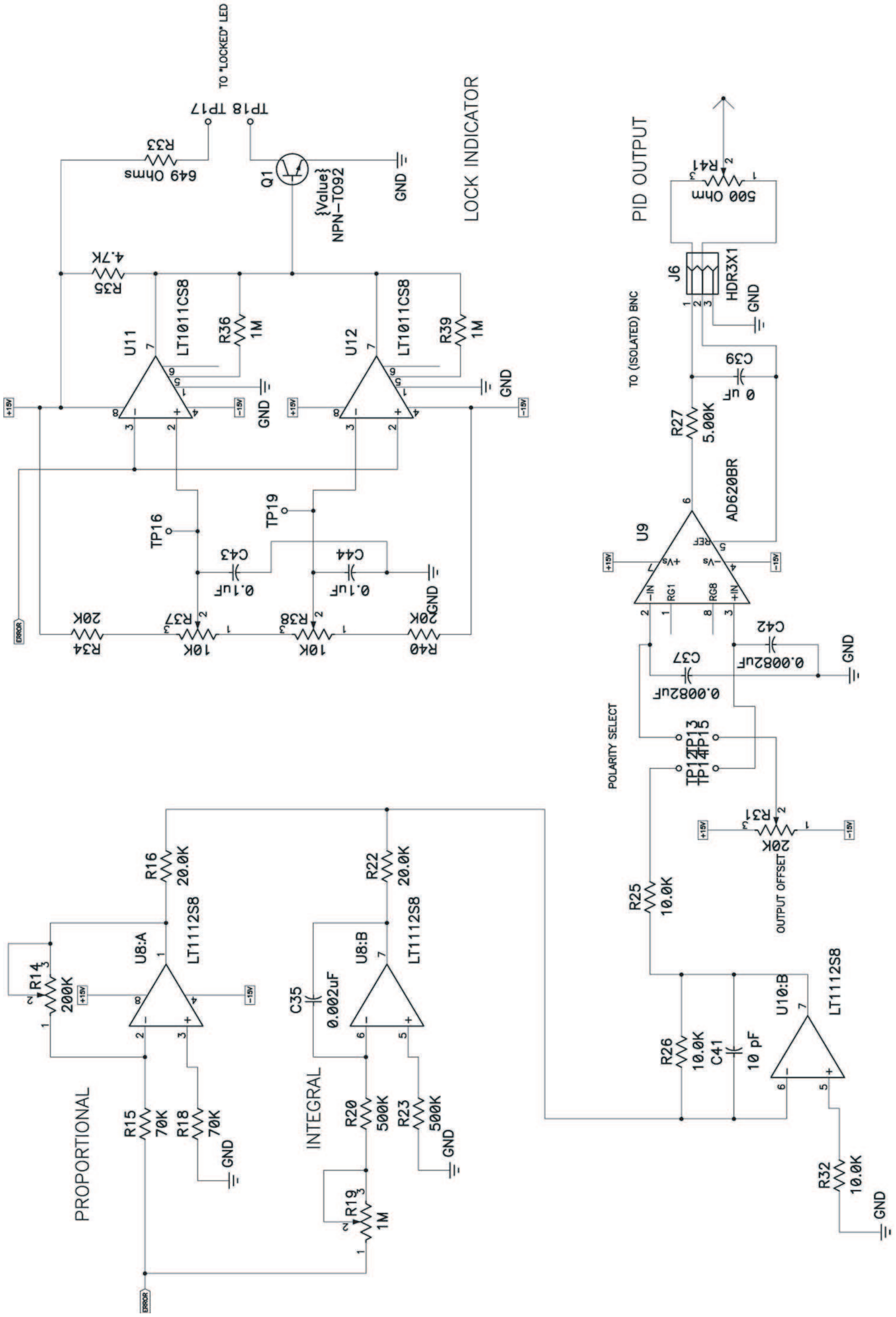

Figure E.2: PID controller (no "D" term) for laser frequency stabilization PID.

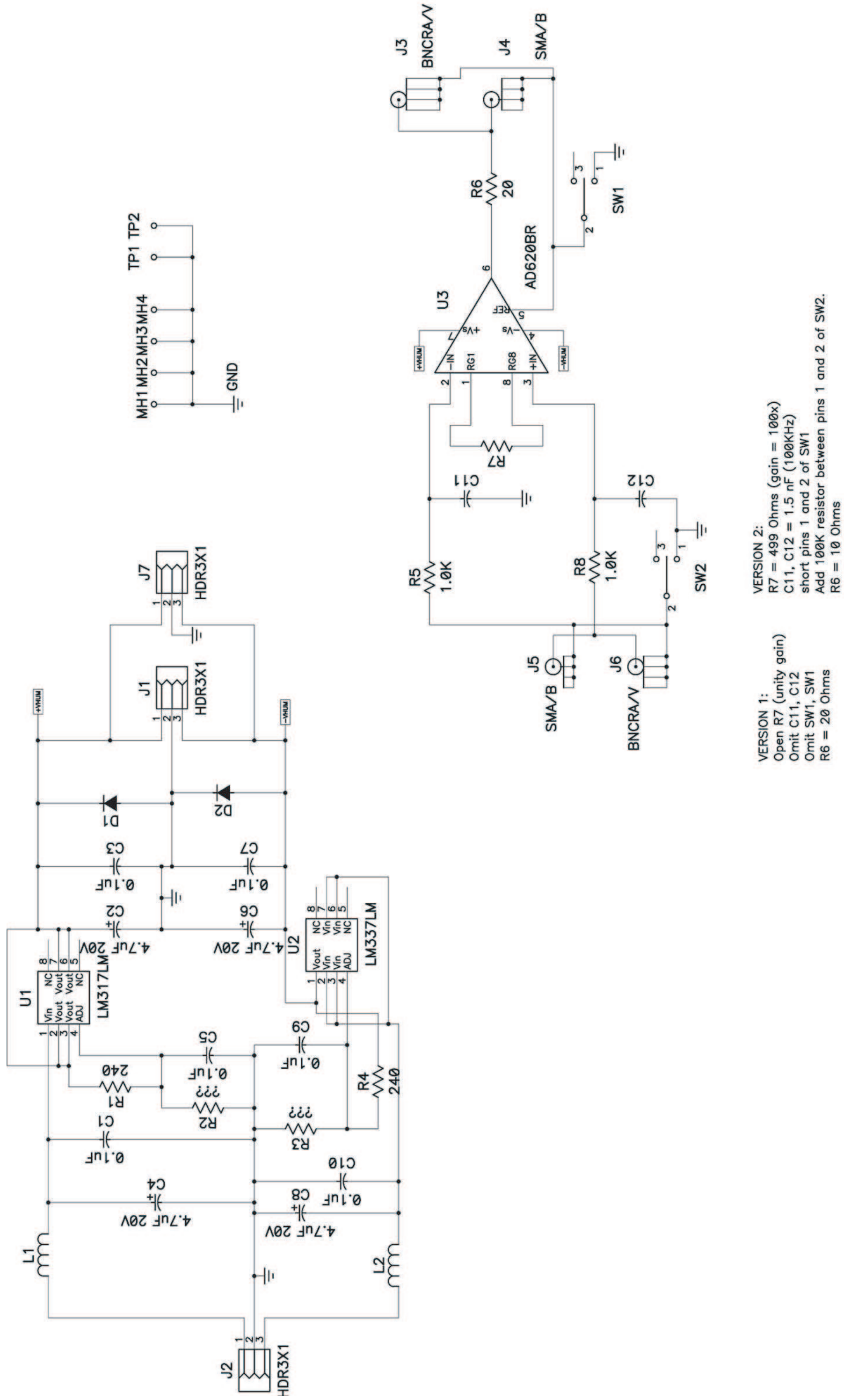

VERSION 2:
R7 = 499 Ohms (gain = 100x)
C11, C12 = 1.5 nF (100KHz)
short pins 1 and 2 of SW1
Add 100K resistor between pins 1 and 2 of SW2.
R6 = 10 Ohms

VERSION 1:
Open R7 (unity gain)
Omit C11, C12
Omit SW1, SW1
R6 = 20 Ohms

Figure E.3: "Humbucker" — instrumentation amp with ground-lift input and output switches and gain.

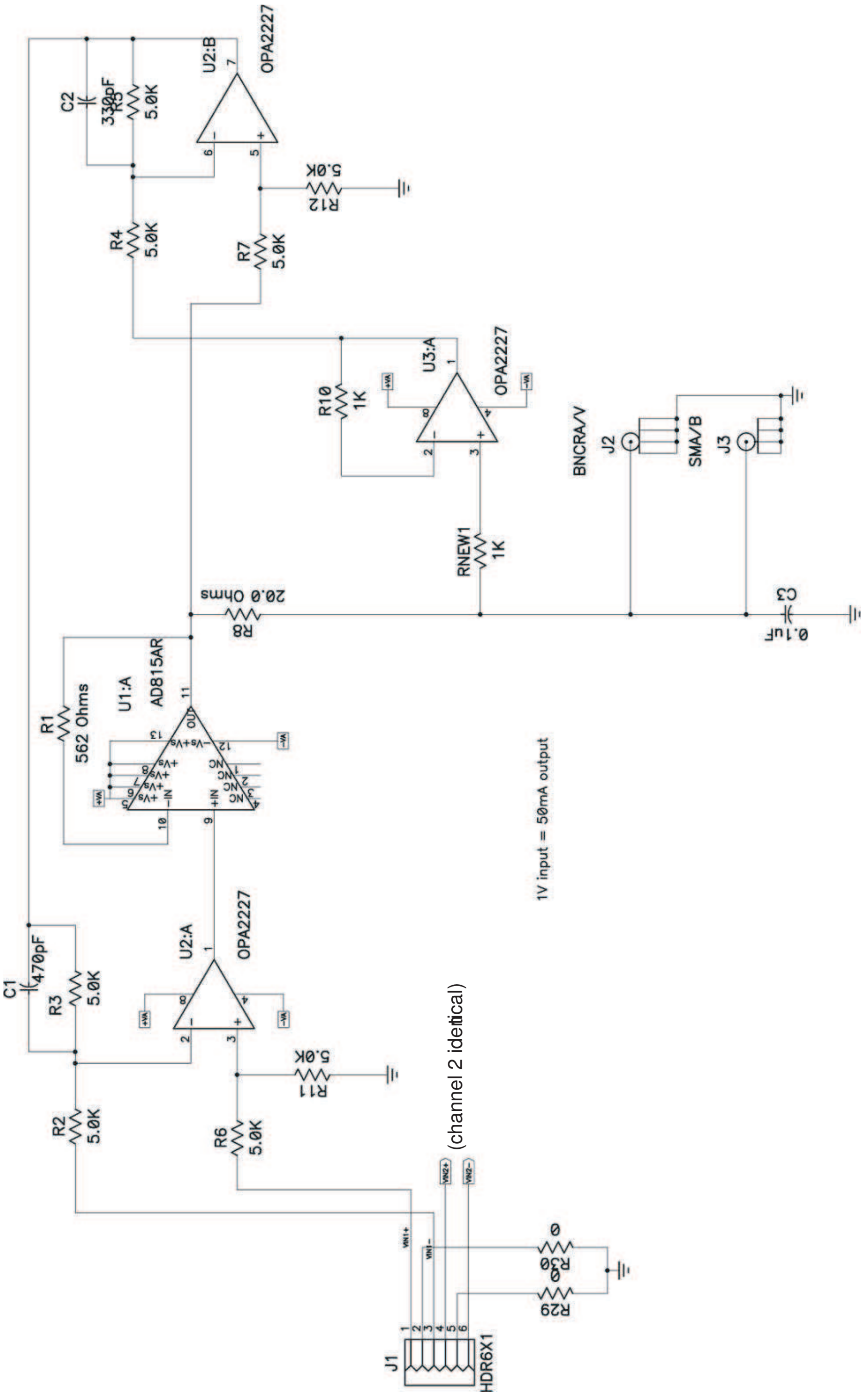

Figure E.4: Howland current amplifier.

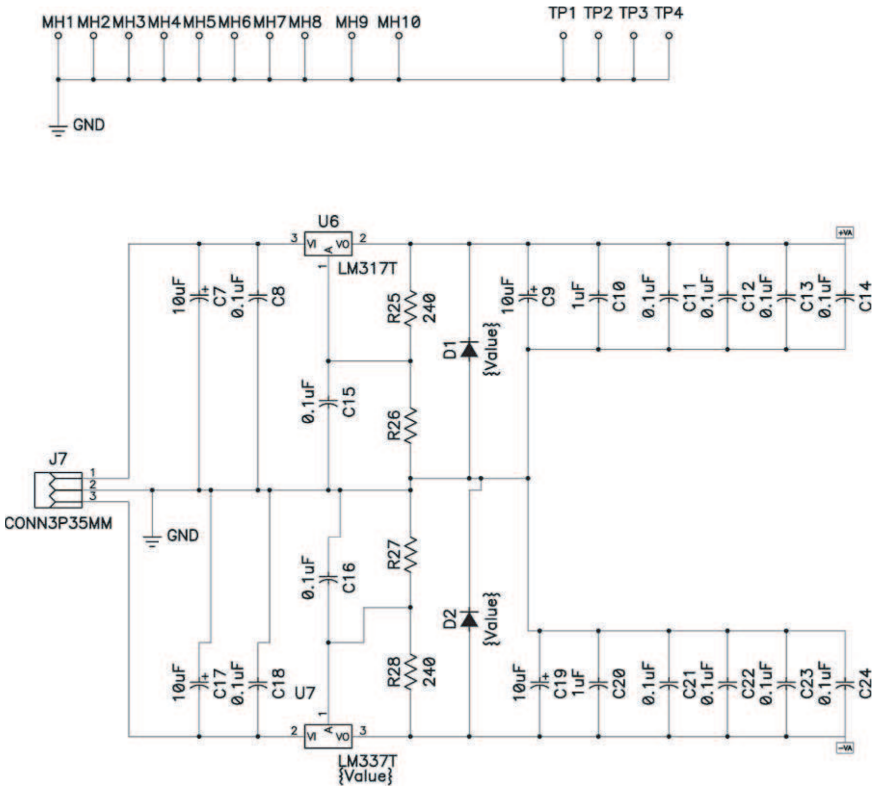

Figure E.5: Regulated voltage supply for Howland amplifier.

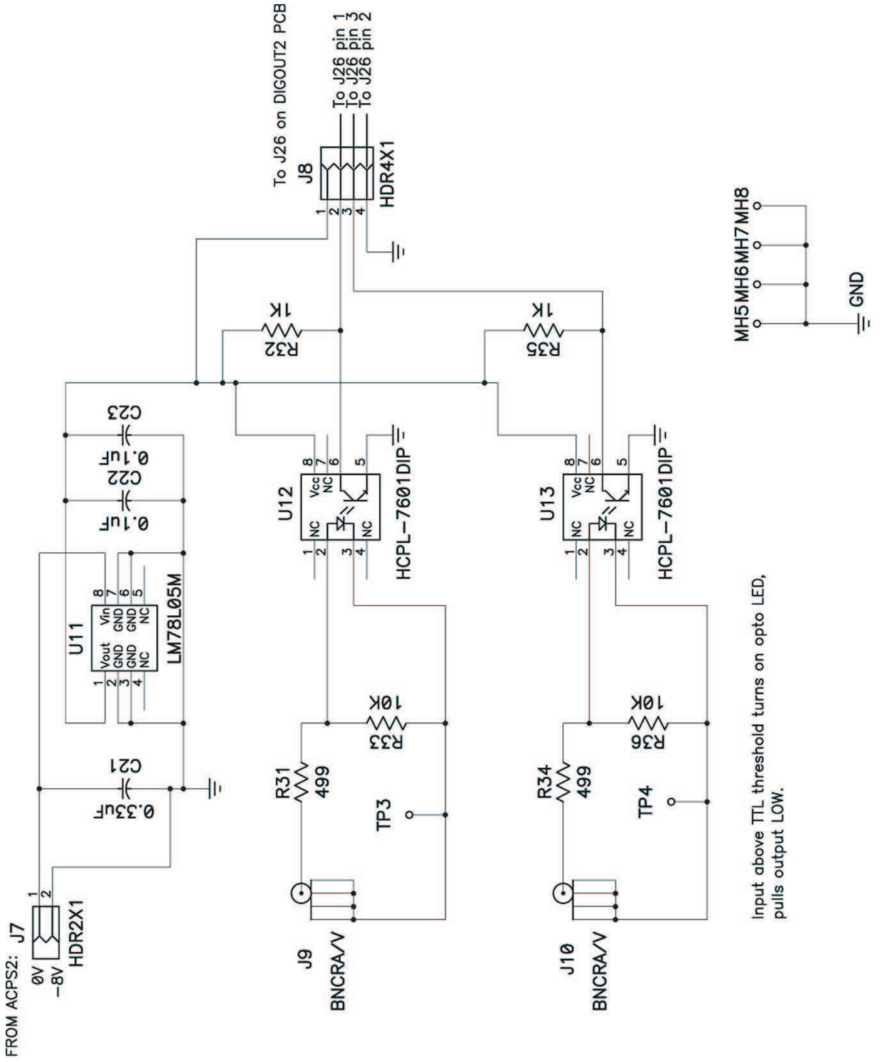

Input above TTL threshold turns on opto LED,
pulls output LOW.

Figure E.6: Magnet quencher optically isolated digital inputs.

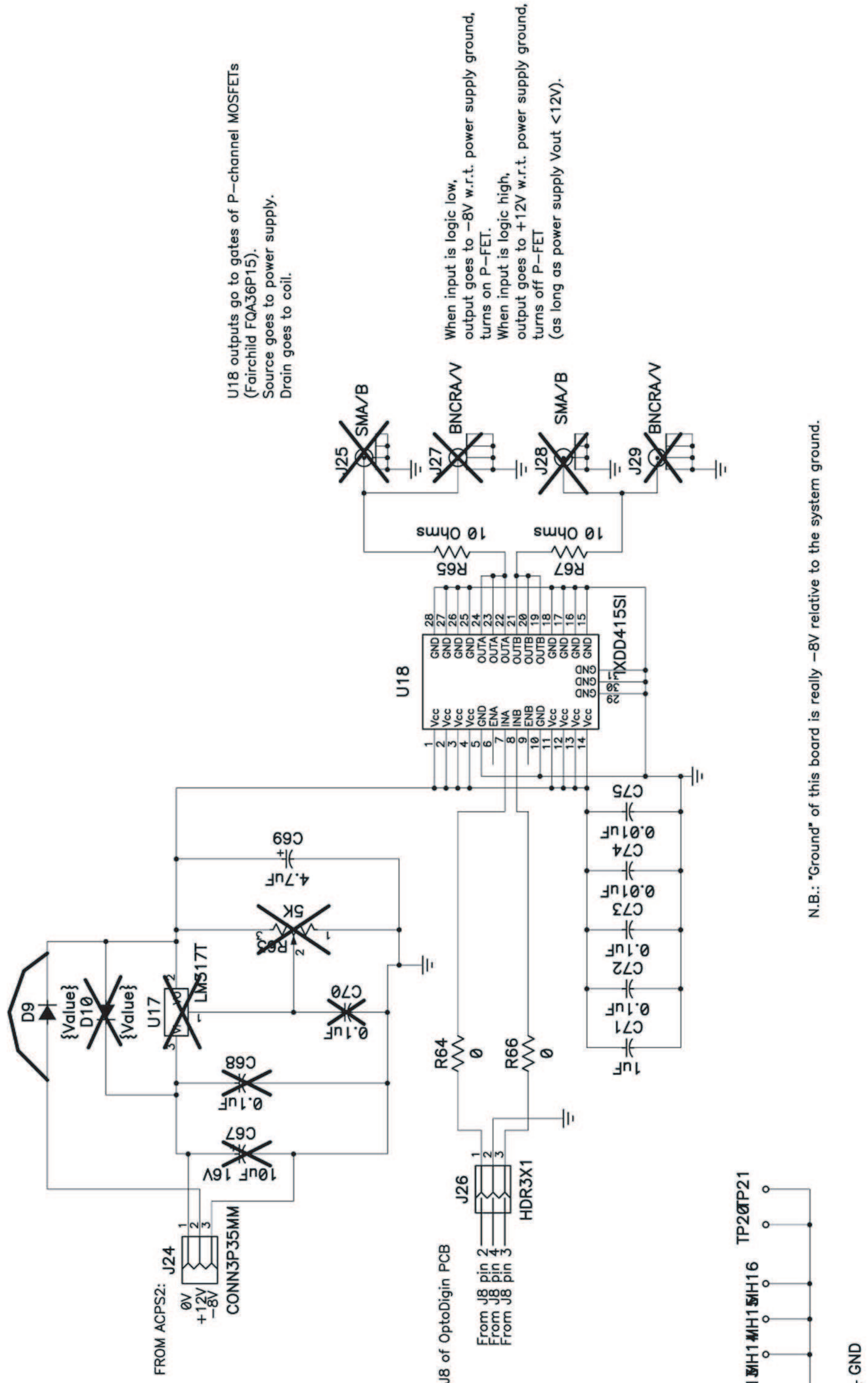

U18 outputs go to gates of P−channel MOSFETs
(Fairchild FQA36P15).
Source goes to power supply.
Drain goes to coil.

When input is logic low,
output goes to −8V w.r.t. power supply ground,
turns on P−FET.
When input is logic high,
output goes to +12V w.r.t. power supply ground,
turns off P−FET
(as long as power supply Vout <12V).

N.B.: "Ground" of this board is really −8V relative to the system ground.

Figure E.7: Magnet quencher digital outputs to MOSFETS.

Bibliography

[1] S. Charles Doret et al. Buffer-gas cooled Bose-Einstein condensate. *Phys. Rev. Lett.* **103**, 103005 (2009).

[2] Scott V. Nguyen et al. Evaporative cooling of metastable helium in the multi-partial-wave regime. *Phys. Rev. A* **72**, 060703(R) (2005).

[3] S. N. Bose. Plancks gesetz und lichtquantenhypothese. *Z. Phys.* **26**, 178 (1924).

[4] Albert Einstein. Quantentheorie des einatomigen idealen gases. *Sitzungsber. Kgl. Preuss. Akad. Wiss.* , 261 (1924).

[5] Albert Einstein. Quantentheorie des einatomigen idealen gases (2nd paper). *Sitzungsber. Kgl. Preuss. Akad. Wiss.* , 3 (1925).

[6] F. London. The λ-phenomenon of liquid helium and the Bose-Einstein degeneracy. *Nature* **141**, 643–644 (1938).

[7] M. H. Anderson et al. Observation of Bose-Einstein condensation in a diulte atomic vapor. *Science* **269**, 198–201 (1995).

[8] K. B. Davis et al. Bose-Einstein condensation in a gas of sodium atoms. *Phys. Rev. Lett.* **75**, 3969–3973 (1995).

[9] C. C. Bradley et al. Evidence of Bose-Einstein condensation in an atomic gas with attractive interactions. *Phys. Rev. Lett.* **75**, 1687–1690 (1995).

[10] Dale G. Fried et al. Bose-Einstein condensation of atomic hydrogen. *Phys. Rev. Lett.* **81**, 3811–3814 (1998).

[11] A. Robert et al. A Bose-Einstein condensate of metastable atoms. *Science* **292**, 461–464 (2001).

[12] F. Pereira Dos Santos et al. Bose-Einstein condensation of metastable helium. *Phys. Rev. Lett.* **86**, 3459–3462 (2001).

[13] G. Modugno et al. Bose-Einstein condensation of potassium atoms by sympathetic cooling. *Science* **294**, 1320–1322 (2001).

[14] Tino Weber et al. Bose-Einstein condensation of cesium. *Science* **299**, 232–235 (2003).

[15] Yosuke Takasu et al. Spin-singlet Bose-Einstein condensation of two-electron atoms. *Phys. Rev. Lett.* **91**, 040404 (2003).

[16] Axel Griesmaier et al. Bose-Einstein condensation of chromium. *Phys. Rev. Lett.* **94**, 160401 (2005).

[17] B. DeMarco and D. S. Jin. Onset of Fermi degneracy in a trapped atomic gas. *Science* **285**, 1703–1706 (1999).

[18] Truscott et al. Observation of Fermi pressure in a gas of trapped atoms. *Science* **291**, 2570–2572 (2001).

[19] M.R. Andrews et al. Observation of interference between two Bose condensates. *Science* **275**, 637–641 (1997).

[20] J.R. Abo-Shaeer et al. Coherent molecular optics using ultracold sodium dimers. *Phys. Rev. Lett.* **94**, 040405 (2005).

[21] S. Inouye et al. Phase-coherent amplification of atomic matter waves. *Nature* **402**, 641–644 (1999).

[22] L. Deng et al. Four-wave mixing with matter waves. *Nature* **398**, 218–220 (1999).

[23] M.W. Zwierlein et al. Vortices and superfluidity in a strongly interacting Fermi gas. *Nature* **435**, 1047–1051 (2005).

[24] K.W. Madison et al. Vortex formation in a stirred Bose-Einstein condensate. *Phys. Rev. Lett.* **84**, 806–809 (2000).

[25] C. A. Regal, M. Greiner, and D. S. Jin. Observation of resonance condensation of fermionic atom pairs. *Phys. Rev. Lett.* **92**, 040403 (2004).

[26] M. W. Zwierlein et al. Condensation of pairs of Fermionic atoms near a Feshbach resonance. *Phys. Rev. Lett.* **92**, 120403 (2004).

[27] M. Bartenstein et al. Crossover from a molecular Bose-Einstein condensate to a degenerate Fermi gas. *Phys. Rev. Lett.* **92**, 120401 (2004).

[28] C. Chin et al. Observation of the pairing gap in a strongly interacting Fermi gas. *Science* **305**, 1128–1130 (2004).

[29] J. Stenger et al. Spin domains in ground-state Bose-Einstein condensates. *Nature* **396**, 345–348 (1998).

[30] Markus Greiner et al. Quantum phase transition from a superfluid to a Mott insulator in a gas of ultracold atoms. *Nature* **415**, 39–44 (2002).

[31] T. W. Hansch and A. L. Schawlow. Cooling of gases by laser radiation. *Opt. Comm.* **13**, 68–69 (1975).

[32] D. J. Wineland and H. Dehmelt. *Bull. Am. Phys. Soc.* **20**, 637 (1975).

[33] Harold J. Metcalf and Peter van der Straten. *Laser cooling and trapping.* Springer, Berlin, 1999.

[34] David E. Pritchard. Cooling neutral atoms in a magnetic trap for precision spectroscopy. *Phys. Rev. Lett.* **51**, 1336–1339 (1983).

[35] Alan L. Migdall, John V. Prodan, and William D. Phillips. First observation of magnetically trapped neutral atoms. *Phys. Rev. Lett.* **54**, 2596–2599 (1985).

[36] Harold F. Hess. Evaporative cooling of magnetically trapped and compressed spin-polarized hydrogen. *Phys. Rev. B* **34**, 3476–3479 (1986).

[37] Wolfgang Ketterle and N. J. van Druten. Evaporative cooling of trapped atoms. *Adv.At. Mol. Opt. Phys.* **37**, 181–231 (1996).

[38] D. Sesko et al. Collisional losses from a light-force atom trap. *Phys. Rev. Lett.* **63**, 961–964 (1989).

[39] Thad Walker, David Sesko, and Carl Wieman. Collective behavior of optically trapped neutral atoms. *Phys. Rev. Lett.* **64**, 408–411 (1990).

[40] Wolfgang Ketterle et al. High densities of cold atoms in a dark spontaneous-force optical trap. *Phys. Rev. Lett.* **70**, 2253–2256 (1993).

[41] Manish Gupta and Dudley Herschbach. A mechanical means to produce intense beams of slow molecules. *J. Phys. Chem. A* **103**, 10670–10673 (1999).

[42] E. Narevicius et al. Coherent slowing of a supersonic beam with an atomic paddle. *Phys. Rev. Lett.* **98**, 103201 (2007).

[43] Hendrick L. Bethlem et al. Alternate gradient focusing and deceleration of a molecular beam. *Phys. Rev. Lett.* **88**, 133003 (2002).

[44] Edvardas Narevicius et al. Stopping supersonic beams with a series of pulsed electromagnetic coils: an atomic coilgun. *Phys. Rev. Lett.* **100**, 093003 (2008).

[45] John M. Doyle et al. Buffer-gas loading of atoms and molecules into a magnetic trap. *Phys. Rev. A* **52**, R2515–2518 (1995).

[46] W. Campbell and J.M. Doyle. *Cold Polar Molecules: Theory, Experiment, Applications*, Chapter 13: Cooling, trap loading, and beam production using a cryogenic helium buffer gas, 473–501. Taylor and Francis, Boca Raton, 2009.

[47] D. B. Sullivan et al. Primary atomic frequency standards at NIST. *J. Res. Natl. Inst. Stand. Technol.* **106**, 47–63 (2001).

[48] A. D. Ludlow et al. Sr lattice clock at 1×10^{-16} fractional uncertainty by remote optical evaluation with a Ca clock. *Science* **319**, 1805–1808 (2008).

[49] T. Rosenband et al. Frequency ratio of Al^+ and Hg^+ single-ion optical clocks: Metrology at the 17th decimal place. *Science* **319**, 1808–1812 (2008).

[50] S. Schiller and V. Korobov. Tests of time independence of the electron and nuclear masses with ultracold molecules. *Phys. Rev. A* **71**, 032505 (2005).

[51] B. E. Sauer et al. *Probing the electron EDM with cold molecules*, 44. AIP, 2006.

[52] Amar C. Vutha et al. Search for the electron's electric dipole moment with a cold molecular beam of ThO. In *DAMOP Bulletin* , 2008.

[53] Thad Walker and Paul Feng. Measurements of collisions between laser-cooled atoms. *Adv. At. Mol. Opt. Phys.* **34**, 125–170 (1994).

[54] J. L. Roberts et al. Resonant magnetic field control of elastic scattering in cold ^{85}Rb. *Phys. Rev. Lett.* **81**, 5109–5112 (1998).

[55] Wesley C. Campbell et al. Mechanism of collisional spin relaxation in $^3\Sigma$ molecules. *Phys. Rev. Lett.* **102**, 013003 (2009).

[56] T. V. Tscherbul and R. V. Krems. Controlling electronic spin relaxation of cold molecules with electric fields. *Phys. Rev. Lett.* **97**, 083201 (2006).

[57] C. Orzel et al. Squeezed states in a Bose-Einstein condensate. *Science* **291**, 2386–2389 (2001).

[58] D. S. Durfee, Y. K. Shaham, and M. A. Kasevich. Long-term stability of an atom-interferometer Sagnac gyroscope. *Phys. Rev. Lett.* **97**, 240801 (2006).

[59] M. Schellekens et al. Hanbury-Brown Twiss effect for ultracold quantum gases. *Science* **310**, 648 (2005).

[60] T. Jeltes et al. Comparison of the Hanbury-Brown Twiss effect for Bosons and Fermions. *Nature* **445**, 402–405 (2007).

[61] Immanuel Bloch, Jean Dalibard, and Wilhelm Zwerger. Many-body physics with ultracold gases. *Rev. Mod. Phys.* **80**, 885–964 (2008).

[62] S. Inouye et al. Observation of Feshbach resonances in a Bose-Einstein condensate. *Nature* **392**, 151–154 (1998).

[63] Ph. Courteille et al. Observation of a Feshbach resonance in cold atom scattering. *Phys. Rev. Lett.* **81**, 69–72 (1998).

[64] W. Hofstetter et al. High-temperature superfluidity of Fermionic atoms in optical lattices. *Phys. Rev. Lett.* **89**, 220407 (2002).

[65] J. I. Cirac and P. Zoeller. Quantum computation with trapped ions. *Phys. Rev. Lett.* **74**, 4091–4094 (1995).

[66] D. DeMille. Quantum computation with trapped polar molecules. *Phys. Rev. Lett.* **88**, 067901 (2002).

[67] A. Andre et al. A coherent all-electrical interface between polar molecules and mesoscopic superconducting resonantors. *Nature Phys.* **2**, 636–642 (2006).

[68] Andre Derevianko and Caleb C. Cannon. Quantum computing with magnetically interacting atoms. *Phys. Rev. A* **70**, 062319 (2004).

[69] A. V. Gorshkov et al. Alkaline-earth-metal atoms as few-qubit quantum registers. *Phys. Rev. Lett.* **102**, 110503 (2009).

[70] T. Chaneliere et al. Quantum telecommunication based on atomic cascade transitions. *Phys. Rev. Lett.* **96**, 093604 (2006).

[71] Johannes Stiehler and Juergen Hinze. Calculation of static polarizabilities and hyperpolarizabilities for the atoms He through Kr with a numerical RHF method. *J. Phys. B: At. Mol. Opt. Phys.* **28**, 4055–4071 (1995).

[72] Hendrick L. Bethlem et al. Electrostatic trapping of ammonia molecules. *Nature* **406**, 491–494 (2000).

[73] T. Rieger et al. Trapping of neutral rubidium with a macroscopic three-phase electric trap. *Phys. Rev. Lett.* **99**, 063001 (2007).

[74] D. DeMille, D. R. Glenn, and J. Petricka. Microwave traps for cold polar molecules. *Eur. Phys. J. D* **31**, 375–384 (2004).

[75] J.G.E. Harris et al. Buffer gas cooling and trapping of atoms with small effective magnetic moments. *Europhysics Letters* **67**, 198–204 (2004).

[76] M. D. Barrett, J. A. Sauer, and M. S. Chapman. All-optical formation of an atomic Bose-Einstein condensate. *Phys. Rev. Lett.* **87**, 010404 (2001).

[77] M. D. DiRosa. Laser-cooling molecules. *Eur. Phys. J. D* **31**, 395–402 (2004).

[78] Benjamin K. Stuhl et al. Magneto-optical trap for polar molecules. *Phys. Rev. Lett.* **101**, 243002 (2008).

[79] Moritz Kirste et al. Nonadiabatic transitions in electrostatically trapped ammonia molecules. *Phys. Rev. A* **79**, 05401(R) (2009).

[80] C. B. Connolly et al. Large spin relaxation rates in trapped submerged-shell atoms. (2009). submitted for publication.

[81] Mei-Ju Lu, Vijay Singh, and Jonathan D. Weinstein. Inelastic titanium-titanium collisions. *Phys. Rev. A* **79**, 050702(R) (2009).

[82] Cindy I. Hancox et al. Magnetic trapping of the rare-earths at millikelvin temperatures. *Nature* **431**, 281–284 (2004).

[83] S. E. Maxwell et al. Spin-orbit interaction and large inelastic rates in bismuth-helium collisions. *Phys. Rev. A* **78**, 042706 (2008).

[84] Mei-Ju Lu, Kyle S. Hardman, and Jonathan D. Weinstein. Fine-structure-changing collisions in atomic titanium. *Phys. Rev. A* **77**, 060701(R) (2008).

[85] N. Brahms et al. Formation and spin relaxation of van der Waals molecules in a magnetic trap. (2009). manuscript in preparation.

[86] Jinha Kim. *Buffer-gas loading and magnetic trapping of atomic europium.* PhD thesis, Harvard, 1997.

[87] Jonathan David Weinstein. *Magnetic trapping of atomic chromium and molecular calcium monohydride.* PhD thesis, Harvard, 2001.

[88] Robert Michniak. *Enhanced buffer gas loading: cooling and trapping of atoms with low effective magnetic moments.* PhD thesis, Harvard, 2004.

[89] Scott Vinh Nguyen. *Buffer gas loading and evaporative cooling in the multi-partial-wave regime.* PhD thesis, Harvard, 2006.

[90] Nathaniel Charles Brahms. *Trapping of 1 μ_B atoms using buffer gas loading.* PhD thesis, Harvard, 2008.

[91] A. Browaeys et al. Thermalization of magnetically trapped metastable helium. *Phys. Rev. A* **64**, 034703 (2001).

[92] Paul J. J. Tol et al. Large numbers of cold metastable helium atoms in a magneto-optical trap. *Phys. Rev. A* **60**, R761–R764 (1999).

[93] Stycast Epoxy
Emerson & Cuming, 46 Manning Road, Billerica, MA 01821
`www.emersoncuming.com`.

[94] J. Reichel, W. Hansel, and T.W. Hansch. Atomic micromanipulation with magnetic surface traps. *Phys. Rev. Lett.* **83**, 3398–3401 (1999).

[95] D. M. Harber et al. Thermally induced losses in ultracold atoms magnetically trapped near room-temperatures surfaces. *J. Low Temp. Phys.* **133**, 229–238 (2003).

[96] Jonathan D. Weinstein et al. Evaporative cooling of atomic chromium. *Phys. Rev. A* **65**, 021604 (2002).

[97] Scott V. Nguyen, Robert deCarvalho, and John M. Doyle. Cold ^{52}Cr elastic and inelastic collision-rate determination using evaporative cooling analysis. *Phys. Rev. A* **75**, 062706 (2007).

[98] Wolfgang Petrich et al. Stable, tightly confining magnetic trap for evaporative cooling of neutral atoms. *Phys. Rev. Lett.* **74**, 3352–3355 (1995).

[99] Kendall B. Davis et al. Evaporative cooling of sodium atoms. *Phys. Rev. Lett.* **74**, 5202–5205 (1995).

[100] Tillman Esslinger, Immanuel Bloch, and Theodor W. Hansch. Bose-Einstein condensation in a quadrupole-Ioffe-configuration trap. *Phys. Rev. A* **58**, R2664–2667 (1998).

[101] Y. H. Huang and G. B. Chen. A practical vapor pressure curve for ^{3}He from 0.01 K to the critical point. *Cryogenics* **46**, 833–839 (2006).

[102] Frank Pobell. *Matter and Methods at Low Temperatures.* 2nd edition. Springer, Berlin, 1996.

[103] MNK126-500 dilution refrigerator
Leiden Cryogenics B.V., Galgewater no. 21, 2311 VZ Leiden, The Netherlands
`www.leidencryogenics.com`.

[104] VCR fittings
The Swagelock Company, 29500 Solon Road, Solon, OH 44139, USA
`www.swagelok.com`.

[105] V-551 Turbopump
Varian, Inc. Corporate Headquarters, 3120 Hansen Way, Palo Alto, CA 94304-1030, USA
`www.varianinc.com/vacuum/`.

[106] XDS-10 scroll pump
BOC Edwards, Inc., 301 Ballardvale St, Wilmington, MA 01887-4440, (978) 658-5410
`www.edwardsvacuum.com`.

[107] Microtech ultra-miniature strip connectors
Microtech, Inc., 1420 Conchester Highway, Boothwyn, Penna, 19061
`www.mmm-microtech.com`.

[108] 2 and 4 pin connectors
International Circuit Sales 574 E Alamo Drive, suite 60, Chandler, AZ 85225.

[109] Lene Vestergaard Hau et al. Near-resonant spatial images of confined Bose-Einstein condensates in a 4-Dee magnetic bottle. *Phys. Rev. A* **58**, R54–57 (1998).

[110] M.-O. Mewes et al. Bose-Einstein condensation in a tightly confining dc magnetic trap. *Phys. Rev. Lett.* **77**, 416–419 (1996).

[111] T. Bergeman, Gidon Erez, and Harold J. Metcalf. Magnetostatic trapping fields for neutral atoms. *Phys. Rev. A* **35**, 1535–1546 (1987).

[112] W. Ketterle, D.S. Durfee, and D.M. Stamper-Kurn. *Bose-Einstein condensation in atomic gases*, Chapter Making, Probing, and Understanding Bose-Einstein Condensates, 67–176. IOS Press, Amsterdam, 1999.

[113] 54S43 multi-filament Cu:NbTi superconducting wire.
Supercon, Inc. 830 Boston Turnpike Rd. Shrewsbury, MA 01545
`www.supercon-wire.com`.

[114] Epon Epoxy
George Washington Hwy., Danbury, CT 06810
`www.miller-stephenson.com`.

[115] Carlo Egon Heinrich Mattoni. *Magnetic trapping of ultracold neutrons produced using a a monochromatic cold neutron beam.* PhD thesis, Harvard University, 2002.

[116] John David Jackson. *Classical Electrodynamics.* 3rd edition. John Wiley and Sons, Inc., New York, 1999.

[117] DL100 diode laser
TOPTICA Photonics Inc. 1286 Blossom Drive Victor, NY 14564
`www.toptica.com`.

[118] Model 1206C acousto-optic modulator.
Isomet Corporation 5263 Port Royal Road Springfield, VA 22151
`www.isomet.com`.

[119] Pixis 1024BR camera
Princeton Instruments - New Jersey, 3660 Quakerbridge Road, Trenton, NJ 08619 USA
`www.princetoninstruments.com`.

[120] Surelite pulsed YAG laser.
Continuum Lasers, 3150 Central Expressway, Santa Clara, CA 95051
`www.continuumlasers.com`.

[121] RF electronic components
Mini-Circuits P.O. Box 350166 Brooklyn, NY 11235 U.S.A.
`www.minicircuits.com`.

[122] RF amplifiers
1387 Brighton Henrietta Townline Road, Rochester, NY 14923 U.S.A.
`www.eandiltd.com`.

[123] Wolfgang Demtroder. *Laser Spectroscopy.* Springer, Berlin, 2003.

[124] Philip A. Lessard. Crogenic adsorption of noncondensibles in the high-vacuum regime. *J. Vac. Sci. Tech. A* **7**, 2373–2376 (1989).

[125] M. Bretz et al. Phases of ^{3}He and ^{4}He monolayer films adsorbed on basal-plane oriented graphite. *Phys. Rev. A* **8**, 1589–1614 (1973).

[126] Robert deCarvalho. *Inelastic scattering of magnetically trapped atomic chromium.* PhD thesis, Harvard University, 2003.

[127] S. Moal et al. Accurate determination of the scattering length of metastable helium atoms using dark resonances between atoms and exotic molecules. *Phys. Rev. Lett.* **96**, 023203 (2006).

[128] A. S. Tychkov et al. Metastable helium Bose-Einstein condensate with a large number of atoms. *Phys. Rev. A* **73**, 013603(R) (2006).

[129] 8647A RF synthesizer
Agilent Techologies, 5301 Stevens Creek Blvd Santa Clara, CA 95051 U.S.A.
`www.agilent.com`.

[130] AFG3022B arbitrary function generator
Tektronix, Inc. 14150 SW Karl Braun Drive, P. O. Box 500, Beaverton, OR 97077
`www.tektronix.com`.

[131] Amnon Yariv. *Optical electronics in modern communications.* Oxford University Press, New York, 1997.

[132] F. Zernike. Phase contrast: a new method for the microscopic observation of transparent objects (Parts I and II). *Physica* **9**, 686–698; 974–986 (1942).

[133] F. Zernike. How I discovered phase contrast imaging (Nobel lecture). *Science* **121**, 345–349 (1955).

[134] Optical coatings
Thin Film Labs, Inc. 112 Sawkill Road, Milford, PA 18337
`www.thinfilmlabs.com`.

[135] Shuyu Zhou et al. Parametric excitation of ^{87}Rb atoms in a quadrupole-Ioffe-configuration trap. *Phys. Rev. A* **75**, 053414 (2007).

[136] T. A. Savard, K. M. O'Hara, and J. E. Thomas. Laser-noise-induced heating in far-off resonance optical traps. *Phys. Rev. A* **56**, R1095–R1098 (1997).

[137] FNR 2-T227 resistors
Riedon, Inc. 300 Cypress Avenue, Alhambra, CA 91801
`www.riedon.com`.

[138] SIM 960 PID controller and chassis
Stanford Research Systems, Inc. 1290-D Reamwood Avenue Sunnyvale, CA 94089
`www.thinksrs.com`.

[139] P. W. Anderson. Theory of flux creep in hard superconductors. *Phys. Rev. Lett.* **9**, 309–311 (1962).

[140] D. A. Herrup et al. Time variatons of fields in superconducting magnets and their effects on accelerators. *IEEE Transactions on magnetics* **25**, 1643–1646 (1989).

[141] C. J. Pethick and H. Smith. *Bose-Einstein condensation in dilute gases.* Cambridge University Press, Cambridge, 2008.

[142] Y. Castin and R. Dum. Bose-Einstein condensates in time dependent traps. *Phys. Rev. Lett.* **77**, 5215–5219 (1996).

[143] P. Pedri, D. Guery-Odelin, and S. Stringari. Dynamics of a classical gas including dissipative and mean-field effects. *Phys. Rev. A* **68**, 043608 (2003).

[144] FQA36P15 P-channel MOSFET
Fairchild Semiconductor Corporation, 82 Running Hill Road, South Portland, ME 04106 USA
`www.fairchildsemi.com`.

[145] 5KP series transient voltage suppressors
Littelfuse World Headquarters, 8755 West Higgins Road Suite 500, Chicago, IL 60631 USA
`www.littelfuse.com`.

[146] Vanderlei Bagnato, David E. Pritchard, and Daniel Kleppner. Bose-Einstein condensation in an external potential. *Phys. Rev. A* **35**, 4354–4358 (1987).

[147] Timur Tscherbul. private communication.

[148] R. Onofrio et al. Observation of superfluid flow in a Bose-Einstein condensed gas. *Phys. Rev. Lett.* **85**, 2228–2231 (2000).

[149] Dale G. Fried. *Bose-Einstein condensation of atomic hydrogen.* PhD thesis, MIT, 1999.

[150] J. Deiglmayr et al. Formation of ultracold polar molecules in the rovibrational ground state. *Phys. Rev. Lett.* **101**, 133004 (2008).

[151] K.-K. Ni et al. A high phase-space-density gas of polar molecules. *Science* **322**, 231–235 (2008).

[152] Manuel Lara et al. Ultracold Rb-OH collisions and prospects for sympathetic cooling. *Phys. Rev. Lett.* **97**, 183201 (2006).

[153] Matthew T. Hummon et al. Magnetic trapping of atomic nitrogen (^{14}N) and cotrapping of NH ($X^3\Sigma^-$). *Phys. Rev. A* **78**, 050702(R) (2008).

[154] S. F. Adams and T. A. Miller. Two-photon absorption laser-induced fluorescence of atomic nitrogen by an alternative excitation scheme. *Chem. Phys. Lett.* **295**, 305–311 (1998).

[155] Matthew T. Hummon. *Magnetic trapping of atomic nitrogen and co-trapping of NH.* PhD thesis, Harvard University, 2009.

[156] G. Uhlenberg, J. Dirscherl, and H. Walther. Magneto-optical trapping of silver atoms. *Phys. Rev. A* **62**, 063404 (2000).

[157] Nathan Brahms et al. Magnetic trapping of silver and copper, and anomalous spin relaxation in the Ag-He system. *Phys. Rev. Lett.* **101**, 103002 (2008).

[158] J. Y. Zhang et al. Long-range interactions of copper and silver atoms with hydrogen, helium, and rare-gas atoms. *Phys. Rev. A* **78**, 062710 (2008).

[159] Kramida A.E. Reader J. Ralchenko, Yu. and NIST ASD Team (2008). NIST Atomic Spectra Database (version 3.1.5). National Institute of Standards and Technology, Gaithersburg, MD.
`http://physics.nist.gov/asd3`.

[160] V. N. Faddeyeva. *Tables of values of the function* $w(z) = \mathrm{Exp}[-z^2](1 + (2i\sqrt{\pi}) \int_0^\infty \mathrm{Exp}[-t^2]\ dt)$ *for complex argument.* Pergamon Press, 1961.

[161] Araya Asfaw. A fast method of modeling spectral lines. *J. Quant. Spec. Rad. Trans.* **70**, 129–137 (2001).

[162] Mofreh R. Zaghloul. Comment on "a fast method of modeling spectral lines". *J. Quant. Spec. Rad. Trans.* **109**, 2895–2897 (2008).

[163] Jan. R. Rubbmark et al. Dynamical effects at avoided level crossings: a study of the Landau-Zener effect using Rydberg atoms. *Phys. Rev. A* **23**, 3107–3117 (1981).

[164] N. V. Vitanov and K.-A Suominen. Time-dependent control of ultracold atoms in magnetic traps. *Phys. Rev. A* **56**, R4377–R4380 (1997).

[165] W. Z. Zhao et al. A computer-based digital feedback control of frequency drift of multiple lasers. *Rev. Sci. Inst.* **69**, 3737–3740 (1998).

[166] A. D. Ludlow et al. Compact, thermal-noise-limited optical cavity for diode laser stabilization at 1×10^{-15}. *Opt. Lett.* **32**, 641–643 (2007).

[167] K. B. MacAdam, A. Steinbach, and C. Wieman. A narrow-band tunable diode laser system with grating feedback and a saturated absorption spectrometer for Cs and Rb. *Am J. Phys.* **60**, 1098–1111 (1992).

[168] J. C. J. Koelemeij, W. Hogervorst, and W. Vassen. High-power frequency-stabilized laser for laser cooling of metastable helium at 389 nm. *Rev. Sci. Inst.* **76**, 033104 (2005).

[169] E. A. Donley et al. Double-pass acousto-optic modulator system. *Rev. Sci. Inst.* **76**, 063112 (2005).

[170] G. Vidali et al. Potentials of physical adsorption. *Surface Science Reports* **12**, 133–181 (1991).

[171] Alexander Roth. *Vacuum technology.* 3rd edition. Elsevier, Amsterdam, 1990.

[172] D. M. Young and A. D. Crowell. *Physical adsorption of gases.* Butterworths, Washington, 1962.

[173] C. E. Campbell and M. Schick. Ground state of ^{4}He monolayers adsorbed on inert substrate. *Phys. Rev. A* **3**, 691–696 (1971).

[174] D. W. Princehouse. High-resolution heat-capacity study of ^{4}He adsorbed on bare copper. *J. Low Temp. Phys.* **8**, 287–303 (1971).

[175] Robert L. Elgin and David L. Goodstein. Thermodynamic study of the ^{4}He monolayer adsorbed on Grafoil. *Phys. Rev. A* **9**, 2657–2675 (1974).

[176] Christian Day. The use of active carbons as cryosorbent. *Colloids and Surfaces A* **187**, 187–206 (2001).